LATE QUATERNARY CLIMATE VARIABILITY AND TERRESTRIAL CARBON CYCLING IN TROPICAL SOUTH AMERICA

By

Kyrstin L. Fornace

S.B., Massachusetts Institute of Technology, 2009

Submitted in partial fulfillment of the requirements for the degree of
Doctor of Philosophy
at the
MASSACHUSETTS INSTITUTE OF TECHNOLOGY
and the
WOODS HOLE OCEANOGRAPHIC INSTITUTION

February 2016

Author _____

Joint Program in Chemical Oceanography
Massachusetts Institute of Technology
and Woods Hole Oceanographic Institution
December 18, 2015

Certified by _____

Valier Galy
Thesis Co-Supervisor

Certified by _____

Konrad A. Hughen
Thesis Co-Supervisor

Accepted by _____

Elizabeth B. Kujawinski
Chair, Joint Committee for Chemical Oceanography

LATE QUATERNARY CLIMATE VARIABILITY AND TERRESTRIAL CARBON CYCLING IN TROPICAL SOUTH AMERICA

By

Kyrstin L. Fornace

Submitted to the MIT/WHOI Joint Program in Chemical Oceanography on December 18, 2015 in partial fulfillment of the requirements for the degree of Doctor of Philosophy

Abstract

Characterizing global and regional climate variability and climate-carbon cycle interactions in the past provides critical context for evaluating present and future climate trends. In this thesis, I use stable isotope and radiocarbon analysis of vascular plant biomarkers in lacustrine and marine sediment cores to explore late Quaternary climate variability and connections between past climate change and terrestrial carbon cycling in tropical South America. I investigate temporal and spatial trends in South American Summer Monsoon precipitation by reconstructing hydrologic variability over the past 50,000 years at two sites: the Lake Titicaca drainage basin in the Central Andes and the Pantanal wetlands in the interior lowlands. Diverging hydrologic trends at these two sites during the last glacial period suggest altered monsoon circulation patterns under glacial conditions, while changes in summer insolation appear to be an important control of precipitation at both sites during the Holocene. I next assess the relationship between climate change and the age structure of terrestrial biospheric carbon exported from two tropical catchments over the past 20,000 years. Radiocarbon dating of leaf waxes in Cariaco Basin and Lake Titicaca sediment records indicates that waxes preserved in sediments are likely composed of a fresh component transported to sediments within decades of production by vegetation and an old component derived from aged soil organic matter with an average age on the order of millennia at time of deposition. Results from both sites show that past hydrologic variability had a significant impact on the mobilization and export of different pools of terrestrial biospheric carbon. In particular, results from Cariaco Basin suggest that wetter conditions in the past resulted in increased export of fresh biospheric carbon to the ocean, representing a potentially important climate feedback mechanism on geologic timescales.

Thesis supervisors:
Valier Galy, Associate Scientist, WHOI
Konrad A. Hughen, Senior Scientist, WHOI

Acknowledgements

Reflecting back on my 5+ years at WHOI, it is amazing to consider all the people who have helped me in some way as I worked towards finishing this thesis. At the center of it all were my thesis advisors, Valier Galy and Konrad Hughen. In my first few years, Konrad guided me in my transition from chemist to paleoclimatologist, while in my later years, I was able to connect past climate with past carbon cycling with the help of Valier and his relentless enthusiasm for all things organic geochemistry. Above all else, I most appreciated the freedom that Valier and Konrad afforded me in my thesis work. They allowed me to follow my own path and pursue different interests inside and outside the lab, which in turn helped me become a better and more independent scientist.

My committee members, Ed Boyle and Chris Hein, and defense chair, Bernhard Peucker-Ehrenbrink, have all been supportive during my thesis work and at different points in my academic career. Eight years ago, I was an MIT undergrad in Course 5 (Chemistry) looking to move into the environmental chemistry world and was fortunate enough to land in Ed's lab. In my time there and later in my thesis work, I have always appreciated the breadth of his knowledge and experience (and subtle sense of humor). Chris has been a source of moral support since his time as a WHOI postdoc and has always provided careful and thoughtful answers to my questions on subjects ranging from sediment transport to moral dilemmas. I have been continually impressed by Bernhard's patience and attention to detail both as a teacher and scientist throughout my time in the Joint Program. I would like to particularly thank him for allowing me to be a teaching assistant for the isotopes course (one of my favorite experiences of grad school) and even encouraging my dinosaur-drawing habit.

I could not have done this work without the support of the amazing scientific, technical, and administrative staff across WHOI. Ann McNichol, Al Gagnon, and the NOSAMS prep lab welcomed me into their lab over the last few years and have been always extremely accommodating with all my sample requests. Sean Sylva always fought valiantly against the whims of mass spectrometers and listened patiently to my complaints about instruments or life in general. (Meanwhile Sebastion likely had all the answers, if only he had been able to overcome the dog-human communication barrier.) My colleagues in Konrad's and Valier's labs, including Linda Ampel, Justin Ossolinski, Carl Johnson, Nathalie Dubois, and Guillaume Soulet, have helped me in countless ways. I also would like to thank all the administrators in Clark, Fye, and the Academic Programs Office for everything they do to make students' lives easier.

I am grateful for support from collaborators outside of WHOI, especially Bronwen Whitney and Frank Mayle, who were generous and trusting enough to share samples with me for the work described in Chapter 3. They have also been incredibly helpful in preparing that chapter for publication and filling botany-related gaps in my knowledge.

Finally, I would like to thank my friends in the WHOI and MIT communities and beyond, especially fellow MCG students Kathleen (my official and unofficial mentor), Britta, Rene, Kate, Emily (and Moxie), Winn, Sarah, Sophie, and Cara, for sharing in celebrations, commiserations, and everything in between. Nick has been incredibly supportive in all things

and has graciously put up with me for the past 4 years. My biggest thanks goes to my family, my parents, sister, and brother, who have managed to do so for almost three decades. I have always been grateful for their support and humor through the highs and lows of my academic career.

The work described in this thesis was supported by an MIT Presidential Fellowship, a WHOI Ocean and Climate Change Institute Fellowship, an EPA STAR Fellowship (Grant F13B20322), and the Joint Program Academic Program Office. Other funding was provided by grants from the WHOI Ocean Ventures Fund and Coastal Ocean Institute and NSF grants OCE-1400805 (VG) and DEB-0447281 (KAH).

Table of Contents

List of Figures

Chapter 1.

Chapter 2.

Chapter 3.

Chapter 4.

Chapter 5.

Chapter 6.

Appendix 1.

List of Tables

Chapter 1. Introduction

1.1 Carbon and climate

The heat-trapping properties of atmospheric carbon dioxide (CO_2) and its ability to influence climate by regulating the exchange of heat between the Earth's surface and outer space were first recognized in the late 19th century (Arrhenius, 1896). Since then, the fundamental link between the global carbon cycle and climate system has been repeatedly confirmed, perhaps most strikingly by the correlation between records of atmospheric CO_2 concentration and Antarctic temperature over the past eight 100-kyr glacial cycles recorded in Antarctic ice cores (Figure 1) (Jouzel et al., 2007; Lüthi et al., 2008). Beyond this first-order relationship, however, our understanding of climate-carbon cycle connections remains limited due to the immense complexity of the global climate system, carbon cycle, and host of chemical, biological, geologic, and physical processes at play. The increasingly apparent effects of anthropogenic CO_2 emissions on global climate impart particular urgency to answering higher order questions about the short- and long-term responses of the carbon cycle to climate change, and vice versa. This thesis focuses on climate and carbon cycle variability in one region, the South American tropics, to address two such questions:

1. How did carbon cycle-mediated global change (e.g., glacial cycles) and external forcing mechanisms (e.g., orbital changes in insolation) affect climate variability in tropical South America over the past 50,000 years?
2. How did climate variability in tropical South America over the past 20,000 years affect the exchange of terrestrial biospheric carbon between terrestrial, atmospheric and coastal ocean reservoirs?

1.2 Past and present climate in the South American tropics

The South American tropics are one of six continental centers of monsoon systems marked by the seasonal reversal of atmospheric circulation patterns and the development of intense convection and precipitation over land. These tropical monsoon systems play key roles in the global energy budget as well as the livelihoods of more than half of the world's population (World Climate Research Programme). However, despite their importance for global climate and socioeconomic patterns, the tropics are underrepresented in studies of past climate variability on glacial-interglacial timescales, which historically have been concentrated in high northern latitudes (Figure 2). Among tropical regions, the southern hemisphere South American tropics in particular are the most poorly represented region in the paleoclimate record over the past 100 kyr. Remedying this deficit thus represents a critical direction for climate research, as our understanding of long-term controls on SASM variability provides the foundation for characterizing past and future climate trends in much of South America, including ecologically important regions such as the Amazon rainforest.

In the present day, monsoon rainfall in South America is linked to seasonal meridional migration of the Intertropical Convergence Zone (ITCZ), the near-equator zone of northeasterly and southeasterly trade wind confluence associated with a band of intense precipitation over the ocean. The South American Summer Monsoon (SASM) develops in austral spring/summer when the ITCZ reaches its southernmost position and controls summer precipitation over much of the South American continent, including the Amazon Basin, Central Andes, and subtropical Brazil (Zhou and Lau, 1998) (Figure 3). The dominant low-level atmospheric circulation pattern during peak monsoon season carries moisture along a path from the tropical Atlantic Ocean towards the Central Andes before turning southeast towards

subtropical Brazil. Mid- and upper-level easterly flow also allows transport of moisture up onto the Altiplano plateau of the Central Andes (Garreaud et al., 2009). The demise of the SASM occurs in austral fall as the ITCZ retreats northwards, shifting the zone of maximum precipitation to the northern South American tropics.

Over the last glacial cycle, SASM variability has been linked to both remote and local forcing mechanisms (Baker et al., 2001; Cheng et al., 2013; Cruz et al., 2005, 2006; 2009; Kanner et al., 2012; Mosblech et al., 2012; Wang et al., 2007). Remote forcing mechanisms include glacial boundary conditions (e.g., the presence of large continental ice sheets in the northern hemisphere, lower atmospheric CO_2) as well as millennial-scale variability generally considered be related to northern hemisphere ice sheet dynamics during the last glacial period and deglaciation (e.g., Heinrich events). Local forcing mechanisms include variability in the magnitude of summer insolation caused by the Earth's ~22 kyr precessional cycle. Given the low number of paleoclimate studies in the southern hemisphere South American tropics, however, important questions about SASM variability in different regions remain unresolved. In Chapter 2 and 3 of this thesis, I reconstruct SASM variability over the past ~50 kyr at two different sites to better characterize the response of regional SASM precipitation to local and remote forcings. In Chapter 2, I present a 60,000-year record of hydrologic variability in the Central Andes from the Lake Titicaca sediment record. I reconstruct changes in precipitation isotopes by measuring the hydrogen isotopic signature of leaf wax compounds, a suite of terrestrial biomarkers increasingly used in paleoclimate studies when traditional isotopic proxies (e.g., foraminifera, authigenic carbonates) are absent. In Chapter 3, I use both leaf wax carbon and hydrogen isotopes to reconstruct vegetation and hydrologic variability at Laguna La Gaiba, a small lake located in the Pantanal wetlands of Brazil/Bolivia/Paraguay. Moreover,

comparison of these records with detailed pollen data from the same site provides new insight into different signals encoded by leaf wax stable isotopes.

1.3 The terrestrial carbon cycle

The concentration of CO_2 in the atmosphere is controlled by the continuous redistribution of carbon among larger carbon reservoirs in the ocean, on land, and in the Earth's subsurface. In particular, the amount of carbon sequestered in vegetation and soil, the "terrestrial biosphere," is an important control on atmospheric CO_2 on both short and long timescales. Carbon enters the terrestrial biosphere via photosynthesis and carbon fixation by vegetation, using CO_2 from the atmosphere to produce organic carbon (OC) (Figure 4). Some fraction of this OC is then transferred to soils and other long-term terrestrial OC reservoirs (e.g., river floodplains, wetlands), where it can be stored for years to millennia (e.g., Trumbore, 2000). OC leaves the terrestrial biosphere by one of two pathways: (1) return to the atmosphere by conversion to CO_2 or other gases via autotrophic/heterotrophic respiration or fire or (2) export to the ocean (or other permanent water bodies) through erosion and fluvial transport. In the ocean, terrestrial OC can either be respired and returned to the atmosphere or buried and sequestered in marine sediments, an entry point to the geologic carbon cycle. Summing across all these reservoirs, the terrestrial biosphere currently contains more than 3 times the carbon present in the atmosphere (~2800 and 830 GtC, respectively; Carvalhais et al., 2014; IPCC, 2013).

The effects of climate change on terrestrial carbon storage and export constitute potentially important climate feedback mechanisms on annual to geologic timescales. Climate variability can impact the terrestrial carbon cycle in two different but related ways: (1) by changing the average storage time of biospheric OC in soil and other terrestrial reservoirs, and

(2) by changing the total flux of biospheric OC from fresh vegetation and soil stocks to the ocean. Both temperature and water availability are known to be important controls on rates of microbial respiration of soil OC (e.g., Amundson, 2001), while hydrologic variability also plays a significant role in soil erosion and fluvial OC transport (e.g., Renard et al., 1997). However, the response of the terrestrial biosphere to climate change on timescales longer than years to decades is poorly understood due to the short window of available direct observations and the complex nature of physical and biological processes that control carbon storage in and transport from terrestrial reservoirs.

The advent of compound-specific radiocarbon analysis two decades ago (Eglinton et al., 1996) has provided a new approach to unraveling the complexity of the terrestrial carbon cycle. Radiocarbon dating of vascular plant biomarkers in modern river sediments in a wide range of geographic settings has provided insight into the influence of climate on rates of terrestrial OC cycling (Drenzek et al., 2009; Feng et al., 2013; Gustafsson et al., 2011; Kusch et al., 2010; Tao et al., 2015; Galy and Eglinton, unpublished). While biomarkers represent only one component of a chemically diverse biospheric OC pool, variability in biomarker ages reflects larger trends in terrestrial storage and export. Specifically, the age structure of terrestrial biomarkers is a function of the age of soil OC pools, as well as the relative proportions of total OC export flux derived from fresh vegetation and aged soil pools. However, spatial comparisons of biomarker ages are complicated by other variables in addition to climate, such as topography and catchment size. An alternative approach is to track the age structure of biomarkers at one site through time by analyzing the ages of biomarkers preserved in independently dated marine or lacustrine sediment records (Douglas et al., 2014; Smittenberg et al., 2006).

In Chapters 4 and 5, I apply this approach to investigate the relationship between climate variability and terrestrial biomarker age at two tropical South American sites. In order to study the effects of large climate shifts, I target two sites with well-characterized but contrasting climate histories over the last 20,000 years. In Chapter 4, I present results of radiocarbon analysis of leaf waxes in the Cariaco Basin sediment record over the past 18.5 kyr. I develop a two-component mixing model to constrain relative contributions from fresh and aged components derived from standing vegetation/leaf litter/young soil OC and older soil material, respectively. I also investigate the effects of varying contributions of aged material on leaf wax stable isotope records commonly used for paleoclimate reconstructions (including those in the first two chapters of this thesis). Finally, I investigate links between leaf wax age structure and climate variability in the Cariaco catchment of coastal Venezuela to assess the potential impacts of hydrologic and temperature change on the terrestrial carbon cycle. In Chapter 5, I present results from a similar study in Lake Titicaca sediments over the past ~15 kyr, building upon the climate history of the Titicaca catchment developed in Chapter 2 to further probe the relationship between past climate change and terrestrial carbon storage and export at a very different tropical site. Finally, in Chapter 6 I synthesize the findings of all chapters and consider the broader implications of my work for global climate and carbon cycle variability.

References

Amundson, R., 2001. The carbon budget in soils. Annu. Rev. Earth Planet. Sci. 29, 535–562.

Arrhenius, S., 1896. On the Influence of Carbonic Acid in the Air Upon the Temperature of the Ground. Philosophical Magazine and Journal of Science 41, 237–276.

Baker, P., Seltzer, G., Fritz, S., Dunbar, R., Grove, M., Tapia, P., Cross, S., Rowe, H., Broda, J., 2001. The history of South American tropical precipitation for the past 25,000 years. Science 291, 640-643.

Bauer, J.E., Cai, W.-J., Raymond, P.A., Bianchi, T.S., Hopkinson, C.S., Regnier, P.A.G., 2013. The changing carbon cycle of the coastal ocean. Nature 504, 61–70.

Berner, R., 1982. Burial of Organic Carbon and Pyrite Sulfur in the Modern Ocean: Its Geochemical and Environmental Significance. Am. J. Sci. 282, 451–473.

Carvalhais, N., Forkel, M., Khomik, M., Bellarby, J., Jung, M., Migliavacca, M., Mu, M., Saatchi, S., Santoro, M., Thurner, M., Weber, U., Ahrens, B., Beer, C., Cescatti, A., Randerson, J.T., Reichstein, M., 2014. Global covariation of carbon turnover times with climate in terrestrial ecosystems. Nature 514, 213–217.

Cheng, H., Sinha, A., Cruz, F.W., Wang, X., Edwards, R.L., D Rsquo Horta, F.M., Ribas, C.C., Vuille, M., Stott, L.D., Auler, A.S., 2013. Climate change patterns in Amazonia and biodiversity. Nature Comm. 4, 1411–1416.

Cruz, F.W., Burns, S.J., Karmann, I., Sharp, W.D., Vuille, M., Cardoso, A.O., Ferrari, J.A., Silva Dias, P.L., Viana Jr., O., 2005. Insolation-driven changes in atmospheric circulation over the past 116,000 years in subtropical Brazil. Nature 434, 63–66.

Cruz, F., Burns, S., Karmann, I., Sharp, W., Vuille, M., 2006. Reconstruction of regional atmospheric circulation features during the late Pleistocene in subtropical Brazil from oxygen isotope composition of speleothems. Earth Planet. Sci. Lett. 248, 495–507.

Cruz, F., Vuille, M., Burns, S., Wang, X., Cheng, H., Werner, M., Edwards, R., Karmann, I., Auler, A., Nguyen, H., 2009. Orbitally driven east–west antiphasing of South American precipitation. Nature Geosci. 2, 210–214.

Douglas, P.M.J., Pagani, M., Eglinton, T.I., Brenner, M., Hodell, D.A., Curtis, J.H., Ma, K.F., Breckenridge, A., 2014. Pre-aged plant waxes in tropical lake sediments and their influence on the chronology of molecular paleoclimate proxy records. Geochim. Cosmochim. Acta 141, 346–364.

Drenzek, N.J., Hughen, K.A., Montlucon, D.B., Southon, J.R., Santos, Dos, G.M., Druffel, E.R., Giosan, L., Eglinton, T.I., 2009. A new look at old carbon in active margin sediments. Geology 37, 239–242.

Eglinton, T., Aluwihare, L., Bauer, J., Druffel, E., McNichol, A., 1996. Gas chromatographic isolation of individual compounds from complex matrices for radiocarbon dating. Anal. Chem. 68, 904–912.

Feng, X., Vonk, J.E., Dongen, B.E.V., Gustafsson, O., Semiletov, I.P., Dudarev, O.V., Wang, Z., Montlucon, D.B., Wacker, L., Eglinton, T.I., 2013. Differential mobilization of terrestrial carbon pools in Eurasian Arctic river basins. Proc. Nat. Acad. Sci. 110, 14168–14173.

Garreaud, R., Vuille, M., Compagnucci, R., Marengo, J., 2009. Present-day South American climate. Palaeogeogr. Palaeoclimatol. Palaeoecol. 281, 180–195.

Gustafsson, O., van Dongen, B.E., Vonk, J.E., Dudarev, O.V., Semiletov, I.P., 2011. Widespread release of old carbon across the Siberian Arctic echoed by its large rivers. Biogeosciences 8, 1737–1743.

IPCC, 2013. *Climate Change 2013: The Physical Science Basis. Contribution of Working Group I to the Fifth Assessment Report*, T.F. Stocker et al., Cambridge University Press.

Jouzel, J., Masson-Delmotte, V., Cattani, O., Dreyfus, G., Falourd, S., Hoffmann, G., Minster, B., Nouet, J., Barnola, J.-M., Chappellaz, J., Fischer, H., Gallet, J.C., Johnsen, S., Leuenberger, M., Loulergue, L., Luethi, D., Oerter, H., Parrenin, F., Raisbeck, G., Raynaud, D., Schilt, A., Schwander, J., Selmo, E., Souchez, R., Spahni, R., Stauffer, B., Steffensen, J.P., Stenni, B., Stocker, T.F., Tison, J.-L., Werner, M., Wolff, E.W., 2007.

Orbital and millennial Antarctic climate variability over the past 800,000 years. Science 317, 793–796.
Kanner, L.C., Burns, S.J., Cheng, H., Edwards, R.L., 2012. High-Latitude Forcing of the South American Summer Monsoon During the Last Glacial. Science 335, 570–573.
Kusch, S., Rethemeyer, J., Schefuß, E., Mollenhauer, G., 2010. Controls on the age of vascular plant biomarkers in Black Sea sediments. Geochim. Cosmochim. Acta 74, 7031–7047.
Lüthi, D., Le Floch, M., Bereiter, B., Blunier, T., Barnola, J.-M., Siegenthaler, U., Raynaud, D., Jouzel, J., Fischer, H., Kawamura, K., Stocker, T.F., 2008. High-resolution carbon dioxide concentration record 650,000–800,000 years before present. Nature 453, 379–382.
Mosblech, N.A.S., Bush, M.B., Gosling, W.D., Hodell, D., Thomas, L., Calsteren, P.V., Correa-Metrio, A., Valencia, B.G., Curtis, J., Woesik, R.V., 2012. North Atlantic forcing of Amazonian precipitation during the last ice age. Nature Geosci. 5, 817–820.
Renard, K.G., Foster, G.R., Weesies, G.A., McCool, D.K., Yoder, D.C., 1997. Predicting Soil Erosion by Water: A Guide to Conservation Planning With the Revised Universal Soil Loss Equation (RUSLE). U.S. Department of Agriculture.
Smittenberg, R., Eglinton, T., Schouten, S., Damsté, J., 2006. Ongoing buildup of refractory organic carbon in boreal soils during the Holocene. Science 314, 1283–1286.
Tao, S., Eglinton, T.I., Montluçon, D.B., McIntyre, C., Zhao, M., 2015. Pre-aged soil organic carbon as a major component of the Yellow River suspended load: Regional significance and global relevance. Earth Planet. Sci. Lett. 414, 77–86.
Trumbore, S., 2000. Age of soil organic matter and soil respiration: radiocarbon constraints on belowground C dynamics. Ecol. Appl. 10, 399-411.
Wang, X., Auler, A.S., Edwards, R.L., Cheng, H., Ito, E., Wang, Y., Kong, X., Solheid, M., 2007. Millennial-scale precipitation changes in southern Brazil over the past 90,000 years. Geophys. Res. Lett. 34, L23701.
World Climate Research Programme. “The Global Monsoon Systems.” <http://www.wcrp-climate.org/documents/monsoon_factsheet.pdf> Accessed October 2, 2015.
Zhou, J., Lau, K., 1998. Does a monsoon climate exist over South America? J. Clim. 11, 1020–1040.

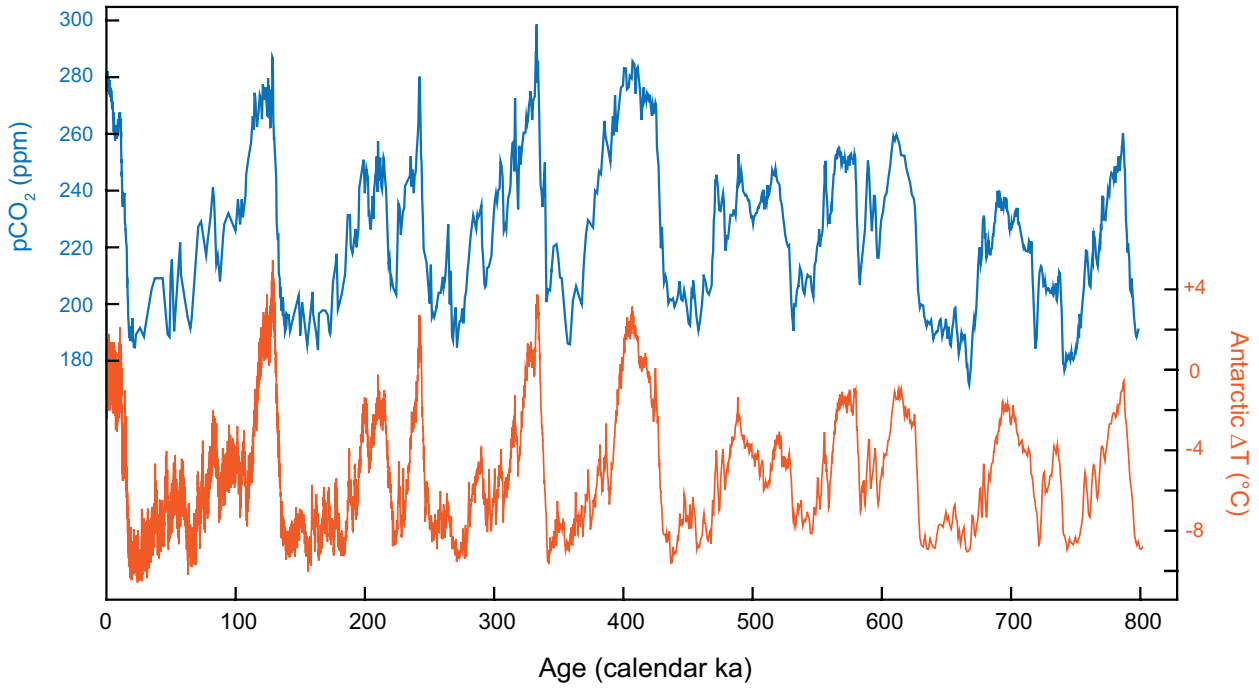

Figure 1. (Above) Evolution of atmospheric CO_2 and Antarctic temperature over the past 800,000 years. Temperature difference was calculated relative to the average temperature of the last 1,000 years. Data from Jouzel et al. (2007) and Luthi et al. (2008).

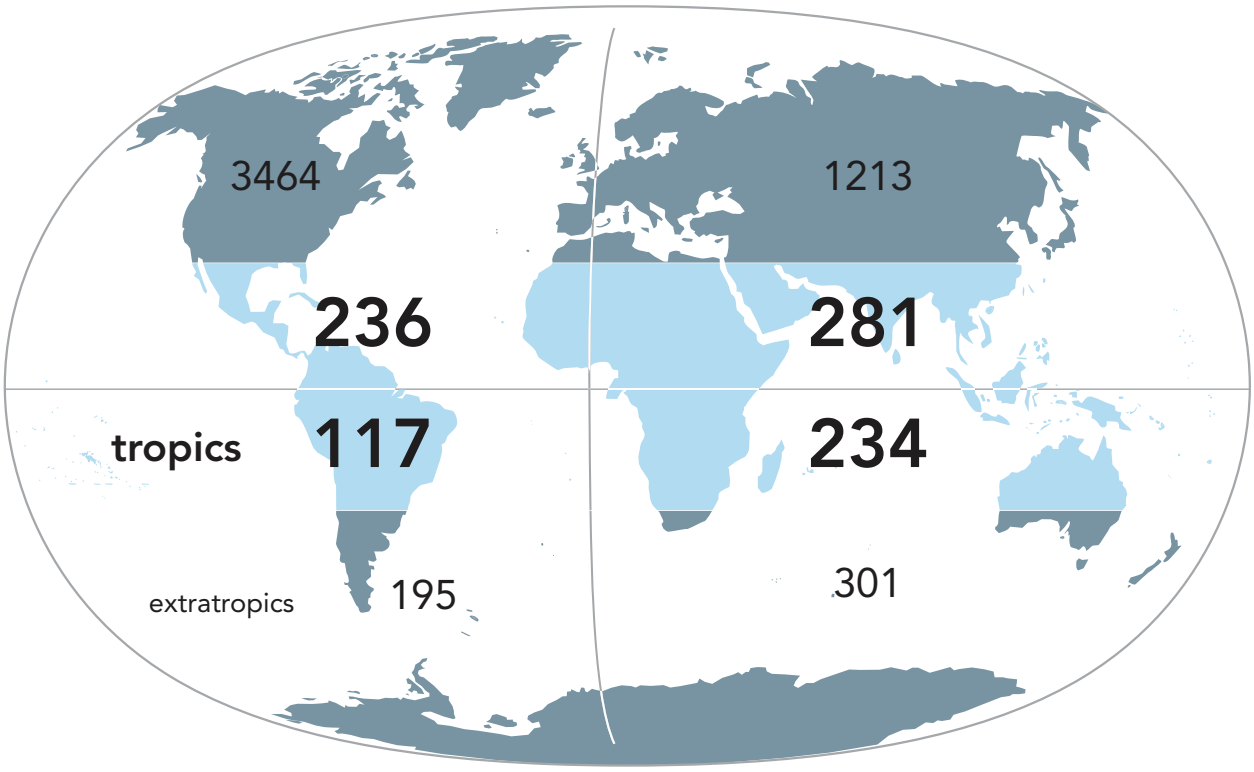

Figure 2. Distribution of existing paleoclimate records by region, 100,000-200 years before present. Numbers represent total tropical or extratropical records that cover any period between 100,000-200 years before present (i.e., before instrumental period) in each quadrant of the globe (e.g., southwest tropical region bounded from 0-30°S, 0-180°W). Tropics were defined as 30°S-30°N. Analysis was based on available datasets unique to each region in NOAA-WDC/Pangaea online repositories as of September 28, 2015.

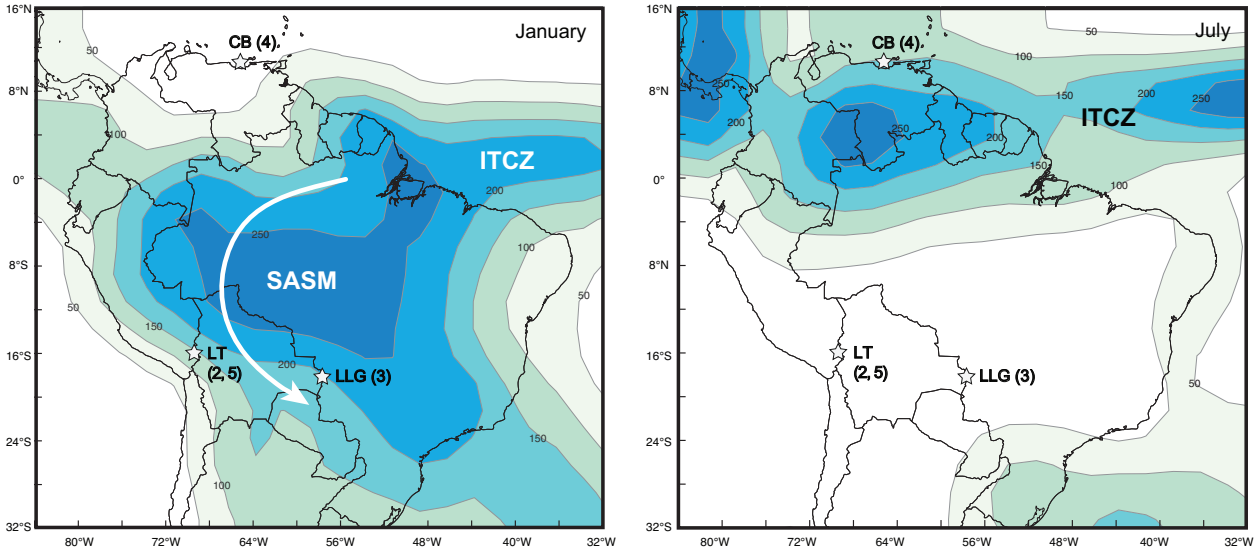

Figure 3. Average January (left) and July (right) precipitation in tropical South America, 1981-2010. Contours indicate increments of 50 mm/month; precipitation data are from CAMS_OPI monthly precipitation dataset (National Centers for Environmental Prediction). Stars indicate thesis study sites Cariaco Basin (CB), Lake Titicaca (LT) and Laguna La Gaiba (LLG) with relevant chapter numbers in parentheses. Arrow indicates general direction of moisture transport during peak season of the South American Summer Monsoon (SASM).

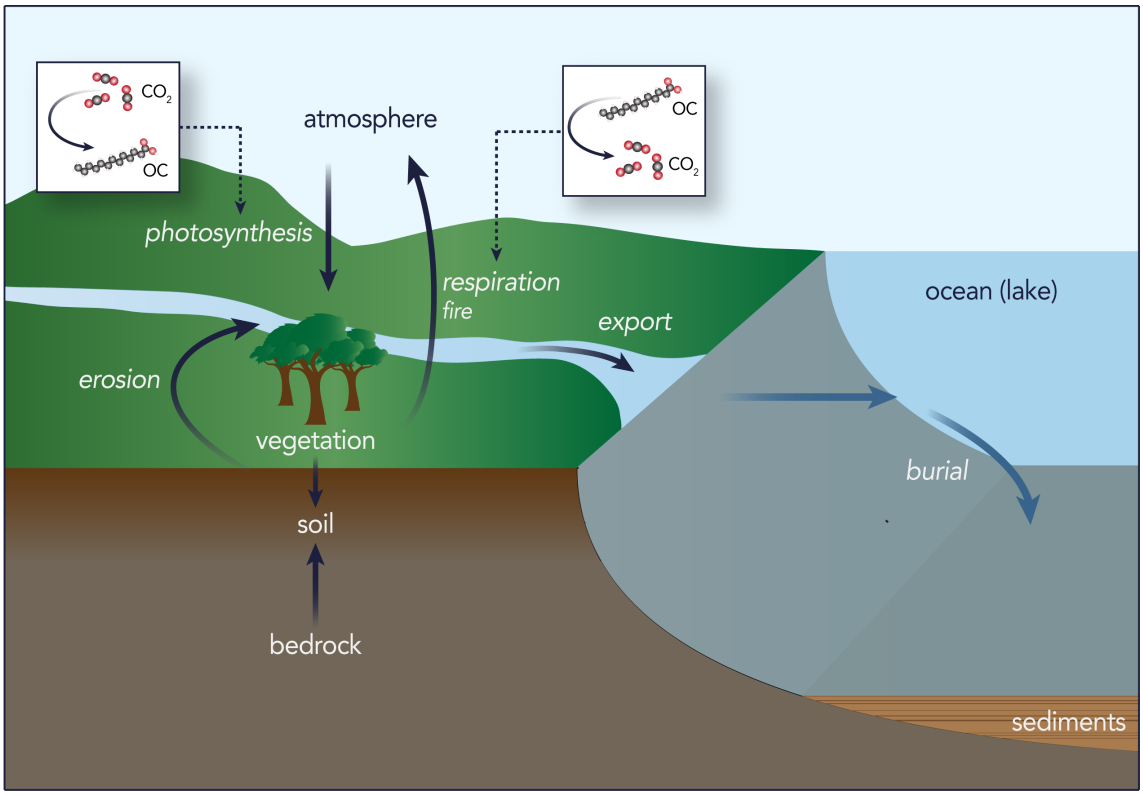

Figure 4. Schematic of terrestrial carbon cycle with major reservoirs and key transport and transformation processes. Arrows indicate movement of carbon between reservoirs.

Chapter 2.

A 60,000-year record of hydrologic variability in the Central Andes from the hydrogen isotopic composition of leaf waxes in Lake Titicaca sediments

This chapter was published in Earth and Planetary Science Letters by Elsevier in 2014 and is reprinted here with their permission as granted in the original copyright agreement.

Fornace, K.L., Hughen, K.A., Shanahan, T.M., Fritz, S.C., Baker, P.A., Sylva, S.P., 2014. A 60,000-year record of hydrologic variability in the Central Andes from the hydrogen isotopic composition of leaf waxes in Lake Titicaca sediments. Earth Plan. Sci. Lett. 408, 263-271.

Abstract

A record of the hydrogen isotopic composition of terrestrial leaf waxes (δD_{wax}) in sediment cores from Lake Titicaca provides new insight into the precipitation history of the Central Andes and controls of South American Summer Monsoon (SASM) variability since the last glacial period. Comparison of the δD_{wax} record with a 19-kyr δD record from the nearby Illimani ice core supports the interpretation that precipitation δD is the primary control on δD_{wax} with a lesser but significant role for local evapotranspiration and other secondary influences on δD_{wax}. The Titicaca δD_{wax} record confirms overall wetter conditions in the Central Andes during the last glacial period relative to a drier Holocene. During the last deglaciation, abrupt δD_{wax} shifts correspond to millennial-scale events observed in the high-latitude North Atlantic, with dry conditions corresponding to the Bølling–Allerød and early Holocene periods and wetter conditions during late glacial and Younger Dryas intervals. We observe a trend of increasing monsoonal precipitation from the early to the late Holocene, consistent with summer insolation forcing of the SASM, but similar hydrologic variability on precessional timescales is not apparent during the last glacial period. Overall, this study demonstrates the relative importance of high- latitude versus tropical forcing as a dominant control on glacial SASM precipitation variability.

2.1 Introduction

Aided by the availability of different paleoclimate archives, the Central Andes have been the target of many studies of late Quaternary tropical South American climate. For example, sediment cores from the Lake Titicaca basin record changes in water balance (precipitation minus evaporation) and lake level on timescales from glacial–interglacial to

millennial (Baker et al., 2001b; Fritz et al., 2007, 2010). Since the majority of regional precipitation falls during austral summer, the Central Andes are particularly sensitive to variability in the South American Summer Monsoon (SASM), a continental-scale circulation that produces much of summer precipitation throughout southern tropical and subtropical South America (Zhou and Lau, 1998). While studies of modern SASM precipitation have identified many controls on interannual to interdecadal SASM variability, including Pacific sea surface temperature (SST)/El Niño Southern Oscillation (ENSO) (Garreaud et al., 2009), Atlantic SST variability (Chiessi et al., 2009), and land surface processes (Collini et al., 2008), SASM behavior on longer timescales is not as well constrained. Characterizing the controls on SASM dynamics on millennial to interglacial–glacial timescales is thus critical to improving our understanding of past and future hydrologic variability throughout much of South America.

Proxies that record the isotopic composition of past precipitation in the Andes, from archives such as ice cores, speleothems and lacustrine calcite deposits, have proven to be particularly powerful tools for reconstructing past monsoon variability on geological timescales (e.g., Ramirez et al., 2003; Bird et al., 2011; Kanner et al., 2012). Although the interpretation of Andean stable isotopic records has been the subject of much debate (e.g., Broecker, 1997; Hoffmann, 2003; Pierrehumbert, 1999; Thompson et al., 1995), a number of recent modeling and observational studies clearly indicate a strong relationship between precipitation isotopes and the amount of precipitation along the SASM trajectory (Vuille et al., 2003; Vuille and Werner, 2005; Vimeux et al., 2005; Insel et al., 2013). Andean ice cores have yielded insight into the influence of global glacial cycles on regional hydrologic variability, with wetter conditions associated with Last Glacial Maximum (LGM) boundary conditions (Ramirez et al., 2003). In addition, changes in SASM precipitation have been linked to high-

latitude millennial-scale variability, including Dansgaard–Oeschger cycles and Heinrich events during the last glacial period (Kanner et al., 2012), as well as the Younger Dryas and Bølling–Allerød intervals during the last deglaciation (Thompson et al., 1995, 1998). A number of Andean lacustrine calcite $\delta^{18}O$ records have pointed to the magnitude of local summer insolation as an important control of SASM intensity during the Holocene (Baker et al., 2009; Bird et al., 2011; Seltzer et al., 2000), consistent with southern Brazilian speleothems (Cruz et al., 2006; Wang et al., 2007) that show a strong influence of insolation on SASM precipitation over the entire last glacial cycle. In contrast, speleothem records from the Andes and western Amazonia do not vary strongly on precessional timescales during the last glacial period (MIS 2–4) (Kanner et al., 2012; Mosblech et al., 2012; Cheng et al., 2013).

Reaching a better understanding of past SASM variability is limited by the small number of continuous isotopic records from the Andes that extend into the last glacial period. Andean ice core records only extend as far back as the LGM (Ramirez et al., 2003; Thompson et al., 1995, 1998), while other extant Andean isotopic records are confined to the Holocene (e.g., Bird et al., 2011) or within the last glacial period (Kanner et al., 2012). Longer records are particularly valuable in light of new speleothem records from the western Amazon that provide important information on SASM activity upstream of the Andes over the last glacial–interglacial cycle (Mosblech et al., 2012; Cheng et al., 2013). The sediment record of Lake Titicaca (LT), continuous over the past four glacial cycles, is a valuable archive of regional climate variability, but traditional stable isotope archives (e.g., authigenic carbonate) are not present in much of the sediment record (Fritz et al., 2007). Compound-specific isotope analysis of biomarkers in LT sediments thus represents a new and advantageous approach to the study of past Andean climate. In particular, the hydrogen isotopic composition (δD) of leaf wax

compounds produced by vascular plants has been shown to be highly correlated to precipitation δD (e.g., Sachse et al., 2012), allowing reconstruction of SASM precipitation variability when carbonate proxies are absent. Here we present a continuous record of regional hydrologic variability over the past 60,000 years from leaf wax δD in LT sediments.

2.2 Study Site

The South American Altiplano is a semi-arid, internally drained plateau situated between the western and eastern cordilleras of the Central Andes (Fig. 1). Located on the Peruvian/Bolivian border on the northern Altiplano, Lake Titicaca (3810 m asl) is a large, freshwater lake comprised of two basins: the larger and deeper Lago Grande (7131 km^2) and the smaller shallow Lago Huiñaimarca (1428 km^2) connected by the Straits of Tiquina. The watershed of the Lago Grande basin consists of six major rivers (total catchment area: 52,800 km^2). Modern natural vegetation surrounding the lake largely consists of grasses, shrubs and herbs and is classified as puna vegetation (Paduano et al., 2003).

Present annual precipitation ranges from >700 mm in regions near Lake Titicaca to <200 mm on the southern Altiplano (Garreaud et al., 2003). The majority of annual precipitation (50–80%) on the Altiplano occurs during the austral summer and is associated with the SASM (Zhou and Lau, 1998). During the mature phase of the SASM (DJF), strengthened easterly trade winds increase moisture transport from the tropical Atlantic into the Amazon Basin towards the tropical Andes. The development of a continental-scale low-pressure system (Chaco Low) centered on the subtropical plains steers low-level flow southeastward along the eastern Andean flank, carrying moisture from the Amazon Basin to the subtropics (Garreaud et al., 2009). An upper-level anticyclone, known as the Bolivian High,

develops over the Altiplano in response to latent heat release by Amazonian and Andean precipitation (Lenters and Cook, 1997). Upper level easterly flow associated with the north branch of the anticyclone allows upslope moisture transport from lowland Amazonia to the high Andes (Garreaud, 1999). During the peak months of the SASM (December–February), convective activity is concentrated over the southern Amazon Basin and Central Andes (Vuille and Werner, 2005). During the austral autumn (March–May), the SASM weakens and the region of maximum precipitation over continental South America retreats to the northern tropics. On the Altiplano, prevailing westerly flow from the arid west Andean slope results in dry conditions throughout much of the remainder of the year (May to October) (Garreaud et al., 2003).

2.3 Methods

2.3.1 Sediment core retrieval

Sediment cores from Lake Titicaca were raised in a 2001 International Continental Drilling Program expedition using the GLAD 800 drilling platform and coring system. Sediment samples analyzed here were taken from core LT01-2B, a 136 m core recovered from the Lago Grande basin at a water depth of 228 m (15.8533°S, 69.1404°W). The core was generally sampled at 2 cm resolution during periods of low sediment accumulation (Holocene) and at 10 cm resolution during periods of higher sedimentation rates (last glacial period). In total, 175 samples were analyzed for δD at an average resolution of ~300–400 yr from 61–3.5 kyr. Sample ages were assigned with the LT01-2B age model developed by Fritz et al. (2007) based on 18 bulk organic radiocarbon ages and U/Th ages of aragonite deposits, as well as tuning glacial terminations to the Vostok CO_2 record from Antarctica. Conversion from

radiocarbon to calendar years was updated to the IntCal13 calibration (Table S1; Reimer et al., 2013). For the period from 3.5 ka to the present, 11 sediment samples were taken from a box core (NE98 4BXB) raised from the Lago Grande basin at a water depth of 145 m (16.1376° S, 69.1545° W) in 1998. Samples ages were assigned from an age model developed by Tapia et al. (2003) based on 4 bulk organic radiocarbon ages. Calendar ages were also updated to reflect calibration from IntCal13.

2.3.2 Sample preparation

Freeze-dried and finely ground sediment samples (~3–10 g) were extracted with a 9:1 dichloromethane:methanol mixture using an accelerated solvent extractor (ASE 200, Dionex). The resulting total lipid extract was dried over Na_2SO_4 and then separated into neutral and acidic fractions by flash column chromatography over aminopropyl-functionalized silica gel (Supelclean LC-NH_2, Sigma Aldrich) using 9:1 dichloromethane:acetone and 2% formic acid in dichloromethane as eluents, respectively. All columns were run on a RapidTrace SPE Workstation. The acidic fraction was transesterified using a 9:1 mixture of anhydrous methanol and acetyl chloride (70°C, 12 h). Fatty acid methyl esters (FAMEs) were further purified on a second LC-NH_2 column using hexane as eluent. FAMEs were identified by comparison of gas chromatograph/flame ionization detector (GC/FID, Agilent 6850) retention times to those of authenticated external FAME standards.

2.3.3 Compound-specific hydrogen isotope analysis

The δD values of individual FAMEs were measured on a Thermo Scientific DeltaV^{Plus} isotope ratio mass spectrometer (IRMS) coupled to an Agilent 6980 GC via a pyrolysis

interface (GC-TC) operated at 1440°C. Each sample was run in duplicate, with the exception of 12 samples distributed throughout the core that were concentration-limited and only measured once. Data were processed using Isodat 3.0 software (Thermo Scientific). The H_3^+ factor (Sessions et al., 2001) was measured daily and ranged from 1.7–2.0 ppm/mV over the course of the measurement period. Peaks of a propane reference gas were inserted at several points before and after analytes during each run and used as internal calibration standards. Instrument variability was accounted for by routinely injecting an external standard mix containing 8 fatty acid methyl and ethyl esters of known δD (F8 mixture, A. Schimmelmann, Indiana University) and adjusting the reference propane δD value to minimize the average offset between the known and measured δD values of the F8 compounds. Average 1σ precision of sample replicates was 3.1‰. Estimated average accuracy is ±4.5‰ based on daily measurements of the F8 mixture. In order to correct for the δD of methyl hydrogen added during transesterfication, a phthalic acid standard of known isotopic composition (A. Schimmelmann, Indiana University) was methylated in parallel to samples using the same batch of anhydrous methanol. The δD of the resulting dimethyl phthalate was measured and used to calculate the δD of the methyl hydrogen by mass balance. Values are reported using standard delta notation (δD) as per mil (‰) deviations from Vienna standard mean ocean water (VSMOW).

2.4 Results and Discussion

Measured δD values for *n*-C_{28} and *n*-C_{30} FAMEs over the past 60,000 years are shown in Fig. 2. These data can also be found online in the NOAA NCDC Paleoclimate database. The δD values for both compounds show similar trends over this time period and are highly correlated ($r^2 = 0.82$, $p < 0.0001$). In interpreting the record, we focus on *n*-C_{28} FAME δD

(heretofore referred to as δD_{wax}) as the more concentrated compound with a more robust signal during δD measurement. Lake Titicaca δD_{wax} has a large dynamic range over the past 60 kyr, with values ranging from −236 to −114‰. Glacial (60–20 ka) values are on the whole more depleted than Holocene (11.5–0 ka) values; average glacial δD_{wax} is −207‰, while average Holocene δD_{wax} is −152‰. Within the last glacial period, values range from −174 to −236‰ and show a high degree of variability on millennial timescales.

The transition from the last glacial period into the Holocene is marked by a series of large and abrupt increases in δD_{wax}. LT δD_{wax} shows an initial rise ca. 16 ka, followed by a reversal from ~13.5–12.5 ka and a further rise at ~12–11 ka into the Holocene. The LT pattern closely resembles that observed in the δD of ice in the nearby Illimani ice core (Ramirez et al., 2003) (see Fig. 3), as well as the pattern of the last deglaciation in the NGRIP Greenland ice core $\delta^{18}O$ (Svensson et al., 2008) (see Fig. 5). Enriched δD_{wax} values from ~15.5–13.8 ka likely correspond to the Bølling–Allerød interstadial (BA) while the following period of depleted δD_{wax} values coincides with Younger Dryas stadial (YD). We note that there is some age offset between the period of depleted δD_{wax} values and the YD interval in the NGRIP record, but the off- set is likely due to uncertainties within the LT01-2B age model since several well-dated speleothem records of SASM precipitation show δD minima in phase with the YD (see Fig. 5). During the Holocene, δD_{wax} ranges from −183 to −114‰. Values decrease from the early Holocene into the present, suggesting an inverse relationship between austral summer insolation and δD_{wax}. However, there is no apparent variability on orbital timescales during the last glacial period.

2.4.1 Interpretation of the LT δD_{wax} *record*

2.4.1.1 Controls on Altiplano meteoric water δD

The isotopic composition of modern precipitation (δD_p) in the Central Andes is determined by a combination of several different climatic variables. SASM precipitation that falls on the Altiplano is ultimately derived from Atlantic Ocean moisture that has been transported across the Amazon Basin and lifted over the eastern cordillera of the Andes. Altiplano δD_p thus integrates upstream effects including rainout and moisture recycling over the Amazon Basin, altitude effects associated with upslope moisture transport, and local effects such as the intensity of precipitation ("amount effect") (Dansgaard, 1964). Changing moisture trajectories can also distinctively impact precipitation isotopic ratios (e.g., Insel et al., 2013). Results from both observational and modeling studies suggest that the dominant control on modern interannual Andean δD_p variability is Rayleigh-type fractionation during rainout along the trajectory of moist air masses across the Amazon Basin up to the Andes (e.g., Rozanski et al., 1993; Hoffmann et al., 2003; Vimeux et al., 2005; Vuille and Werner, 2005). Increased rainout along this trajectory, as well as increased local precipitation in the Andes, results in more depleted δD_p, consistent with the continentality and amount effects that dominate δD_p variability throughout most of tropical South America (Vuille et al., 2003). Accordingly, the intensity of the SASM is significantly negatively correlated with $\delta^{18}O$ (and correspondingly δD) of modern precipitation in the Central Andes, as well as throughout much of southern tropical South America (Vuille and Werner, 2005).

On glacial–interglacial timescales, there may be additional factors that influence δD_p at LT. First, the effects of changing ice volume caused changes in the isotopic composition of the original moisture source for the SASM (the equatorial Atlantic Ocean). However, given that

mean ocean isotopic composition was approximately 8‰ more enriched in δD during the LGM (i.e., $\delta^{18}O$ enrichment of 1.0‰ scaled by meteoric water line) (Schrag et al., 2002), this correction is very small compared to the scale of LT δD_{wax} changes. Second, an increased temperature gradient between high and low altitude during the last glacial period could have resulted in an "enhanced" altitude effect and more depleted δD_p at high altitude. However, Vimeux et al. (2005) conclude based on modeling simulations that this effect was likely relatively minor (~10%) compared to the dominant hydrologic signal in the Illimani ice core δD record. Finally, changing moisture trajectories and changing rates of evapotranspiration in the Amazon forest may have influenced Altiplano δD_p, but it is difficult to constrain either process. Despite these caveats, we interpret past δD_p variability on the Altiplano as a reasonable indicator of regional SASM precipitation intensity that integrates the effects of rainout in both the Amazon Basin and Central Andes.

2.4.1.2 Controls on δD_{wax}

Long-chain (C_{24}–C_{32}) *n*-fatty acids with a strong even over odd carbon number preference are produced nearly exclusively by vascular plants as components of leaf epicuticular waxes (Eglinton and Hamilton, 1967). Leaf wax compounds are deposited in lacustrine or marine sediments by eolian or fluvial transport. Though these compounds may be transported over long distances (Conte and Weber, 2002), the steep Andean topography and isolation of the LT basin make any significant contribution of leaf waxes from long-range transport unlikely. The relatively good preservation of long-chain fatty acids in sediments (Meyers, 1997) and very slow rates of isotopic exchange of the alkyl chain hydrogen (Sessions et al., 2004) make these compounds well suited for isotopic reconstructions.

The hydrogen isotopic composition of leaf wax compounds in sediments has previously been demonstrated to reliably track the isotopic composition of plant source water, i.e., meteoric water for terrestrial plants, thus allowing reconstruction of past trends of precipitation isotopes (Hou et al., 2008; Sachse et al., 2004, 2006). However, a number of secondary effects may obfuscate this primary signal. Such effects include soil water evaporation and leaf transpiration, which can cause isotopic enrichment of soil and leaf water, respectively. Furthermore, a number of studies have shown variability in biosynthetic fractionation between source water and leaf waxes among different vegetation growth forms (i.e., trees, shrubs, grasses) (Sachse et al., 2012). Because the magnitudes of these effects in different environments are not well constrained, there is some uncertainty about their combined influence on δD_{wax} in records of past climate.

We assessed the extent to which LT δD_{wax} reflects isotopic variability of precipitation versus local environmental influences by comparing the LT record to the δD record of the Illimani ice core (Ramirez et al., 2003), which provides a more direct record of isotopic variation of precipitation. Nevado Illimani is situated in the eastern cordillera of the Andes approximately 100 km directly east (generally upwind) of LT. Illimani δD should thus provide a good estimate of δD_p variability over the LT basin. Over the past 19 kyr, LT δD_{wax} and linearly interpolated Illimani δD data are well correlated (Fig. 3, $r^2 = 0.69$, $p < 0.0001$). This correlation is comparable to that of modern calibration studies of δD_{wax} across spatial climate gradients (Sachse et al., 2012) and shows that LT δD_{wax} variability is closely related to δD_p variability. δD_{wax} may be particularly successful in capturing precipitation isotopic variability at this site because of the relatively large changes in δD_p over this time period and the isolated and relatively small source area of leaf waxes in the LT watershed, helping to focus the

precipitation signal in LT sediments. Although we cannot compare δD_{wax} with ice core data before 19 ka, we assume that the observed correlation between δD_{wax} and δD_p from 19–0 ka remained intact over the duration of our record.

Although LT δD_{wax} and Illimani δD are well correlated, the slope of this relationship is significantly greater than 1. Thus while the isotopic composition of precipitation appears to be the primary control on the structure of the LT δD_{wax} record, it is clear that secondary effects also contribute to this signal. Most notably, the much larger range at LT (102‰) than at Illimani (58‰) over the past 19 kyr suggests the influence of compounding effects on LT δD_{wax}, such as decreased regional precipitation, resulting in a more enriched δD_p, and low local humidity, which would tend to further enrich plant source water by soil water evaporation and/or leaf transpiration. Since such local evapotranspiration feedbacks would be expected to act in step with δD_p changes, this would serve to amplify the δD_{wax} signal and increase its sensitivity to δD_p variability.

Another potential source of variability in the LT δD_{wax} record is vegetation change. However, pollen records from LT sediments do not reveal major vegetation shifts since the last glacial period (Paduano et al., 2003; Hanselman et al., 2011). Vegetation in the LT basin over the past 60,000 years was dominated by puna (grassland) and sub-puna (shrubland) taxa, particularly *Poaceae*. The most significant difference between the last glacial period and the Holocene was an increase in vegetation density in the LT watershed rather than large shifts in vegetation composition (Paduano et al., 2003). However, during the Holocene, a large drop in lake level between ~8 and 4 ka caused a significant retreat in the LT shoreline (Cross et al., 2000; D'Agostino et al., 2002) and likely increased the amount of littoral organic detritus delivered to deep-water sites (Baker et al., 2001b). A change in the relative contributions of

purely terrestrial versus emergent aquatic plants residing near the shoreline could thus have significantly affected δD_{wax}. Several studies have shown aquatic plants to have more depleted δD_{wax} compared to purely terrestrial plants, presumably due to accessing different water sources (i.e., lake water/groundwater vs. soil water) and the absence of soil evaporation (Shuman et al., 2006; Douglas et al., 2012). After removing the long-term negative trend through the Holocene, we observe generally more depleted δD_{wax} values during periods of low rather than high lake level (Fig. 4). Furthermore, an increased proportion of *n*-C_{24} fatty acids relative to total abundance of long-chain fatty acids (*n*-C_{24}–*n*-C_{30}) during the mid-Holocene lowstand is consistent with an increased contribution from macrophytes at this time (Gao et al., 2011). We note that Holocene δD_{wax} trends are complicated by the switch between LT01-2B and NE98-4BXB cores at 3.5 ka, but the chain length pattern remains generally consistent across the two cores. Shifts in the sources of leaf waxes to the core site are thus a possible explanation for some of the variability in δD_{wax} during the Holocene, although some large deviations (i.e., at ~8.5 ka) do not appear associated with lake level change.

2.4.2 Remote forcing of SASM variability

2.4.2.1 Glacial-interglacial variability

The substantial difference between glacial and Holocene δD_{wax} values at Lake Titicaca points to higher precipitation along the SASM trajectory during the last glacial period than during the Holocene. The similar patterns of LT δD_{wax} and Greenland temperature over the last 60 kyr suggest that glacial boundary conditions, e.g., the buildup of large northern continental ice sheets, exerted important control on SASM dynamics (Fig. 5). As LT δD_{wax} is influenced by both local and upstream precipitation variability, a number of other tropical South American

records help to constrain the geographical extent of glacial precipitation increases. Ample evidence of wetter conditions in the Central Andes and Altiplano during the LGM (Baker et al., 2001a, 2001b) and the previous three glacial periods (Fritz et al., 2004, 2007) clearly indicate significant increases in Central Andean precipitation under glacial conditions. Enhanced Andean rainfall under glacial conditions is also supported by regional climate simulations that suggest a mechanism whereby atmospheric circulation changes induced by cooler tropical Atlantic temperatures could have led to increased moisture transport from the Amazon to the Andes (Vizy and Cook, 2007).

Outside the Andes, there is some evidence of moderate precipitation increases in western Amazonia (Cheng et al., 2013) and southern Brazil (Cruz et al., 2007) throughout the last glacial period. Such widespread changes imply a larger regional mechanism to increase precipitation during the last glacial period. Based on simulations of LGM boundary conditions, Chiang et al. (2003) and Chiang and Bitz (2005) have suggested that the presence of large ice sheets at high northern latitudes could have resulted in a southward shift of the Atlantic ITCZ. The latitudinal position of the Atlantic ITCZ controls the rainy season over northern South America and also affects moisture transport into the Amazon Basin, with a southward shift in mean ITCZ position associated with increased Amazon moisture transport and a more intense SASM on a range of timescales (Vuille et al., 2012). A southward displacement of the ITCZ during the last glacial period together with increased moisture transport to the Andes could thus have caused widespread SASM precipitation increases throughout southern tropical South America. However, greater geographic coverage of records of tropical South American hydrologic variability over the last glacial cycle would be necessary to test this idea.

2.4.2.2 Millennial-scale variability

The pattern of LT δD_{wax} during the last deglaciation suggests a period of reduced precipitation intensity corresponding to the BA and wetter conditions during the YD, a pattern also suggested by other paleolimnological data from the Altiplano (Baker et al., 2001a, 2001b). A well-dated paleolake sequence further shows that the timing of lake highstands on the central Altiplano coincides with Heinrich Event 1 and the YD, providing evidence of synchronicity between temperature fluctuations in the North Atlantic region and Andean hydrologic variability (Blard et al., 2011). Intervals of depleted $\delta^{18}O$ in the Botuverá speleothem (southern Brazil) and El Condor speleothem (western Amazonia) coincident with the YD (Fig. 5) also point to increased precipitation across southern tropical South America due to a more intense SASM at that time (Wang et al., 2007; Cheng et al., 2013).

In contrast, a reconstruction of C_3/C_4 vegetation from the Cariaco Basin in northern tropical South America shows wetter conditions coincident with the BA followed by a drier YD (Hughen et al., 2004). This observed anti-phase relationship between changes in northern and southern tropical South American precipitation is consistent with meridional shifts of the Atlantic ITCZ during the last deglaciation. Southward ITCZ shifts on millennial timescales during the deglaciation were likely due to remote forcing from high-latitude North Atlantic cooling and an increase in the latitudinal temperature gradient. Southward displacements of the Atlantic ITCZ are consistently reproduced in general circulation model simulations of reduced North Atlantic SST associated with weakened Atlantic meridional overturning circulation (AMOC) (e.g., Vellinga and Wood, 2002; Zhang and Delworth, 2005), thereby linking southward ITCZ migration with cold North Atlantic events and Greenland stadials.

North Atlantic forcing has also been invoked during the last glacial period to explain

connections between millennial-scale tropical South American hydrologic variability and high-latitude climate fluctuations (Baker et al., 2001a, 2001b). Cold North Atlantic conditions, associated with cold phases of Dansgaard–Oeschger (D-O) cycles and Heinrich events, coincided with dry conditions in northern South America inferred from a longer record of C_3/C_4 vegetation shifts from the Cariaco Basin (Drenzek, 2007). In the Central Andes, more depleted $\delta^{18}O$ values in the Pacupahuain cave speleothem record point to a more intense SASM during Heinrich events and most cold phases of D-O cycles (Kanner et al., 2012). Millennial fluctuations of several paleolimnological indicators (including grain size, biogenic silica, bulk organic carbon $\delta^{13}C$, and planktonic/benthic diatom ratio) in the sediments of Lake Titicaca during MIS 3 are consistent with increased precipitation, terrestrial runoff, and shallow water input to deep water sediments coincident with North Atlantic cold events (Fritz et al., 2010). Due to relatively low resolution of the LT δD_{wax} record and uncertainty in the LT01-2B age model during the same time period, we cannot unequivocally correlate δD_{wax} variability to North Atlantic events, but it is likely that Andean hydrologic variability tied to high-latitude forcing contributed to the large fluctuations of LT δD_{wax} between 60 and 20 ka.

2.4.3 Local forcing of SASM variability

The magnitude of local summer insolation does not show a consistent relationship with δD_{wax} variability at Lake Titicaca over the past 60 kyr (Fig. 5). The LT record instead shows a much stronger relationship between summer insolation and δD_{wax} variability over the last 20 kyr than during the last glacial period (60–20 ka). The negative trend in δD_{wax} from the early to late Holocene is consistent with increasingly wet conditions in response to increasing summer insolation. This Holocene trend has also been seen in a number of isotopic records from the

Central Andes, including the Illimani and Huascaran ice cores (Ramirez et al., 2003; Thompson et al., 1995) and carbonate records from Lake Pumacocha (Bird et al., 2011) and Lake Junin (Seltzer et al., 2000), as well as speleothem records from southern Brazil (Cruz et al., 2006; Wang et al., 2007) and western Amazonia (Cheng et al., 2013). As discussed by Bird et al. (2011), the uniformity of Holocene records throughout southern tropical South America suggests an insolation-controlled strengthening of the SASM throughout the Holocene.

In contrast, there does not appear to be any significant relationship between LT δD_{wax} and summer insolation from 60 to 20 ka, consistent with absent or very weak precessional signals in speleothem $\delta^{18}O$ records from the Andes (Kanner et al., 2012) and western Amazonia (Mosblech et al., 2012; Cheng et al., 2013) over this interval. Although there is strong evidence of insolation forcing of monsoonal precipitation in southern Brazil throughout the last glacial period (Cruz et al., 2006; Wang et al., 2007), insolation forcing of Andean and Amazonian precipitation intensity was apparently diminished during the same period, presumably due to the competing influence of glacial boundary conditions. The interaction between insolation forcing and glacial boundary conditions thus appears to have been regionally variable, with glacial conditions suppressing the effects of insolation changes in western Amazonia and the Central Andes, while insolation forcing remained dominant in southern Brazil.

2.5 Conclusion

The hydrogen isotopic composition of terrestrial leaf waxes in Lake Titicaca sediments reveals large amplitude changes in regional precipitation on a range of timescales over the last 60 kyr. The coherence of LT δD_{wax} and the δD record from the nearby Illimani ice core

demonstrates that variability in precipitation isotopes is the dominant influence on δD_{wax} at this site, reaffirming the value of δD_{wax} as a paleoclimate proxy. Local environmental factors are also significant, and changes in the extent of evapotranspiration of plant source water likely accentuated δD_{wax} sensitivity to isotopic shifts in precipitation.

Considerably depleted δD_{wax} values suggest wetter conditions during the last glacial period relative to the Holocene along the SASM trajectory from the Amazon Basin to the Central Andes. On millennial timescales, the LT δD_{wax} record is consistent with a number of SASM records that show drier conditions coincident with the Bølling–Allerød interstadial followed by a return to wetter conditions concurrent with the Younger Dryas stadial. The LT record further supports a model of meridional shifts in Atlantic ITCZ position, possibly related to AMOC and North Atlantic SST variability during the last deglaciation. Local insolation forcing appears to have been strong during the Holocene, evidenced by a general negative trend of δD_{wax} concomitant with increasing summer insolation. Insolation control of SASM intensity throughout the last glacial period, however, is not apparent in the record, suggesting that glacial boundary conditions led to dampening of local insolation forcing. Overall, the LT δD_{wax} record underscores the importance of remote forcing from high latitudes as a control of tropical South American hydrology over the past 60 kyr, with cold periods at high northern latitudes generally associated with increases in SASM precipitation.

Acknowledgements

This work was supported by an MIT Presidential Fellowship and a WHOI Ocean and Climate Change Institute fellowship (KLF) and NSF grants DEB-0447281 (KAH), ATM-0502517 (KAH), and EAR-1338694 (PAB and SCF). We thank Eva Niedermeyer and one anonymous

reviewer for comments that helped to improve the manuscript.

References

Baker, P.A., Rigsby, C.A., Seltzer, G.O., Fritz, S.C., Lowenstein, T.K., Bacher, N.P., Veliz, C., 2001a. Tropical climate changes at millennial and orbital timescales on the Bolivian Altiplano. Nature 409, 698–701.

Baker, P.A., Seltzer, G.O., Fritz, S.C., Dunbar, R.B., Grove, M.J., Tapia, P.M., Cross, S.L., Rowe, H.D., Broda, J.P., 2001b. The history of South American tropical precipitation for the past 25,000 years. Science 291, 640–643.

Baker, P.A., Fritz, S.C., Burns, S.J., Ekdahl, E., Rigsby, C.A., 2009. The nature and origin of decadal to millennial scale climate variability in the southern tropics of South America: the Holocene record of Lago Umayo, Peru. In: Past Climate Variability in South America and Surrounding Regions, pp. 301–322.

Bird, B.W., Abbott, M.B., Rodbell, D.T., Vuille, M., 2011. Holocene tropical South American hydroclimate revealed from a decadally resolved lake sediment $\delta^{18}O$ record. Earth Planet. Sci. Lett. 310, 192–202.

Blard, P.-H., Sylvestre, F., Tripati, A.K., Claude, C., Causse, C., Coudrain, A., Condom, T., Seidel, J.-L., Vimeux, F., Moreau, C., Dumoulin, J.-P., Lavé, J., 2011. Lake high- stands on the Altiplano (Tropical Andes) contemporaneous with Heinrich 1 and the Younger Dryas: new insights from ^{14}C, U–Th dating and $\delta^{18}O$ of carbonates. Quat. Sci. Rev. 30, 3973–3989.

Broecker, W.S., 1997. Mountain glaciers: recorders of atmospheric water vapor content? Glob. Biogeochem. Cycles 11, 589–597.

Cheng, H., Sinha, A., Cruz, F.W., Wang, X., Edwards, R.L., d'Horta, F.M., Ribas, C.C., Vuille, M., Stott, L.D., Auler, A.S., 2013. Climate change patterns in Amazonia and biodiversity. Nat. Commun. 4, 1411–1416.

Chiang, J.C.H., Biasutti, M., Battisti, D.S., 2003. Sensitivity of the Atlantic Intertropical Convergence Zone to Last Glacial Maximum boundary conditions. Paleoceanography 18, 1094.

Chiang, J.C.H., Bitz, C.M., 2005. Influence of high latitude ice cover on the marine Intertropical Convergence Zone. Clim. Dyn. 25, 477–496.

Chiessi, C.M., Mulitza, S., Pätzold, J., Wefer, G., Marengo, J.A., 2009. Possible impact of the Atlantic Multidecadal Oscillation on the South American summer monsoon. Geophys. Res. Lett. 36, L21707.

Collini, E.A., Berbery, E.H., Barros, V.R., Pyle, M.E., 2008. How does soil moisture influence the early stages of the South American monsoon? J. Climate 21, 195–213.

Conte, M.H., Weber, J.C., 2002. Plant biomarkers in aerosols record isotopic discrimination of terrestrial photosynthesis. Nature 417, 639–641.

Cross, S., Baker, P., Seltzer, G., Fritz, S., Dunbar, R., 2000. A new estimate of the Holocene lowstand level of Lake Titicaca, central Andes, and implications for tropical palaeohydrology. Holocene 10, 21–32.

Cruz, F., Burns, S., Karmann, I., Sharp, W., Vuille, M., 2006. Reconstruction of regional atmospheric circulation features during the late Pleistocene in subtropical Brazil from oxygen isotope composition of speleothems. Earth Planet. Sci. Lett. 248, 495–507.

Cruz, F.W., Burns, S.J., Jercinovic, M., Karmann, I., Sharp, W.D., Vuille, M., 2007. Evidence of rainfall variations in Southern Brazil from trace element ratios (Mg/Ca and Sr/Ca) in a

Late Pleistocene stalagmite. Geochim. Cosmochim. Acta 71, 2250–2263.
D'Agostino, K.D., Seltzer, G., Baker, P.A., Fritz, S.C., Dunbar, R., 2002. Late-Quaternary lowstands of Lake Titicaca: evidence from high-resolution seismic data. Palaeogeogr. Palaeoclimatol. Palaeoecol. 179, 97–111.
Dansgaard, W., 1964. Stable isotopes in precipitation. Tellus 16, 436–468.
Douglas, P.M.J., Pagani, M., Brenner, M., Hodell, D.A., Curtis, J.H., 2012. Aridity and vegetation composition are important determinants of leaf-wax δD values in southeastern Mexico and Central America. Geochim. Cosmochim. Acta 97, 24–45.
Drenzek, N.J., 2007. The temporal dynamics of terrestrial organic matter transfer to the oceans: initial assessment and application. PhD Thesis. MIT/WHOI Joint Program in Oceanography/Applied Ocean Science & Engineering.
Eglinton, G., Hamilton, R.J., 1967. Leaf epicuticular waxes. Science 156, 1322.
Fritz, S.C., Baker, P.A., Lowenstein, T.K., Seltzer, G.O., Rigsby, C.A., Dwyer, G.S., Tapia, P.M., Arnold, K.K., Ku, T.L., Luo, S., 2004. Hydrologic variation during the last 170,000 years in the southern hemisphere tropics of South America. Quat. Res. 61, 95–104.
Fritz, S.C., Baker, P.A., Seltzer, G.O., Ballantyne, A., Tapia, P., Cheng, H., Edwards, R.L., 2007. Quaternary glaciation and hydrologic variation in the South American tropics as reconstructed from the Lake Titicaca drilling project. Quat. Res. 68, 410–420.
Fritz, S.C., Baker, P.A., Ekdahl, E., Seltzer, G.O., Stevens, L.R., 2010. Millennial-scale climate variability during the Last Glacial period in the tropical Andes. Quat. Sci. Rev. 29, 1017–1024.
Gao, L., Hou, J., Toney, J., MacDonald, D., Huang, Y., 2011. Mathematical modeling of the aquatic macrophyte inputs of mid-chain n-alkyl lipids to lake sediments: implications for interpreting compound specific hydrogen isotopic records. Geochim. Cosmochim. Acta 75, 3781–3791.
Garreaud, R.D., 1999. Multiscale analysis of the summertime precipitation over the central Andes. Mon. Weather Rev. 127, 901–921.
Garreaud, R., Vuille, M., Clement, A.C., 2003. The climate of the Altiplano: observed current conditions and mechanisms of past changes. Palaeogeogr. Palaeoclimatol. Palaeoecol. 194, 5–22.
Garreaud, R.D., Vuille, M., Compagnucci, R., Marengo, J., 2009. Present-day South American climate. Palaeogeogr. Palaeoclimatol. Palaeoecol. 281, 180–195.
Hanselman, J.A., Bush, M.B., Gosling, W.D., Collins, A., Knox, C., Baker, P.A., Fritz, S.C., 2011. A 370,000-year record of vegetation and fire history around Lake Titicaca (Bolivia/Peru). Palaeogeogr. Palaeoclimatol. Palaeoecol. 305, 201–214.
Hoffmann, G., 2003. Taking the pulse of the tropical water cycle. Science 301, 776.
Hoffmann, G., Ramirez, E., Taupin, J.D., Francou, B., Ribstein, P., Delmas, R., Dürr, H., Gallaire, R., Simoes, J., Schotterer, U., 2003. Coherent isotope history of Andean ice cores over the last century. Geophys. Res. Lett. 30, 1179.
Hou, J., D'Andrea, W.J., Huang, Y., 2008. Can sedimentary leaf waxes record D/H ratios of continental precipitation? Field, model, and experimental assessments. Geochim. Cosmochim. Acta 72, 3503–3517.
Hughen, K.A., Eglinton, T.I., Xu, L., Makou, M., 2004. Abrupt tropical vegetation response to rapid climate changes. Science 304, 1955–1959.
Insel, N., Poulsen, C.J., Sturm, C., Ehlers, T.A., 2013. Climate controls on Andean precipitation $\delta^{18}O$ interannual variability. J. Geophys. Res. 118, 1–22.

Kanner, L.C., Burns, S.J., Cheng, H., Edwards, R.L., 2012. High-latitude forcing of the South American summer monsoon during the Last Glacial. Science 335, 570–573.
Laskar, J., Robutel, P., Joutel, F., Gastineau, M., Correia, A.C.M., Levrard, B., 2004. A long-term numerical solution for the insolation quantities of the Earth. Astron. Astrophys. 428, 261–285.
Lenters, J., Cook, K., 1997. On the origin of the Bolivian high and related circulation features of the South American climate. J. Atmos. Sci. 54, 656–678.
Meyers, P.A., 1997. Organic geochemical proxies of paleoceanographic, paleolimnologic, and paleoclimatic processes. Org. Geochem. 27, 213–250.
Mosblech, N.A.S., Bush, M.B., Gosling, W.D., Hodell, D., Thomas, L., Calsteren, P.V., Correa-Metrio, A., Valencia, B.G., Curtis, J., Woesik, R.V., 2012. North Atlantic forcing of Amazonian precipitation during the last ice age. Nat. Geosci. 5, 817–820.
Paduano, G.M., Bush, M.B., Baker, P.A., Fritz, S.C., Seltzer, G.O., 2003. A vegetation and fire history of Lake Titicaca since the Last Glacial Maximum. Palaeogeogr. Palaeoclimatol. Palaeoecol. 194, 259–279.
Paillard, D., Labeyrie, L., Yiou, P., 1996. Macintosh program performs time-series analysis. EosTrans. AGU 77, 379.
Pierrehumbert, R., 1999. Huascaran δ18O as an indicator of tropical climate during the Last Glacial Maximum. Geophys. Res. Lett. 26, 1345–1348.
Ramirez, E., Hoffmann, G., Taupin, J., Francou, B., Ribstein, P., Caillon, N., Ferron, F., Landais, A., Petit, J., Pouyaud, B., 2003. A new Andean deep ice core from Nevado Illimani (6350 m), Bolivia. Earth Planet. Sci. Lett. 212, 337–350.
Reimer, P.J., Bard, E., Bayliss, A., Beck, J.W., Blackwell, P.G., Ramsey, C.B., Buck, C.E., Cheng, H., Edwards, R.L., Friedrich, M., Grootes, P.M., Guilderson, T.P., Haflidison, H., Hajdas, I., Hatté, C., Heaton, T., Hoffmann, D.L., Hogg, A., Hughen, K.A., Kaiser, K., Kromer, B., Manning, S.W., Niu, M., Reimer, R., Richards, D.A., Scott, E.M., Southon, J.R., Staff, R.A., Turney, C., Plicht, J., 2013. IntCal13 and Marine13 radiocarbon age calibration curves 0–50,000 years cal BP. Radiocarbon 55, 1869–1887.
Rozanski, K., Araguás-Araguás, L., Gonfiantini, R., 1993. Isotopic Patterns in Modern Global Precipitation. Geophysical Monograph Series, vol. 78, pp. 1–36.
Sachse, D., Radke, J., Gleixner, G., 2004. Hydrogen isotope ratios of recent lacustrine sedimentary n-alkanes record modern climate variability. Geochim. Cosmochim. Acta 68, 4877–4889.
Sachse, D., Radke, J., Gleixner, G., 2006. δD values of individual n-alkanes from terrestrial plants along a climatic gradient – implications for the sedimentary biomarker record. Org. Geochem. 37, 469–483.
Sachse, D., Billault, I., Bowen, G.J., Chikaraishi, Y., Dawson, T.E., Feakins, S.J., Freeman, K.H., Magill, C.R., Mcinerney, F.A., Van Der Meer, M.T.J., Polissar, P., Robins, R.J., Sachs, J.P., Schmidt, H.-L., Sessions, A.L., White, J.W.C., West, J.B., Kahmen, A., 2012. Molecular paleohydrology: interpreting the hydrogen-isotopic composition of lipid biomarkers from photosynthesizing organisms. Annu. Rev. Earth Planet. Sci. 40, 221–249.
Schrag, D.P., Adkins, J.F., McIntyre, K., Alexander, J.L., Hodell, D.A., Charles, C.D., McManus, J.F., 2002. The oxygen isotopic composition of seawater during the Last Glacial Maximum. Quat. Sci. Rev. 21, 331–342.
Seltzer, G., Rodbell, D., Burns, S., 2000. Isotopic evidence for late Quaternary climatic change in tropical South America. Geology 28, 35–38.

Sessions, A.L., Burgoyne, T.W., Hayes, J.M., 2001. Determination of the H_3 factor in hydrogen isotope ratio monitoring mass spectrometry. Anal. Chem. 73, 200–207.
Sessions, A.L., Sylva, S.P., Summons, R.E., Hayes, J.M., 2004. Isotopic exchange of carbon-bound hydrogen over geologic timescales 1. Geochim. Cosmochim. Acta 68, 1545–1559.
Shuman, B., Huang, Y., Newby, P., Wang, Y., 2006. Compound-specific isotopic analyses track changes in seasonal precipitation regimes in the Northeastern United States at ca. 8200 cal yr BP. Quat. Sci. Rev. 25, 2992–3002.
Svensson, A., Andersen, K.K., Bigler, M., Clausen, H.B., Dahl-Jensen, D., Davies, S.M., Johnsen, S.J., Muscheler, R., Parrenin, F., Rasmussen, S.O., Rothlisberger, R., Seierstad, I., Steffensen, J.P., Vinther, B.M., 2008. A 60,000 year Greenland stratigraphic ice core chronology. Clim. Past 4, 47–57.
Tapia, P.M., Fritz, S.C., Baker, P.A., Seltzer, G.O., Dunbar, R.B., 2003. A Late Quaternary diatom record of tropical climatic history from Lake Titicaca (Peru and Bolivia). Palaeogeogr. Palaeoclimatol. Palaeoecol. 194, 139–164.
Thompson, L., Mosley-Thompson, E., Davis, M., Lin, P.N., Henderson, K.A., Cole-Dai, J., Bolzan, J., Liu, K.B., 1995. Late glacial stage and Holocene tropical ice core records from Huascaran, Peru. Science 269, 46–50.
Thompson, L.G., Davis, M.E., Mosley-Thompson, E., Sowers, T.A., Henderson, K.A., Zagorodnov, V.S., Lin, P.N., Mikhalenko, V.N., Campen, R.K., Bolzan, J.F., 1998. A 25,000-year tropical climate history from Bolivian ice cores. Science 282, 1858–1864.
Vellinga, M., Wood, R.A., 2002. Global climatic impacts of a collapse of the Atlantic thermohaline circulation. Clim. Change 54, 251–267.
Vimeux, F., Gallaire, R., Bony, S., Hoffmann, G., Chiang, J.C.H., 2005. What are the climate controls on δD in precipitation in the Zongo Valley (Bolivia)? Implications for the Illimani ice core interpretation. Earth Planet. Sci. Lett. 240, 205–220.
Vizy, E.K., Cook, K.H., 2007. Relationship between Amazon and high Andes rainfall. J. Geophys. Res. 112, D07107.
Vuille, M., Werner, M., 2005. Stable isotopes in precipitation recording South American summer monsoon and ENSO variability: observations and model results. Clim. Dyn. 25, 401–413.
Vuille, M., Bradley, R., Werner, M., Healy, R., Keimig, F., 2003. Modeling $\delta^{18}O$ in precipitation over the tropical Americas: 1. Interannual variability and climatic controls. J. Geophys. Res. 108, 4174.
Vuille, M., Burns, S.J., Taylor, B.L., Cruz, F.W., Bird, B.W., Abbott, M.B., Kanner, L.C., Cheng, H., Novello, V.F., 2012. A review of the South American Monsoon history as recorded in stable isotopic proxies over the past two millennia. Clim. Past Discuss. 8, 637–668.
Wang, X., Auler, A.S., Edwards, R.L., Cheng, H., Ito, E., Wang, Y., Kong, X., Solheid, M., 2007. Millennial-scale precipitation changes in southern Brazil over the past 90,000 years. Geophys. Res. Lett. 34, L23701.
Zhang, R., Delworth, T.L., 2005. Simulated tropical response to a substantial weakening of the Atlantic thermohaline circulation. J. Climate 18, 1853–1860.
Zhou, J., Lau, K., 1998. Does a monsoon climate exist over South America? J. Climate 11, 1020–1040.

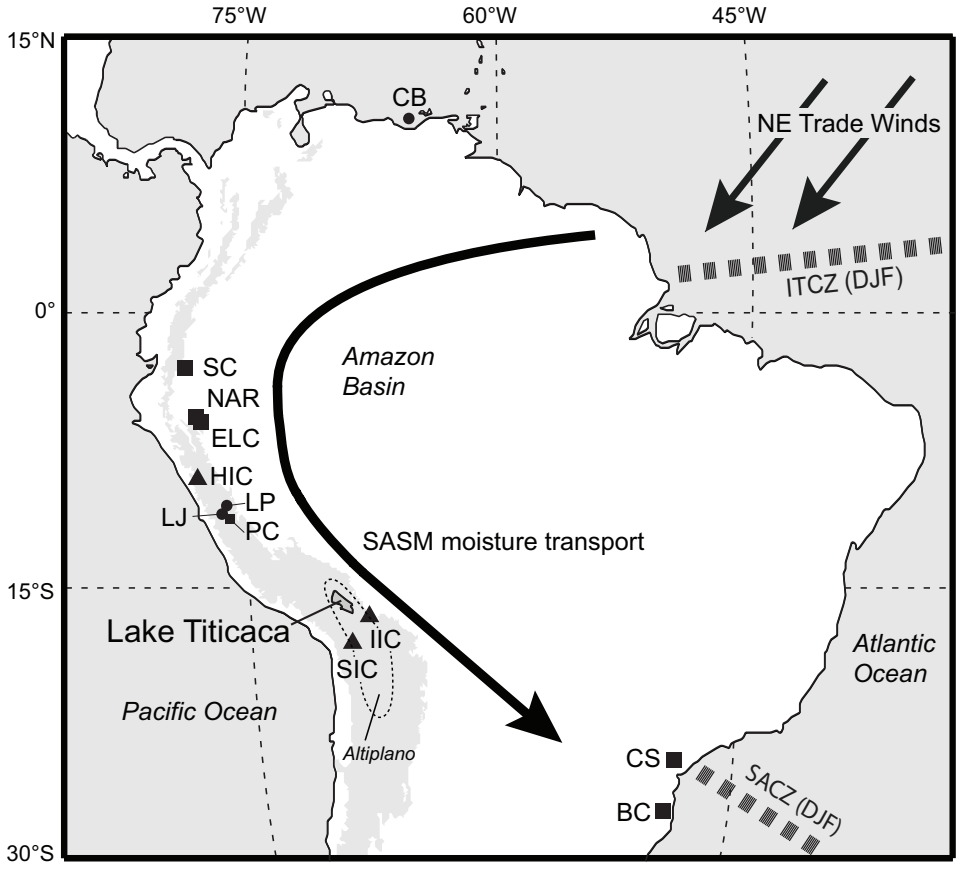

Figure 1. Map of South American tropics showing location of Lake Titicaca and locations of ice core (triangles), speleothem (squares) and sediment (circles) records discussed in text. CB: Cariaco Basin (Hughen et al., 2004), SC: Santiago cave (Mosblech et al., 2012), NAR/ELC: Cueva del Diamante/El Condor (Cheng et al., 2013), HIC: Huascarán ice core (Thompson et al., 1995), LP: Laguna Pumacocha (Bird et al., 2011), LJ: Lake Junin (Seltzer et al., 2000), PC: Pacupahuain cave (Kanner et al., 2012), IIC: Illimani ice core (Ramirez et al., 2003), SIC: Sajama ice core (Thompson et al., 1998), CS: Santana cave (Cruz et al., 2006), BC: Botuverá cave (Cruz et al., 2006, 2007; Wang et al., 2007). Also shown are general features of the South American Summer Monsoon (SASM) including northeast trade winds, connections to the marine Intertropical Convergence Zone (ITCZ) and South Atlantic Convergence Zone (SACZ), and a representation of the general SASM moisture trajectory during austral summer. Shaded area indicates extent of Andes (area with elevation ≥2000 m), while dashed line indicates approximate extent of Altiplano.

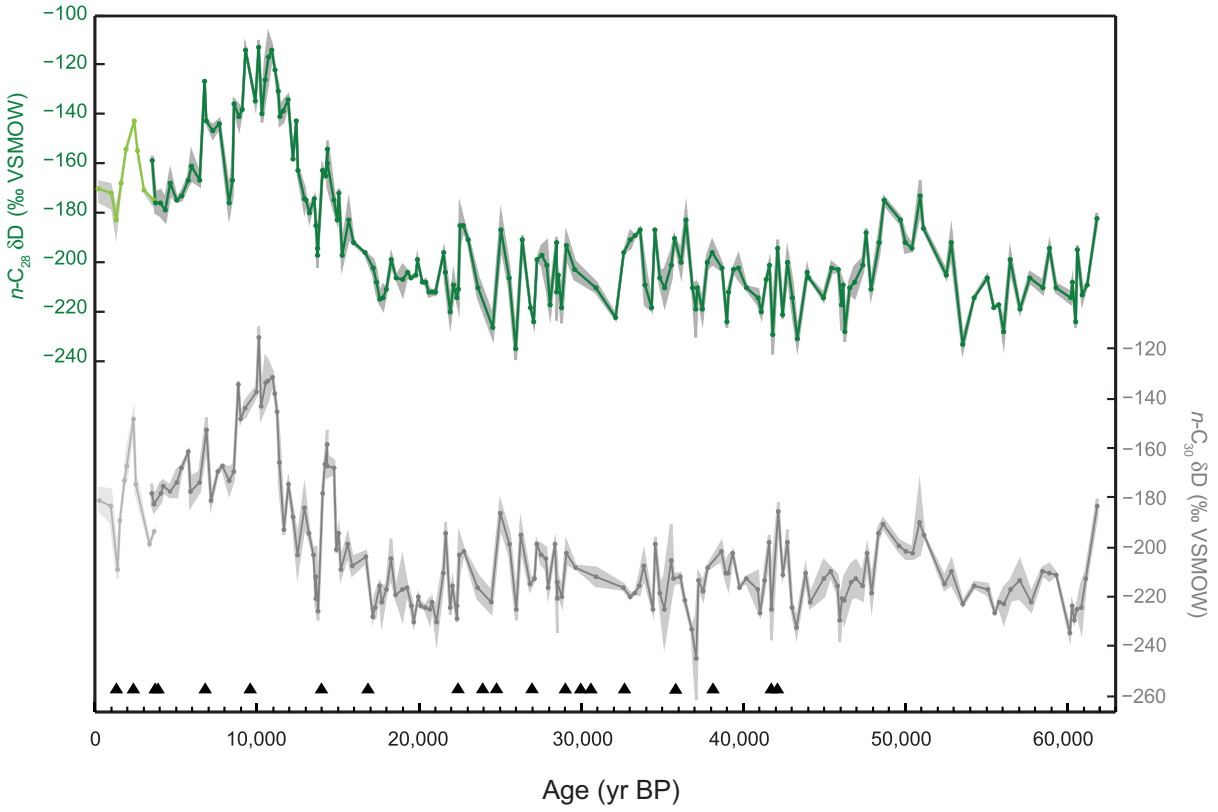

Figure 2. Time series of Titicaca C_{28} (green) and C_{30} (gray) *n*-alkanoic acid δD over the past 60 kyr. Darker colors indicate samples from LT01-2B core, and lighter colors indicate samples from NE98-4BXB core. Error clouds indicate 1σ precision of replicate sample measurements. For samples with no replicates, an error of 4.5‰ was assigned based on average uncertainty of external standards. Triangles denote age points from radiocarbon dating of sediment organic matter (Table S1) (Tapia et al., 2003; Fritz et al., 2007). We note that despite the strong correlation between *n*-C_{28} and *n*-C_{30} ($r^2 = 0.82$, $p < 0.0001$), there are some discrepancies between the δD records of the two compounds, possibly due to different vegetation contributions to each chain length. For interpretation of past precipitation variability, we opted to focus on *n*-C_{28} δD as the more concentrated compound and generally more robust signal during δD measurement.

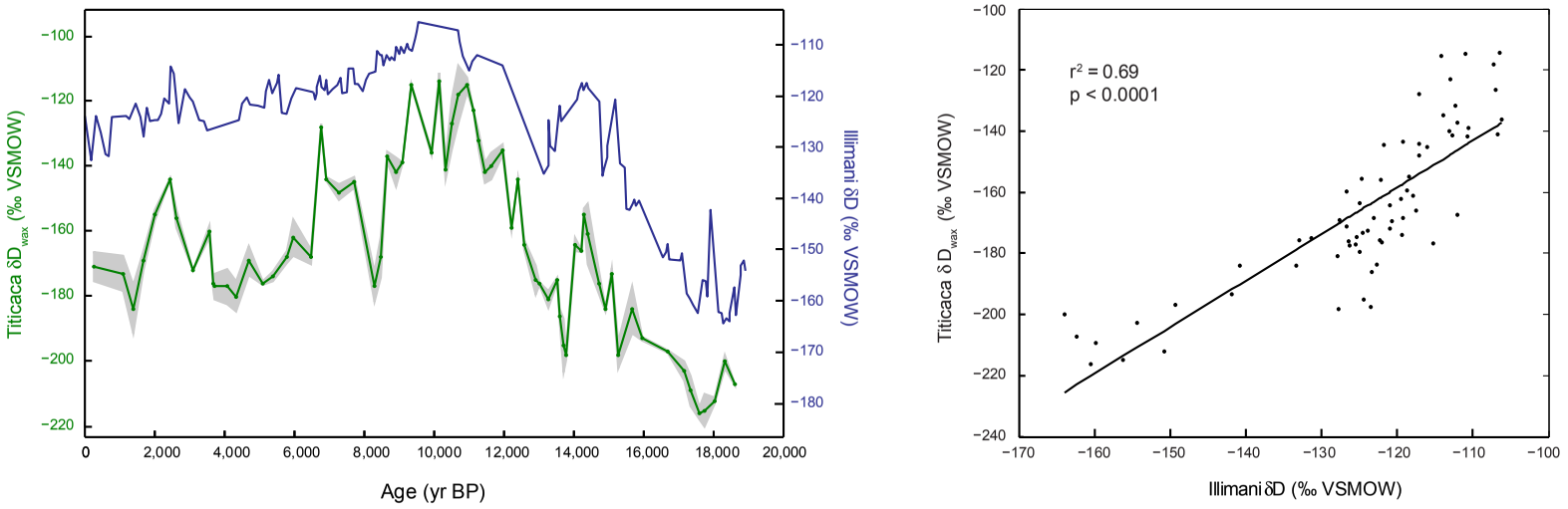

Figure 3. (Left) Comparison of Titicaca δD_{wax} and Illimani ice core δD over past 20 kyr. Note difference in scales between left and right axes. (Right) Regression between Titicaca δD_{wax} and corresponding Illimani δD data at interpolated time points.

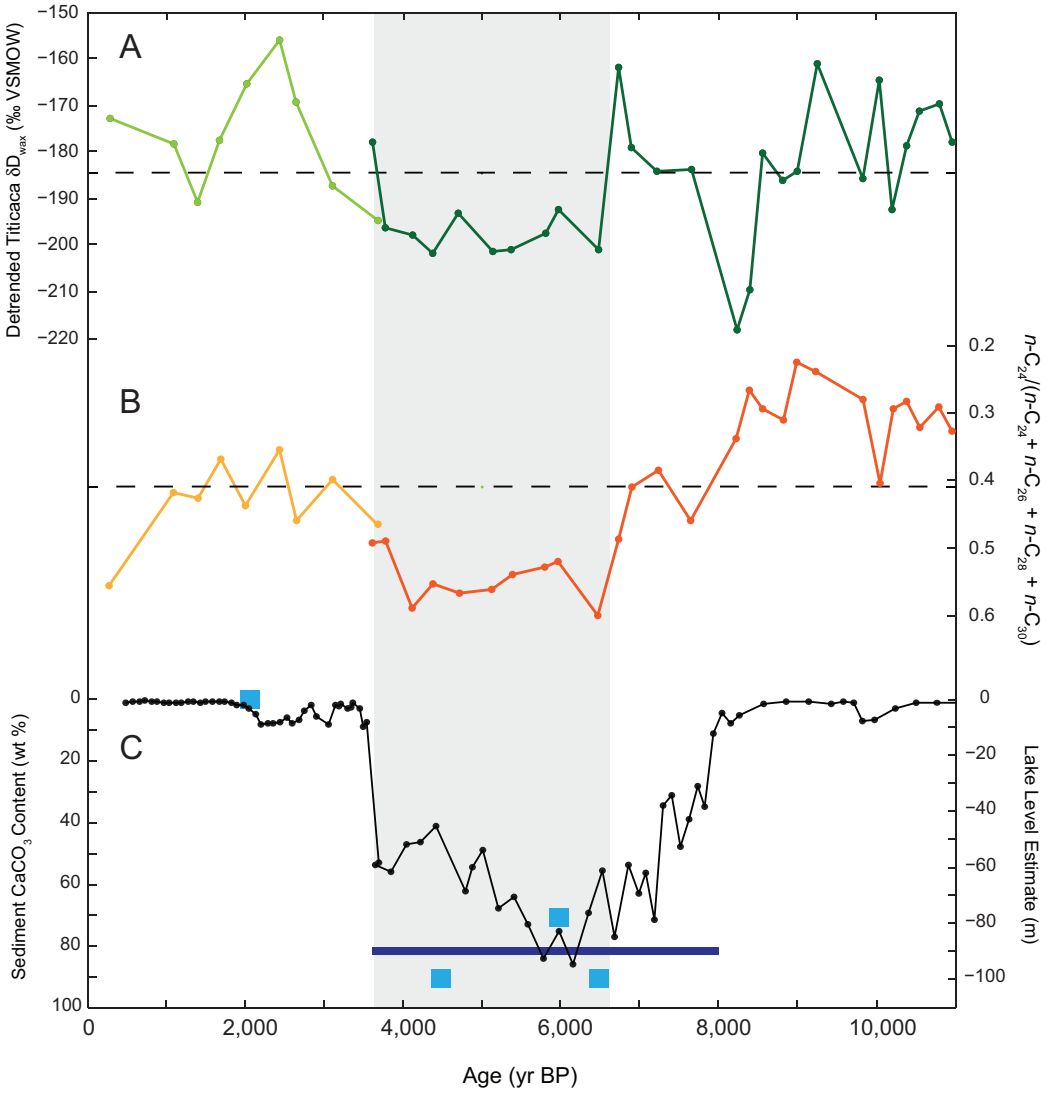

Figure 4. Comparison of Holocene detrended Titicaca δD_{wax} record (A), changes in *n*-alkanoic chain length abundance (B), and lake level indicators (C). A. Titicaca δD_{wax} data from 11–0 ka was fit with a linear regression and the slope subtracted to remove long-term trend. Dark green indicates LT01-2B samples, light green indicates NE98-4BXB samples, and dashed line shows average Holocene value. B. Ratio of C_{24} *n*-alkanoic acid abundance to total long-chain even carbon number fatty acid (n-C_{24}–n-C_{30}) abundance. Dark orange indicates LT01-2B samples, light orange indicates NE98-4BXB samples, and dashed line shows average Holocene value. C. Black line shows weight percent $CaCO_3$ in Lake Titicaca sediments from Baker et al. (2001b). $CaCO_3$ content is inversely related to lake level due to salinity and pressure effects on CaCO3 precipitation/dissolution. Blue squares indicate lake level estimates from Cross et al. (2000) using sedimentological, geochemical and biological analyses of Lake Titicaca sediment cores. Solid dark blue line indicates lowstand level estimate from seismic data (D'Agostino et al., 2002). Shaded bar shows correspondence between depleted δD_{wax} values, high n-C_{24} abundance and low lake level during mid-Holocene.

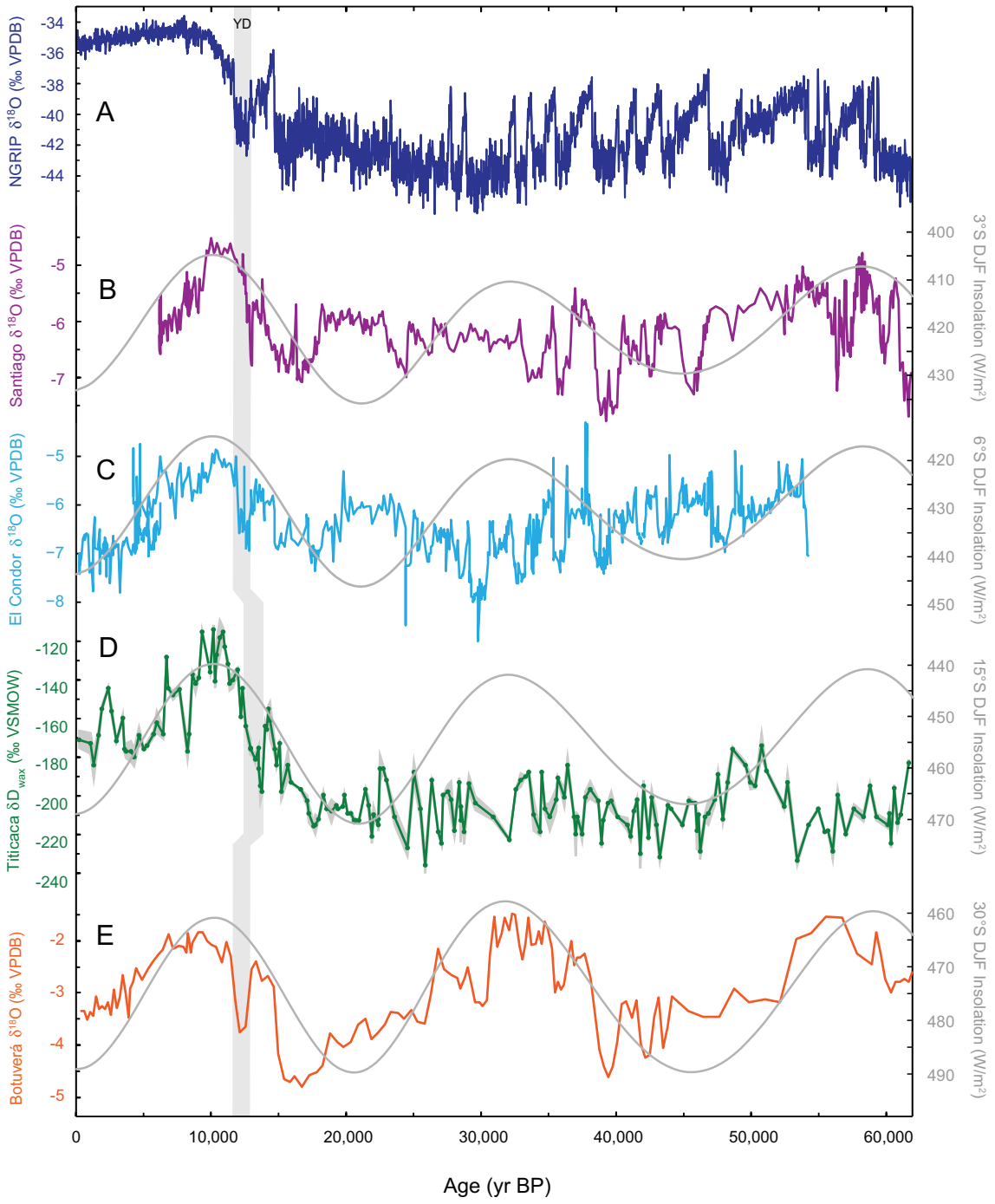

Figure 5. Comparison of Titicaca δD_{wax} with Greenland and southern tropical South American isotopic records over the past 60 kyr. A. Greenland (NGRIP) ice core $\delta^{18}O$ (Svensson et al., 2008). B. Speleothem $\delta^{18}O$ from Santiago cave in western Amazonia (Mosblech et al., 2012). C. Speleothem $\delta^{18}O$ from El Condor cave in western Amazonia (Cheng et al., 2013). D. Titicaca δD_{wax}. E. Speleothem $\delta^{18}O$ from Botuverá cave in southern Brazil (Wang et al., 2007). For South American records, gray lines show mean summer (December–February) insolation for latitude of each study site. Note that insolation axes are reversed (increasing down). Insolation values were calculated with AnalySeries 2.0 (Paillard et al., 1996) using data from Laskar et al. (2004). Shaded bar indicates Younger Dryas (YD) interval in all records.

Table S1. NE98-4BXB and LT01-2B bulk organic carbon radiocarbon ages (Tapia et al., 2003; Fritz et al., 2007) updated to IntCal13 calibration.

Core	Depth (m)	^{14}C age (yr BP)	Age Error (yr)	Original Calendar Age (yr BP)	IntCal13 Calendar Age (yr BP)	1σ Age Error (yr)
NE98-4BXB	0	0	0	0	0	0
NE98-4BXB	0.30	1490	45	1366	1368	43
NE98-4BXB	0.60	2370	40	2357	2392	48
NE98-4BXB	0.83	3490	40	3765	3772	57
LT01-2B	0.108	3050	30	3268	3282	75
LT01-2B	0.28	3625	43	3933	3928	56
LT01-2B	1	5988	52	6818	6832	58
LT01-2B	1.83	8601	62	9584	9576	54
LT01-2B	2.9	12,123	81	14217	13970	120
LT01-2B	3.12	14,360	50	17211	17508	89
LT01-2B	6.135	18,790	65	22311	22625	110
LT01-2B	7.21	20,000	150	23210	24065	186
LT01-2B	9.04	20,760	80	24046	25075	162
LT01-2B	11.84	22,310	140	25752	26550	239
LT01-2B	15.04	24,190	160	27821	28217	204
LT01-2B	16.78	25,110	222	28834	29147	256
LT01-2B	16.78	25,310	220	29054	29346	284
LT01-2B	18.04	28,390	180	32444	32301	354
LT01-2B	21.15	33,370	200	37925	37755	427
LT01-2B	21.72	31,230	660	35569	35179	633
LT01-2B	24.16	36,680	270	41142	41324	269
LT01-2B	25.99	37,900	1900	41416	41977	1668

Updated Age-Depth Models

Core	Upper Depth (mblf)	Lower Depth (mblf)	Age-depth equations, x = depth (m)
NE98-4BXB	0	0.83	$4399x - 20$
LT01-2B	0	4.56	$4320x + 2531$
LT01-2B	4.56	16.78	$576x + 19605$
LT01-2B	16.78	38.57	$1486x + 4410$

Chapter 3.

Late Quaternary environmental change in the interior South American tropics: new insight from leaf wax stable isotopes

This chapter has been submitted to Earth and Planetary Science Letters and is in revision.

Late Quaternary environmental change in the interior South American tropics: new insight from leaf wax stable isotopes

Kyrstin L. Fornace,[a,b*] Bronwen S. Whitney,[c] Valier Galy,[b] Konrad A. Hughen,[b] Francis E. Mayle[d]

a. MIT/WHOI Joint Program in Oceanography/Applied Ocean Science and Engineering, Cambridge, MA 02139, USA.
b. Department of Marine Chemistry and Geochemistry, Woods Hole Oceanographic Institution 266 Woods Hole Rd, Woods Hole, MA 02543, USA.
c. Department of Geography, Northumbria University Newcastle, Ellison Place, Newcastle-Upon-Tyne, NE1 8ST, UK.
d. Department of Geography and Environmental Science, University of Reading, Whiteknights, Reading, RG6 6AB, UK.

*corresponding author: kfornace@whoi.edu

Abstract

Stable isotope analysis of leaf waxes in a sediment core from Laguna La Gaiba, a shallow lake located at the Bolivian margin of the Pantanal wetlands, provides new perspective on vegetation and climate change in the lowland interior tropics of South America over the past 40,000 years. The carbon isotopic compositions ($\delta^{13}C$) of long-chain *n*-alkanes reveal large shifts between C_3- and C_4-dominated vegetation communities since the last glacial period, consistent with landscape reconstructions generated with pollen data from the same sediment core. Leaf wax $\delta^{13}C$ values during the last glacial period reflect an open landscape composed of C_4 grasses and C_3 herbs from 41-20 ka. A peak in C_4 abundance during the Last Glacial Maximum (LGM, ~21 ka) suggests drier or more seasonal conditions relative to the earlier glacial period, while the development of a C_3-dominated forest community after 20 ka points to increased humidity during the last deglaciation. Within the Holocene, large changes in the abundance of C_4 vegetation indicate a transition from drier or more seasonal conditions during the early/mid-Holocene to wetter conditions in the late Holocene coincident with increasing austral summer insolation. Strong negative correlations between leaf wax $\delta^{13}C$ and δD values over the entire

record indicate that the majority of variability in leaf wax δD at this site can be explained by variability in the magnitude of biosynthetic fractionation by different vegetation types rather than changes in meteoric water δD signatures. However, positive δD deviations from the observed $\delta^{13}C$-δD trends are consistent with more enriched source water and drier or more seasonal conditions during the early/mid-Holocene and LGM. Overall, our record adds to evidence of varying influence of glacial boundary conditions and orbital forcing on South American Summer Monsoon precipitation in different regions of the South American tropics. Moreover, the relationships between leaf wax stable isotopes and pollen data observed at this site underscore the complementary nature of pollen and leaf wax $\delta^{13}C$ data for reconstructing past vegetation changes and the potentially large effects of such changes on leaf wax δD signatures.

Keywords: Pantanal, leaf wax, compound-specific stable isotopes, South American Summer Monsoon, last glacial period, Holocene

3.1 Introduction

Characterizing the controls on South American Summer Monsoon (SASM) dynamics on geological timescales provides critical context for investigating present and future trends in South American tropical climate. Changes in the distribution and intensity of SASM precipitation can alter hydrologic and vegetation patterns across much of the South American continent with potentially significant ramifications for both the global carbon cycle and climate system. An increasingly coherent picture of late Quaternary SASM behavior has begun to emerge from a number of records of SASM precipitation from the Central Andes, western Amazonia and southern Brazil (Fornace et al., 2014; Wang et al., 2007; Cruz et al., 2005; Mosblech et al., 2012; Cheng et al., 2013; Kanner et al., 2012). These records indicate that

generally wet conditions prevailed during the Last Glacial Maximum (LGM) and late glacial period, followed by a shift towards drier conditions in the early/mid-Holocene. After this dry period, SASM precipitation has gradually increased into the present, a trend widely attributed to increasing summer insolation through the Holocene (e.g., Bird et al., 2011).

Missing from this discussion of past SASM trends are critical records from the interior tropics, where climate archives such as lacustrine sediments or speleothems rarely extend back to the last glacial period. Available pollen records from several sites in the southern Amazon Basin point to drier conditions during the last glacial period (Mayle et al. 2000; Burbridge et al., 2004), suggesting a disconnect between the interior tropics and other regions. Several recent studies have focused on reconstructing hydrologic conditions in the Pantanal, a large wetland expanse primarily located in the Mato Grosso do Sul region of Brazil and roughly equidistant between the well-studied Central Andes and southern Brazil regions (Metcalfe et al., 2014; Whitney et al., 2011; Whitney and Mayle, 2012; McGlue et al., 2012). Evidence from pollen, diatoms and other biological proxies in a continuous ~45,000-year sediment record from Laguna La Gaiba (LLG) suggest drier and cooler conditions in the Pantanal during the last glacial period (Metcalfe et al., 2014; Whitney et al., 2011). During the Holocene, hydrologic patterns in the Pantanal appear to be consistent with other SASM records, with a relatively dry early/mid-Holocene followed by wetter conditions in the late Holocene (Metcalfe et al., 2014; Whitney et al., 2011; Whitney and Mayle, 2012; McGlue et al., 2012). However, existing evidence of hydrologic change in the Pantanal derived from past biota assemblages is complicated by complex or non-specific relationships between climate and species distributions. Independent climate proxies can thus offer further insight into landscape and hydrologic changes in this region and allow for more robust comparison with other tropical South American records.

In this study, we use stable isotope analysis of terrestrial biomarkers in LLG sediments to better characterize environmental changes at this site and regional SASM precipitation patterns during glacial and interglacial periods. Specifically, we analyze the carbon ($\delta^{13}C$) and hydrogen (δD) isotopic compositions of leaf waxes, a suite of long-chain lipids produced by terrestrial and emergent aquatic vascular plants now commonly employed to reconstruct past climate change in a wide range of environments (see review by Eglinton and Eglinton, 2008). We use C_{27}-C_{33} *n*-alkane $\delta^{13}C$ to reconstruct changes in the distribution of C_3 vs. C_4 vegetation, which is controlled by a range of climatic factors, including atmospheric CO_2 concentration, temperature, and water availability (Ehleringer et al., 1997). In particular, the prevalence of C_4 vegetation at warm tropical or subtropical sites is often linked to drier or more seasonal conditions (Still, 2003). Leaf wax δD has been shown to reliably track trends in meteoric water δD, providing direct information about climatic trends. However, the relationship between meteoric water and leaf wax δD can be influenced by a number of secondary effects, including soil evaporation and leaf transpiration processes as well as variability in biosynthetic fractionation among different vegetation types (see review by Sachse et al., 2012). The combination of leaf wax $\delta^{13}C$ and δD data with detailed pollen information from the same sediment core thus provides a unique opportunity to investigate the fidelity of pollen and leaf wax $\delta^{13}C$ vegetation reconstructions and address outstanding questions about the effects of vegetation change on leaf wax δD signatures.

3.2 Background

3.2.1 Study site description

The Pantanal is a large (140,000 km^2) expanse of wetlands situated in a low-lying sedimentary basin in central western Brazil with smaller areas in Bolivia and Paraguay (Figure 1,

2). The landscape of the basin mostly consists of large fluvial fans deposited by a number of rivers that flow from upland regions to the western side of the basin, eventually converging with the north-south flowing Paraguay River (Assine et al., 2015). Laguna La Gaiba (LLG, 17.75°S, 57.58°W) is a large, shallow lake (maximum area and depth of ~100 km^2 and 4-6 m, respectively) located along the upper Paraguay River (Figure 2). The lake is also connected to the Corixo Grande River, which flows along the western border of the Pantanal basin towards the lake. In the present day, the lowland areas immediately surrounding the lake are populated by wetland and savanna vegetation found throughout the seasonally or permanently flooded grasslands of the Pantanal basin (Whitney et al., 2011). The margins of the lake are confined by bordering highland areas populated by seasonally dry tropical forest (SDTF).

The LLG sediment record is largely continuous over the past ~40 kyr, as supported by 17 macrofossil and two sediment radiocarbon dates over 38 kyr (Whitney et al., 2011). However, a ~5-10-fold increase in the LLG sedimentation rate at ~13 ka indicates a dramatic increase in sediment input to the lake (Whitney et al., 2011; Metcalfe et al., 2014). This change could be related to large-scale reorganization of Pantanal basin drainage pathways thought to be driven by hydrologic change around the onset of the Holocene (Assine and Soares, 2004). There is clear geomorphological evidence that the Paraguay River has shifted eastward across its fluvial fan upstream of LLG multiple times in the past, although the absolute timing of these shifts is not known (Assine and Silva, 2009) (Figure 2). In previous configurations, the Paraguay River likely would have converged with the Corixo Grande River at a point further north than LLG. Thus, the establishment of the modern configuration of the Paraguay River could have increased sediment delivery to LLG through increased erosion and/or creation of a more direct connection between the river and the lake. However, such a change probably did not significantly affect the water

balance of LLG since in pre-modern configurations, water would presumably still have been channeled from the Paraguay headwaters to LLG through the Corixo Grande, which flows into the lake along a route more constrained by local topography (Figure 2). Evidence of lake level rise between ~13-12 ka thus supports a mechanism of landscape reshaping driven by changes in regional hydroclimate (Whitney et al., 2011).

3.2.2 Overview of regional climate patterns

The modern climate of the Pantanal is highly seasonal, with the majority of annual precipitation (1000-1500 mm) falling between November and March and little precipitation during the winter months (Hamilton, 2002). Temperatures in the Pantanal range from highs of 40-44°C in spring and summer months to occasional lows near freezing in the winter, with a mean annual temperature of 25°C (Alho, 2005). Summer precipitation causes widespread seasonal flooding, which generally progresses from north to south and can result in simultaneous inundation of >75% of the total area of the Pantanal. Wet season precipitation is associated with the development of the SASM in austral spring (Zhou and Lau, 1998). During the mature phase of the monsoon (December-February), strengthened easterly trade winds increase moisture transport from the tropical Atlantic into equatorial South America, and widespread deep convection develops throughout the southern Amazon Basin (Figure 1). The development of the South American Low Level Jet carries moisture in a general arc along the eastern Andean flank and to the southeast towards the Pantanal and subtropical Brazil (Garreaud et al., 2009). After the demise of the monsoon in austral autumn, the zone of maximum precipitation retreats to the northern hemisphere South American tropics, resulting in little precipitation in the Pantanal outside of the monsoon season.

The influence of SASM precipitation is reflected in the large seasonal signal in the hydrogen isotopic composition of precipitation (δD_p) that falls in the Pantanal. According to 1961-1987 data from the Cuiabá IAEA station (15.60°S, 56.10°W) on the northern edge of the Pantanal, precipitation δD (δD_p) is significantly lower in the monsoon season (average DJFM δD_p = -41‰ VSMOW) than during the dry season (average JJAS = +4‰ VSMOW) with a weighted annual average of -31‰. In the southern hemisphere South American tropics, the dominant climatic influence on δD_p is the amount of precipitation that falls along the SASM trajectory from the Amazon Basin to the site of interest (Vuille et al., 2003; Vuille and Werner, 2005). Increased precipitation along this trajectory results in more negative δD_p values through Rayleigh-type fractionation. Higher local precipitation can also result in more D-depleted precipitation due to the "amount effect" (Dansgaard, 1964), although upstream and local precipitation intensity may not necessarily act in concert given the significant spatial variability in SASM rainfall (Vuille and Werner, 2005).

3.3 Methods

3.3.1 Sediment collection

Sediment samples (1-2 cm) were taken from overlapping piston cores LLG1 (5.6 m) and LLG1a (4.8 m) and a 1m surface core LGS raised from the deepest part of LLG (see Whitney et al., 2011 for further details on sediment core retrieval and sediment description). Sample ages were assigned using depth-age models developed by Whitney et al. (2011) based on radiocarbon dating of plant macrofossils and sedimentary organic matter. Surface sediment samples were also collected from the core site and at the flooded wetland margin of the lake that lies along the course of the Paraguay River.

3.3.2 Sample preparation

n-Alkanes were extracted and purified from sediment samples as detailed in supplementary material. Average chain length (ACL, *n*-C_{25}–C_{35} odd carbon numbers) was calculated according to the formula:

$$\mathrm{ACL}_{25-35} = \sum_{n=25,27\ldots}^{35} n * [C_n] / \sum_{n=25,27\ldots}^{35} [C_n]$$

The carbon preference index (CPI) was calculated according to the formula (Marzi et al., 1993):

$$\mathrm{CPI} = \frac{([C_{25}] + [C_{27}] + [C_{29}] + [C_{31}] + [C_{33}]) + ([C_{27}] + [C_{29}] + [C_{31}] + [C_{33}] + [C_{35}])}{2([C_{24}] + [C_{26}] + [C_{28}] + [C_{30}] + [C_{32}])}$$

3.3.3 Compound-specific stable isotope analysis

The $\delta^{13}C$ values of individual *n*-alkanes were measured in triplicate on a Finnegan Delta^{plus} isotope ratio mass spectrometer (IRMS) coupled to an HP 6890 gas chromatograph (GC) via a combustion interface operated at 850°C. Several pulses of a CO_2 reference gas were inserted during each run and used to correct for instrument drift. The reference gas was calibrated prior to sample measurement by running multiple external standards at a range of concentrations. Average precision of sample replicates was 0.2‰ (1σ). Estimated average accuracy was ≤ 0.3‰.

The δD values of individual *n*-alkanes were measured on a Thermo Scientific DeltaV^{Plus} IRMS coupled to an Agilent 6980 GC via a pyrolysis interface operated at 1440°C. Each sample was analyzed in duplicate with the exception of two out of 40 total samples that were concentration-limited and measured once. The H_3^+ factor (Sessions et al., 2001) was measured daily and was under 2 ppm/mV throughout the measurement period. Peaks of a propane reference gas were inserted at several points before and after analytes during each run and used

as internal calibration standards. Variability in instrumental fractionation was accounted for by routinely injecting an external standard mix containing 8 fatty acid methyl and ethyl esters of known δD (F8 mixture, A. Schimmelmann, Indiana University) and adjusting the reference propane δD value to minimize the average offset between the known and measured δD values of the F8 compounds. Average precision of sample replicates was 2.5‰ (1σ). Estimated average accuracy was 4‰ based on daily measurements of the F8 mixture.

3.4 Results

n-Alkanes in LLG sediments are dominated by long chain lengths (*n*-C_{25}-C_{35}) with consistently high carbon preference index (CPI) values found throughout the core (range = 2.9-4.5). Such a distribution is typical of fresh vegetation and renders any significant contamination from oil or other fossil carbon sources unlikely (Bray and Evans, 1961; Eglinton and Hamilton, 1967). $\delta^{13}C$ values for C_{27}-C_{33} *n*-alkanes and δD values for C_{29}-C_{33} *n*-alkanes, as well as $ACL_{25\text{-}35}$ values, are shown in Figure 3. All data will also be made available online in the NOAA/NCEI Paleoclimatology Database. We restrict our discussion of δD variability to *n*-C_{29}-C_{33} data, as considerable differences between *n*-C_{27} and *n*-C_{29}-C_{33} δD values during the Holocene suggest significant input from a different *n*-alkane source. One possible source is submerged aquatic plants, which have been found to produce significant amounts of *n*-alkanes in the n-C_{23}-C_{27} range (e.g., Do Amaral et al., 1990; Ficken et al., 2000). This effect is not apparent in *n*-C_{27} $\delta^{13}C$ data, perhaps due to similar $\delta^{13}C$ signatures of submerged aquatic plants compared to other vegetation. All reported δD values have been corrected for ice volume effects on ocean isotopic composition using reconstructions of ocean surface water $\delta^{18}O$ from Bintanja et al. (2005) scaled by a factor

of 8 (i.e., meteoric water line slope). Ranges for $\delta^{13}C$ and δD values over the record are -21.5 to -35.8‰ and -157 to -195‰, respectively.

3.4.1 Surface sediment samples

n-Alkanes in two surface samples from the core site and wetland margin of LLG (see Figure 2 for locations) show relatively uniform $\delta^{13}C$ values between -32.1 and -29.3‰ (Table 1). δD values from the core site sample are slightly higher (~8-10‰) than those in the lake margin sample.

3.4.2 Glacial samples (~41-12 ka)

From 41-20 ka, there is a large offset (~3-4 ‰) between relatively high *n*-C_{33} $\delta^{13}C$ values (-23 to -25 ‰) and shorter *n*-alkane $\delta^{13}C$ values. After a local minimum at ~37.5 ka, all chain lengths show a steady increase in $\delta^{13}C$ into the LGM. δD values for all chain lengths remain relatively constant from 41-20 ka, although C_{29} and C_{31} *n*-alkanes show slightly higher δD values around ~33-29 ka. There is a large spread in δD values (>20‰) between different *n*-alkanes, with mean glacial δD value decreasing with increasing chain length. High $ACL_{25\text{-}35}$ values are found throughout the full glacial period, driven by relatively large amounts of *n*-C_{33}.

The late glacial period (~20-12 ka) is marked by a sustained period of low $\delta^{13}C$ values (< -30‰) in all chain lengths, with mean $\delta^{13}C$ values increasing with chain length. As in the full glacial section, mean δD values decrease with increasing chain length, but after 20 ka, there is a narrower spread of δD values across different chain lengths. After higher δD values at ~19 ka, δD values for all chain lengths show reduced variability from ~17.5-12.5 ka. $ACL_{25\text{-}35}$ values are markedly lower than in the full glacial period and remain relatively constant from 20-12 ka.

3.4.3 Holocene samples (~12 ka–present)

Between ~12.7 and 11.6 ka, δD values for all *n*-alkane chain lengths decrease sharply by ~10-20‰, coincident with a ~3-5‰ increase in $\delta^{13}C$ values. $\delta^{13}C$ values continue to rise further into a mid-Holocene maximum from 8.9-6.4 ka ($\delta^{13}C$ for all compounds ≥ -26‰) and then steadily decrease into the present. In contrast to the glacial period, there is no systematic offset of $\delta^{13}C$ values by chain length. δD values are generally lower during the Holocene compared to the late glacial period except for two periods of higher values during the mid-Holocene (~7.6 ka) and in the late Holocene (~2.2-0 ka). $ACL_{25\text{-}35}$ values further decrease during the Holocene as the abundances of shorter chain lengths (*n*-C_{25}, *n*-C_{27}) increase relative to those of longer chain length compounds.

3.5 Discussion

3.5.1 Modern leaf wax $\delta^{13}C$ at LLG

Leaf wax $\delta^{13}C$ values from surface sediment samples collected at the core site and near the Paraguay River establish a context for interpreting past changes in C_3 and C_4 vegetation distributions. We assume any contributions of waxes from crassulacean acid metabolism (CAM) plants at LLG are minor since CAM plants are relatively minor components of the vegetation cover in tropical savannas and forests (Lüttge, 2010) and generally not found in Pantanal macrophyte populations (Do Prado et al., 1994). Extensive analyses of diverse vegetation types have shown that C_3 plants produce leaf waxes with $\delta^{13}C$ values that range from -30 to -40‰ while those using the C_4 pathway produce much more enriched waxes (-15 to -23‰) (e.g., Chikaraishi and Naraoka, 2003; Garcin et al., 2014). The relatively low $\delta^{13}C$ values (-29.3 to -32.1‰) found at the core site thus point to a mostly C_3 vegetation community at LLG in the

present day. Similarly low $\delta^{13}C$ values (-29.8 to -31.3‰) found in sediment from the LLG wetland margin along the Paraguay River show that the proximity of large areas of SDTF to LLG is not solely responsible for the low $\delta^{13}C$ signature of *n*-alkanes at the core site. We thus conclude that the seasonally flooded savannas and wetlands northeast of LLG support mostly C_3 vegetation with smaller amounts of C_4 plants at present.

This conclusion is consistent with a number of vegetation surveys of the Pantanal (Pott et al., 2011; Schessl, 1999; Alho, 2005). The lower lying areas of the Pantanal are permanently or seasonally flooded grasslands, while higher elevations are saturated and/or occasionally inundated during the wet season and experience drought during the dry season. Woody vegetation (C_3) is generally found in these higher elevation areas, as well as in gallery forests along rivers and streams (Alho, 2005). Herbaceous vegetation in the Pantanal includes a wide range of C_3 and C_4 terrestrial and aquatic species. In tropical flooded savannas, flooding depth and duration have been found to be major controls on the C_3/C_4 distribution of grasses, with the proportion of C_3 grasses increasing with the extent of flooding (Medina and Motta, 1990; Knapp and Medina, 1998). In the Pantanal, C_4 grasses (e.g., *Elyonurus miticus, Axonopus purpusii*) dominate in higher elevation areas that never or rarely flood as well as in seasonally flooded grasslands during the dry season (Alho, 2005), while aquatic or semi-aquatic C_3 grasses (e.g., *Panicum laxum*, *Hymenachne amplexicaulis*) grow in wet or flooded areas (Rodela et al., 2007). Isotopic studies also show that most macrophytes (both grasses and forbs) in inundated regions use the C_3 pathway (Fellerhoff et al., 2003; Wantzen et al., 2002). Thus, considering the mostly-C_3 signature of modern leaf waxes, the widespread flooding of the Pantanal at present allows contributions from both C_3 grasses/macrophytes and trees to outweigh those from C_4 grasses.

3.5.2 Past vegetation change at LLG

The very large range of $\delta^{13}C$ values (-35.3 to -21.5‰) in the LLG record suggests the site experienced a wide spectrum of C_3-dominated to C_4-dominated plant communities over the past 40 kyr. Comparison of $\delta^{13}C$ changes to detailed pollen data provides additional perspective on vegetation patterns at LLG (Figure 4). The three major pollen zones described by Whitney et al. (2011) are clearly delineated in the LLG $\delta^{13}C$ record with large shifts at ~20 and ~12 ka, pointing to general coherence between the two records.

Closer inspection of the $\delta^{13}C$ trends within different periods yields further insight into vegetation patterns at LLG and controls on leaf wax $\delta^{13}C$. During the full glacial period (41-20 ka), *n*-alkane $\delta^{13}C$ values reflect a mixed C_3/C_4 community. While the estimated 1-4°C cooler temperatures during the last glacial period (Whitney et al., 2011; Punyasena et al., 2008) would tend to promote the growth of C_3 vegetation, this effect was likely counteracted at least in part by lower glacial pCO_2, which decreased the temperature threshold for C_4 favorability and increased the sensitivity of C_3 plants to water stress (Ehleringer and Monson, 1993; Ehleringer et al., 1997). A long-term increasing trend in $\delta^{13}C$ values of all *n*-alkanes after ~35 ka also shows that the abundance of C_4 vegetation peaked during the LGM, suggesting increased water stress at this time relative to the earlier glacial period. Positive linear correlations between $\delta^{13}C$ values and graminoid (*Cyperaceae* + *Poaceae*) pollen abundance indicate that C_3 herbs and C_4 grasses were likely the two major vegetation groups present from 41-20 ka (Table 2). $ACL_{25\text{-}35}$ values also show strong correlations to graminoid pollen abundance and individual *n*-alkane $\delta^{13}C$ values, indicating that $ACL_{25\text{-}35}$ was also controlled by mixing between a C_4 grass group that produced longer *n*-alkanes and C_3 herbs with relatively shorter *n*-alkanes (Table 2). The ~3-4‰ offset

between *n*-C_{33} and shorter *n*-alkane $\delta^{13}C$ values further shows that C_4 grasses were the dominant source of *n*-C_{33}.

After 20 ka, there is a sharp drop in $\delta^{13}C$ values across all chain lengths coincident with the rise of floodplain trees around LLG indicated by pollen data. The development of a C_3-dominated vegetation community before the glacial-interglacial rise of pCO_2 suggests abundant water availability after 20 ka. As observed in the full glacial period, $\delta^{13}C$ values increase with increasing chain length, indicating larger contributions from C_4 grasses at the longest chain lengths. However, even though pollen data show similar or increased abundance of grasses during the late glacial compared to the full glacial period, the influence of C_4 grasses on leaf wax $\delta^{13}C$ is diminished. The discrepancy between pollen and leaf wax data can be explained by either (1) an increasing proportion of C_3 grasses due to alleviation of water stress or (2) differences in the rates of production and/or transport mechanisms of pollen and waxes by different vegetation types. In support of the latter explanation, wind-pollinated grass species have been observed in some cases to be overrepresented by pollen data compared to floodplain tree species, which can have low pollen dispersal rates (Burn et al., 2010; Bush, 2002). Moreover, there is strong evidence that floodplain trees formed a fringing community on the lake shores (Whitney et al., 2011), suggesting the leaf wax $\delta^{13}C$ signal was likely dominated by floodplain tree input due to their proximity to the lake.

A sharp increase in $\delta^{13}C$ values across all chain lengths from ~12.7-11.6 ka is similar in timing to the observed increase in sedimentation rate at ~13 ka and lake level rise between ~13-12 ka (Whitney et al., 2011). While the source region for leaf waxes was likely similar before and after any hydrologic reorganization at this time (see Section 3.2.1), increased sediment input to the lake likely increased the proportion of waxes derived from the Paraguay River catchment.

Furthermore, the large increase in lake level destroyed most of the fringing floodplain tree community around LLG (Whitney et al., 2011), eliminating one source of C_3 waxes close to the core site. Thus, the increase in $\delta^{13}C$ values could reflect vegetation change (i.e., removal of floodplain trees, establishment of mixed C_3/C_4 wetland vegetation communities in the lowland regions of the Paraguay River catchment) and/or increased fluvial input of leaf waxes to LLG from previously established wetland communities in the Paraguay River catchment. Given the evidence of widespread hydrologic change throughout the Pantanal basin in the early Holocene (Assine et al., 2004), it is likely a combination of all factors.

In contrast to the glacial period, leaf wax $\delta^{13}C$ during the Holocene shows significant changes independent of changes in pollen composition. After the initial increase of ~4-6‰ at the beginning of the Holocene, $\delta^{13}C$ values reach the highest values of the record in the mid-Holocene. During the mid-Holocene, all *n*-alkanes have $\delta^{13}C$ values greater than -26‰ with little or no offset between different chain lengths, indicating a C_4-dominated community. Pollen data show a significant presence (~20-30% of major vegetation pollen) of SDTF near LLG at this time, and a strong negative correlation between $ACL_{25\text{-}35}$ and SDTF pollen abundance ($r^2 = 0.87$, $p < 0.0001$) provides evidence that SDTF was indeed contributing to the leaf wax pool over the entire Holocene. This requires nearly all remaining herbaceous vegetation to have been C_4 plants in order to produce such high $\delta^{13}C$ values in the mid-Holocene. Since the modern flooding regime in the Pantanal is associated with majority C_3 vegetation, this suggests more seasonal or drier conditions during the mid-Holocene reduced the extent/duration of flooding and promoted widespread growth of C_4 grasses. This conclusion is further supported by evidence of lower lake level, minima in rainforest species and the increased abundance of drought-tolerant trees from 10-3 ka (Whitney et al., 2011; Whitney and Mayle, 2012). After the mid-Holocene, $\delta^{13}C$ values

decrease steadily into the present, reflecting increasing contributions from C_3 vegetation. Since the abundance of SDTF pollen does not dramatically change in the late Holocene, we posit that the decreasing trend in $\delta^{13}C$ is due to increasing flooding, which resulted in the rise of C_3 macrophytes and other C_3 vegetation (e.g., gallery forest) common in the extensively flooded regions of the modern Pantanal.

3.5.3 Interpreting the LLG δD record

The similarities between the LLG δD and $\delta^{13}C$ records (i.e., distinct shifts in δD values and distribution of δD values across chain length at pollen zone transitions) provide the first indication that vegetation composition may be a significant influence on leaf wax δD at this site (Figure 3). The likely influence of changing vegetation is made clear by comparing measured δD and $\delta^{13}C$ values for *n*-C_{29} -C_{33} (Figure 5). Leaf wax δD and $\delta^{13}C$ values show a consistent negative relationship across all time periods, contradicting the expected association of low δD values (i.e., more intense monsoon/higher humidity) and low $\delta^{13}C$ values (i.e., C_3 vegetation) if climatic factors were the main control on δD. Thus, much of the variability in LLG δD can be explained by mixing between C_3 herb and C_4 grass end members from 41-20 ka and C_3 tree/macrophyte and C_4 grass end members from 20-0 ka. More negative δD values for C_4 grasses are in line with the larger *n*-alkane/water fractionation factors ($\varepsilon_{l/w}$) previously found for grasses compared to forbs and trees (Sachse et al., 2012). However, assuming a constant source water δD, the large difference (~40-50‰) between δD values corresponding to C_3 and C_4 end members requires a larger range in $\varepsilon_{l/w}$ values for different vegetation types than the <20‰ range in average $\varepsilon_{l/w}$ values reported for forbs, trees and C_4 graminoids in the Sachse et al. (2012)

compilation. Nevertheless, a ~50‰ range in $\varepsilon_{l/w}$ is quite reasonable given the large variability of published values for different taxa within the same vegetation groups.

Significant correlations between graminoid pollen abundance and *n*-C_{29} and *n*-C_{31} leaf wax δD values across the entire record further support a relationship between vegetation and leaf wax δD (Figure 6). These results are also consistent with the strong relationship between δD and $\delta^{13}C$ as any C_4 plants present at LLG are likely graminoids. The lack of significant correlation between *n*-C_{33} δD and graminoid pollen abundance is likely because *n*-C_{33} is produced dominantly by graminoids, while other compounds provide better averages of total vegetation.

While vegetation effects appear to dominate the δD signal at LLG, there is also some evidence of climatic influence on leaf wax δD in the distinct $\delta^{13}C$-δD trends for 41-20 ka and 20-0 ka (Figure 5). These trends have similar slopes but are offset by ~10‰ in δD, suggesting an additional influence on leaf wax δD independent of vegetation change. This influence could be a change in source water δD resulting from changes in soil evaporation/leaf transpiration processes (e.g., Kahmen et al., 2013) or in the initial δD_p value. We note that the 20-0 ka regression excludes the set of values corresponding to 7.6-6.4 ka, which appear to plot separately from other 20-0 ka points. The statistical significance of the difference between 7.6-6.4 ka and other 20-0 ka data was confirmed with a one-way ANOVA test of residuals from a linear regression of all 20-0 ka δD and $\delta^{13}C$ data ($p < 0.0001$). However, calculated slopes for 7.6-6.4 ka and other 20-0 ka $\delta^{13}C$-δD trends are statistically identical within uncertainties (2σ level).

If the offset between 41-20 ka and 20-0 ka trends is in fact the result of source water δD differences, normalizing δD values for vegetation change could allow extraction of some climatic information. Therefore, we removed $\delta^{13}C$-δD trends by normalizing all δD values to a

hypothetical pure C_4 grass endmember (i.e., the vegetation type common to both Holocene and glacial periods) with $\delta^{13}C = -22‰$ using the formula:

$$\delta D_{vn} = \delta D_o - m(\delta^{13}C_o + 22)$$

where δD_o and $\delta^{13}C_o$ are the original δD and $\delta^{13}C$ values for each sample, m is the slope of the $\delta^{13}C$-δD correlation for either 20-0 or 41-20 ka. We then subtract the mid-range of all δD_{vn} values to only consider relative changes in δD_{vn}. The resulting *n*-C_{29}-C_{33} δD_{vn} time series are shown in Figure 7. We caution that the amplitudes of δD_{vn} signals are small considering both analytical uncertainty and the potential for further vegetation or non-climatic influences on δD not accounted for by our $\delta^{13}C$-based normalization procedure. For example, the slight offset between *n*-alkane δD values for the two surface sediment samples, despite very similar $\delta^{13}C$ values (Table 1), could reflect further biosynthetic variability between different C_3 vegetation types. Despite all these caveats, periods of higher δD_{vn} from 35-19 ka and 7.6-6.4 ka are broadly consistent with drier/more seasonal conditions as indicated by leaf wax $\delta^{13}C$ and other proxies (Whitney et al., 2011; McGlue et al., 2012; Metcalfe et al., 2014). More positive δD_{vn} values during these periods could thus reflect source water enrichment due to lower local humidity and increased evapotranspiration and/or higher δD_p due to decreased local or regional precipitation intensity.

3.5.4 Paleoclimate implications

Our results provide further support for climate patterns described in previous studies at LLG but also reveal several new features in the climate history of the Pantanal (Figure 8). Leaf wax $\delta^{13}C$ values from 41-20 ka reflect an open landscape dominated by C_4 grass and C_3 herb communities. Lower glacial pCO_2 could contribute to the significant presence of C_4 grasses

(Ehleringer et al., 1997). However, the prevalence of C_4 grasses is also consistent with drier or more seasonal conditions during the last glacial period relative to the Holocene, as inferred from other proxies (Whitney et al., 2011) and observed at southern Amazon sites (Mayle et al., 2004). Considering the complex influences of temperature and pCO_2 changes on C_3/C_4 distributions, as well as the likely hydrologic reorganization of the Pantanal at ~13-12 ka, we do not draw any conclusions about relative Holocene and glacial mean precipitation patterns from our data.

Within the glacial period, increased abundance of C_4 vegetation from 26-21 ka do suggest decreased humidity or increased seasonality during the LGM relative to the earlier glacial period. If δD_{vn} does reflect changes in source water δD signals, higher δD_{vn} values from 35-19 ka also support this conclusion. Relative drought during the LGM at LLG stands in contrast to clear evidence of wet conditions in the Central Andes (Baker et al., 2001; Fornace et al., 2014) at this time. However, speleothem records from western Amazonia do not show increased SASM intensity during the LGM as would be expected during a period of high austral summer insolation (Mosblech et al., 2012; Cheng et al., 2013). Model simulations of South American climate under LGM boundary conditions offer one possible explanation for the discrepancy between the Central Andes and lowland interior tropics. Using regional climate models, Cook and Vizy (2006) and Vizy and Cook (2007) found that a delayed onset of the monsoon under LGM conditions resulted in a longer dry season in the lowland tropics but also led to increased total annual precipitation in the Central Andes. Speleothem records from subtropical Brazil reveal a further complexity in glacial SASM dynamics as they generally indicate increasing monsoon precipitation from ~32 ka into the LGM, tracking increasing summer insolation (e.g., Cruz et al., 2005; Wang et al., 2007). These results suggest that circulation changes under LGM boundary conditions increased moisture transport to the subtropics during the monsoon season

but that this moisture was confined to regions south of LLG. Increases in LGM SASM precipitation may thus have been confined to the extremities of the SASM domain, similar to the "South American precipitation dipole" pattern defined by Cheng et al. (2013). Further modeling work, particularly in southern Brazil, would help to illuminate possible mechanisms for the variability in glacial-interglacial precipitation patterns throughout southern tropical South America.

After the LGM, vegetation at LLG went through a pronounced shift to a forested C_3-dominated landscape, which was present around the lake throughout the late glacial period (~19-13 ka). Whitney et al. (2011) attribute the rise of tropical trees at this time to deglacial warming, which pushed temperatures at LLG above the threshold for tropical forest, but it is likely that increased humidity during the last deglaciation also fostered the development of a C_3-dominated community despite lower pCO_2 levels. A sustained period of relatively low δD_{vn} values from ~17-10 ka is also consistent with increased humidity following the easing of LGM conditions. Wetter conditions at LLG could be related to increases in SASM precipitation throughout southern tropical South America from ~18-15 ka concurrent with Heinrich Event 1 (e.g., Blard et al., 2011; Mosblech et al., 2012; Wang et al., 2007), but the limits of the LLG record chronology and resolution preclude definitive identification of this event. Following a relatively stable late glacial period, the transition into the Holocene at LLG is marked by a dramatic shift to a mixed C_3/C_4 community from ~12.7 to 11.6 ka. This shift was likely the result of both hydrology-driven changes in the Pantanal landscape and increased leaf wax contribution from wetland regions.

The influence of orbital forcing on precessional timescales at LLG becomes evident during the Holocene (Figure 8). Leaf wax $\delta^{13}C$ and δD data point to drier conditions ca. 9-6 ka, consistent with evidence of drier conditions throughout Amazonia during a period of generally

low austral summer insolation (Mayle and Power, 2008). In the Central Andes, lake level records from Lake Titicaca also show a prolonged lowstand during the mid-Holocene (~8-4 ka) (Baker et al., 2001; Cross et al., 2000). These findings are consistent with the results of model simulations that show reduced SASM precipitation due to lower summer insolation in the mid-Holocene (Liu et al., 2004). However, the timing of vegetation change recorded by $\delta^{13}C$ at LLG appears to lag behind the insolation trend for the peak monsoon season (DJF), instead matching more closely the late summer (March) insolation curve. This trend stands in contrast to a number of isotopic records of SASM precipitation that generally show SASM intensity closely tracking DJF insolation (e.g., Bird et al., 2011). This discrepancy may be related to the different information contained in precipitation isotopes versus proxies directly tied to local hydrologic conditions. Precipitation isotopes are linked to intensity of monsoonal precipitation on a regional scale but do not necessarily reflect changes in the total amount or seasonality of local precipitation. Thus, widespread mid-Holocene drought may be related to a change in seasonality, namely a longer dry season, rather than a change in monsoon intensity during peak season. Based on the correlation between LLG $\delta^{13}C$ and March insolation, it is possible the magnitude of late summer insolation may be an important control on the timing of the monsoon demise and resulting seasonality. After the mid-Holocene, conditions at LLG became increasingly wet into the present, consistent with most records from SASM-dominated regions.

Overall, the climate history of LLG is distinct from most well-studied regions in southern tropical South America. While the Central Andes and southern Brazil experienced a relatively wet LGM, a trend towards drier conditions from ~35-21 ka at LLG suggests a reorganization of monsoon circulation under LGM boundary conditions that led to decreased precipitation in the lowland interior tropics. We do not find any strong evidence of precessional orbital forcing at

LLG during the last glacial period, consistent with several Central Andes and western Amazon records (Fornace et al., 2014; Cheng et al., 2013; Mosblech et al., 2012; Kanner et al., 2012) and in contrast to the strong precessional signal in southern Brazilian speleothem records (Cruz et al., 2005, Wang et al., 2007). During the Holocene, however, our record, along with most other SASM records, does support hydrologic change driven by precessional changes in insolation.

3.5.5 Implications for leaf wax isotope reconstructions

This study highlights the complementary nature of leaf wax stable isotopes and pollen data in assessing past environmental change. In the case of LLG, $\delta^{13}C$ data from multiple *n*-alkanes both confirm original vegetation reconstructions over the past 41 kyr and provide additional insight into past C_3/C_4 distributions, which are more directly tied to climate variables. In particular, $\delta^{13}C$ data allows differentiation of C_3 and C_4 grasses during the last glacial period and mid-Holocene, which carry very different implications for climate. In turn, pollen reconstructions of vegetation cover provide critical context for interpreting LLG $\delta^{13}C$ and differentiating between vegetation types with similar $\delta^{13}C$ signatures (i.e., C_3 herbs/trees).

At sites that likely experienced significant shifts in landscape cover, leaf wax δD records should be interpreted cautiously and whenever possible used in conjunction with other climate proxies. At LLG, a ~40-50‰ range in $\varepsilon_{l/w}$ values between different vegetation types likely overwhelmed changes in δD_p, but we were able to extract a putative hydrologic signal by removing $\delta^{13}C$-δD trends and thus accounting for vegetation change. However, if the magnitude of δD_p change exceeded the magnitude of vegetation effects, such a strong $\delta^{13}C$-δD relationship would be unlikely. In that case, there is no clear procedure for correcting for vegetation change. Some authors have used available data to apply corrections to leaf wax δD records by combining

existing $\varepsilon_{l/w}$ data with pollen records (Feakins, 2013) or leaf wax $\delta^{13}C$ (Magill et al., 2013). At LLG though, these correction procedures would underestimate the magnitude of vegetation effects on leaf wax δD because current compilations of $\varepsilon_{l/w}$ values do not accurately represent of the range of vegetation types at this site. In working towards quantitative reconstructions of source water δD, the ideal approach would be to combine detailed information about vegetation composition from pollen or other data with measured $\varepsilon_{l/w}$ values for those taxa (or modern analogues) to produce accurate vegetation corrections. However, this approach requires an extensive and globally representative database of $\varepsilon_{l/w}$ values. An alternative approach would be to target sites with independent constraints on vegetation composition (e.g., high altitude, temperature limitations) that may minimize complications from climate-induced vegetation change.

3.6 Conclusions

Our results attest to the complexity of the SASM system and the controls on SASM variability over the past 40,000 years. Trends in SASM precipitation in the Pantanal appear to diverge from other regions under glacial conditions, while our record and other SASM records are largely coherent during the Holocene. This discrepancy suggests a redistribution of SASM precipitation during the LGM that additional paleoclimate records and modeling studies could help to resolve. Our record further shows that the Pantanal experienced significant hydrologic changes within the Holocene, possibly due to longer dry seasons during periods of low summer insolation. Elucidating the controls on the seasonality of SASM precipitation is thus another critical direction for future research. Finally, our results also represent an important development for reconstructions of past hydrologic conditions using leaf wax δD and reveal competing

influences on δD signatures at this site. In particular, the effects of vegetation change on leaf wax δD signatures should be considered carefully in future studies as we work towards a better understanding of variability in isotopic fractionation during leaf wax synthesis. The combination of leaf wax δD records with detailed vegetation reconstructions from pollen data or leaf wax $\delta^{13}C$ data can therefore help to improve the robustness of leaf wax δD as a climate proxy.

Acknowledgements

We wish to acknowledge Carl Johnson and Sean Sylva for assistance with isotope analysis. We thank the editor and two anonymous reviewers for comments that helped to improve the manuscript. This work was supported by an EPA STAR fellowship and WHOI internal grant to K.L.F.

References

Alho, C.J.R., 2005. The Pantanal. In *The World's Largest Wetlands: Ecology and Conservation*, L.H. Fraser, P.A. Keddy, Eds., Cambridge University Press, 203-271.

Assine, M.L., Merino, E.R., Pupim, F.N., Warren, L.V., Guerreiro, R.L., McGlue, M.M., 2015. Geology and Geomorphology of the Pantanal Basin. In *Dynamics of the Pantanal Wetland in South America*, I. Bergier, M. Assine, Eds., Springer International Publishing, 23-50.

Assine, M.L., Silva, A., 2009. Contrasting fluvial styles of the Paraguay River in the northwestern border of the Pantanal wetland, Brazil. Geomorphology 113, 189–199.

Assine, M.L., Soares, P.C., 2004. Quaternary of the Pantanal, west-central Brazil. Quat. Int. 114, 23–34.

Baker, P., Seltzer, G., Fritz, S., Dunbar, R., Grove, M., Tapia, P., Cross, S., Rowe, H., Broda, J., 2001. The history of South American tropical precipitation for the past 25,000 years. Science 291, 640–643.

Bintanja, R., Van De Wal, R.S., Oerlemans, J., 2005. Modeled atmospheric temperatures and global sea levels over the past million years. Nature 437, 125–128.

Bird, B.W., Abbott, M.B., Rodbell, D.T., Vuille, M., 2011. Holocene tropical South American hydroclimate revealed from a decadally resolved lake sediment $\delta^{18}O$ record. Earth Planet. Sci. Lett. 310, 192–202.

Blard, P.-H., Sylvestre, F., Tripati, A., Claude, C., Causse, C., Coudrain, A., Condom, T., Seidel, J.-L., Vimeux, F., Moreau, C., Dumoulin, J.-P., Lavé, J., 2011. Lake highstands on the Altiplano (Tropical Andes) contemporaneous with Heinrich 1 and the Younger Dryas: new

insights from ^{14}C, U–Th dating and $\delta^{18}O$ of carbonates. Quat. Sci. Rev. 30, 3973–3989.
Bray, E.E., Evans, E.D., 1961. Distribution of *n*-paraffins as a clue to recognition of source beds. Geochim. Cosmochim. Acta 22, 2–15.
Burbridge, R., Mayle, F., Killeen, T., 2004. Fifty-thousand-year vegetation and climate history of Noel Kempff Mercado National Park, Bolivian Amazon. Quaternary Research 61, 215–230.
Burn, M.J., Mayle, F.E., Killeen, T.J., 2010. Pollen-based differentiation of Amazonian rainforest communities and implications for lowland palaeoecology in tropical South America. Palaeogeogr. Palaeoclimatol. Palaeoecol. 295, 1–18.
Bush, M., 2002. On the interpretation of fossil Poaceae pollen in the lowland humid neotropics. Palaeogeogr. Palaeoclimatol. Palaeoecol. 177, 5–17.
Cheng, H., Sinha, A., Cruz, F.W., Wang, X., Edwards, R.L., D Rsquo Horta, F.M., Ribas, C.C., Vuille, M., Stott, L.D., Auler, A.S., 2013. Climate change patterns in Amazonia and biodiversity. Nature Comm. 4, 1411–1416.
Chikaraishi, Y., Naraoka, H., 2003. Compound-specific δD– $\delta^{13}C$ analyses of *n*-alkanes extracted from terrestrial and aquatic plants. Phytochemistry 63, 361–371.
Cook, K.H., Vizy, E.K., 2006. South American climate during the Last Glacial Maximum: Delayed onset of the South American monsoon. J. Geophys. Res 111, D02110.
Cross, S., Baker, P., Seltzer, G., Fritz, S., Dunbar, R., 2000. A new estimate of the Holocene lowstand level of Lake Titicaca, central Andes, and implications for tropical palaeohydrology. The Holocene 10, 21–32.
Cruz, F.W., Burns, S.J., Karmann, I., Sharp, W.D., Vuille, M., Cardoso, A.O., Ferrari, J.A., Silva Dias, P.L., Viana Jr., O., 2005. Insolation-driven changes in atmospheric circulation over the past 116,000 years in subtropical Brazil. Nature 434, 63–66.
Dansgaard, W., 1964. Stable isotopes in precipitation. Tellus 16, 436–468.
Do Amaral, M., Da Silva, A., Salatino, A., 1990. Alkanes of surface waxes from eight species of aquatic angiosperms. Aquat. Bot. 36, 281–286.
Do Prado, A., Heckman, C., Martins, F., 1994. The Seasonal Succession of Biotic Communities in Wetlands of the Tropical Wet and Dry Climatic Zone: II. The Aquatic Macrophyte Vegetation in the Pantanal of Mato Grosso, Brazil. Internationale Revue der gesamten Hydrobiologie und Hydrographie 79, 569–589.
Eglinton, G., Hamilton, R., 1967. Leaf epicuticular waxes. Science 156, 1322.
Eglinton, T., Eglinton, G., 2008. Molecular proxies for paleoclimatology. Earth Planet. Sci. Lett. 275, 1–16.
Ehleringer, J., Cerling, T., Helliker, B., 1997. C_4 photosynthesis, atmospheric CO_2, and climate. Oecologia 112, 285–299.
Ehleringer, J.R., Monson, R.K., 1993. Evolutionary and ecological aspects of photosynthetic pathway variation. Ann. Rev. Ecol. Syst. 24, 411–439.
Feakins, S.J., 2013. Pollen-corrected leaf wax D/H reconstructions of northeast African hydrological changes during the late Miocene. Palaeogeogr. Palaeoclimatol. Palaeoecol. 374, 62–71.
Fellerhoff, C., Voss, M., Wantzen, K., 2003. Stable carbon and nitrogen isotope signatures of decomposing tropical macrophytes. Aquat. Ecol. 37, 361–375.
Ficken, K., Li, B., Swain, D., Eglinton, G., 2000. An *n*-alkane proxy for the sedimentary input of submerged/floating freshwater aquatic macrophytes. Org. Geochem. 31, 745–749.
Fornace, K.L., Hughen, K.A., Shanahan, T.M., Fritz, S.C., Baker, P.A., Sylva, S.P., 2014. A 60,000-year record of hydrologic variability in the Central Andes from the hydrogen isotopic

composition of leaf waxes in Lake Titicaca sediments. Earth Planet. Sci. Lett. 408, 263–271.
Garcin, Y., Schefuß, E., Schwab, V.F., Garreta, V., Gleixner, G., Vincens, A., Todou, G., Séné, O., Onana, J.-M., Achoundong, G., Sachse, D., 2014. Reconstructing C_3 and C_4 vegetation cover using *n*-alkane carbon isotope ratios in recent lake sediments from Cameroon, Western Central Africa. Geochim. Cosmochim. Acta 142, 482–500.
Garreaud, R., Vuille, M., Compagnucci, R., Marengo, J., 2009. Present-day South American climate. Palaeogeogr. Palaeoclimatol. Palaeoecol. 281, 180–195.
Hamilton, S.K., 2002. Hydrological Controls of Ecological Structure and Function in the Pantanal Wetland (Brazil). In *The Ecohydrology of South American Rivers and Wetlands*, M. McClain, Ed., International Association of Hydrological Sciences, 133–158.
Kahmen, A., Hoffmann, B., Schefuß, E., Arndt, S.K., Cernusak, L.A., West, J.B., Sachse, D., 2013. Leaf water deuterium enrichment shapes leaf wax *n*-alkane δD values of angiosperm plants II: Observational evidence and global implications. Geochim. Cosmochim. Acta 111, 50–63.
Kanner, L.C., Burns, S.J., Cheng, H., Edwards, R.L., 2012. High-Latitude Forcing of the South American Summer Monsoon During the Last Glacial. Science 335, 570–573.
Knapp, A.K., Medina, E., 1999. Success of C_4 Photosynthesis in the Field: Lessons from Communities Dominated by C_4 Plants. In *C_4 Plant Biology*, R.F. Sage, R.K. Monson, Eds., Academic Press, 251-283.
Laskar, J., Robutel, P., Joutel, F., Gastineau, M., Correia, A.C.M., Levrard, B., 2004. A long-term numerical solution for the insolation quantities of the Earth. Astron. Astrophys. 428, 261-285.
Liu, Z., Harrison, S.P., Kutzbach, J., Otto-Bliesner, B., 2004. Global monsoons in the mid-Holocene and oceanic feedback. Clim. Dyn. 22, 157–182.
Lüttge, U., 2010. Ability of crassulacean acid metabolism plants to overcome interacting stresses in tropical environments. AoB Plants 2010, plq005.
Magill, C.R., Ashley, G.M., Freeman, K.H., 2013. Water, plants, and early human habitats in eastern Africa. Proc. Nat. Acad. Sci. 110, 1175–1180.
Marzi, R., Torkelson, B.E., Olson, R.K., 1993. A revised carbon preference index. Org. Geochem. 20, 1303–1306.
Mayle, F.E., Burbridge, R., Killeen, T.J., 2000. Millennial-scale dynamics of southern Amazonian rain forests. Science 290, 2291-2294.
Mayle, F.E., Power, M.J., 2008. Impact of a drier Early-Mid-Holocene climate upon Amazonian forests. Philos. Trans. R. Soc. B 363, 1829–1838.
McGlue M.M., Silva, A., Zani, H., Corradini, F.A., Parolin, M., Abel, E.J., Cohen, A.S., Assine, M.L., Ellis, G.S., Trees, M.A., Kuerten, S., dos Santos Gradella, F., Rasbold, G.G., 2012. Lacustrine records of Holocene flood pulse dynamics in the Upper Paraguay River watershed (Pantanal Wetlands, Brazil). Quat. Res. 78: 285–294.
Medina, E., Motta, N., 1990. Metabolism and distribution of grasses in tropical flooded savannas in Venezuela. J. Trop. Ecol. 6, 77–89.
Metcalfe, S.E., Whitney, B.S., Fitzpatrick, K.A., Mayle, F.E., Loader, N.J., Street-Perrott, F.A., Mann, D.G., 2014. Hydrology and climatology at Laguna La Gaiba, lowland Bolivia: complex responses to climatic forcings over the last 25 000 years. J. Quat. Sci. 29, 289–300.
Mosblech, N.A.S., Bush, M.B., Gosling, W.D., Hodell, D., Thomas, L., Calsteren, P.V., Correa-Metrio, A., Valencia, B.G., Curtis, J., Woesik, R.V., 2012. North Atlantic forcing of Amazonian precipitation during the last ice age. Nature Geosci. 5, 817–820.

Pott, A., Oliveira, A.K.M., Damasceno-Junior, G.A., Silva, J.S.V., 2011. Plant diversity of the Pantanal wetland. Braz. J. Biol. 71, 265-273.
Punyasena, S., Mayle, F., McElwain, J., 2008. Quantitative estimates of glacial and Holocene temperature and precipitation change in lowland Amazonian Bolivia. Geology 36, 667.
Rodela, L.G., Queiroz Neto, J.P., Santos, S.A., 2007. Classifição das pastagens nativas do Pantanal da Nhecolandia, Mato Grosso do Sul, por meio de imagens de satellite. Anais XIII Simpósio Brasileiro de Sensoriamento Remoto, Florianópolis, Brasil, 21-26 abril 2007, pp. 4187-4194.
Sachse, D., Billault, I., Bowen, G.J., Chikaraishi, Y., Dawson, T.E., Feakins, S.J., Freeman, K.H., Magill, C.R., Mcinerney, F.A., Van Der Meer, M.T., Polissar, P., Robins, R.J., Sachs, J.P., Schmidt, H.-L., Sessions, A.L., White, J.W., West, J.B., Kahmen, A., 2012. Molecular Paleohydrology: Interpreting the Hydrogen-Isotopic Composition of Lipid Biomarkers from Photosynthesizing Organisms. Annu. Rev. Earth Planet. Sci. 40, 221–249.
Schessl, M., 1999. Floristic composition and structure of floodplain vegetation in the Northern Pantanal of Mato Grosso, Brazil. Phyton (Horn, Austria) 39, 303-336.
Sessions, A.L., Burgoyne, T.W., Hayes, J.M., 2001. Determination of the H_3 factor in hydrogen isotope ratio monitoring mass spectrometry. Anal. Chem. 73, 200–207.
Still, C.J., 2003. Global distribution of C_3 and C_4 vegetation: Carbon cycle implications. Global Biogeochem. Cycles 17, 1006.
Vizy, E., Cook, K., 2007. Relationship between Amazon and high Andes rainfall. J. Geophys. Res. 112, D07107.
Vuille, M., Bradley, R.S., Werner, M., Healy, R., Keimig, F., 2003. Modeling $\delta^{18}O$ in precipitation over the tropical Americas: 1. Interannual variability and climatic controls. J. Geophys. Res. 108, 4174.
Vuille, M., Werner, M., 2005. Stable isotopes in precipitation recording South American summer monsoon and ENSO variability: observations and model results. Clim. Dyn. 25, 401–413.
Wang, X., Auler, A.S., Edwards, R.L., Cheng, H., Ito, E., Wang, Y., Kong, X., Solheid, M., 2007. Millennial-scale precipitation changes in southern Brazil over the past 90,000 years. Geophys. Res. Lett 34, L23701.
Wantzen, K., de Arruda Machado, F., Voss, M., Boriss, H., Junk, W., 2002. Seasonal isotopic shifts in fish of the Pantanal wetland, Brazil. Aquat. Sci. 64, 239–251.
Whitney, B., Mayle, F., Punyasena, S., Fitzpatrick, K., Burn, M., Guillen, R., Chavez, E., Mann, D., Pennington, R., Metcalfe, S., 2011. A 45 kyr palaeoclimate record from the lowland interior of tropical South America. Palaeogeogr. Palaeoclimatol. Palaeoecol. 307, 177-192.
Whitney, B.S., Mayle, F.E., 2012. Pediastrum species as potential indicators of lake-level change in tropical South America. J. Paleolimnol. 47, 601–615.

Table 1. Surface sediment *n*-alkane $\delta^{13}C$ and δD values.

Compound	Core site				Paraguay River margin sediment			
	$\delta^{13}C$	σ	δD	σ	$\delta^{13}C$	σ	δD	σ
n-C_{27}	-32.1	0.2	---	---	-31.0	0.1	---	---
n-C_{29}	-31.2	0.1	-167	3.2	-31.0	0.1	-175	2.4
n-C_{31}	-30.7	0.3	-170	2.6	-31.3	0.1	-180	3.7
n-C_{33}	-29.3	0.1	-172	1.9	-29.8	0.1	-182	6.3

Table 2. Coefficients of determination (r^2) for linear regressions between $ACL_{25\text{-}35}$, $\delta^{13}C$ values and pollen data from 41-20 ka. P values are shown in parentheses.

	$ACL_{25\text{-}35}$	Graminoid pollen (%)
n-C_{27} $\delta^{13}C$	0.61 (0.002)	0.70 (<0.001)
n-C_{29} $\delta^{13}C$	0.60 (0.002)	0.58 (0.003)
n-C_{31} $\delta^{13}C$	0.54 (0.004)	0.56 (0.001)
n-C_{33} $\delta^{13}C$	0.39 (0.02)	0.48 (0.008)
$ACL_{25\text{-}35}$	---	0.69 (<0.001)

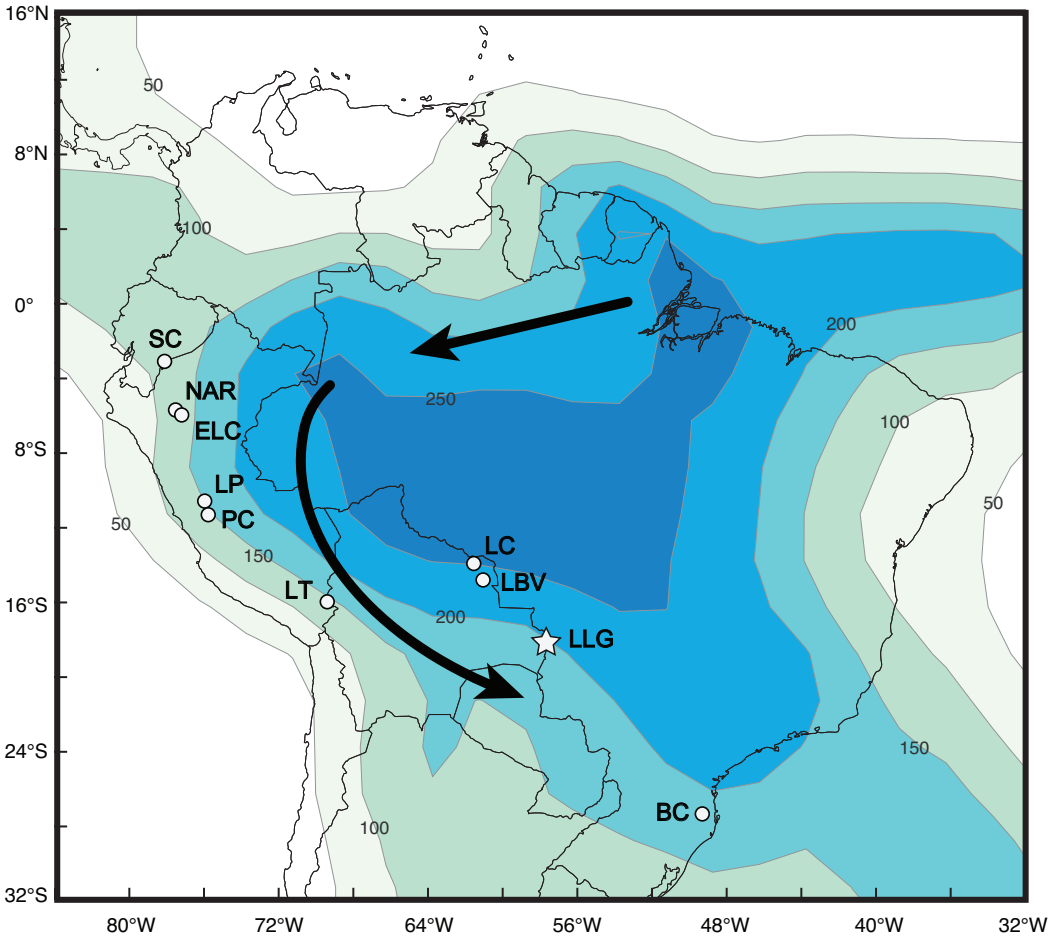

Figure 1. Map of South American tropics with sites discussed in text and average January precipitation (mm/month, 1981-2010). Contours indicate increments of 50 mm/month; precipitation data are from CAMS_OPI monthly precipitation dataset (NCEP). Study site Laguna La Gaiba (LLG) is marked with a star; other sites include Santiago Cave (SC; Mosblech et al., 2012), Cueva del Diamante/El Condor (NAR/ELC; Cheng et al., 2013), Laguna Pumacocha (LP; Bird et al., 2011), Pacupahuain Cave (PC; Kanner et al., 2012), Lake Titicaca (LT; Fornace et al., 2014, Baker et al., 2001), Laguna Chaplin/Laguna Bella Vista (LC/LBV; Mayle at al., 2000, Burbidge et al., 2004), and BC (Botuverá Cave; Cruz et al., 2005, Wang et al., 2007). Arrows indicate general direction of moisture transport from tropics to subtropics during monsoon season.

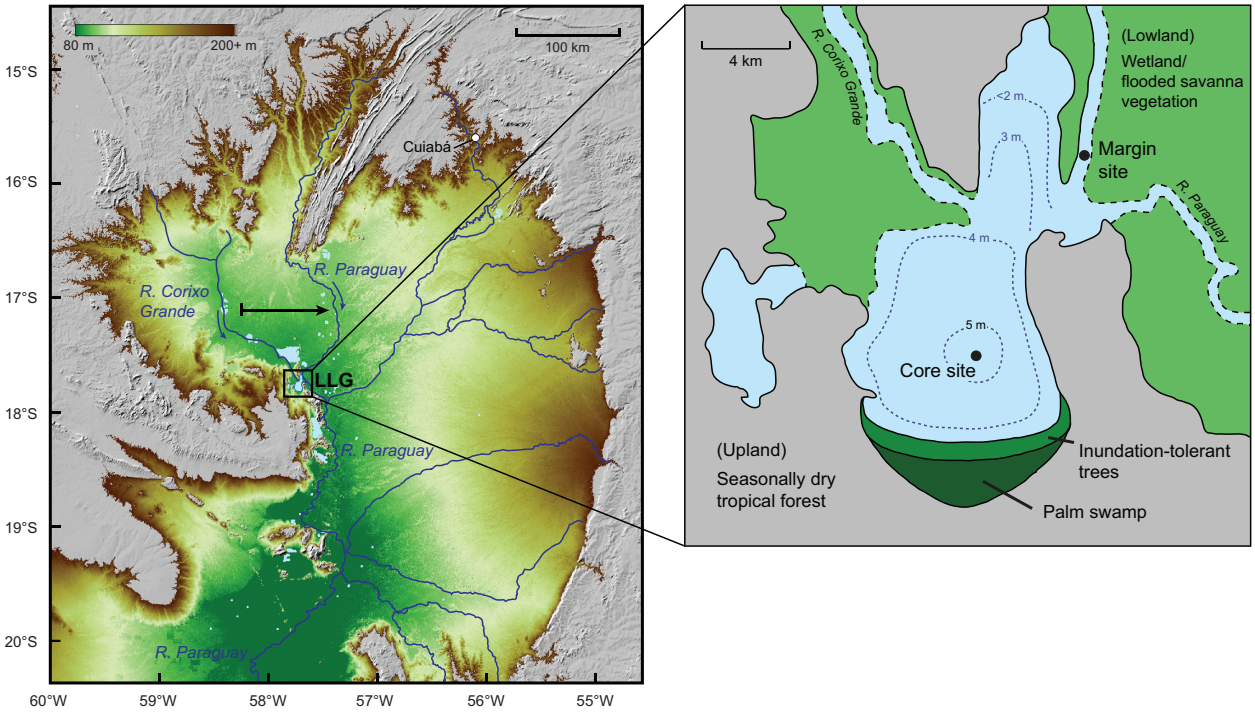

Figure 2. Elevation map of Pantanal basin (left) and schematic of modern configuration of Laguna La Gaiba and surrounding vegetation (right). Elevation map with constructed with SRTM3 Digital Elevation Model (NASA). Black arrow in left panel shows past migration of main stem of Paraguay River as reconstructed by Assine and Silva (2009), while blue arrows show direction of river flow. Right panel was adapted from Whitney et al. (2011). Locations of core site and margin surface sediment collection site are shown by black circles in right panel.

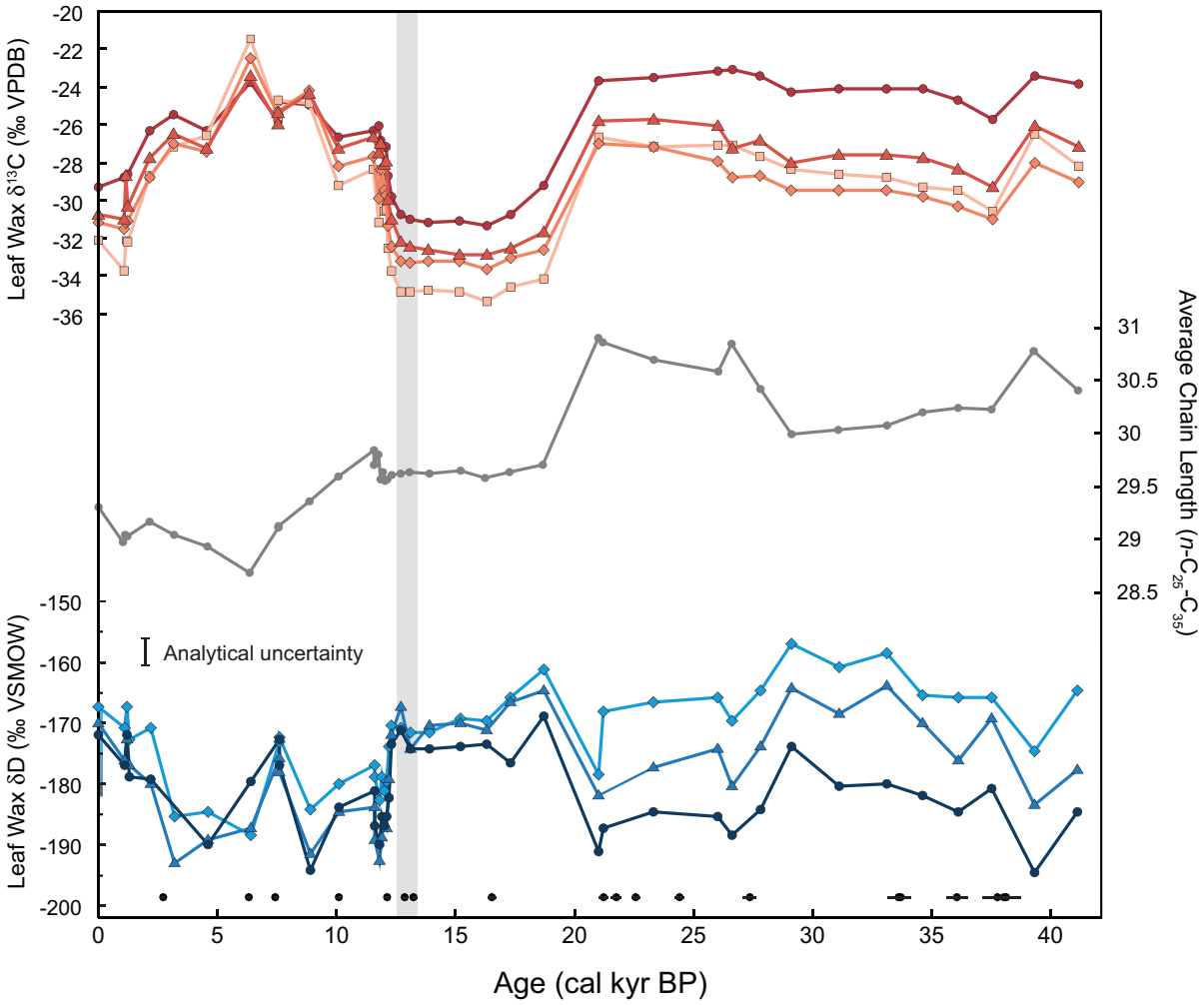

Figure 3. Time series of LLG *n*-alkane $\delta^{13}C$ (top), average chain length (middle), and δD values (bottom) over past 40 kyr. Isotopic data are shown for *n*-C_{27} (squares, $\delta^{13}C$ only), *n*-C_{29} (diamonds), *n*-C_{31} (triangles), and *n*-C_{33} (circles). Average analytical uncertainty for $\delta^{13}C$ measurements was smaller than the size of symbols; average analytical uncertainty for δD is indicated by error bar on bottom plot. Errors for individual points are not shown in order to reduce the complexity of the plots but are provided in dataset archived online. Bars at 0 ka on the δD time series indicate range of δD values measured for *n*-alkanes from two surface sediment samples. Black symbols on bottom plot denote age points derived from 17 terrestrial macrofossil and two sediment organic carbon radiocarbon dates used to construct core chronology (Whitney et al., 2011). Gray shaded bar indicates approximate timing of abrupt ~5-10-fold increase in lake sedimentation rate.

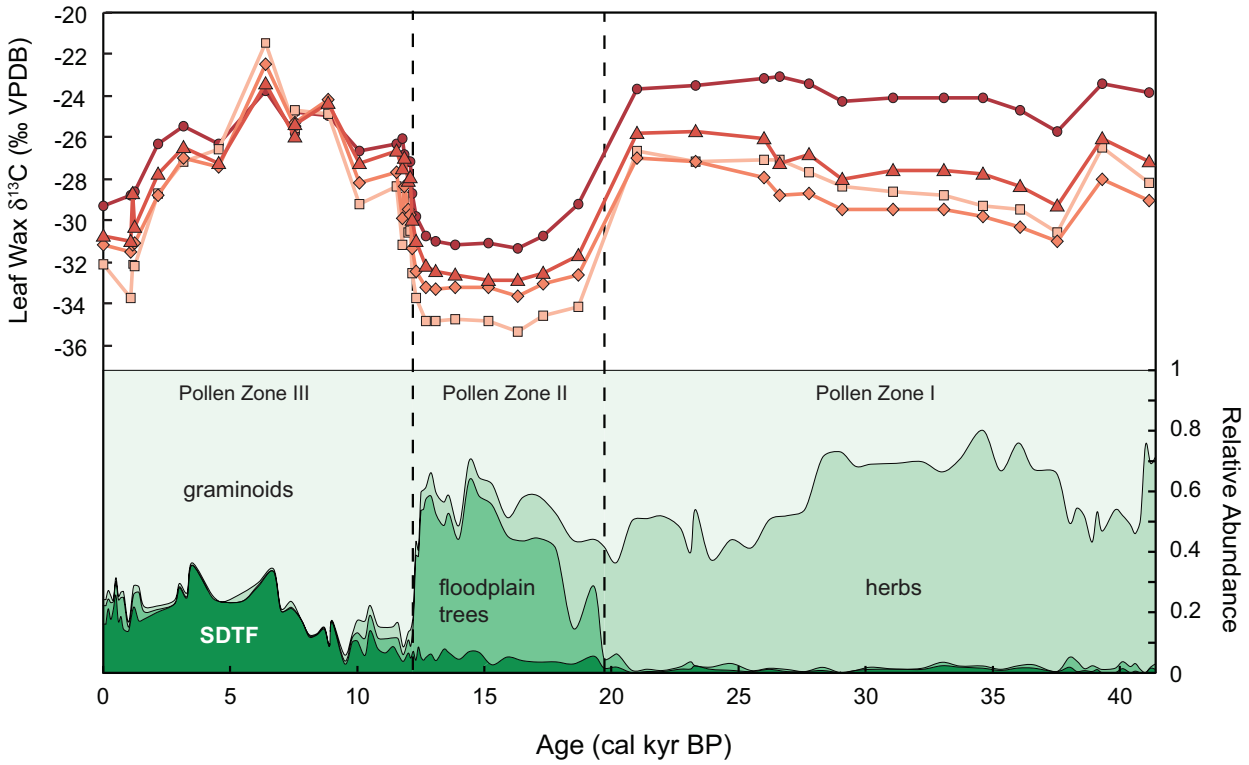

Figure 4. Comparison of LLG *n*-alkane $\delta^{13}C$ values (top) and abundance of major vegetation groups from pollen data (bottom) over past 40 kyr. $\delta^{13}C$ values are shown for *n*-C_{27} (squares), *n*-C_{29} (diamonds), *n*-C_{31} (triangles), and *n*-C_{33} (circles). Vegetation types, in order of lightest to darkest shading, include graminoids, herbs, floodplain trees, and seasonally dry tropical forest (SDTF). Dashed lines indicate transitions between pollen zones as defined by Whitney et al. (2011).

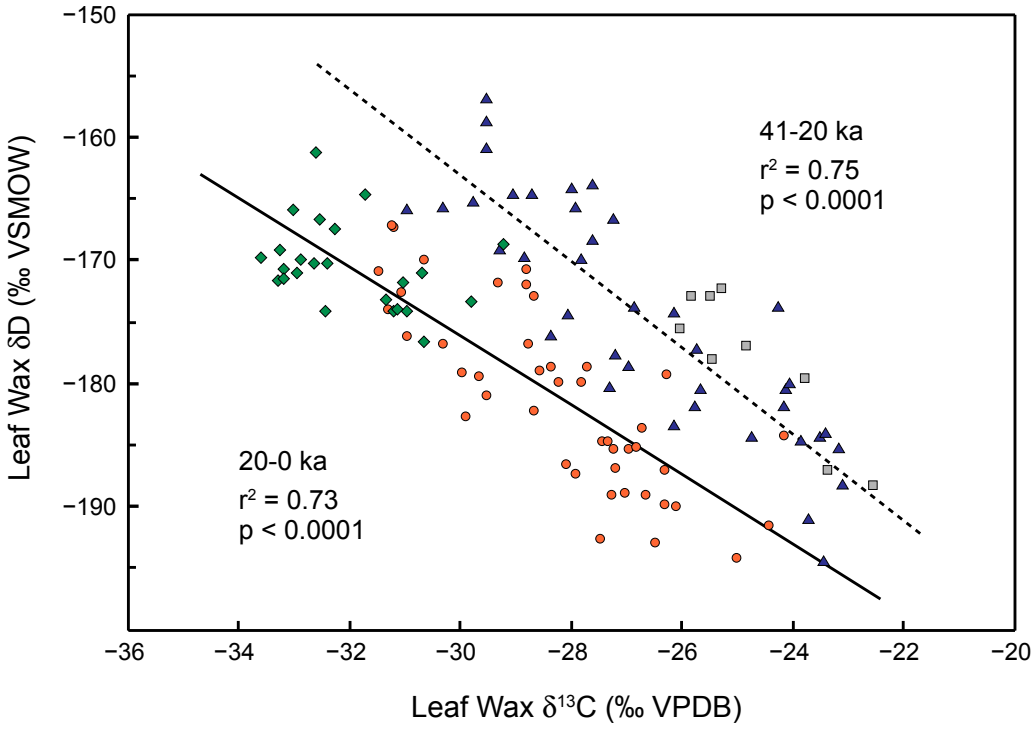

Figure 5. Comparison of all downcore *n*-C_{29}, *n*-C_{31} and *n*-C_{33} alkane $\delta^{13}C$ and δD values. Full glacial (41-20 ka) points are shown as blue triangles, late glacial (20-12.2 ka) as green diamonds, early/mid-Holocene (7.6-6.4 ka) as gray squares, and remaining Holocene (12.2-8.9 ka, 4.6-0 ka) as orange circles. Correlations for 41-20 ka and 20-0 ka are shown by dashed line and solid line, respectively. Note that correlation for 20-0 ka excludes early/mid-Holocene points (see text for further explanation).

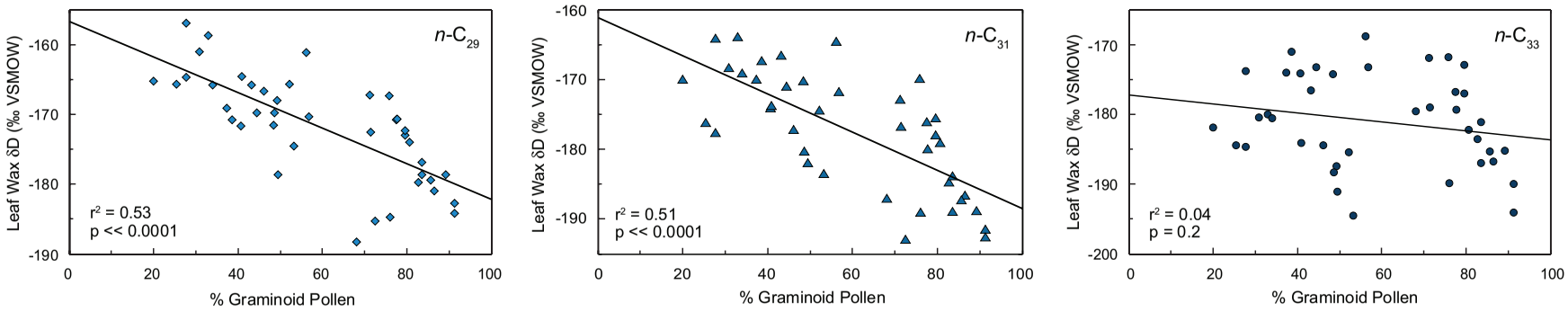

Figure 6. Comparison of *n*-alkane δD values and graminoid (*Poaceae* + *Cyperaceae*) pollen abundance for all downcore samples. From left to right: *n*-C_{29}, *n*-C_{31}, *n*-C_{33} data.

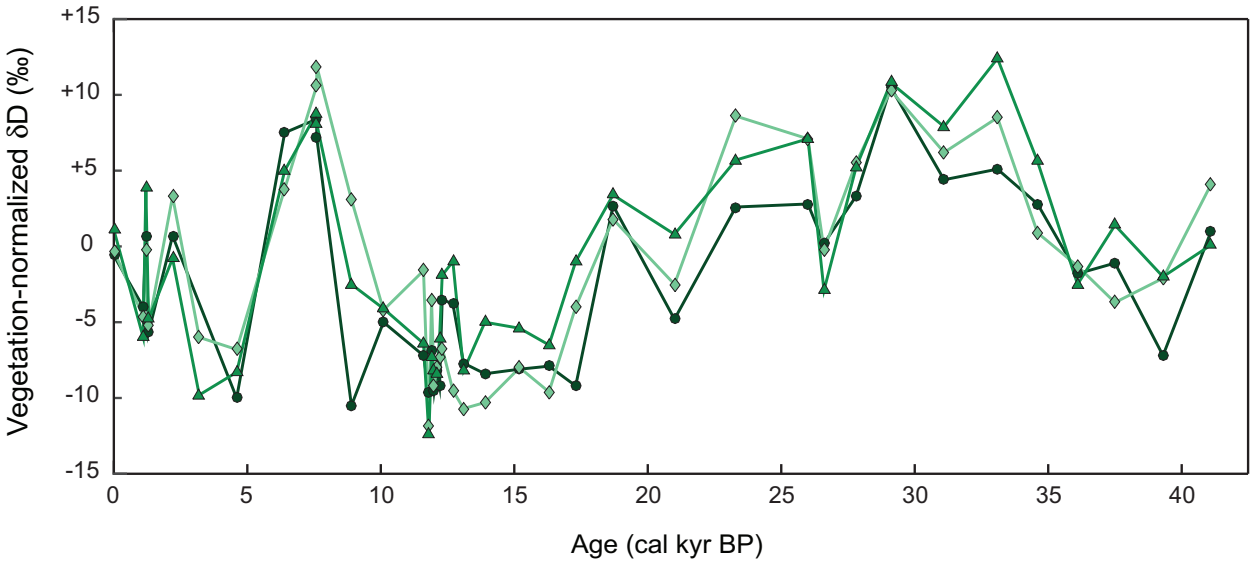

Figure 7. Time series of relative changes in vegetation-normalized δD values (δD_{vn}) for C_{29}-C_{33} *n*-alkanes at LLG over the past 40 kyr. δD values were corrected for vegetation change by normalizing values to a pure C_4 endmember using 41-20 ka and 20-0 ka $\delta^{13}C$-δD trends. *n*-C_{29} δD_{vn} values are shown in light green diamonds, *n*-C_{31} in medium green triangles and *n*-C_{33} in dark green circles.

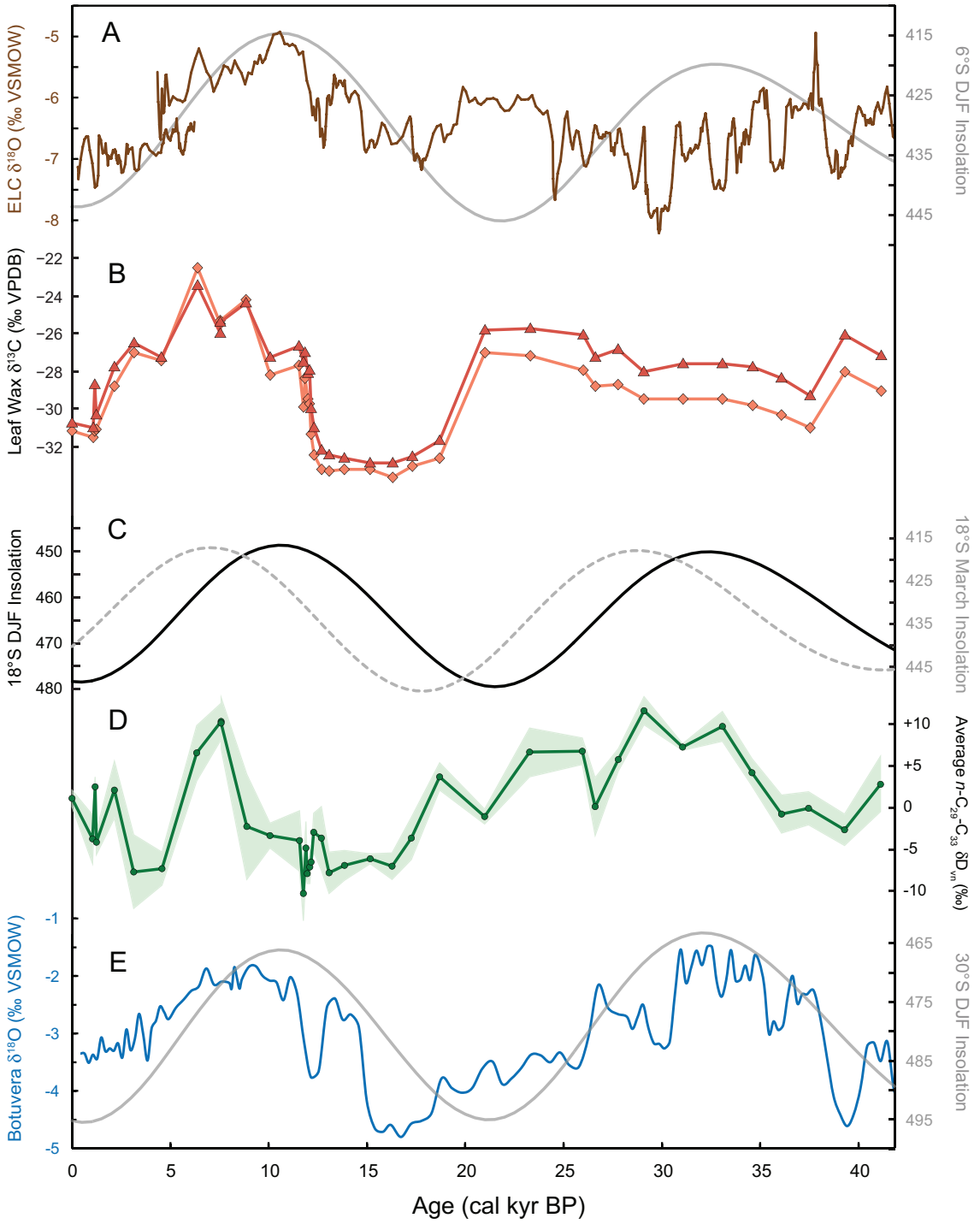

Figure 8. Time series of LLG *n*-alkane $\delta^{13}C$ and δD values and other tropical South American climate records over the past 40 kyr. A. El Condor speleothem $\delta^{18}O$ (western Amazon; Cheng et al., 2013) and mean 6°S summer (DJF) insolation. B. LLG C_{29} (diamonds) and C_{31} (triangles) *n*-alkane $\delta^{13}C$. C. Mean 18°S DJF insolation (black solid line) and March insolation (dotted gray line). D. Relative changes in average vegetation-normalized δD for *n*-C_{29}-C_{33}. Standard deviation (1σ) of average *n*-C_{29}-C_{33} values is shown by light green shading. E. Botuverá Cave speleothem $\delta^{18}O$ (southern Brazil; Wang et al., 2007) and mean 30°S DJF insolation. Note that for all plots insolation axes are reversed (increasing down). Insolation values were calculated according to Laskar et al. (2004).

Supplementary material

Appendix: additional sample preparation details

Sediment samples (~1-10 g) were freeze-dried and finely ground, and lipids were extracted with a 9:1 dichloromethane:methanol mixture using either an accelerated solvent extractor (ASE 200, Dionex) or microwave-assisted reaction system (MARS, CEMS corporation). Lipid extracts were dried over sodium sulfate and separated into hydrocarbon and polar fractions using 1% deactivated silica gel in Pasteur pipette columns (filled to 4 cm) using 5 mL hexane and 10 mL dichloromethane:methanol (1:1) as eluents, respectively.

n-Alkanes were further purified from the hydrocarbon fraction by urea adduction and $AgNO_3$-impregnated silica gel column chromatography. For urea adduction, 0.5 mL of a solution of urea in methanol (40 mg/mL) was added to *n*-alkanes dissolved in 1.5 mL 2:1 hexane:dichloromethane. The mixture was dried under nitrogen at room temperature, allowing urea crystals to form. The adduction procedure was repeated a total of three times, each time adding 1.5 mL 2:1 hexane:dichloromethane followed by 0.5 mL of the urea solution. After the final adduction, crystals were rinsed three times with 4 mL hexane to remove non-adducts. Urea crystals were then dissolved in 25 mL MilliQ water, and adducts (including *n*-alkanes) were extracted five times with 5 mL 4:1 hexane:dichloromethane. Silver ion chromatography was performed in Pasteur pipette columns with 4 cm $AgNO_3$-impregnated silica gel (Sigma Aldrich). Saturated and unsaturated hydrocarbons were eluted with 4.5 mL hexane and 6 mL dichloromethane, respectively.

Compounds were identified by comparison of gas chromatograph/flame ionization detector (GC/FID, Agilent 5890) retention times to those of authenticated external standards.

Chapter 4.

Hydrologic control on terrestrial biospheric carbon export from a tropical catchment since the last glacial period I: Cariaco Basin catchment

Abstract

The terrestrial biosphere plays a key role in carbon cycle feedbacks on climate, but current understanding of the long-term terrestrial carbon cycle response to climate change is limited by the short period of direct observations. In this study, we use compound-specific radiocarbon dating of vascular plant biomarkers (leaf waxes) in an independently dated sediment record from Cariaco Basin to investigate the relationship between past tropical climate variability and the age structure of terrestrial biospheric carbon exported to the ocean over the past 20 kyr. Our results indicate that sedimentary leaf waxes are composed of two pools of distinct age, a relatively fresh component derived from standing vegetation, leaf litter, or young soil organic matter and an old component derived from aged soil organic matter. By comparing relative signals in leaf wax stable carbon isotope and pollen records, we are then able to constrain the average ages of these pools to <100 years (decadal pool) and >5000 years (millennial pool) at time of deposition, respectively. Past hydrologic variability appears to be a significant control on the relative sizes of these components, with wetter conditions linked to increased export of decadal waxes in addition to a relatively constant background of millennial waxes. This

relationship suggests that higher precipitation drives increased mobilization and transport of young terrestrial biospheric carbon to the ocean, representing a negative climate feedback mechanism on geologic timescales. Furthermore, variability in leaf wax age structure may impact the amplitude and timing of climate signals in biomarker-based paleoclimate reconstructions.

4.1 Introduction

The fate of the estimated 2800 Pg of carbon stored in the terrestrial biosphere (Carvalhais et al., 2014) plays a critical role in modulating atmospheric CO_2 levels and global climate on annual to geologic timescales. While most organic carbon fixed by terrestrial plants is respired and returned to the atmosphere as CO_2 relatively quickly (i.e., within years to decades), biospheric carbon can be retained in terrestrial reservoirs such as soils, wetlands, and river floodplains on centennial to millennial timescales (Trumbore, 2000). Some fraction of terrestrial biospheric carbon is also mobilized by erosion and exported via rivers to lakes and oceans, where it can be buried and preserved in marine and lacustrine sediments on geologic timescales (e.g., Galy et al., 2007). The different effects of climate change on the transfer of terrestrial biospheric carbon to less active soil and sediment reservoirs represent important but poorly understood climate feedback mechanisms. There is ample evidence that temperature and precipitation patterns exert control on soil carbon stocks (e.g., Amundson, 2001) and erosion processes (e.g., Renard et al., 1997), but assessing the combined long-term response of these processes to climate variability is limited by the relatively short window of direct observations, as well as poor preservation and high spatial variability of longer soil records.

In this study, we target the fraction of terrestrial biospheric carbon preserved in marine sediments to investigate the influence of past climate changes on biospheric carbon storage integrated over a tropical catchment since the last glacial period. Specifically, we use compound-specific radiocarbon dating to determine the age distributions of vascular plant biomarkers (leaf waxes) at the time of sediment deposition under different climate conditions. The age distribution of these compounds relative to sediment deposition age provides a measure of average storage time in soils and other terrestrial reservoirs between the time of synthesis and the time of export and burial. Radiocarbon dating of leaf waxes in soils (Douglas et al., 2014), modern river sediments (Kusch et al., 2010; Galy and Eglinton, 2011; Gustafsson et al., 2011; Tao et al., 2015), and Holocene sediment records (Douglas et al., 2014; Smittenberg et al., 2006) has consistently shown ages ranging from modern to several millennia, indicating that these compounds are present in both active and recalcitrant terrestrial carbon pools. We focus our study on the Cariaco Basin catchment of northern South America as a site with a well-established history of hydrologic and temperature variability and highly constrained sediment chronology over the past 20 ka. By tracking changes in the age of one component of terrestrial biospheric carbon, we are able to gauge changes in terrestrial organic carbon cycling through climate transitions of much greater magnitude than those that have occurred in the observational period.

Furthermore, on a more practical level, leaf wax stable isotope signatures are increasingly used for paleoclimate reconstructions (e.g., Sachse et al., 2012) with the implicit assumption that biomarker proxies and sediments share a common chronology. However, pre-aging of leaf waxes in terrestrial reservoirs may distort the timing and magnitude of the climate signals they record (Douglas et al., 2014). Thus, we also explore the potential effects of variable leaf wax age

structures on biomarker-based climate records at a site with a range of different proxy records over the past 20 ka (Haug et al., 2001; Hughen et al., 2004a; Lea et al., 2003; Peterson and Haug, 2006).

4.2 Study Site

Cariaco Basin is a pull-apart basin situated on the continental shelf off the central coast of Venezuela in the northern tropics of South America (Figure 1). The basin is connected to the Caribbean Sea by shallow (<150 m) sills, which limit the exchange of deep water between the basin and open ocean. In the present day, the relative isolation of the basin and high upwelling-driven productivity result in anoxic conditions below 300 m (Peterson et al., 2000b). Due to its proximity to shore and limited exchange with the Caribbean Sea, the basin acts as a natural sediment trap for terrigenous and autochthonous material. The basin receives continental runoff from several small mountainous rivers and lowland rivers that empty directly onto the Unare Platform, a wide shallow (<100 m) shelf off the Venezuelan coast (total catchment area: 36,500 km^2). Despite its proximity to the very large Orinoco River delta, there is no evidence that Orinoco-derived sediment has contributed significantly to terrigenous material in the basin in the present day or over the last glacial cycle (Martinez et al., 2012). Present day vegetation in the Cariaco watershed ranges from savanna and semi-arid forest in the Rio Unare drainage basin to evergreen and montane cloud forest at higher elevations (González et al., 2008). Northern Venezuela has a warm, tropical climate with mean annual temperature >25°C in the lowlands and cooler temperatures at higher altitudes. Precipitation is controlled by seasonal migration of the Intertropical Convergence Zone (ITCZ): the majority of annual precipitation (~900 mm/y) falls during the boreal summer/autumn when the ITCZ is furthest north, while the remainder of

the year, when the ITCZ shifts southward, is dry (University of East Anglia, 1961-1990 Monthly Climatology).

4.2.1 Past climate variability at Cariaco Basin

Over the past 20,000 years, hydrologic variability on the northern coast of Venezuela was driven by shifts in the average latitudinal position of the ITCZ, with a more southerly position resulting in decreased precipitation and vice versa. Evidence of higher salinity in the Caribbean Sea during the Last Glacial Maximum (LGM) and late glacial period suggests increased water deficits (evaporation-precipitation) in the northern South American tropics due to southward displacement of the ITCZ (Schmidt et al., 2004). Terrestrial records of LGM conditions in northern South America are generally consistent with drier glacial conditions (e.g., Sylvestre, 2009), but consistently depleted stable carbon isotopic signatures of terrestrial biomarkers ($\delta^{13}C$ values ranging from -32 to -31‰) in Cariaco sediments ca. ~23-19 ka suggest that glacial decreases in humidity were not severe enough to disrupt the C_3 forest landscape (Drenzek, 2007). It is also possible that glacial decreases in precipitation were not uniform throughout the Cariaco catchment and that increased trade wind strength associated with a more southerly ITCZ favored increased orographic precipitation in higher altitude forested areas (González et al., 2008). During the last deglaciation, Cariaco records show clear teleconnections between high latitude northern hemisphere climate variability and hydrologic variability in northern Venezuela (Hughen et al., 2004a; Peterson and Haug, 2006; Peterson et al., 2000a). Based on records of vegetation biomarker $\delta^{13}C$ values, Heinrich Event 1 (H1, ~17-15 ka) was marked by increased abundance of C_4 plants and markedly dry conditions (Drenzek, 2007; Hughen et al., 2004a). This period was punctuated by an abrupt shift to more humid conditions coincident with the Bølling-

Allerød (BA) interstadial followed by a return to dry conditions coincident with the Younger Dryas (YD) stadial (Hughen et al., 2004a). The beginning of the Holocene was marked by a rapid shift to wetter conditions (Hughen et al., 2004a), which a record of riverine sediment input to Cariaco indicates lasted through the early-mid Holocene or Holocene "thermal maximum" (10.5-5.4 ka) (Peterson and Haug, 2006). However, lake level records from Lake Valencia, an endorheic lake just west of the Cariaco catchment, show some hydrologic variability on centennial timescales during the early-mid Holocene, including sustained low lake levels and dry conditions from ~8400-7600 cal yr BP (Binford, 1982; Curtis et al., 1999). Following the generally wet early-mid Holocene, the mean position of the ITCZ has drifted to the south and northern Venezuela has become gradually drier coincident with decreasing local summer insolation (Drenzek, 2007; Haug et al., 2001).

As a lowland tropical region, the Cariaco catchment likely experienced limited glacial-interglacial temperature change compared to higher latitude areas. Sea surface temperature (SST) records from Cariaco and Tobago Basin show 2-4°C cooling in the late glacial period compared to the Holocene (Lea et al., 2003; Rühlemann et al., 1999), consistent with estimates of 2-3°C cooling in the northern hemisphere tropics (0-30° N) from model simulations (Broccoli, 2000; Farrera et al., 1999) and a global synthesis of tropical records (Shakun and Carlson, 2010). The Cariaco SST record also shows 3-4°C cooling coincident with the YD but may be influenced to some extent by increased upwelling associated with a more southerly ITCZ position during this period. The nearby Tobago Basin SST record, as well as other tropical temperature records globally, do not show any pronounced cooling during the YD event (Rühlemann et al., 1999; Shakun and Carlson, 2010).

4.3 Methods

4.3.1 Sample collection

Sediment samples were taken from cores raised from a depth of 893 m at Site 1002 by the Ocean Drilling Program (ODP) Leg 165 expedition (Peterson et al., 2000b). Depending on sediment availability, samples were taken from cores raised from either Hole 1002D or 1002E. Full descriptions of all samples are provided in Table 1.

4.3.2 Sediment age assignment

Sediment calendar ages were assigned using high-resolution 1002D and 1002E chronologies from Hughen et al. (2004b) and Hughen et al. (2006) based on correlation of Cariaco Basin climate events to independently dated GISP2 and Hulu Cave records. For most samples, sediment radiocarbon ages were derived from reservoir-corrected radiocarbon ages of foraminifera in 1002D sediments (Hughen et al., 2004b). For the sample corresponding to the YD stadial (12.0 ka horizon), sediment radiocarbon age was assigned using a Hulu Cave ^{230}Th calendar age-^{14}C age calibration (Southon et al., 2012) to avoid uncertainties associated with changes in Cariaco Basin reservoir age during this period.

4.3.3 Bulk sediment property measurement

Aliquots of freeze-dried and finely ground sediment were measured for total organic carbon (TOC) and total carbon (TC) on an elemental analyzer coupled to a Finnegan Delta^{plus} isotope ratio mass spectrometer (EA/IRMS). Following Whiteside et al. (2011), samples measured for TOC were sealed in a vacuum desiccator with a beaker of 50 mL 12N HCl and fumigated for 60-72 hours at 60-65°C to remove carbonates. Samples were then moved to a

different desiccator and allowed to dry for 24 hours prior to measurement. The carbonate content was calculated using the difference between %TOC and %TC scaled by the carbon content of $CaCO_3$ (12% by mass), i.e., assuming that all carbonate minerals were present as $CaCO_3$. Due to limited sediment availability and measurement irregularities, the 18.4 ka sediment horizon was assumed to have the same $CaCO_3$ content as the adjacent sediment sample (18.3 ka horizon).

4.3.4 Compound-specific sample preparation

Sediment samples were freeze-dried and finely ground, and lipids were extracted with a 9:1 dichloromethane:methanol (DCM:MeOH) mixture using either an accelerated solvent extractor (ASE 200, Dionex) or microwave-assisted reaction system (MARS, CEMS corporation). Lipid extracts were dried and saponified with 15 mL 0.5 M KOH in MeOH and ~150 μL water (70°C, 2 h). Following saponification, a neutral lipid fraction was extracted with 5 x 5 mL hexane. The pH of the remaining mixture was then lowered to ~2.5 by dropwise addition of concentrated HCl, and an acidic lipid fraction was extracted with 5 x 5 mL 4:1 hexane:DCM. Neutral and acidic lipid fractions were separated independently by column chromatography with a stationary phase of 1g aminopropyl-functionalized silica gel (LC-NH_2). Five fractions were eluted with 4 mL hexane (F1, hydrocarbons), 6 mL 3:1 hexane:DCM (F2, ketones/esters), 7 mL 9:1 DCM:acetone (F3, alcohols and other polar lipids), 15 mL 98:2 DCM:formic acid (F4, acids), and 15 mL 1:1 MeOH:DCM (F5, flush).

F4 fractions containing fatty acids were methylated with 5-15 mL acidified MeOH (95:5 MeOH:HCl or 95:5 MeOH:acetyl chloride) for 12-16 hours at 70°C. The resulting fatty acid methyl esters (FAMEs) were purified with a second LC-NH_2 column. FAMEs were eluted with 7 mL 4:1 hexane:DCM, and remaining material was flushed with 1:1 DCM:MeOH.

Due to the relatively high level of purity required for collection with preparative capillary gas chromatography (PCGC), FAMEs were further purified with urea adduction (to remove branched or aromatic contaminants) and silver nitrate ($AgNO_3$) chromatography (to remove unsaturated contaminants). For urea adduction, 0.5 mL of a solution of urea in methanol (40 mg/mL) was added to FAMEs dissolved in 1.5 mL 2:1 hexane:DCM. The mixture was dried under nitrogen at room temperature, allowing urea crystals to form. The adduction procedure was repeated a total of three times, each time adding 1.5 mL 2:1 hexane:DCM followed by 0.5 mL of the urea solution. After the final adduction, crystals were rinsed three times with 4 mL hexane to remove non-adducts. Urea crystals were then dissolved in 25 mL MilliQ water, and adducts (including *n*-FAMEs) were extracted five times with 5 mL 4:1 hexane:DCM. Silver nitrate chromatography was performed in Pasteur pipette columns with 4 cm $AgNO_3$-impregnated silica gel (Sigma Aldrich). Saturated and unsaturated FAMEs were eluted with 5 mL DCM and 7 mL 9:1 DCM:acetone, respectively.

FAMEs were identified and quantified by comparison of gas chromatograph/flame ionization detector (GC/FID, Agilent 5890) retention times and peak areas to those of authenticated external standards. Average chain length (ACL) of *n*-FAMEs was calculated using GC/FID quantification data according to the formula:

$$\mathrm{ACL}_{28-34} = \sum_{n=28,30\ldots}^{34} n * [C_n] / \sum_{n=28,30\ldots}^{34} [C_n] \quad (1)$$

4.3.5 Compound-specific radiocarbon analysis

Individual FAMEs (n-C_{26}-C_{34}) were collected using PCGC techniques as described in Eglinton et al. (1996) using either an Agilent 7890A or HP 5890 Series II GC coupled to a Gerstel preparative fraction collector. FAMEs were dissolved in iso-octane and run at maximum

concentrations of ~0.5-1 μg compound/injection for a total of ~30-250 injections. Post-PCGC yields were generally ~50-70% of starting material. Trapped compounds were eluted from traps with 4 mL DCM and purified by elution through a Pasteur pipette column of 1% deactivated silica gel (filled to ~2-3 cm) with 4 mL DCM. Purity of trapped compounds was verified by GC/FID.

In order to increase sample size and reduce analytical uncertainty during radiocarbon measurement, *n*-C_{30}, C_{32} and C_{34} FAMEs from all sediment horizons were combined prior to combustion. For the 15.4 ka horizon, very low FAMEs concentrations required combination of *n*-C_{28}, C_{30}, C_{32} and C_{34}. All other compounds (*n*-C_{26}, *n*-C_{28}) were analyzed individually. To prepare for combustion, individual or combined compounds were dissolved in a small volume (< 1 mL) of DCM and transferred to quartz tubes. Solvent was completely evaporated from each tube under a high-purity N_2 stream and a small amount of precombusted copper oxide (~150 mg) added to the dry tubes. Tubes were chilled in an dry ice/isopropanol bath and evacuated for ~1 minute to < 30 μTorr. The dry ice bath was then replaced with liquid N_2 (LN2), and tubes were flame-sealed under vacuum. Sealed samples were combusted at 850°C for 5 hours. Following combustion, tubes were cracked under vacuum in the presence of a water trap chilled with a dry ice/isopropanol bath. CO_2 was trapped with LN2, manometrically quantified and flame-sealed in pyrex tubes to submit for radiocarbon analysis.

All samples were submitted to the National Ocean Sciences Accelerator Mass Spectrometry facility (NOSAMS, Woods Hole, MA, USA) for radiocarbon dating and analyzed between May 2014 and June 2015. Due to limited sample sizes, most samples were graphitized on the NOSAMS ultra-small graphitization line as detailed by Shah Walter et al. (2015). The

remainder was processed on the NOSAMS small sample or main graphitization lines (http://www.whoi.edu/nosams/SPL).

4.3.6 Data reduction

Compound-specific radiocarbon data received from NOSAMS was corrected for blank carbon added during PCGC collection and subsequent combustion, while graphitization and other AMS analytical blanks were assessed and accounted for by NOSAMS prior to reporting results. Blank-corrected fraction modern (F_m) values were calculated according to the mass balance equation:

$$F_{m,wax} = m_t F'_{m,wax} + m_b F_{m,b} \quad (2)$$

where $F_{m,wax}$ is the reported fraction modern, m_t is the true sample mass excluding blank carbon, $F'_{m,wax}$ is the blank-corrected fraction modern, m_b is the blank carbon mass and $F_{m,b}$ is the fraction modern of blank carbon. Details of PCGC and combustion blank characterization are provided in Appendix 1. FAMEs ^{14}C data were also corrected for carbon added during derivatization with the reported F_m of the batch of methanol used for methylation reactions. Data were corrected according to the equation:

$$F''_{m,wax} = \frac{F'_{m,wax}(ACL + 1) - F_{m,MeOH}}{ACL} \quad (3)$$

where $F''_{m,wax}$ is the methyl- and blank-corrected $F_{m,wax}$, $F'_{m,wax}$ is the blank-corrected $F_{m,wax,}$ $F_{m,MeOH}$ is the measured F_m of MeOH used for methylation, and ACL is the average chain length of the compound(s) in each sample. All error has been propagated through each correction step. Carbon masses quantified manometrically were assumed to have an error of ± 5%.

4.3.7 Wax age calculations and notation

In most previous studies of wax ages in sediments, average radiocarbon and calendar ages have been calculated directly from measured F_m values. However, these calculations rely on the implicit assumption that all waxes are narrowly distributed around one uniform age (Figure 2a). Instead, it is more likely that waxes present in a given sediment layer are a mixture derived from multiple pools with a range of ages, as depicted in Figure 2b and 2c. Wax F_m values can be expressed as a linear combination of multiple components:

$$F_{m,wax} = \sum_{1}^{n} f_n \cdot F_{m,n} \tag{4}$$

where $F_{m,wax}$ represents the measured fraction modern of a wax mixture and f_n represents the carbon mass fraction of component n. The ^{14}C age of waxes is calculated using the equation:

$$^{14}C\ Age = -8033 \cdot \ln\left(F_{m,wax}\right) = -8033 \cdot \ln\left(\sum_{1}^{n} f_n \cdot F_{m,n}\right) \tag{5}$$

and represents a log-average radiocarbon age across an unknown age distribution. If there are multiple wax pools of different ages, converting wax ^{14}C ages to calibrated calendar ages using a non-linear calibration curve can introduce significant artifacts into the data, especially if there is a large age separation between different components (Figures 2b, 2c). The potential for calibration bias is particularly high when the average age of waxes happens to fall during a period of relatively rapid changes in atmospheric $^{14}C/^{12}C$ ratios, for instance during the YD (Hughen et al., 2004b).

With these complexities in mind, we report wax-sediment ^{14}C differences primarily using the fractional relative disequilibrium ($F^{14}R$) notation described by Soulet et al. (in press), where $F^{14}R_{wax}$ is defined as:

$$F^{14}R_{wax} = {F_{m,wax}}\Big/{F_{m,sed}} = {F_{m,wax}\,(t_0)}\Big/{F_{m,atm}\,(t_0)} \tag{6}$$

and $F_{m,wax}$ and $F_{m,sed}$ are the fractions modern of wax compounds in a sediment layer and the material used to assign sediment deposition age (i.e., reservoir-corrected foraminifera), respectively. (For simplicity, in all following discussion we use 'sediment' as shorthand for the dated material in the sediment matrix.) Assuming the sediment was in equilibrium with the atmospheric ^{14}C reservoir when it was deposited, $F^{14}R_{wax}$ is also equivalent to the fraction modern of waxes normalized to the atmospheric ^{14}C composition ($F_{m,atm}$) at the time of sediment deposition (t_0). This ratio does not change through time after sediment deposition since the ^{14}C content of the waxes and sediment both decay with the same exponential term. Importantly, $F^{14}R_{wax}$ can be used in isotope mass balance or mixing equations since it is a linear function of $^{14}C/^{12}C$ ratios, unlike ^{14}C ages. $F^{14}R_{wax}$ is thus a convenient metric for comparing mixtures of waxes with a range of ages for different sediment horizons.

While $F^{14}R_{wax}$ normalizes $F_{m,wax}$ to atmospheric ^{14}C activity at the time of sediment deposition, the radiocarbon content of any components of a wax mixture older than the sediment will be set by the initial atmospheric ^{14}C signature at the time of synthesis followed by decay between the time of wax synthesis and sediment deposition. To illustrate the effect of variable atmospheric ^{14}C activity, we can again express $F^{14}R_{wax}$ as a linear combination of components with different F_m values:

$$F^{14}R_{wax} = \frac{1}{F_{m,sed}} \sum_{1}^{n} f_n \cdot F_{m,n} \tag{7}$$

We can then express the F_m of each component n as a function of $F_{m,sed}$:

$$F_{m,n} = \frac{A_n}{A_0} \cdot e^{-\lambda(t_n - t_0)} \cdot F_{m,sed} \tag{8}$$

where A_n is the atmospheric ^{14}C activity at the time of formation of component n (t_n), A_0 is the atmospheric ^{14}C activity at the time of sediment deposition (t_0), and λ is the true ^{14}C decay constant (1/8267 yr^{-1}). Combining equations (7) and (8), we obtain the full equation for $F^{14}R_{wax}$:

$$F^{14}R_{wax} = \sum_{1}^{n} f_n \cdot \frac{A_n}{A_0} \cdot e^{-\lambda(t_n - t_0)} \quad (9)$$

The effects of changes in atmospheric ^{14}C activity are contained in the A_n/A_o term. This term is generally negligible if waxes are synthesized within 1000 years of the time of sediment deposition, as the maximum change in atmospheric ^{14}C activity over any 1000 year period from 50-0 ka is -6.7% (between 15.19-14.19 cal kyr BP). However, as the time window between wax synthesis and sediment deposition increases, the effects of changes in atmospheric ^{14}C activity can become more substantial given the ~50% decrease in atmospheric ^{14}C activity over the past 25-30 kyr.

4.4 Results

4.4.1 Compound-specific radiocarbon measurements

Raw and corrected F_m and ^{14}C ages, as well as calculated $F^{14}R_{wax}$ values, for measured compounds are shown in Table 2. Radiocarbon age differences between waxes and sediments (i.e., radiocarbon residence times; Soulet et al., in press) are also provided for reference but this metric is not used in further analysis. We emphasize that radiocarbon years do not have a consistent relationship with calendar years over the past 50,000 years so direct comparison of radiocarbon age differences may be somewhat misleading.

Over the past 18.5 kyr, $F^{14}R_{wax}$ values range from 0.56-1.06. $F^{14}R_{wax}$ values greater than 1 indicate that waxes are enriched in ^{14}C relative to sediment (i.e., waxes are younger than

sediments) (Figure 3). We find only one sample (*n*-C_{26} in 10.4 ka sediment horizon) with $F^{14}R_{wax}$ > 1, and the reported $F^{14}R_{wax}$ value for this sample is within uncertainty (2σ) of 1 (i.e., no age difference between waxes and sediment). The absence of any other such wax-sediment age discrepancies likely reflects the excellent age control of the Cariaco sediment record, as well as the low probability of significant downward wax migration through the sediment column.

With the exception of the 18.3 and 18.4 ka horizons, *n*-C_{26} consistently shows the highest $F^{14}R_{wax}$ values ($F^{14}R_{wax} \geq 0.9$), indicating that *n*-C_{26} is generally of similar age to sediments. Furthermore, the amount of *n*-C_{26} relative to total *n*-C_{26}-C_{34} shows a marked increase at 14.1 ka (Figure 3), suggesting a new source of relatively fresh *n*-C_{26} became available at this time. In Holocene and YD (12.0 ka) horizons, $F^{14}R_{wax}$ decreases with increasing chain length, a pattern that has been observed in previous compound-specific ^{14}C studies of long chain *n*-fatty acids (Drenzek, 2007; Kusch et al., 2010). However, this pattern is reversed in BA (14.1 ka) and late glacial horizons (18.3, 18.4 ka). Coincidentally, we observe a change in the distribution of *n*-C_{28}-C_{34} concentrations during the last deglaciation, with $ACL_{28\text{-}34}$ decreasing from the late glacial into the Holocene (Figure 3).

Considering the sum of *n*-C_{28}-C_{34} fatty acids, we observe a generally positive relationship between wax concentration (μg compound/g sediment, normalized for $CaCO_3$ content) and the weighted average of *n*-C_{28}-C_{34} $F^{14}R_{wax}$. When *n*-C_{28}-C_{34} $F^{14}R_{wax}$ is plotted versus the inverse of *n*-C_{28}-C_{34} concentration (Figure 4), most samples appear to fall on one mixing line ($r^2 = 0.94$), with the exception of two Holocene samples (1.3, 7.7 ka horizons) and one glacial sample (15.4 ka). On this mixing line, $F^{14}R_{wax}$ reaches a limit of 0.99 at infinite wax concentration ($1/[n\text{-}C_{28}\text{-}C_{34}] = 0$). This pattern suggests that the dominant control of $F^{14}R_{wax}$ is the addition of fresh waxes (i.e., a decadal fraction) on top of an older component (millennial fraction) with lower and relatively

constant concentration/$F^{14}R_{wax}$. The two Holocene samples that fall below the main mixing line likely reflect contributions from older and/or more concentrated millennial components. The large discrepancy between the 15.4 ka sample and other samples is likely the result of very different composition of sediments deposited during H1 compared to other time periods. The sediment unit corresponding to H1 is a distinct blue/gray clay layer marked by very low OC and $CaCO_3$ compared to other sediment units deposited from 20-0 ka (Meckler et al., 2007). Thus, the anomalous composition of this sediment layer may skew the relationship between $F^{14}R_{wax}$ and concentration due to dilution by a silicate rich mineral matrix.

4.5 Discussion

4.5.1 Leaf wax sources and transport pathways

Long-chain (C_{26} – C_{34}) *n*-fatty acids with a strong even over odd chain length preference are produced nearly exclusively by vascular plants as components of leaf waxes (Eglinton and Hamilton, 1967). Leaf wax compounds are abundant in fresh vegetation biomass and leaf litter, as well as in aged organic matter of deeper soil layers (e.g., Douglas et al., 2014). Waxes are transported to marine or lacustrine sediments primarily by riverine transport of particulate organic matter derived from vegetation biomass or soils. Due to the hydrophobic nature of waxes, contributions of waxes from riverine or marine dissolved organic matter are generally very small compared to particulate sources (e.g., Mannino and Harvey, 1999). Waxes can also be transported via eolian pathways by transport of dust particles derived from soil or other terrestrial sources. However, despite the potential for long-range atmospheric transport of waxes (Conte and Weber, 2002), rivers are likely the dominant source of waxes at a coastal site like Cariaco Basin. Estimates of eolian input based on analyses of surface sediment and sediment trap material range from <2% to ~10% of total sediment deposited in the basin with the vast majority

delivered by local rivers (Elmore et al., 2009; Martinez et al., 2012). Furthermore, stable isotope and chain length patterns of waxes in late glacial Cariaco sediments are inconsistent with significant contribution from long-range sources (i.e., Saharan dust), even during intervals of greater trade wind intensity in the Cariaco region (e.g., YD stadial) (Hughen et al., 2004a).

4.5.2 Age structure of waxes

Since waxes are present in both fresh vegetation and aged soil material, there are at least two potential pools of waxes within a given sediment layer: a decadal component, primarily derived from standing vegetation biomass, leaf litter, or young (<100 yr) soil organic matter, and a millennial component derived from aged soil organic matter or other reservoirs of old terrestrial carbon, such as wetlands or river floodplains. A multi-component age structure of sedimentary waxes is supported by the observed relationship between concentration and $F^{14}R_{wax}$ consistent with mixing between a fresh component and background millennial component. Cariaco wax $\delta^{13}C$ values over the last deglaciation provide further evidence of the existence of a relatively modern component in sedimentary wax mixtures, as C_3/C_4 vegetation shifts recorded by wax $\delta^{13}C$ lag climate transitions during the northern hemisphere deglaciation sequence by <50 years (Hughen et al., 2004a). These vegetation shifts in the Cariaco catchment are mechanistically linked to well-dated latitudinal ITCZ shifts recorded by independent marine proxies in Cariaco sediments. Thus, there must be some fraction of waxes that are produced and transported to sediments on decadal timescales to record abrupt vegetation shifts.

While the decadal pool is limited to a relatively narrow range of ages, the average age and age distribution of the remaining waxes that cycle on centennial to millennial timescales are more difficult to constrain. The most likely source of old waxes to sediments is soil, the largest reservoir of biospheric terrestrial organic carbon. Although it is possible that sediment

redistribution processes contribute aged waxes to marine sediments, the depleted ^{14}C content of waxes in Unare river samples collected in 2004 ($\Delta^{14}C$ ranging from -20 to -116 ‰) confirm that waxes do acquire significantly aged signatures before export to the ocean (Dickens, unpublished data). Radiocarbon dating of bulk organic matter from deep soil horizons have routinely yielded ages >10,000 ^{14}C years, including in tropical forest soils (de Camargo et al., 1999) and soils overlying volcanic bedrock with negligible radiocarbon-dead petrogenic carbon contribution (Torn et al., 1997). Based on a meta-analysis of available soil radiocarbon data, Mathieu et al. (2015) found that for a typical modern (post-bomb) soil profile in tropical savanna climates (i.e., the Köppen climate classification for northern Venezuela) bulk organic soil $\Delta^{14}C$ values range from +48 ‰ at soil surface to a background of -423‰ (^{14}C age of 4420 yr) at depth. They also calculate that fresh carbon is incorporated down to a depth of 54 cm in the soil profile through mixing activity and root growth. Furthermore, bulk soil ^{14}C composition represents an average of an organic carbon mixture, meaning that the oldest or "passive" fractions may be significantly older than the reported mixture age.

While there is limited data on the ages of waxes in soil profiles, Mikutta et al. (2006) found that older soil fractions had high (>50%) alkyl C content, suggesting that lipids such as fatty acids are indeed present or even enriched in passive pools. Thus, the potential age range of waxes in the millennial fraction is 0-50,000+ years. There may be some contribution from waxes with ages greater than 50,000 years, but these ages will be indistinguishable by radiocarbon measurement since they are effectively radiocarbon dead.

4.5.3 Modeling wax age structure

We illustrate the range of possible age structures for $F^{14}R_{wax}$ values using a two-component mixing model based on Equation (9). Following the approach of Drenzek (2007) and

Douglas et al. (2014), we model the wax age structure as a mixture between a fresh or decadal component <100 years older than sediment and an old or millennial component with an unconstrained age range. The decadal and millennial components are both assumed to have a normal age distribution centered on some age offset μ (defined relative to sediment age such that distribution is centered on sediment age when μ = 0) with a standard deviation σ. The mass balance of a wax mixture can thus be expressed as a linear combination of two Gaussian probability density functions integrated from the time of sediment deposition (t_0) to infinite years before present:

$$m_{wax} = f_{mill} \cdot \int_{t_0}^{\infty} \frac{1}{\sigma_{mill}\sqrt{2\pi}} e^{-(t-\mu_{mill})^2 / 2\sigma_{mill}^2} + f_{dec} \cdot \int_{t_0}^{\infty} \frac{1}{\sigma_{dec}\sqrt{2\pi}} e^{-(t-\mu_{dec})^2 / 2\sigma_{dec}^2} \quad (10)$$

where subscripts "mill" and "dec" refer to millennial and decadal components, respectively, and f_{mill} and f_{dcc} represent carbon mass fractions of the two components such that $f_{mill} + f_{dec} = 1$. $F^{14}R_{wax}$ can be similarly expressed as a linear combination of the sums of the product of probability p and corresponding atmospheric ^{14}C ratio at each time t for both components:

$$F^{14}R_{wax} = f_{dec} \cdot \sum_{t=t_0}^{\infty} p_{dec}(t) \cdot \frac{A_t}{A_0} \cdot e^{-\lambda(t-t_0)} + f_{mill} \cdot \sum_{t=t_0}^{\infty} p_{mill}(t) \cdot \frac{A_t}{A_0} \cdot e^{-\lambda(t-t_0)} \quad (11)$$

We can then calculate the fractional contributions of millennial and decadal components while varying μ and σ (see Appendix 2 for Matlab script). For these calculations, we restrict the possible time range of wax formation from t_0 to 100,000 cal yr BP and exclude any contribution from waxes with ages outside this range. F_m for each year from 50,000-0 cal yr BP is calculated with the Intcal13 atmospheric ^{14}C activity curve (linearly interpolated to yearly resolution) (Reimer et al., 2013), while for any time >50,000 cal yr BP F_m is set to 0.

Based on data from soil radiocarbon profiles, we impose several conditions on the age distribution of the millennial component. First, we restrict the age offset to ages within two

standard deviation of the sediment age (i.e., $u_{mill} - t_0 \leq 2\sigma_{mill}$). This restriction is based on observations that both ^{14}C content and organic carbon content decay exponentially with increasing depth in a soil profile (e.g., Torn et al., 1997). Thus any contribution of waxes from soil erosion should be weighted towards modern carbon even if the average age is very old due to a very broad age distribution. However, we refrain from assigning a value of 0 to u_{mill} to accommodate possible cases when surface soil is older than modern, as has been observed in some arid tropical regions (Mathieu et al., 2015), or irregular age distributions from other terrestrial reservoirs such as wetlands or floodplains. In any case, restricting the age offset to within 2σ represents a generous compromise given the preponderance of carbon of decadal and centennial age in non-fossil terrestrial reservoirs.

Secondly, we set the condition that the average age of the millennial component must be of similar or older age to any chain lengths of samples that fall on the main mixing line (Figure 4). This restricts millennial fraction to average ages greater than ~2800-3000 cal yr to accommodate a $F^{14}R_{wax}$ value of 0.75 found for both *n*-C_{30}-C_{34} in the 12.0 ka horizon and *n*-C_{28} in the 18.3 ka horizon. Following the first condition, this also constrains σ_{mill} to values greater than ~1500 cal yr. Thus, the combined result of both conditions is a millennial component with a very wide continuous distribution of ages and average age of at least several millennia, as depicted in Figure 2c. This model is reasonable given the absence of any known non-fossil terrestrial reservoirs that both (1) have millennial ages with narrow age distributions and (2) can be accessed without some input of fresher carbon. For instance, deep soil carbon cannot easily be eroded and transported without some contribution from shallower layers.

We note that the possibility exists that there are two or more components of distinct age distributions within the millennial pool, particularly for anomalously low Holocene samples. In

this case, additional components could be added to equations (10) and (11). However, adding one extra component introduces 3 additional free parameters (ratio of contributions from two millennial components, age offset and standard deviation of additional component) to an already under-constrained system. We therefore opt to restrict our model to two components to limit the number of parameters that must be specified. Another possible exception to the conditions of our model is the case when the millennial fraction is completely radiocarbon dead, either due to fossil carbon input or extremely old soil carbon. Although we consider both scenarios unlikely, the fractional contribution of a uniformly radiocarbon dead millennial pool can be calculated as:

$$f_{mill,dead} = 1 - \frac{F^{14}R_{wax}}{F^{14}R_{dec}} \quad (12)$$

and represents the minimum possible millennial fraction.

Calculated decadal (f_{dec}) and millennial (f_{mill}) fractions corresponding to reported *n*-C_{28}-C_{34} $F^{14}R_{wax}$ values for a range of theoretical wax age structures are shown in Figure 5. Scenarios 1-3 correspond to millennial age standard deviation (σ_{mill}) of 2500, 5000, and 10,000 years, respectively, in the permitted range ($0 \leq \mu_{mill} \leq 2\sigma_m$, millennial average age > 3000 y). For all scenarios, we set μ_{dec} to 0 (i.e., same age as sediment) and σ_{dec} to 20 years, as f_{dec} and f_{mill} are relatively insensitive to changes in the decadal pool age offset and distribution. This insensitivity results from (1) the absence of large changes in ^{14}C activity on decadal timescales in the pre-bomb atmosphere and (2) the very small change in ^{14}C content of waxes due to decay on decadal timescales. The results show that as expected, f_{mill} values for all sediment horizons generally increase with decreasing $F^{14}R_{wax}$ across all values of μ_m and σ_m. One exception to this rule is f_{mill} values for the 5.3 and 18.4 ka horizons for low millennial fraction average ages (< ~5000 y). These samples have very similar *n*-C_{28}-C_{34} $F^{14}R_{wax}$ values (0.85 and 0.86, respectively) but the

significant difference in atmospheric ^{14}C activity in the millennia preceding deposition of these two sediment horizons inverts the expected order of f_{mill} values.

4.5.4 Constraints on wax age structure from wax $\delta^{13}C$

In order to further constrain the age distribution of waxes, we next simulate the effects of different wax age structures on wax $\delta^{13}C$ signals using estimates of C_3/C_4 vegetation composition from Cariaco pollen records (Delusina, unpublished; González et al., 2008). We then compare these results to existing wax $\delta^{13}C$ records to find which millennial age structures produce simulated $\delta^{13}C$ patterns most similar to actual data. For these simulations, we assume C_3/C_4 pollen abundance is a good proxy for the ratio of fresh waxes produced by C_3/C_4 vegetation in the Cariaco catchment. This assumption is supported by strong correlations between pollen and leaf wax $\delta^{13}C$ data observed in Chapter 3 of this thesis. We also assume that pollen grains are delivered to the sediments rapidly and that any pollen grains that have been retained on land for extended periods of time either show sufficient signs of degradation to be excluded from analysis or form only very minor components of the sedimentary pollen mixture. This assumption is reasonable given high rates of visible damage to pollen grains subjected to repeated wet-dry cycles as would be experienced in tropical soils (Campbell, 1991). Moreover, pollen grains cannot be stabilized on mineral surfaces like organic compounds in soils. Comparison of pollen radiocarbon ages and independently dated sediment layers has shown mixed results, with some pollen ages matching that of a proximal ash layer (Brown et al., 1989) and others showing significant pre-aging of pollen grains compared to foraminifera dates (Neulieb et al., 2013). Nonetheless, uncertainty in vegetation reconstructions resulting from minor contributions of

reworked pollen is likely insignificant compared to the large vegetation change signal during this period.

We focus simulations on 19.3-10 ka, a period of multiple abrupt and large climate transitions and an interval for which both high-resolution wax $\delta^{13}C$ and pollen data are available. However, we incorporate pollen data from 70-30 ka (González et al., 2008) in order to represent the $\delta^{13}C$ composition of the millennial fraction as accurately as possible. We convert pollen-based C_3/C_4 ratios to $\delta^{13}C$ values using typical C_4 and C_3 endmember values of -22‰ and -36‰ (Chikaraishi et al., 2004). For the missing section (~28-20 ka) of the pollen record, we construct an artificial pollen $\delta^{13}C$ curve including a C_4 excursion during H2 (~24.5-23.5 ka) of similar scale to previous Heinrich events (+3.2‰) and a baseline value equal to the 70-30 ka average excluding Heinrich events (-31.5‰). Following equation (11), we calculate the expected $\delta^{13}C$ signal of waxes in a sediment horizon with age t_0 according to the equation:

$$\delta^{13}C(t_0) = f_{dec} \cdot \sum_{t=t_0}^{\infty} p_{dec}(t) \cdot \delta^{13}C(t) + f_{mill} \cdot \sum_{t=t_0}^{\infty} p_{mill}(t) \cdot \delta^{13}C(t) \quad (13)$$

Furthermore, we use *n*-C_{28}-C_{34} $F^{14}R_{wax}$ values to calculate f_{dec} and f_{mill} for each combination of offset (μ_{mill}) and standard deviation (σ_{mill}) of the millennial fraction. We assume that the age structure of millennial fraction (i.e., μ_{mill} and σ_{mill} values) remains constant for all samples from 19.3-10 ka and that $F^{14}R_{wax}$ values of samples are representative of their respective climate interval (e.g., late glacial, H1, BA, YD, Preboreal).

Predicted wax $\delta^{13}C$ curves for eight representative scenarios are shown in Figure 6, along with actual wax (*n*-C_{32} fatty acid) $\delta^{13}C$ variability from Hughen et al. (2004a) and Drenzek (2007). Parameters for each scenario are provided in Table 3. We plot $\delta^{13}C$ deviations from mean $\delta^{13}C$ values from 19.3-10 ka for both predicted and actual curves to remove any offsets in

absolute $\delta^{13}C$ related to either our choice of C_3/C_4 end member $\delta^{13}C$ values or different plant production rates of pollen versus *n*-C_{32} fatty acid.

The results of our simulations show that wax age structure controls the predicted $\delta^{13}C$ signal by modulating both the timing and amplitude of $\delta^{13}C$ variability. We observe significant time lags between predicted and actual $\delta^{13}C$ signals during intervals corresponding to wax mixtures with high f_{mill} values (> ~0.5). This effect is most apparent during the transition from the late glacial period to H1 in Scenarios 1a, 1b, and 2a, which have the three youngest millennial pools and thus the largest contributions from the millennial pool. The amplitude of simulated $\delta^{13}C$ variability generally increases with increasing age of the millennial fraction and decreasing millennial contribution to the wax mixture. To compare the amplitudes of predicted $\delta^{13}C$ variability for different scenarios, we calculate average $\delta^{13}C$ shifts for the four distinct climate transitions from the late glacial to Preboreal period (Table 4). It should be noted that calculated $\delta^{13}C$ shifts in the case of a radiocarbon dead millennial pool (Scenario 4) depend on the assigned $\delta^{13}C$ composition of the dead carbon pool. For our simulation, we used the average of all *n*-C_{32} $\delta^{13}C$ measurements for the period 188-50 ka (-31‰) (Drenzek, 2007), but the amplitude of average $\delta^{13}C$ shifts can vary by ± 25% from simulations run with end member $\delta^{13}C$ values. We assess the fit of each scenario by calculating the sum of square errors (distances) of predicted $\delta^{13}C$ shifts from the perfect fit line ($\Delta_{predicted} = \Delta_{measured}$) according to the equation:

$$SSE = \left(\Delta_{YD/PB} - \Delta_{YD/PB,m}\right)^2 + \left(\Delta_{BA/YD} - \Delta_{BA/YD,m}\right)^2 + \left(\Delta_{H1/BA} - \Delta_{H1/BA,m}\right)^2 + \left(\Delta_{LG/H1} - \Delta_{LG/H1,m}\right)^2 \qquad (14)$$

where Δ is the absolute value of the difference of average $\delta^{13}C$ values for each set of consecutive intervals and the subscript m denotes the measured value. Using this metric, we find that Scenarios 2b and 3a (millennial average ages of 6436 and 7956 cal yr, respectively) best

approximate the scale of measured $\delta^{13}C$ variability. Millennial fractions in these scenarios are also low enough (0.15-0.46) to eliminate significant time lags between measured and predicted $\delta^{13}C$ variability.

While the exact age structure of the millennial fraction cannot be determined without additional constraints on μ_{mill} and σ_{mill}, our representative simulations allow us to draw several important conclusions. First, our simulations show that from 20-10 ka the majority (~55-90%) of waxes in Cariaco sediments are of decadal age, with a smaller fraction contributed by a very old millennial pool. Furthermore, we can constrain the average age of this millennial fraction to >5000 cal yr to preserve the timing of observed $\delta^{13}C$ variability. We further posit that this requires a very broad millennial age distribution (σ_{mill} > ~3000 cal yr) given that all non-fossil terrestrial reservoirs of waxes contain mixtures of young and old carbon.

4.5.5 Relationships between past climate variability and wax age structure

We observe a clear relationship between past hydrologic variability in northern Venezuela and wax age structure over the past 20 ka (Figure 7). The lowest *n*-C_{28}-C_{34} $F^{14}R_{wax}$ values occur during intervals for which there is evidence of drier conditions (H1, YD, mid-Holocene dry event, late Holocene). Correspondingly, modeled contributions from the decadal wax pool are lower in these horizons (Figure 7). Moreover, in Figure 4, samples on the main mixing line generally follow a trajectory from wetter interval samples (high concentration, high $F^{14}R_{wax}$ values) to drier interval samples (low concentration, low $F^{14}R_{wax}$ values). This pattern suggests that wetter conditions favored increased delivery of fresh waxes to marine sediments on top of a relatively constant background millennial wax pool. Increased precipitation in the Cariaco catchment could act through either biological or physical mechanisms, or a combination

of both, to increase the flux of fresh waxes to sediments. In the biological scenario, wetter conditions could increase wax production and stocks in the catchment by driving increased vegetation growth/density, resulting in increased fresh organic carbon export without any change in the efficiency of wax transport to the ocean. In the physical scenario, increased precipitation and overland flow could increase the fraction of fresh waxes material delivered to sediments through enhanced erosion and fluvial transport. However, following the model of fresh carbon addition to a constant old background, changes in precipitation would not significantly affect the mobilization and delivery rates of millennial waxes. This mechanism is plausible given the higher sensitivity of surface reservoirs containing fresh waxes (standing vegetation, leaf litter, surface soil horizons) to changes in hydrology and overland flow compared to deeper soil horizons containing old waxes.

To distinguish between these possible mechanisms, we can use the results of our wax age structure modeling to estimate the magnitude of changes in fresh wax export from wet to dry periods. Using the age structure parameters that best fit observed $\delta^{13}C$ variability (Scenarios 2b and 3a in Section 5.4) for the YD and BA as representative dry and wet periods, respectively, we calculate that decadal wax delivery to sediments decreased by more than a factor of 3 from the BA to the YD assuming constant mass and age structure of the millennial fraction. Since a >300% decline in vegetation density between these two periods is unrealistic given the limited change in vegetation composition in the pollen record, changes in erosion and fluvial sediment transport are more likely to be the dominant controls on delivery of fresh terrestrial material to Cariaco sediments. Erosion control of fresh wax delivery is consistent with an observed global correlation between riverine suspended sediment yield and exported fraction of terrestrial biospheric carbon (Galy et al., 2015). According to this relationship, a 3-fold increase in

biospheric carbon export would require an increase in suspended sediment yield by roughly an order of magnitude. Such an increase in sediment yield would only require a ~3.5-4-fold increase in runoff based on observed relationships between runoff and sediment yield for low elevation (100-1000 m) rivers (Milliman and Syvitski, 1992). This scale of runoff variability is plausible considering the large interannual variability observed in northern South American river discharge records even over the last century (Hastenrath, 1990). Thus, we posit that the primary relationship between wax age structure and precipitation reflects hydrologic control of the efficiency of erosion and transport of fresh terrestrial material to marine sediments.

While thus far we have considered a variable fresh component on top of an unchanging millennial background, the different behavior of glacial and Holocene samples in Figure 4 also provides evidence of a shift in the age/concentration of old wax fractions exported to sediments. The two anomalously low Holocene $F^{14}R_{wax}$ values at 7.7 and 1.3 ka suggest that more concentrated and/or older millennial wax pools were accessible during Holocene dry periods. The presence of such pools could reflect increased refractory soil carbon stocks in the Holocene, but the buildup of refractory soil carbon stocks under overall wetter and warmer conditions is at odds with the expected influence of climate on organic carbon decomposition rates in soils (e.g., Carvalhais et al., 2014). Moreover, the low $F^{14}R_{wax}$ value at 7.7 ka requires substantial contribution from waxes that predate the Holocene. Changes in the Cariaco catchment due to the ~120 m rise in sea level from the LGM to the Holocene (Siddall et al., 2003) also do not appear to have played a major role, as samples from the interval of fastest sea level rise (~15-9 ka) do not show any deviation from the main mixing line. Thus, the most plausible mechanism is some shift in physical erosion and river transport pathways that increased mobilization of very old waxes from deeper soil horizons. This could be caused by an increase in the frequency of deep

soil erosion episodes or riverbank failure due to more seasonal or irregular precipitation during the drier intervals of a generally warmer and wetter Holocene.

In contrast to evidence of hydrologic forcing, we note that there does not appear to be any direct influence of glacial-interglacial temperature change on the age structure of waxes at Cariaco Basin. This minimal influence of temperature change on wax ages is consistent with a synthesis of global data that generally shows precipitation to be the more important control of terrestrial carbon turnover at low latitudes (Carvalhais et al., 2014). Moreover, even with ~2-4°C of glacial cooling, the Cariaco catchment with a modern MAT of ~25°C likely remained relatively warm throughout the past 20 ka. Thus, any effects of temperature change on soil carbon turnover at Cariaco were likely dampened due to the lower temperature sensitivity of decomposition rates at high temperatures (Davidson and Janssens, 2006).

4.6 Conclusions

This study represents the first application of compound-specific radiocarbon analysis in the context of a well-characterized tropical climate record to investigate the age of terrestrial biomarkers as a function of past climate. We find that the average age of leaf waxes in Cariaco sediments over the past 20 kyr is consistently on the order of centuries to millennia. However, we also show that waxes of decadal ages generally constitute a dominant fraction of total waxes in addition to some fraction of very old (millennial) waxes. This age distribution of waxes preserves temporal signals in Cariaco wax $\delta^{13}C$ records but contributes to some dampening of the amplitude of $\delta^{13}C$ shifts. Overall, our results are encouraging for the accuracy of biomarker-based paleoclimate reconstructions if wax age structures do not vary significantly in different geographic and climatic settings. However, differences in aboveground and belowground carbon stocks, as well as slower rates of soil decomposition rates in temperate and boreal climates (e.g.,

Trumbore, 2000) likely increase contributions from old wax pools in higher latitude regions. Further studies at different sites will help to elucidate the controls of wax age distributions and the effects of different sources of waxes on paleoclimate records.

The observed links between the age of waxes and past climate change at this site suggest that past hydrologic change modulated the export of fresh waxes to the ocean. If other components of terrestrial organic matter behave similarly to waxes, this pattern carries important implications for the interaction between the terrestrial carbon cycle and the global climate system. Increased export and burial of terrestrial organic matter in marine sediments in wetter climates would represent a larger carbon sink and negative climate feedback on geologic timescales. On shorter timescales, however, the direction of this feedback hinges on the balance between increased carbon burial in marine sediments (carbon sink) and any increases in respiration associated with mobilization of terrestrial organic carbon out of soils (carbon source). The magnitude of the latter effect further depends on relative rates of terrestrial organic carbon decomposition in soils versus rivers, estuaries, and marine settings, which remain an open question (e.g., Cai et al., 2011). In either case, hydrologic forcing of biospheric carbon export to the ocean may play a significant role in the long-term response of the terrestrial carbon cycle to a more intense global water cycle in a warmer world (IPCC, 2013). This effect will be particularly important in tropical regions where the relative magnitude of hydrologic change often outweighs that of temperature change.

Acknowledgements

This chapter is co-authored by Valier Galy, Konrad Hughen, and Irina Delusina (UC Davis). I thank the NOSAMS staff, especially Ann McNichol and Al Gagnon, for their help with

radiocarbon sample preparation and analysis. This work was supported by an EPA STAR fellowship and WHOI Coastal Ocean Institute grant to K.L.F.

References

Amundson, R., 2001. The carbon budget in soils. Annu. Rev. Earth Planet. Sci. 29, 535–562.

Binford, M.W., 1982. Ecological History of Lake Valencia, Venezuela: Interpretation of Animal Microfossils and Some Chemical, Physical and Geological Features. Ecol. Monogr. 52, 307-333.

Broccoli, A., 2000. Tropical cooling at the Last Glacial Maximum: An atmosphere-mixed layer ocean model simulation. J. Clim. 13, 951–976.

Brown, T.A., Nelson, D.E., Mathewes, R.W., Vogel, J.S., Southon, J.R., 1989. Radiocarbon dating of pollen by accelerator mass spectrometry. Quat. Res. 32, 205–212.

Cai, W.-J., 2011. Estuarine and Coastal Ocean Carbon Paradox: CO2 Sinks or Sites of Terrestrial Carbon Incineration? Ann. Rev. Mar. Sci. 3, 123-145.

Campbell, I.D., 1991. Experimental Mechanical Destruction of Pollen Grains. Palynology 15, 29–33.

Carvalhais, N., Forkel, M., Khomik, M., Bellarby, J., Jung, M., Migliavacca, M., Mu, M., Saatchi, S., Santoro, M., Thurner, M., Weber, U., Ahrens, B., Beer, C., Cescatti, A., Randerson, J.T., Reichstein, M., 2014. Global covariation of carbon turnover times with climate in terrestrial ecosystems. Nature 514, 213-217.

Chikaraishi, Y., Naraoka, H., Poulson, S., 2004. Hydrogen and carbon isotopic fractionations of lipid biosynthesis among terrestrial (C_3, C_4 and CAM) and aquatic plants. Phytochemistry 65, 1369–1381.

Conte, M., Weber, J., 2002. Plant biomarkers in aerosols record isotopic discrimination of terrestrial photosynthesis. Nature 417, 639–641.

Curtis, J.H., Hodell, D.A., Brenner, M., 1999. Climate change in the Lake Valencia Basin, Venezuela, |12600 yr BP to present. The Holocene 9, 609–619.

Davidson, E.A., Janssens, I.A., 2006. Temperature sensitivity of soil carbon decomposition and feedbacks to climate change. Nature 440, 165–173.

de Camargo, P.B., Trumbore, S.E., Martinelli, L.A., Davidson, E.A., Nepstad, D.C., Victoria, R.L., 1999. Soil carbon dynamics in regrowing forest of eastern Amazonia. Glob. Change Biol. 5, 693–702.

Delusina, I. Unpublished data.

Douglas, P.M.J., Pagani, M., Eglinton, T.I., Brenner, M., Hodell, D.A., Curtis, J.H., Ma, K.F., Breckenridge, A., 2014. Pre-aged plant waxes in tropical lake sediments and their influence on the chronology of molecular paleoclimate proxy records. Geochim. Cosmochim. Acta 141, 346–364.

Drenzek, N.J., 2007. The temporal dynamics of terrestrial organic matter transfer to the oceans: initial assessment and application. PhD Thesis. MIT/WHOI Joint Program in Oceanography/Applied Ocean Science & Engineering.

Eglinton, G., Hamilton, R., 1967. Leaf epicuticular waxes. Science 156, 1322.

Eglinton, T.I., Aluwihare, L., Bauer, J., Druffel, E., McNichol, A., 1996. Gas chromatographic isolation of individual compounds from complex matrices for radiocarbon dating. Anal.

Chem. 68, 904–912.
Elmore, A.C., Thunell, R.C., Styles, R., Black, D., Murray, R.W., Martinez, N., Astor, Y., 2009. Quantifying the seasonal variations in fluvial and eolian sources of terrigenous material to Cariaco Basin, Venezuela. J. S. Am. Earth Sci. 27, 197–210.
Farrera, I., Harrison, S., Prentice, I., Ramstein, G., Guiot, J., Bartlein, P., Bonnefille, R., Bush, M., Cramer, W., Grafenstein, Von, U., 1999. Tropical climates at the Last Glacial Maximum: a new synthesis of terrestrial palaeoclimate data. I. Vegetation, lake-levels and geochemistry. Clim. Dyn. 15, 823–856.
Galy, V., Eglinton, T., 2011. Protracted storage of biospheric carbon in the Ganges-Brahmaputra basin. Nature Geosci. 4, 843–847.
Galy, V., Peucker-Ehrenbrink, B., Eglinton, T., 2015. Global carbon export from the terrestrial biosphere controlled by erosion. Nature 521, 204–207.
González, C., Dupont, L., Behling, H., Wefer, G., 2008. Neotropical vegetation response to rapid climate changes during the last glacial period: Palynological evidence from the Cariaco Basin. Quat. Res. 69, 217–230.
Gustafsson, O., van Dongen, B.E., Vonk, J.E., Dudarev, O.V., Semiletov, I.P., 2011. Widespread release of old carbon across the Siberian Arctic echoed by its large rivers. Biogeosciences 8, 1737–1743.
Hastenrath, S., 1990. Diagnostics and Prediction of Anomalous River Discharge in Northern South America. J. Clim. 3, 1080–1096.
Haug, G., Hughen, K., Sigman, D., Peterson, L., Röhl, U., 2001. Southward migration of the Intertropical Convergence Zone through the Holocene. Science 293, 1304-1308.
Hughen, K., Eglinton, T., Xu, L., Makou, M., 2004a. Abrupt tropical vegetation response to rapid climate changes. Science 304, 1955-1959.
Hughen, K., Lehman, S., Southon, J., Overpeck, J., Marchal, O., Herring, C., Turnbull, J., 2004b. ^{14}C activity and global carbon cycle changes over the past 50,000 years. Science 303, 202–207.
Hughen, K., Southon, J., Lehman, S., Bertrand, C., Turnbull, J., 2006. Marine-derived ^{14}C calibration and activity record for the past 50,000 years updated from the Cariaco Basin. Quat. Sci. Rev. 25, 3216–3227.
IPCC, 2013. *Climate Change 2013: The Physical Science Basis. Contribution of Working Group I to the Fifth Assessment Report,* T.F. Stocker, et al., Eds., Cambridge University Press.
Kusch, S., Rethemeyer, J., Schefuß, E., Mollenhauer, G., 2010. Controls on the age of vascular plant biomarkers in Black Sea sediments. Geochim. Cosmochim Acta 74, 7031–7047.
Lea, D., Pak, D., Peterson, L., Hughen, K., 2003. Synchroneity of tropical and high-latitude Atlantic temperatures over the last glacial termination. Science 301, 1361.
Mannino, A., Harvey, H., 1999. Lipid composition in particulate and dissolved organic matter in the Delaware Estuary: sources and diagenetic patterns. Geochim. Cosmochim. Acta 63, 2219–2235.
Martinez, N., Murray, R., Thunell, R., Peterson, L., Muller-Karger, F., Astor, Y., Varela, R., 2007. Modern climate forcing of terrigenous deposition in the tropics (Cariaco Basin, Venezuela). Earth Planet. Sci. Lett. 264, 438–451.
Martinez, N.C., Murray, R.W., Thunell, R.C., Peterson, L.C., Muller-Karger, F., Lorenzoni, L., Astor, Y., Varela, R., 2012. Local and regional geochemical signatures of surface sediments from the Cariaco Basin and Orinoco Delta, Venezuela. Geology 38: 159-162.
Mathieu, J.A., Hatté, C., Balesdent, J., Parent, É., 2015. Deep soil carbon dynamics are driven

more by soil type than by climate: a worldwide meta-analysis of radiocarbon profiles. Glob. Change Biol. 21, 4278–4292.
Meckler, A.N., Haug, G.H., Sigman, D.M., Plessen, B., Peterson, L.C., Thierstein, H.R., 2007. Detailed sedimentary N isotope records from Cariaco Basin for Terminations I and V: Local and global implications. Global Biogeochem. Cycles 21, GB4019.
Mikutta, R., Kleber, M., Torn, M.S., Jahn, R., 2006. Stabilization of Soil Organic Matter: Association with Minerals or Chemical Recalcitrance? Biogeochemistry 77, 25–56.
Milliman, J., Syvitski, J., 1992. Geomorphic/tectonic control of sediment discharge to the ocean: the importance of small mountainous rivers. J. Geol. 100, 525–544.
Neulieb, T., Levac, E., Southon, J., Lewis, M., Pendea, I.F., Chmura, G.L., 2013. Potential Pitfalls of Pollen Dating. Radiocarbon 55, 1142–1155.
Peterson, L., Haug, G., 2006. Variability in the mean latitude of the Atlantic Intertropical Convergence Zone as recorded by riverine input of sediments to the Cariaco Basin (Venezuela). Palaeogeogr. Palaeoclimatol. Palaeoecol. 234, 97–113.
Peterson, L., Haug, G., Hughen, K., Röhl, U., 2000a. Rapid changes in the hydrologic cycle of the tropical Atlantic during the last glacial. Science 290, 1947.
Peterson, L., Haug, G., Murray, R., Yarincik, K., King, J., Bralower, T., Kameo, K., Rutherford, S., Pearce, R., 2000b. Late Quaternary stratigraphy and sedimentation at site 1002, Cariaco Basin (Venezuela). In *Proceedings of the Ocean Drilling Program, Scientific Results*, Vol. 165, R.M. Leckie, H. Sigurdsson, G.D. Acton, and G. Draper, Eds., IODP, 200085–99.
Reimer, P.J., Bard, E., Bayliss, A., Beck, J.W., Blackwell, P.G., Ramsey, C.B., Buck, C.E., Cheng, H., Edwards, R.L., Friedrich, M., Grootes, P., Guilderson, T.P., Haflidason, H., Hajdas, I., Hatté, C., Heaton, T.J., Hoffmann, D.L., Hogg, A.G., Hughen, K.A., Kaiser, K.F., Kromer, B., Manning, S.W., Niu, M., Reimer, R.W., Richards, D., Scott, E.M., Southon, J.R., Staff, R.A., Turney, C.S.M., van der Plicht, J., 2013. IntCal13 and Marine13 radiocarbon age calibration curves 0-50,000 years cal BP. Radiocarbon 55, 1869–1887.
Renard, K.G., Foster, G.R., Weesies, G.A., McCool, D.K., Yoder, D.C., 1997. Predicting Soil Erosion by Water: A Guide to Conservation Planning With the Revised Universal Soil Loss Equation (RUSLE). U.S. Department of Agriculture.
Rühlemann, C., Mulitza, S., Müller, P., Wefer, G., Zahn, R., 1999. Warming of the tropical Atlantic Ocean and slowdown of thermohaline circulation during the last deglaciation. Nature 402, 511–514.
Sachse, D., Billault, I., Bowen, G.J., Chikaraishi, Y., Dawson, T.E., Feakins, S.J., Freeman, K.H., Magill, C.R., Mcinerney, F.A., Van Der Meer, M.T., Polissar, P., Robins, R.J., Sachs, J.P., Schmidt, H.-L., Sessions, A.L., White, J.W., West, J.B., Kahmen, A., 2012. Molecular Paleohydrology: Interpreting the Hydrogen-Isotopic Composition of Lipid Biomarkers from Photosynthesizing Organisms. Annu. Rev. Earth Planet. Sci. 40, 221–249.
Schmidt, M.W., Spero, H.J., Lea, D.W., 2004. Links between salinity variation in the Caribbean and North Atlantic thermohaline circulation. Nature 428, 160–163.
Shah Walter, S., Gagnon, A., Roberts, M., McNichol, A., Lardie Gaylord, M., Klein, E., 2015. Ultra-Small Graphitization Reactors for Ultra-Microscale 14C Analysis at the National Ocean Sciences Accelerator Mass Spectrometry (NOSAMS) Facility. Radiocarbon 57, 109–122.
Shakun, J.D., Carlson, A.E., 2010. A global perspective on Last Glacial Maximum to Holocene climate change. Quat. Sci. Rev. 29, 1801–1816.
Siddall, M., Rohling, E.J., Almogi-Labin, A., Hemleben, C., Meischner, D., Schmelzer, I.,

Smeed, D.A., 2003. Sea-level fluctuations during the last glacial cycle. Nature 423, 853–858.
Smittenberg, R., Eglinton, T., Schouten, S., Damsté, J., 2006. Ongoing buildup of refractory organic carbon in boreal soils during the Holocene. Science 314, 1283–1286.
Soulet, G., Skinner, L.C., Beaupré, S.R., Galy, V., 2015. A note on reporting of reservoir ^{14}C disequilibria and age offsets. Radiocarbon, in press.
Southon, J., Noronha, A.L., Cheng, H., Edwards, R.L., Wang, Y., 2012. Quaternary Science Reviews. Quat. Sci. Rev. 33, 32–41.
Tao, S., Eglinton, T.I., Montluçon, D.B., McIntyre, C., Zhao, M., 2015. Earth and Planetary Science Letters. Earth Planet. Sci. Lett. 414, 77–86.
Torn, M.S., Trumbore, S.E., Chadwick, O.A., Vitousek, P.M., Hendricks, D.M., 1997. Mineral control of soil organic carbon storage and turnover. Nature 389, 170–173.
Trumbore, S., 2000. Age of soil organic matter and soil respiration: radiocarbon constraints on belowground C dynamics. Ecol. Appl. 10, 399-411.

Table 1. Sediment horizon and sample descriptions.

Hole	Section	Top depth (cm)	Bottom depth (cm)	Total depth[1] (mbsf)	Calendar age (cal kyr BP)	Radiocarbon age (^{14}C kyr BP)	Sediment extracted (g)
1002D	1H1	65	67.5	0.663	1.34	1.46	13.1
1002D	1H1	140	142.5	1.413	3.46	3.31	19.1
1002D	1H2	55	57.5	2.063	5.29	4.91	18.6
1002E	2H1	30	32.5	2.910	7.59	6.99	26.6
1002D	1H3	95	97.5	3.963	10.42	9.59	17.8
1002E	2H2	40	47.5	4.472	11.96	10.22	45.4
1002D	2H1	55	57.5	5.263	14.10	12.22	16.8
1002E	2H3 2H4	132 0	146 6	5.987	15.40	13.03	314.2
1002E	2H5	3	9	7.922	18.30	15.23	77.0
1002E	2H5	9	15	7.990	18.41	15.42	97.4

1. 1002D equivalent depth for 1002E samples.

Table 2. Reported and calculated radiocarbon results for individual wax chain lengths.

Sample name	Sediment calendar age	Sediment ^{14}C age	Chain length	Mass C (μg)	Raw F_m	Raw F_m error	Corrected F_m	Total F_m error	Wax ^{14}C Age	Wax ^{14}C age error	$F^{14}R_{wax}$	$F^{14}R_{wax}$ error	Wax-sed ^{14}C age difference
1002D 1H1-65	1340	1460	26	24.9	0.6971	0.0044	0.789	0.024	1900	240	0.946	0.028	440
			28	12.4	0.5406	0.0078	0.652	0.049	3440	600	0.782	0.058	1980
			30-34	16.9	0.5071	0.0062	0.575	0.031	4440	430	0.690	0.037	2980
			28-34[1]	29.3	---	---	0.606	0.027	4030	360	0.727	0.032	2570
1002D 1H1-140	3460	3310	26	30.4	0.5697	0.0037	0.626	0.016	3760	210	0.945	0.024	450
			28	16.5	0.5446	0.0058	0.628	0.033	3730	420	0.949	0.049	420
			30-34	23.2	0.5100	0.0049	0.562	0.021	4630	290	0.849	0.031	1320
			28-34[1]	39.7	---	---	0.588	0.018	4260	250	0.888	0.027	950
1002D 1H2-55	5290	4910	26	25.0	0.4817	0.0056	0.529	0.019	5120	290	0.974	0.035	210
			28	15.0	0.4350	0.0062	0.489	0.033	5750	540	0.900	0.061	840
			30-34	19.4	0.4097	0.0055	0.445	0.023	6510	420	0.819	0.043	1600
			28-34[1]	34.4	---	---	0.463	0.019	6190	340	0.853	0.036	1280
1002E 2H1-30	7680	6990	26	28.5	0.3664	0.0042	0.388	0.015	7600	310	0.926	0.035	610
			28	20.5	0.2987	0.0048	0.306	0.021	9510	560	0.731	0.050	2520
			30-34	20.8	0.2421	0.0051	0.235	0.021	11640	720	0.560	0.050	4650
			28-34[1]	41.3	---	---	0.270	0.015	10520	450	0.645	0.036	3530
1002D 1H3-95	10420	9590	26	43.9	0.3094	0.0066	0.321	0.011	9130	280	1.059	0.037	-460
			28	19.3	0.2714	0.0053	0.271	0.023	10480	680	0.895	0.076	890
			30-34	20.4	0.2750	0.0060	0.275	0.022	10360	630	0.909	0.072	770
			28-34[1]	39.7	---	---	0.273	0.016	10420	460	0.902	0.052	830
1002E 2H2-40	11960	10220	26	41.5	0.2558	0.0034	0.260	0.010	10820	310	0.928	0.036	600
			28	25.4	0.2549	0.0038	0.254	0.017	11000	520	0.907	0.059	780
			30-34	27.6	0.2178	0.0038	0.210	0.015	12530	590	0.750	0.055	2310
			28-34[1]	53.0	---	---	0.231	0.011	11770	390	0.825	0.040	1550
1002D 2H1-55	14100	12220	26	34.6	0.2020	0.0041	0.197	0.012	13070	510	0.900	0.057	850
			28	15.3	0.2080	0.0061	0.183	0.032	13650	1390	0.84	0.14	1430

			30-34	32.8	0.2169	0.0034	0.212	0.013	12470	480	0.970	0.058	250
			28-34[1]	48.1	---	---	0.204	0.013	12790	510	0.932	0.059	570
1002E 2H3-132	15420	13030	28-34	25.3	0.1751	0.0043	0.158	0.018	14830	890	0.799	0.088	1800
1002E 2H5-3	18280	15230	28	28.3	0.1344	0.0042	0.113	0.016	17520	1140	0.75	0.11	2290
			30-34	37.6	0.1439	0.0032	0.130	0.012	16360	710	0.869	0.076	1130
			28-34[1]	65.9	---	---	0.123	0.0095	16830	620	0.819	0.063	1600
1002E 2H5-9	18390	15420	26	43.6	0.1316	0.0032	0.120	0.010	17030	670	0.819	0.069	1610
			28	51.5	0.1308	0.0028	0.122	0.0084	16930	560	0.829	0.057	1510
			30-34	38.0	0.1450	0.0033	0.132	0.011	16270	690	0.899	0.077	850
			28-34[1]	89.5	---	---	0.126	0.0068	16650	440	0.859	0.046	1230

1. Calculated from results for *n*-C_{28} and *n*-C_{30}-C_{34}.

Table 3. Millennial fraction parameters for $\delta^{13}C$ simulation scenarios.

Scenario		σ_{mill} (cal yr)	μ_{mill} (cal yr)	f_{mill} average age
1	a	2,500	2,500	3,217
	b	2,500	5,000	5,138
2	a	5,000	0	3,986
	b	5,000	5,000	6,436
	c	5,000	10,000	10,276
3	a	10,000	0	7,956
	b	10,000	10,000	12,874
	c	10,000	20,000	20,552
4		n/a	>50,000	>50,000

Table 4. Comparison of simulated amplitudes of $\delta^{13}C$ shifts for deglaciation climate transitions. Shifts were calculated as difference between average $\delta^{13}C$ values for each period (Preboreal, PB; Younger Dryas, YD; Bølling-Allerød, BA; H1, Heinrich Event 1; LG, late glacial). Preboreal and late glacial periods were bounded at 10 and 19.3 ka, respectively.

Scenario	1a	1b	2a	2b	2c	3a	3b	3c	4	Measured *n*-C_{32} $\delta^{13}C$
$\Delta_{YD/PB}$ (‰)	1.98	2.06	1.89	2.13	2.34	2.25	2.44	2.58	2.65	2.68
$\Delta_{BA/YD}$ (‰)	2.03	2.47	2.02	2.29	2.38	2.32	2.46	2.57	2.60	1.66
$\Delta_{H1/BA}$ (‰)	0.92	2.08	1.69	2.62	3.31	2.91	3.41	3.69	3.82	1.73
$\Delta_{LG/H1}$ (‰)	1.75	2.16	2.09	2.51	2.95	2.76	3.10	3.35	3.49	3.48
SSE	4.28	2.90	2.67	2.43	3.41	2.53	3.67	4.69	5.24	---

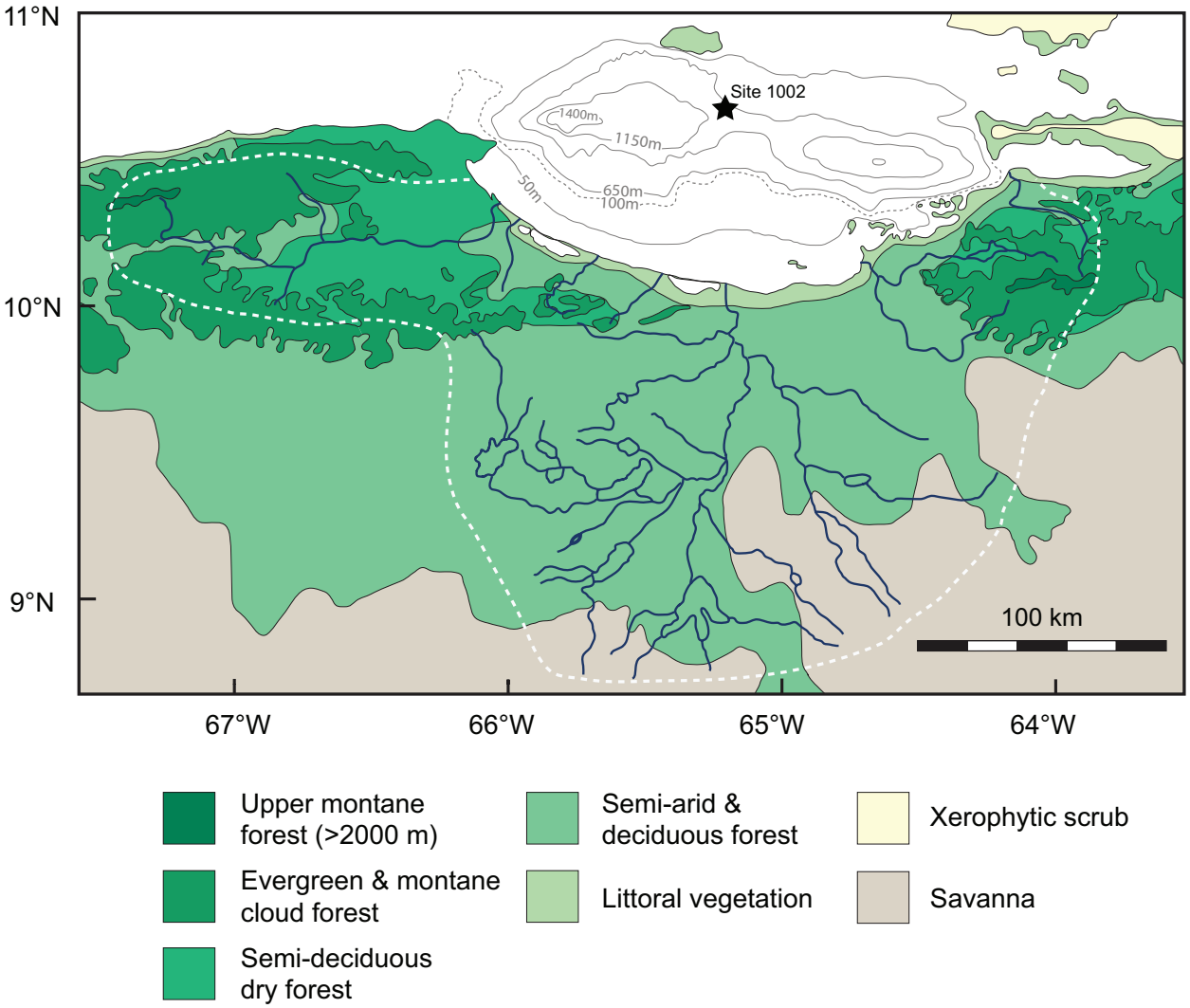

Figure 1. Map of Cariaco Basin catchment with major rivers and vegetation groups (adapted from Gonzalez et al, 2008). White dashed line indicates approximate extent of catchment area. Gray dashed bathymetric contour indicates approximate extent of Unare Platform, and black star shows location of core site 1002 (ODP Leg 165).

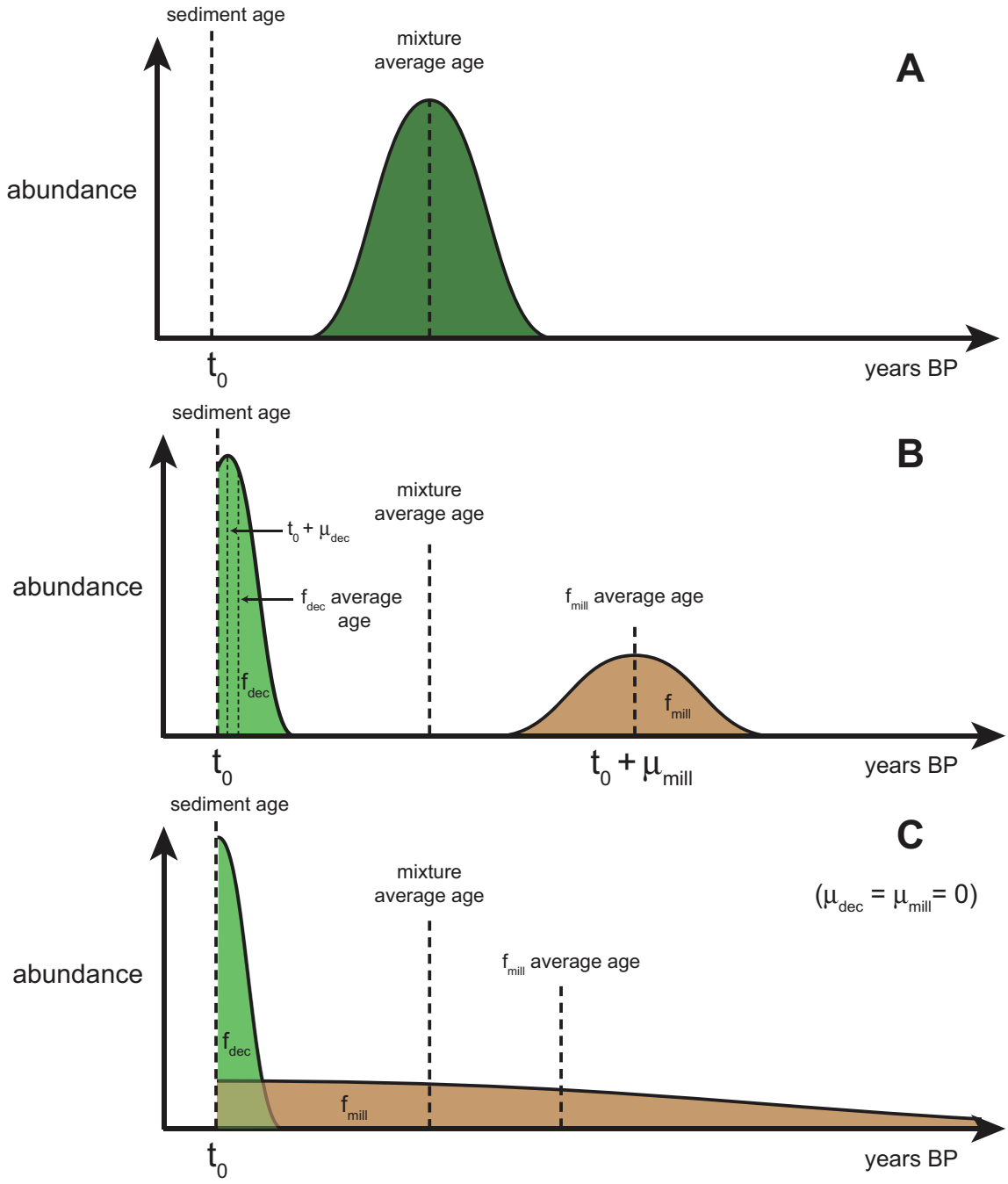

Figure 2. Schematic of three theoretical age distributions of wax mixtures. A. Single component model in which all waxes are distributed evenly around one age. B, C. Binary model in which wax mixture consists of two normally distributed components of decadal age (f_{dec}) and millennial age (f_{mill}) with a narrow (B) or wide age distribution (C). Decadal and millennial fraction age distributions are centered on age offsets μ_{dec} and μ_{mill} relative to sediment deposition age (t_o) with standard deviations σ_{dec} and σ_{mill}, respectively.

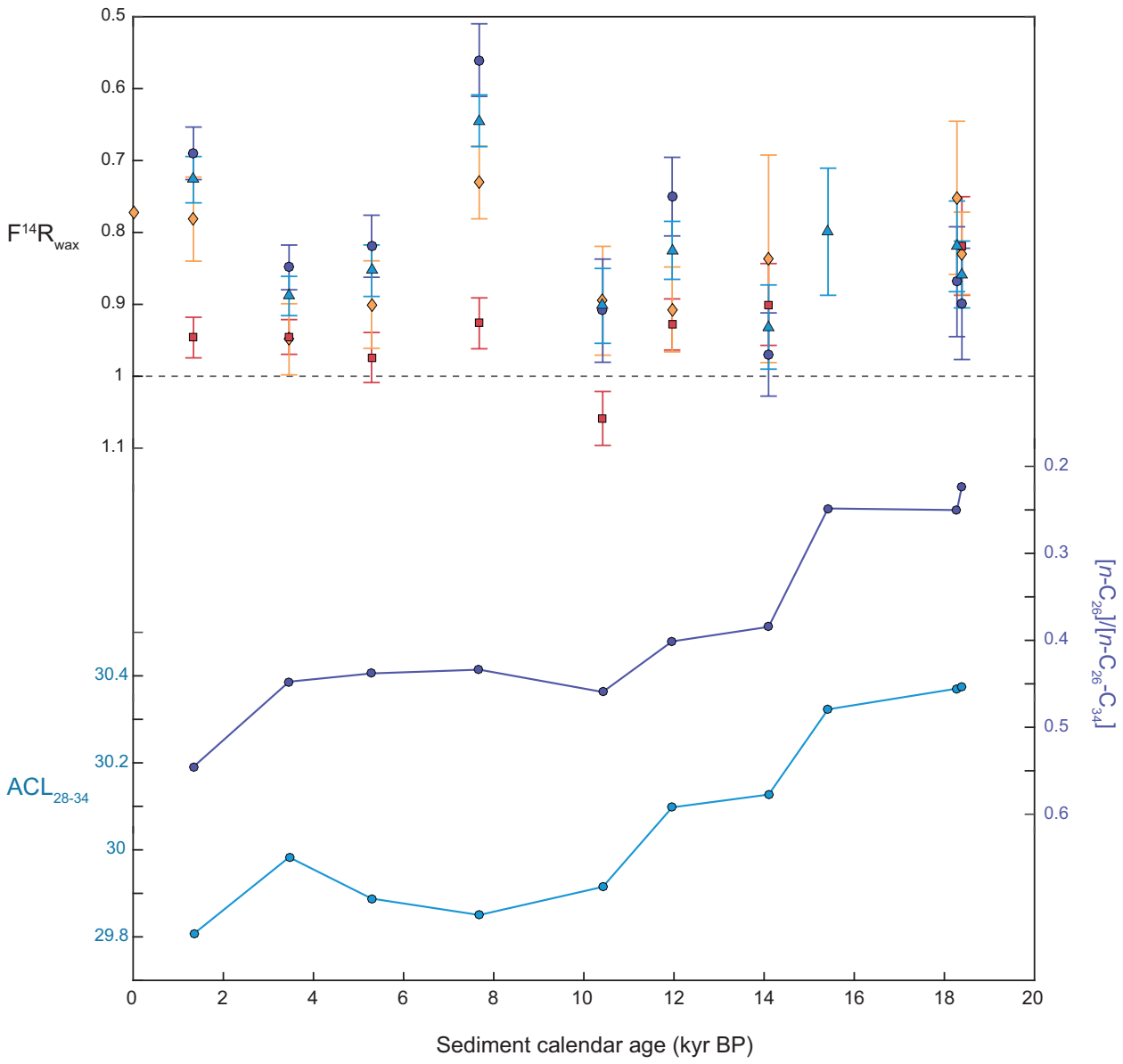

Figure 3. (Top) Time series of Cariaco *n*-alkanoic acid $F^{14}R_{wax}$ values vs. sediment horizon age, including *n*-C_{26} (red squares), *n*-C_{28} (orange diamonds), *n*-C_{30}-C_{34} (purple circles), and weighted average of *n*-C_{28}-C_{34} (blue triangles). Error bars represent 1σ analytical uncertainty. *n*-C_{28} $F^{14}R_{wax}$ value at 4 cal yr BP is derived from compound-specific ^{14}C data for 1946 sediment horizon of core MC 5 raised from a depth of 305 m in the eastern sub-basin of the Cariaco trench (Drenzek, 2007). (Bottom) Time series of relative abundance of *n*-C_{26} (purple) and average chain length of *n*-C_{28}-C_{34} (blue).

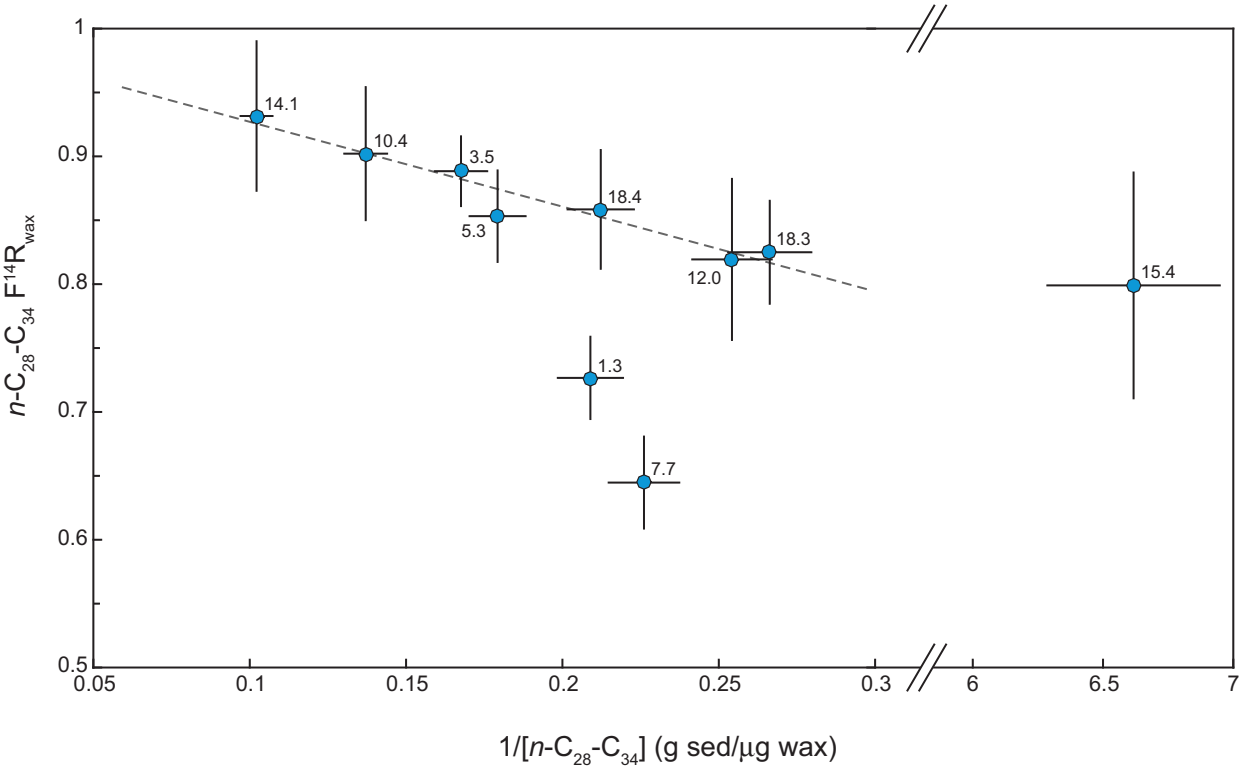

Figure 4. Plot of n-C_{28}-C_{34} $F^{14}R_{wax}$ values vs. inverse concentration in sediment. Concentrations were normalized for sediment $CaCO_3$ content and assumed to have an error of ±5%. Dashed line shows main mixing line. Labels denote sample sediment horizon age (calendar ka).

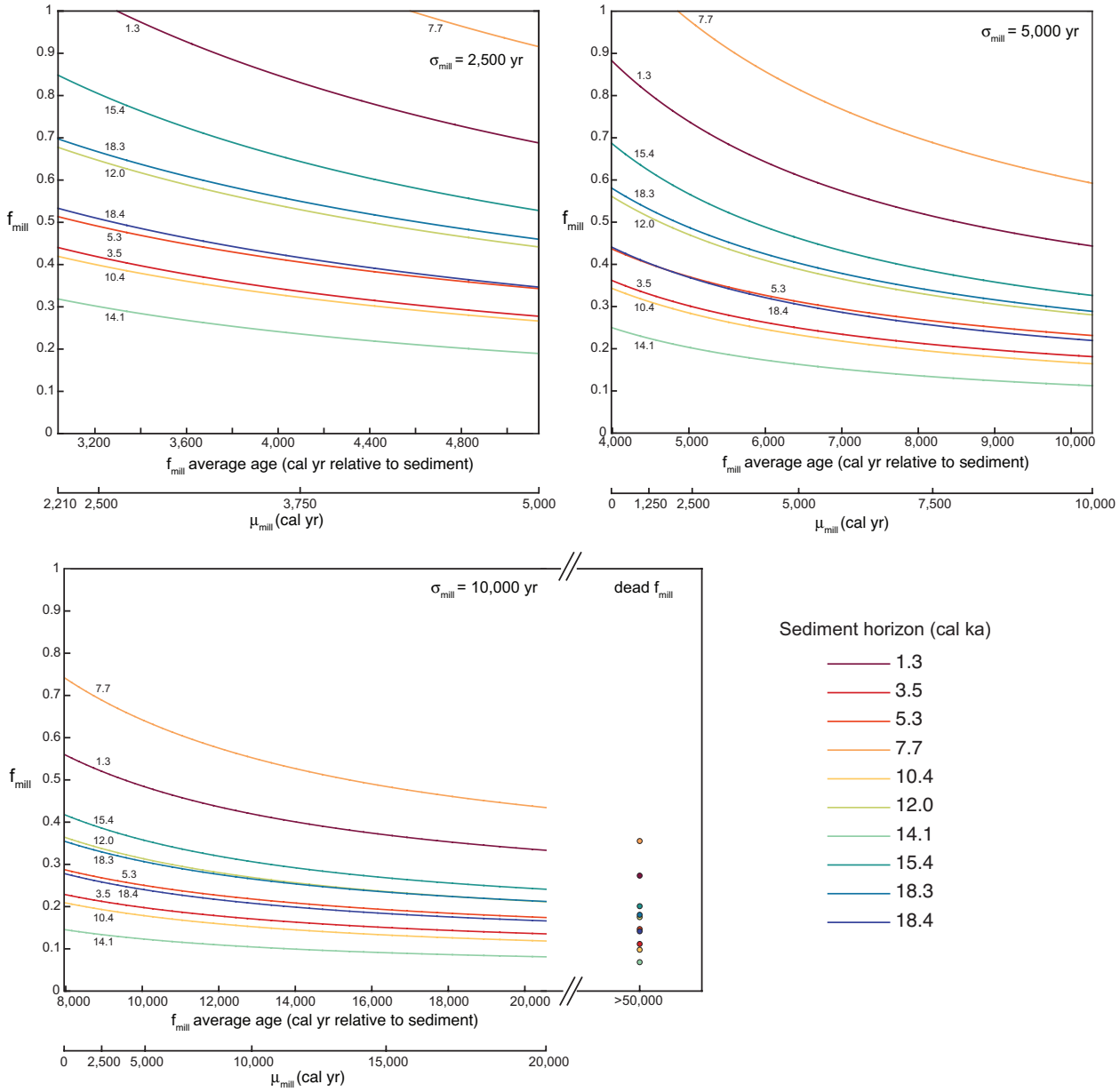

Figure 5. Calculated ranges of f_{mill} values for *n*-C_{28}-C_{34} as a function of millennial fraction average age/age offset (μ_{mill}) for different standard deviation (σ_{mill}) values. Top left: σ_{mill} = 2,500 yr, top right: σ_{mill} = 5,000 yr, bottom left: σ_{mill} = 10,000 yr, bottom right: radiocarbon dead millennial fraction end member. Lines are labeled with sample sediment horizon age for clarity.

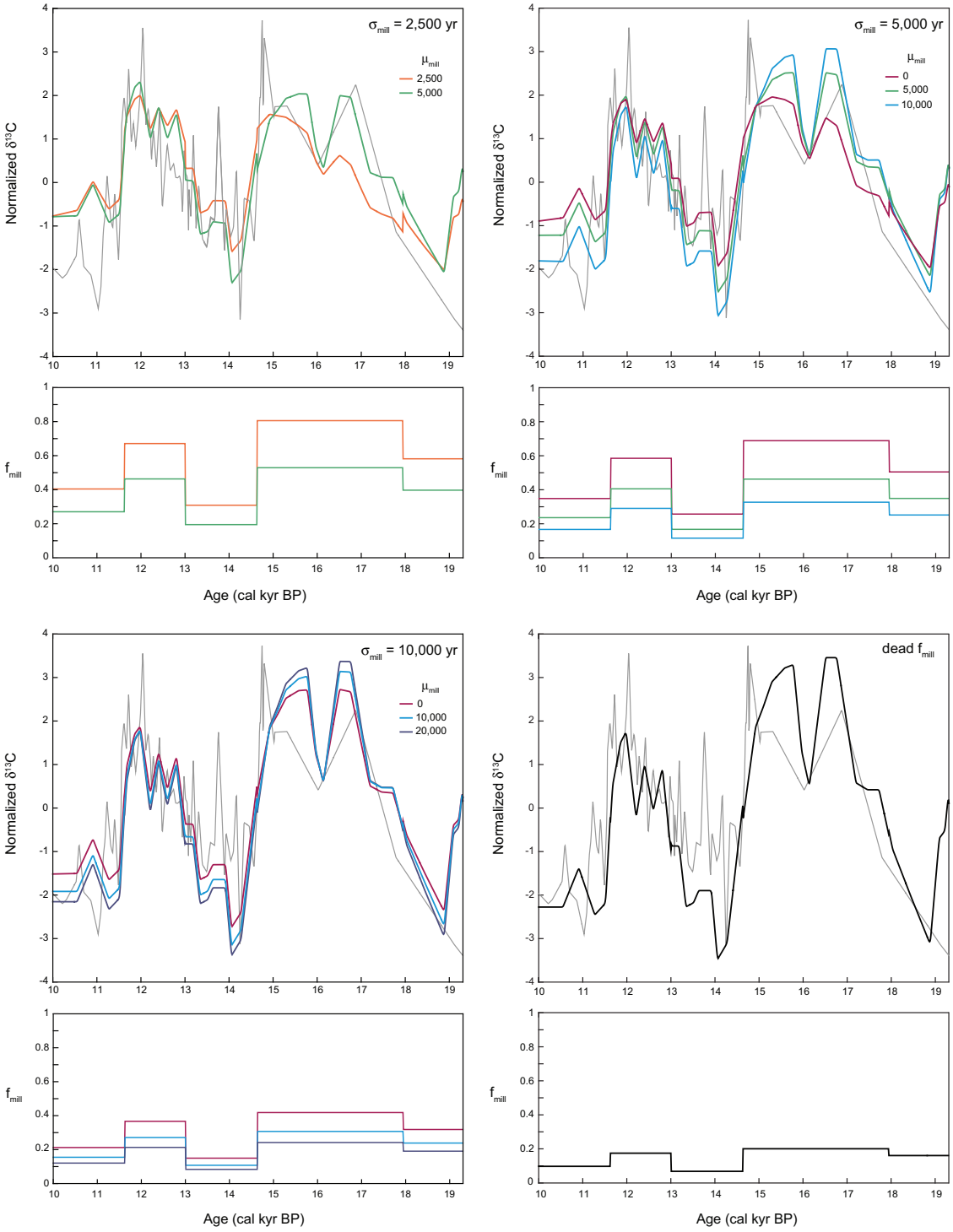

Figure 6. Predicted wax $\delta^{13}C$ curves (top panels) and f_{mill} values (bottom panels) from 20-10 ka for representative age structures scenarios as listed in Table 3. Actual *n*-C_{32} $\delta^{13}C$ data is plotted in gray for comparison. Clockwise from upper left: Scenarios 1a-b (σ_{mill} = 2,500 yr), Scenarios 2a-c (σ_{mill} = 5,000 yr), Scenario 4 (radiocarbon dead millennial fraction), Scenarios 3a-c (σ_{mill} = 10,000 yr).

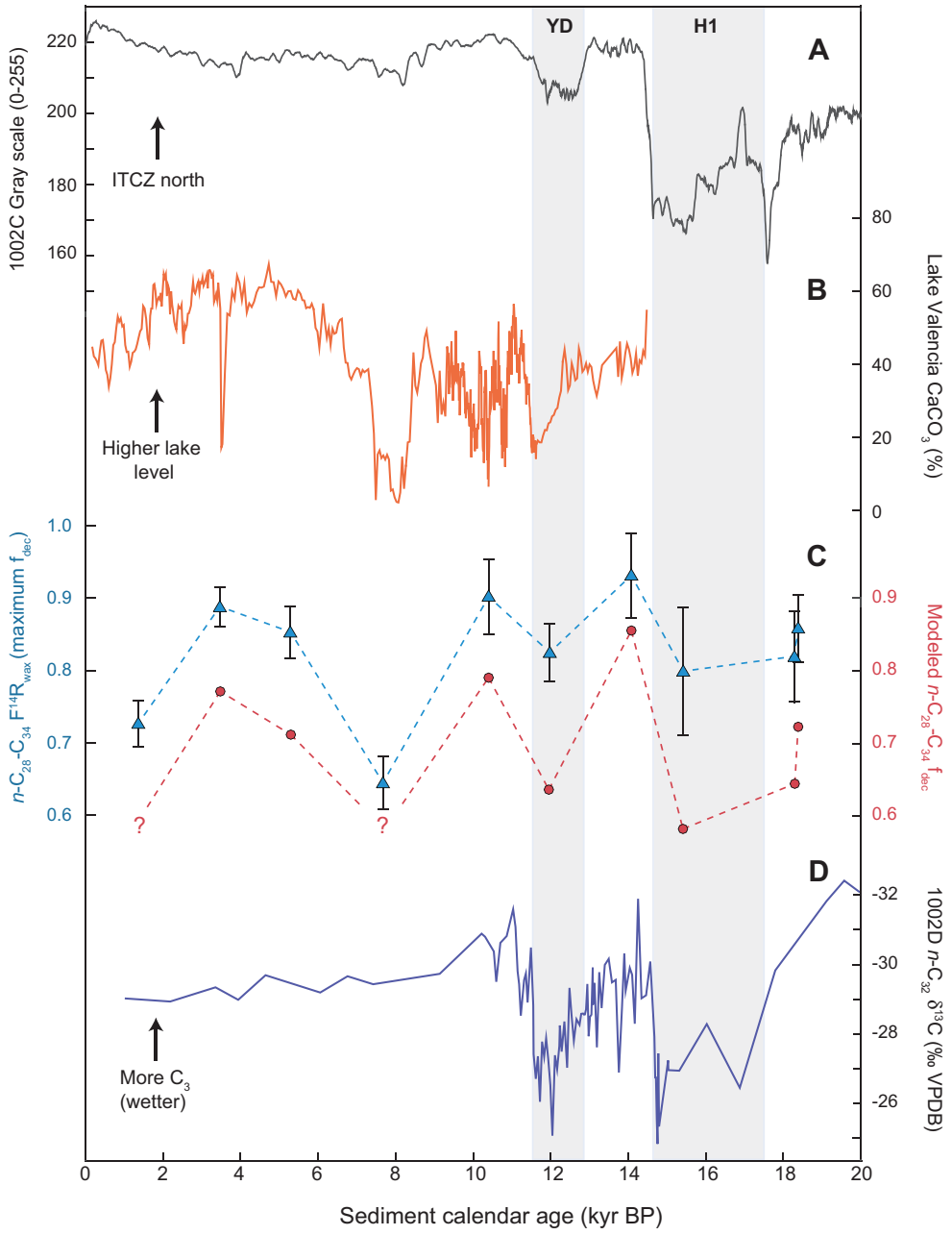

Figure 7. Comparison of *n*-C_{28}-C_{34} $F^{14}R_{wax}$ and modeled f_{dec} values with northern Venezuela climate records over the past 20 kyr. A. Percent reflectance (gray scale) data for 1002C sediments (Peterson et al., 2000a). B. Lake Valencia sediment $CaCO_3$ content (Curtis et al., 1999). Original radiocarbon age model was converted to calendar ages using Intcal13 calibration. C. *n*-C_{28}-C_{34} $F^{14}R_{wax}$ (blue triangles) and modeled f_{dec} (red circles) plotted versus sediment horizon calendar age. Note that $F^{14}R_{wax}$ is equal to the maximum possible size of the decadal fraction, which occurs in the case of a mixture between a modern decadal fraction and radiocarbon dead millennial fraction. Modeled f_{dec} values were calculated with parameters from one of the best-fit scenarios (Scenario 3a) discussed in Section 4.5.4. We do not plot modeled f_{dec} values for 7.7 and 1.3 ka horizons as these samples do not fall on the observed mixing line and could not be constrained by comparison of stable isotope/pollen data. D. *n*-C_{32} $\delta^{13}C$ from 1002D sediments (Hughen et al., 2004; Drenzek, 2007). Note that $\delta^{13}C$ axis is reversed (decreasing up). Gray shaded bars indicate timing of Younger Dryas (YD) and Heinrich Event 1 (H1) events.

Chapter 5.

Hydrologic control on terrestrial biospheric carbon export from a tropical catchment since the last glacial period II: Lake Titicaca drainage basin

Abstract

The impact of climate variability on the mobilization and transport of carbon from the terrestrial biosphere to oceans and lakes has important implications for terrestrial carbon cycle feedbacks to climate change, as well as for the reliability of terrestrial biomarker-based paleoclimate reconstructions. In this study, we use compound-specific radiocarbon analysis of terrestrial biomarkers in Lake Titicaca sediments to investigate the impacts of past climate variability on terrestrial carbon cycling over the past 20 kyr at a high-altitude tropical site. We refine the original chronology for LT01 sediment cores using radiocarbon dating of aquatic biomarkers (alkenones) and ramped oxidation-pyrolysis analysis of sediments. Radiocarbon dating of leaf waxes in modern river and downcore sediments reveals highly variable wax age structures since the last glacial period, with waxes ranging in age from <200 to >8,000 years at time of sediment deposition. Large differences in radiocarbon content among homologs further indicate the presence of multiple wax pools with distinct ages and chain length distributions. In general, wetter periods are associated with increased contribution from fresh waxes derived from vegetation, leaf litter or young soil organic matter. A large shift towards older wax ages in the

mid-Holocene also suggests mobilization of very old biospheric carbon during a prolonged period of low lake level and dry conditions. Large contributions of aged waxes likely resulted in some distortion of wax stable isotope signals, particularly in longer chain homologs. Overall, the temporal evolution of wax age structures in Lake Titicaca sediments reflects complex relationships between climate change, landscape variability, and mobilization of fresh and aged terrestrial biospheric carbon pools since the last glacial period.

5.1 Introduction

Over the last decade, compound-specific radiocarbon dating of leaf wax compounds in riverine, marine, and lacustrine sediments has provided new insight into the export of fresh and aged carbon from the terrestrial biosphere to oceans and lakes (Douglas et al., 2014; Drenzek, 2007; Galy and Eglinton, 2011; Gustafsson et al., 2011; Kusch et al., 2010; Smittenberg et al., 2006; Tao et al., 2015). These compounds, including long-chain *n*-alkanoic acids or *n*-alkanes produced as part of the waxy coatings on vascular plant leaves (Eglinton and Hamilton, 1967), are specific to higher plants and found in both fresh vegetation and aged soil reservoirs (e.g., Douglas et al., 2014). The age structure of leaf waxes thus reflects variability in the relative proportions of terrestrial biospheric carbon export derived from fresh vegetation versus aged stocks in soils, floodplains, or wetlands, as well in the age of carbon stored in these reservoirs. Such variability carries important implications for the global carbon cycle, as well as more practically for leaf wax-based paleoclimate reconstructions. The wide range of terrestrial biomarker ages observed in rivers around the world suggests that climate is an important control on terrestrial biospheric carbon storage and export (Galy and Eglinton, unpublished), thus modulating atmospheric CO_2 and setting up a potentially important climate feedback loop.

As demonstrated in the previous chapter, tracking the age structure of terrestrial biomarkers at one site through past intervals of different climate conditions provides an opportunity to explore this relationship between climate and terrestrial biospheric carbon storage/export in a relatively controlled system. Analysis of the age structure of leaf waxes in the Cariaco Basin sediment record provided evidence for a link between past hydrologic variability and transport of terrestrial biospheric carbon from tropical catchments to marine sediments over the past ~20 kyr. This chapter further explores this connection between leaf wax age structure and past climate change at a very different tropical site: the high-altitude catchment of Lake Titicaca in the Central Andes. While the Titicaca and Cariaco catchments are similar in scale, the high altitude, cool, and more sparsely vegetated Titicaca catchment provides a good contrast to the generally low relief and warm conditions at Cariaco. Moreover, the two sites experienced similar temperature trends from the last glacial period to the Holocene but opposite trends in precipitation due to their positions near the southernmost and northernmost extents of ITCZ/tropical rain belt influence, respectively. Thus, analysis of leaf wax ages in Titicaca sediments offers an opportunity to further test (1) the individual influences of hydrologic and temperature variability on the terrestrial biospheric carbon cycle and (2) potential impacts of biomarker pre-aging on stable isotope records under different conditions.

5.2 Study Site

Lake Titicaca (LT, elevation: 3810 m) is a large freshwater lake located on the South American Altiplano, an internally drained plateau situated between the western and eastern cordilleras of the Central Andes in southern tropical South America. The watershed around LT consists of a number of mountainous rivers that drain the northern Altiplano (total drainage area: 49,010 km^2) (Figure 1). Of the five major inflows to the lake, the Ramis River, which drains a

large area to the north of LT, and Ilave River, which drains the western cordillera, have the largest catchment areas. Together these rivers account for 46% of the total LT catchment (31% and 15% respectively).

The northern Altiplano has a cool, semi-arid to semi-humid climate at present, with annual precipitation of 600-800 mm/year and mean annual temperature of 7-10°C (Roche et al., 1992). At present, permanent snow cover exists in areas at or above an elevation of ~5000-5100 m, which comprise a very small fraction of total catchment area (Klein et al., 1999). The majority of annual precipitation (50-80%) falls during the austral summer and is associated with the South American Summer Monsoon (Garreaud et al., 2003). Modern vegetation in the Titicaca catchment mostly consists of grasses, herbs and shrubs characteristic of puna (3700-4500 m) and sub-puna (3200-3700 m) vegetation groups found above the continuous tree line (~3200 m) on the Altiplano (Hanselman et al., 2011). Vegetation in areas above 4500 m also consists of grasses and herbs, but vegetation cover is much sparser.

5.2.1 Past climate variability at Lake Titicaca

As discussed extensively in Fornace et al. (2014) (Chapter 2 of this thesis), the Titicaca catchment has experienced large changes in precipitation since the last glacial period. Multiple lines of evidence point to wetter conditions on the Altiplano during the last glacial maximum (LGM) and late glacial period (Baker et al., 2001; Blard et al., 2011; Fornace et al., 2014) compared to the Holocene. Estimates of glacial cooling from snowline reconstruction and pollen composition range from 5 to 9°C below modern temperatures (Klein et al., 1999; Paduano et al., 2003). Increased precipitation and lower temperatures caused snowlines in the Titicaca catchment to descend to elevations of ~4400-4600 m (Klein et al., 1999), resulting in significant glacial expansion. The presence of glaciers and generally wet conditions also resulted in a long

period of sediment aggradation in Titicaca watershed rivers during the LGM and late glacial period, as evidenced by high terraces (~20-40 m, ~10-20 m above modern river level, respectively) in both Ramis and Ilave river valleys thought to be deposited during this time (Farabaugh, 2005; Rigsby et al., 2003).

During the last deglaciation, a period of decreased precipitation coincided with the Bølling-Allerød (BA) interstadial (~14.7-12.9 ka) in the northern hemisphere (Blard et al., 2011; Fornace et al., 2014). Evidence from exposure dating of glacial moraines on the southern Altiplano suggests glaciers reached their maximum extent at ~15.5 ka and then retreated dramatically around the onset of the BA. Wetter conditions returned from ~12.5-11.9 ka coincident with the Younger Dryas (YD) stadial (Blard et al., 2011). The early-mid Holocene was marked by the driest conditions of the last 20 kyr and a ~100 m drop in lake level from ~8-4 ka (Cross et al., 2000; D'Agostino et al., 2002). Reduced precipitation and lower lake level also contributed to erosion of fluvial deposits and episodic downcutting throughout the early-mid Holocene in the Ramis and Ilave river valleys (Farabaugh, 2005; Rigsby et al., 2003). Precipitation gradually increased into the late Holocene, tracking the increasing trend in local summer insolation (Bird et al., 2011). With wetter conditions, new terrace development suggests rivers switched from a largely erosional phase to an aggradation phase in the late Holocene (~3 ka to present) (Farabaugh, 2005; Rigsby et al., 2003).

5.3 Methods

5.3.1 Sample collection

Sediment samples were taken from cores raised at Site 2 (water depth: 228 m) by the Lake Titicaca Drilling Project, a 2001 International Continental Drilling Program (ICDP)

expedition. Holocene and deglacial (~15-0 ka) samples were taken from the LT01-2B core, while glacial samples were taken from replicate core LT01-2A due to limited sediment availability in the glacial section of the 2B core. Sample descriptions are provided in Table 1.

Modern river sediments were collected from the Ramis and Ilave rivers in March 2014. River water and bank sediment were collected at sites close to the lake but sufficiently upstream to avoid any mixing from lake water (see Figure 1 for sampling locations). Suspended sediment was collected from approximately ~100 L river water by filtration through MilliPore polyethersulfone filters (0.22 μm). Bank sediments were collected from undisturbed bank areas at the edge of each river. Since sediments were collected in late March at the end of the rainy season, bank sediments were likely relatively recently deposited as rivers contracted from peak flow in February to early March. Full sample and collection site details are provided in Table 2.

5.3.2 Lipid extraction and purification

Freeze-dried sediments were extracted with 9:1 dichloromethane:methanol (DCM:MeOH) using a Microwave-Assisted Reaction System (MARS) or Accelerated Solvent Extractor (ASE). Extracts were saponified and lipids were separated by a five-fraction aminopropyl silica gel (LC-NH_2) column chromatography procedure. Fatty acids that eluted in the fourth column fraction were converted to methyl esters (FAMEs) and purified with a second LC-NH_2 column, followed by urea adduction and silver nitrate ($AgNO_3$) chromatography. Individual FAME compounds were isolated and collected using preparative capillary gas chromatography (PCGC). Full details of all extraction and purification procedures can be found in Section 3.4 in Chapter 4. FAMEs were identified and quantified by comparison of gas chromatograph/flame ionization detector (GC/FID, Agilent 5890) retention times and peak areas to those of authenticated external standards. FAMEs concentrations (µg compound/g sediment)

were corrected for dilution by variable $CaCO_3$ content using $CaCO_3$ content data for LT01-2B (Fritz et al., 2007). $CaCO_3$ content in river sediments was assumed to be zero, as the measured pH at both sites was ≤ 6, suggesting minimal contribution from carbonate-rich bedrock. Average chain length (ACL) was calculated according to the formula:

$$ACL_{26-34} = \sum_{n=26,28...}^{34} n * [C_n] / \sum_{n=26,28...}^{34} [C_n] \quad (1)$$

When present, alkenones (C_{37}-C_{40}) were isolated and dated to constrain sediment deposition ages. Alkenones eluted in the second column fraction of the neutral lipid fraction after saponification. For two sediment horizons (1.45 m and 1.66 m), alkenones were isolated from non-saponified total lipid extracts from adjacent 2 cm sediment samples (1.42 and 1.64 m, respectively) that were previously processed to collect fatty acids for work in Chapter 2. Alkenones were purified by urea adduction and silver nitrate ($AgNO_3$) column chromatography with the same procedures as for FAMEs, except alkenones were eluted in the second (unsaturated) fraction from the $AgNO_3$ column. Attempts to isolate individual alkenones compounds with preparative capillary gas chromatography (PCGC) were unsuccessful as yields were extremely low (<10%). Both sample alkenones compound and compounds from an alkenones standard run on the PCGC also appeared to degrade in traps, as evidenced by the consistent appearance of small amounts of "contaminating" compounds in addition to targeted compounds in traps. When analyzed by a gas chromatograph time-of-flight mass spectrometer (GC-TOF-MS), the "contaminating" compounds appeared to generally have straight-chain hydrocarbon and ketone/ester features, further suggesting they were derived from alkenones. In order to obtain the necessary level of purity for compound-specific radiocarbon analysis without the use of PCGC, alkenone compounds were instead further purified using a second

$AgNO_3$ column procedure. For this procedure, 6 cm of $AgNO_3$-impregnated silica gel was loaded into a Pasteur pipette and three fractions were eluted with 10 mL dichloromethane (DCM), 10 mL 95:5 DCM:acetone, and 10 mL 9:1 DCM:acetone. All alkenones compounds eluted from the column in the second fraction. Following this procedure, the purity of the C_{37}-C_{40} series of alkenone compounds was 95% or greater as assessed on a gas chromatograph coupled to a flame ionization detector (GC-FID). Alkenones were eluted through a final column with 2-3 cm 1% deactivated silica gel with 4 mL DCM to remove any remaining traces of $AgNO_3$ or urea.

5.3.3 Compound-specific hydrogen isotope analysis

Aliquots of purified FAMEs from river sediments were analyzed for hydrogen isotope composition as detailed in Fornace et al. (2014). Average precision (1σ) for this set of FAMEs was 1.4‰ (n = 11). At the time of this thesis, hydrogen isotope ratios for the methyl hydrogen added during methylation were not yet available due to instrument malfunction. The composition of methyl hydrogen was thus estimated at -100 ± 50‰ (VSMOW). Due to the small contribution of methyl hydrogen to total FAME hydrogen, however, this resulted in only 2-3‰ additional error.

5.3.4 Compound-specific radiocarbon analysis

FAMEs and alkenone compounds were combusted and submitted for radiocarbon analysis as detailed in Section 3.5 of Chapter 4. *n*-C_{26} and *n*-C_{28} FAMEs were generally combusted individually, while *n*-C_{30} and *n*-C_{32} were combined prior to combustion to increase the amount of carbon available for radiocarbon dating. For several samples, low FAME

abundances required combination of n-C_{28}-C_{32}. All radiocarbon dating was performed in 2014 and 2015.

5.3.5 Ramped pyrolysis-oxidation analysis of sediments

Due to the lack of sufficient quantities of alkenones in some sediment horizons (250-254, 383.5-458.5 cm), we performed ramped pyrolysis-oxidation (PyrOx) radiocarbon analysis to constrain sediment ages for three sediment horizons (254, 403.5, 453.5 cm) following the approach of Rosenheim et al. (2008). Aliquots of dry sediment (18 mg for 254 cm horizon, 100-150 mg for 403.5 cm and 453.5 cm horizons) were loaded into a flow-through quartz reactor and heated from 80°C to 800°C at a constant ramp rate of 5°C/min, as depicted in Figure 2. Sediments were not treated to remove $CaCO_3$ before PyrOx analysis as $CaCO_3$ contents of all analyzed samples were very low (<1%; Fritz et al., 2007). Volatile pyrolysis products passed into a combustion reactor under a constant stream of He (35 mL/min) and were oxidized in the presence of O_2 and a copper/platinum/nickel catalyst. Evolved CO_2 was quantified by a CO_2 analyzer and was dynamically trapped using liquid nitrogen (LN2). Five fractions corresponding to different temperature intervals were collected over the course of each analysis. After isolation from the PyrOx system, each CO_2 fraction was purified in the presence of a dry ice/isopropanol trap, quantified manometrically, and flame-sealed in pyrex tubes that had been previously loaded with small amounts of copper oxide (~100 mg) and granulated silver (several flakes). Pyrex tubes containing CO_2 aliquots were heated at 525°C for 5 hours to ensure complete combustion and removal of any contaminating gases. All CO_2 fractions were then submitted to NOSAMS for radiocarbon dating.

5.3.6 Data reduction

Compound-specific radiocarbon results were corrected for blank carbon added during PCGC collection (FAMEs only) and combustion (both FAMEs and alkenones) processes using the formula:

$$F_{m,wax} = m_t F'_{m,wax} + m_b F_{m,b} \quad (2)$$

where $F_{m,wax}$ is the reported fraction modern, m_t is the sample mass excluding blank carbon, $F'_{m,wax}$ is the blank-corrected fraction modern, m_b is the blank carbon mass and $F_{m,b}$ is the fraction modern of blank carbon. Characterization of procedural blanks is described in Appendix 1. The ^{14}C content of MeOH used for methylation was characterized and used to correct fractions modern of FAMEs for added methyl carbon using the formula:

$$F''_{m,wax} = \frac{F'_{m,wax}(ACL + 1) - F_{m,MeOH}}{ACL} \quad (3)$$

where $F''_{m,wax}$ is the methyl- and blank-corrected $F_{m,wax}$, $F'_{m,wax}$ is the blank-corrected $F_{m,wax,}$ $F_{m,MeOH}$ is the measured F_m of MeOH used for methylation, and ACL is the average chain length of the compound(s) in each sample.

PyrOx fractions were not corrected for blank carbon added during the PyrOx process, but blank contributions are likely negligible given the large size of samples (>100 μg C). For a similar PyrOx system, Fernandez et al. (2014) report a blank contribution of 12.9 ± 7.0 μg with F_m = 0.68 ± 0.50 for the entire ramp cycle from 25-1000°C at 5°C/min.

5.3.7 Calculations and notation

As in Chapter 4, we use the $F^{14}R$ notation (Soulet et al., in press) to describe the radiocarbon deficit of waxes relative to sediments to avoid uncertainties associated with defining ages for mixtures of components of different ages. $F^{14}R$ is defined according to the equation:

$$F^{14}R_{wax} = {F_{m,wax}}/{F_{m,sed}} = {F_{m,wax}\,(t_0)}/{F_{m,atm}\,(t_0)} \quad (4)$$

where $F_{m,wax}$ and $F_{m,sed}$ are reported fraction modern values for a wax compound and sediment, respectively. $F^{14}R_{wax}$ is also equivalent to the $F_{m,wax}$ at the time of sediment deposition (t_0) normalized to the F_m of the atmosphere ($F_{m,atm}$) at t_0. For a mixture with n components of different ages, $F^{14}R_{wax}$ can be written as:

$$F^{14}R_{wax} = \frac{1}{F_{m,sed}} \sum_{1}^{n} f_n \cdot F_{m,n} = \sum_{1}^{n} f_n \cdot \frac{A_n}{A_0} \cdot e^{-\lambda(t_n - t_0)} \quad (5)$$

where f_n is the mass fraction of component n, $F_{m,n}$ is the fraction modern of component n, A_n is the atmospheric ^{14}C activity at the time of formation of component n (t_n), A_0 is the atmospheric ^{14}C activity at the time of sediment deposition (t_0), and λ is the true decay constant of ^{14}C (1/8267 yr^{-1}).

Although we generally use F_m and $F^{14}R$ notation, radiocarbon age can also be calculated according to the equation:

$$^{14}C\ Age = -8033 \cdot \ln (F_m) \quad (6)$$

The radiocarbon age difference (R) between a wax mixture and sediment can thus be expressed as:

$$R = -8033 \cdot \ln (F^{14}R_{wax}) \quad (7)$$

However, in the case of a mixture, ^{14}C age represents a log average and not a true average age unless the mixture has a log-normal (or log-symmetric) distribution.

5.4 Results and Discussion

5.4.1 Sediment age model

5.4.1.1 Previous geochronological work at Lake Titicaca

The original LT01-2B age model for the past 50 kyr was constructed with radiocarbon dates of bulk sedimentary organic matter, as other common targets for sediment chronology (e.g., foraminifera, plant macrofossils, charcoal) are largely absent from Titicaca sediments (Fritz et al., 2007). However, since sedimentary organic matter may contain a significant fraction of old terrestrial biospheric or petrogenic carbon in addition to fresh organic matter derived from primary productivity, the LT01-2B age model is likely biased towards older ages, particularly in organic-lean glacial sediments. Rowe et al. (2003) indeed found significantly older ages for bulk decalcified organic matter compared to humate (base soluble/acid insoluble) and humin (acid and base insoluble) organic fractions in Titicaca glacial sediments (prior to ~13.5 cal ka). Moreover, humate fractions consistently showed younger ages than humin fractions. In contrast, for the period ~13.5 cal ka to the present, there are no significant differences between humin, humate and bulk organic ages. We note that Rowe et al. (2003) attributed young humate ages during the glacial period to contamination from downward migration of humic material through the sediment column and thus concluded that the humin fraction is the best representative of true sediment age.

5.4.2.1 New approaches for refining sediment chronology

Compound-specific radiocarbon dating of algal biomarkers represents an alternative approach for establishing sediment chronology that eliminates uncertainty associated with dating heterogeneous organic mixtures. Alkenones, unsaturated methyl and ethyl $C_{37\text{-}40}$ *n*-ketones

derived from coccolithophores and other phytoplankton, are ubiquitous in marine settings and also commonly found in lacustrine settings worldwide, including Lake Titicaca (Cranwell, 1985; Theissen et al., 2005). While the exact species producing lacustrine alkenones have not yet been identified, these molecules are almost certainly derived from aquatic algal organisms (Cranwell, 1985). Due to the relatively shallow depth of Lake Titicaca, it can be further expected that alkenones are produced and rapidly transferred to sediments and thus represent a source of fresh organic matter. Moreover, the highly hydrophobic structures of alkenones render migration of these compounds through sediment pore waters unlikely. However, the age of alkenones would reflect mixing by bioturbation or other sediment redistribution processes that affect the fine fraction of sediment mixture (i.e., fraction containing FAMEs), as well as any reservoir effects in the dissolved inorganic carbon pool in the lake.

When algal biomarkers or other suitable dating targets are absent from sediment, complex organic mixtures are the only available material for radiocarbon dating. However, separating and dating different fractions of the heterogeneous mixture can provide better constraints on sediment age than one bulk age. Complex organic mixtures in soils and sediments have traditionally been fractionated with different chemical separation procedures, for instance with sequential acid and base extractions as in Rowe et al. (2003). However, such chemical techniques are labor-intensive and generally separate organic matter into only 2-3 fractions of unclear composition. Programmed-temperature or ramped pyrolysis-oxidation (PyrOx) of complex organic mixtures represents an alternative to chemical separation procedures that instead exploits differences in the rates of thermal decomposition of organic mixture components. PyrOx allows for characterization of the age and abundance of many components within a complex mixture across a continuous spectrum of thermal stability. Correlations between thermal

stability and age of components in complex mixtures have been observed in both soils and sediments, with younger ages generally found for more thermally labile fractions (Plante et al., 2011; Rosenheim et al., 2008; Rosenheim and Galy, 2012). The youngest PyrOx fraction from a sedimentary organic mixture thus provides an estimate of the age of fresh organic matter and sediment deposition age. However, since it is unlikely that PyrOx completely separates fresh and old carbon pools, the age of the youngest PyrOx fraction generally represents a maximum possible sediment deposition age.

5.4.1.3 Sediment age assignment

For Holocene sediment horizons, we assign sediment ages with alkenone radiocarbon dates (Table 3). We have not applied any reservoir correction to these ages as surface sediments from the main basin of the lake do not show any reservoir effect (Baker et al., 2001). Alkenones generally show younger ages compared to sediment ages assigned with Fritz et al. (2007) age model (Table 5), with the discrepancy between alkenone and original sediment ages increasing with depth (Figure 3). However, when compared to the four bulk radiocarbon dates from the original age model from 8.6-3.1 ^{14}C kyr BP, alkenone dates fit reasonably well with the line defined by bulk dates (range of offsets between alkenone dates and bulk age model = 92-842 ^{14}C yr) (Figure 3).

For sediment horizons corresponding to the YD (identified by low leaf wax δD as detailed in Fornace et al., 2014), we assign sediment ages using results from dating of PyrOx fractions of a sediment sample from the 254 cm horizon (Figure 4, Table 4). PyrOx fractions from this sample show remarkably uniform ages of 10,350-10,950 ^{14}C yr BP despite significant δ^{13}C variability, pointing to dominance of fresh organic carbon from both terrestrial and aquatic

sources. The youngest fraction age (calibrated range 12.0-12.4 ka) matches the timing of the YD stadial defined by the most recent NGRIP chronology (12,896-11,703 yr BP; Rasmussen et al., 2006). This PyrOx -based sediment age thus resolves the age discrepancy between the YD stadial and the YD-related δD excursion in the Fornace et al. (2014) record, which used the Fritz et al. (2007) age model. The assigned age for the 254 cm horizon also fits well with alkenone-based Holocene sediment ages (Figure 3, $r^2 = 0.99$), pointing to a relatively constant post-glacial sedimentation rate.

Sediment horizons corresponding to the BA, as identified by a positive δD excursion in Fornace et al. (2014), showed evidence of significant ^{14}C contamination. The measured age of alkenones from the 274 cm horizon (9,850 ^{14}C yr/11,120 cal yr BP) is younger than the assigned age of overlying sediments that are linked to the timing of the YD stadial by multiple lines of evidence. Similarly young ages of FAMEs in these samples (Table 6) points to possible contamination of the 271.5 and 274 cm horizons with modern sediment, either during core retrieval or during sampling. Unfortunately, without knowing the ratio of alkenone to FAME contamination, results from these horizons cannot be used to calculate FAMEs-sediment ^{14}C deficits. We note that any sediment contamination would not significantly impact previously reported leaf wax δD values due to the relatively small mass fraction of modern carbon (<10%) required to shift the ^{14}C ages of 15-14 ka sediments by several thousand years.

Finally, we assign sediment ages for glacial sediments (383.5-458.5 cm) using results from dating of PyrOx fractions of sediment samples from the 403.5 and 453.5 cm horizons (Table 4, Figure 4). The youngest (lowest temperature) PyrOx fractions represent maximum sediment ages, as low-temperature fractions could contain trace amounts of the older material apparent in higher-temperature fractions. Significant contamination of younger carbon

introduced by downward migration of water-soluble compounds (as suggested by Rowe et al. (2003) to explain young humate ages) is unlikely given that hydrophobic FAMEs are very in close in age to the youngest PyrOx fractions (see Section 5.4.2). The very similar ages (13120, 13070 ^{14}C yr BP) for the lowest-temperature PyrOx fractions from two horizons separated by 50 cm point to a much higher sedimentation rate during this interval compared to the Holocene. A much higher sedimentation rate at this time (~15.5 cal ka) is reasonable given that this period coincides with the timing of the local last glacial maximum on the Altiplano (Blard et al., 2013). Moreover, there is evidence for increased precipitation on the Altiplano throughout the last glacial period (Fornace et al., 2014), particularly during Heinrich Event 1 (~17-15 cal ka) (Blard et al., 2011). Such increases in precipitation, estimated to be up to 50% above modern levels (Blodgett et al., 1997), would likely further enhance fluvial sediment transport to the lake.

A dramatic change in sedimentation rate likely occurred following the retreat of glaciers on the Altiplano from ~15.5-14.5 cal ka as estimated by ^{3}He exposure ages of glacial moraines (Blard et al., 2013). This glacial retreat preceded the regression of the Tauca paleolake on the southern Altiplano dated more precisely to 12.2 ^{14}C kyr/14.1 cal kyr BP by several hundred years (Blard et al., 2013 and references therein). The retreat of glaciers in the Titicaca catchment is reflected by a large drop in magnetic susceptibility (MS) in LT01-2B sediments at a depth of ~293 cm (Fritz et al., 2007). Assuming this MS drop is synchronous with or preceded the retreat of Altiplano glaciers, we can constrain the minimum sediment age for 383.5-408.5 cm horizons to the timing of glacial retreat. The estimate of glacial retreat timing of ~15 cal ka from Blard et al. (2013) matches the age of ~12.9 ^{14}C kyr BP (15.3 ± 0.2 cal ka) estimated for the MS transition in Titicaca core NE98-1PC with humate fraction ^{14}C data from Rowe et al. (2003). However, to be conservative, we use the much better constrained timing of the Tauca lake regression (12243

± 85 ^{14}C yr BP) as the minimum bound for 383.5-408.5 cm horizon ages. The age range for all 383.5-408.5 cm horizons is thus assigned as 12243-13095 ^{14}C kyr BP, with all uncertainties in sediment deposition age propagated in all further calculations.

The assigned ages of glacial samples are significantly younger (3500-6000 ^{14}C yr) than ages calculated with the Fritz et al. (2007) age model (Table 5). The offset in timing between glacial retreat and Tauca paleolake regression may contribute to slightly younger assigned sediment ages by several hundred years. However, the bulk of the discrepancy is likely to due to the lack of dates between 3.12-6.135 m in the original age model, obscuring the timing of the glacial/interglacial change in sedimentation rate. Moreover, the PyrOx thermograms for both glacial samples show a large amount of very old refractory organic carbon within glacial sediments, which would significantly bias bulk organic radiocarbon ages (Figure 4). The lack of such a refractory pool of carbon in the 254 cm sediment horizon above the MS transition suggests that glaciers facilitated delivery of very old terrestrial organic carbon to the lake. This delivery of old carbon compounded with generally low levels of primary productivity during the glacial period likely caused large discrepancies between bulk organic carbon ages and true sediment deposition ages.

5.4.2. Wax radiocarbon analysis results

Raw F_m and calculated $F^{14}R_{wax}$ values for measured FAMEs are shown in Figure 5 and listed in Table 6. Distributions of individual FAME homolog concentrations for all samples are also shown for reference in Figure 6. Over the past ~15 kyr, measured $F^{14}R_{wax}$ values range from 0.64-1.13 with the greatest variability observed for *n*-C_{30}-C_{32} $F^{14}R_{wax}$ values. $F^{14}R_{wax}$ values greater than 1 measured for three samples (*n*-C_{28} in 26 cm horizon; *n*-C_{28}-C_{32} in 403.5 and 453.5

cm horizons) are the likely the result of variability in blank contributions not accounted for by our blank correction procedure. However, considering uncertainty in sediment age assignment and analytical uncertainty, all are within 2σ of 1. Three samples (*n*-C_{30}-C_{32} in 166 cm horizon, *n*-C_{30}-C_{32} in 250 cm horizon, *n*-C_{28}-C_{32} in 383.5 cm horizon) were excluded from further analysis due to significant mass discrepancies between measured PCGC fractions and CO_2 yields on the vacuum line, suggesting contamination from solvent.

For horizons older than 8 ka, we generally find $F^{14}R_{wax}$ close to 1 for *n*-C_{28} and *n*-C_{30}-C_{32}, indicating that waxes were relatively young at the time of sediment deposition. Average *n*-C_{28}-C_{32} $F^{14}R_{wax}$ for glacial horizons (383.5-408.5 cm/15.5-14.2 ka) is 1.01 ± 0.10 (n = 4), or excluding the anomalously young and smallest sample at 403.5 cm, 0.97 ± 0.09 (n = 3). Thus, within error, *n*-C_{28}-C_{32} FAMEs are contemporaneous with sediments. We can also calculate average glacial minimum $F^{14}R_{wax}$ values for *n*-C_{28} and *n*-C_{30}-C_{32} individually by the mass balance equation:

$$F^{14}R_{wax,measured} = f_n \cdot F^{14}R_{wax,n} + (1 - f_n) \quad (8)$$

where f_n is the mass fraction of the compound of interest and all other compounds are assumed to have an $F^{14}R_{wax}$ value of 1. The resulting minimum values, 0.95 and 0.94 for *n*-C_{28} and *n*-C_{30}-C_{32}, respectively, show that all compounds were close in ^{14}C age to sediment (Figure 7). Moving into the deglaciation, all measured FAMEs in the first YD sediment horizon (254 cm) are similar in ^{14}C age to sediment (*n*-C_{26}-C_{30} $F^{14}R_{wax}$ = 0.95-0.98), although the only available measurement (*n*-C_{28}) in the adjacent horizon (250 cm) shows significant ^{14}C depletion ($F^{14}R_{wax}$ = 0.76). However, this value represents an outlier for *n*-C_{28} compared to all other sediment horizons and river samples (*n*-C_{28} $F^{14}R_{wax}$ range = 0.89-1.05). In the first Holocene horizon (170 cm/8.4 ka), we again calculate relatively high minimum values for *n*-C_{28} and *n*-C_{30}-C_{32} of 0.97 and 0.90,

respectively. In contrast to results for *n*-C_{28}-C_{32}, there is evidence of ^{14}C depletion in *n*-C_{26} in glacial sediments (average $F^{14}R_{wax} = 0.81 \pm 0.13$, n = 2). However, in YD and early Holocene horizons, *n*-C_{26} is relatively close in ^{14}C age to sediments ($F^{14}R_{wax}$ values of 0.98 and 0.92, respectively).

For sediments younger than 8 ka, we find evidence of significant pre-aging of waxes, with measured $F^{14}R_{wax}$ values as low as 0.64. One of the most striking features of samples from <8 ka horizons is the systematic difference in $F^{14}R_{wax}$ values among different FAME homologs. Most notably, with one exception (*n*-C_{26} in 26 cm/3.7 ka horizon), *n*-C_{26} and *n*-C_{28} are close in age to sediment ($F^{14}R_{wax} \geq 0.91$, n = 5), while *n*-C_{30}-C_{32} is significantly older ($F^{14}R_{wax}$ = 0.64-0.78, n = 2). We calculate the possible range of *n*-C_{30}-C_{32} $F^{14}R_{wax}$ values by mass balance for the 145 cm horizon for which it was only possible to measure combined *n*-C_{28}-C_{32} $F^{14}R_{wax}$ (Figure 7). Since $F^{14}R_{wax}$ values for *n*-C_{28} are greater than or equal to *n*-C_{26} values for all samples, we constrain the possible range of *n*-C_{30}-C_{32} $F^{14}R_{wax}$ in this horizon by using the measured *n*-C_{26} $F^{14}R_{wax}$ value (0.94) as the minimum bound for *n*-C_{28} $F^{14}R_{wax}$ (with a maximum bound of 1). Although the error is very large due to the small mass of *n*-C_{30}-C_{32}, the resulting range ($F^{14}R_{wax}$ = 0.40-0.52) is consistent with measured *n*-C_{30}-C_{32} $F^{14}R_{wax}$ values in later Holocene horizons and further supports the existence of a source of extremely old waxes during the early-mid Holocene.

$F^{14}R_{wax}$ values for FAMEs in modern river sediments range from 0.76-0.90 (Table 6). Like in <8 ka Holocene sediments, *n*-C_{30}-C_{32} is more depleted in ^{14}C than shorter chain length compounds, although the differences in ^{14}C content between compounds are less extreme. We note that direct comparison of river and downcore $F^{14}R_{wax}$ values is complicated by possible contributions of bomb ^{14}C to waxes in modern river sediments. This effect is explored more fully in Section 4.3.

Although there are relatively few points, relative ^{14}C deficits in *n*-C_{30}-C_{32} in both <8 ka Holocene horizons and modern river sediments generally track concentration disparities between FAMEs homologs, with the age of *n*-C_{30}-C_{32} increasing with decreasing *n*-C_{30}-C_{32} abundance relative to other FAMEs (Figure 8). The pattern of decreasing age with increasing *n*-C_{30}-C_{32} concentration suggests variable addition of fresh material to a very old background end member. Considering all measured chain lengths, the generally low relative abundance and $F^{14}R_{wax}$ values of *n*-C_{30}-C_{32} suggest that Holocene vegetation predominantly produced shorter chain length compounds (≤ 28 carbons), while old wax pools were more evenly distributed or weighted towards longer chain lengths. As a result of this difference, *n*-C_{30}-C_{32} $F^{14}R_{wax}$ values are particularly sensitive to contributions of old carbon.

5.4.3 Wax age structure

We explore possible age structures of *n*-C_{30}-C_{32} waxes using the two-component mixing model developed in Chapter 4. This model is constructed such that wax age structure is controlled by mixing between normally distributed decadal and millennial pools, presumably derived from standing vegetation/leaf litter/young soil material and aged soil material, respectively. The age structure of a wax mixture is described by the following equations:

$$f_{mill} + f_{dec} = 1 \tag{9}$$

$$m_{wax} = f_{mill} \cdot \int_{t_0}^{\infty} \frac{1}{\sigma_{mill}\sqrt{2\pi}} e^{-(t-\mu_{mill})^2 / 2\sigma_{mill}^2} + f_{dec} \cdot \int_{t_0}^{\infty} \frac{1}{\sigma_{dec}\sqrt{2\pi}} e^{-(t-\mu_{dec})^2 / 2\sigma_{dec}^2} \tag{10}$$

$$F^{14}R_{wax} = f_{dec} \cdot \sum_{t=t_0}^{\infty} p_{dec}(t) \cdot \frac{A_t}{A_0} \cdot e^{-\lambda(t-t_0)} + f_{mill} \cdot \sum_{t=t_0}^{\infty} p_{mill}(t) \cdot \frac{A_t}{A_0} \cdot e^{-\lambda(t-t_0)} \tag{11}$$

where "mill" and "dec" subscripts refer to millennial and decadal fractions, respectively. In Equation 10, m_{wax} denotes the total mixture mass, f is the mass fraction of each component, σ is the standard deviation of age distribution, and μ is the offset of the center of the age distribution (defined relative to sediment age). In Equation 11, p refers to the Gaussian probability distribution of each component as defined in Equation 10.

Based on possible sources of waxes in the Titicaca catchment, we consider this two-component mixing model to be a reasonable approximation of wax age structure in Titicaca sediments. Despite significantly depleted *n*-C_{30}-C_{32} $F^{14}R_{wax}$ values in <8 ka sediment horizons, some contribution of fresh *n*-C_{30}-C_{32} waxes is highly likely considering the relative freshness of shorter chain length waxes, as well as the low probability that standing vegetation/leaf litter could be eliminated entirely as a source of waxes to lake sediments. The age structure of the millennial wax pool could take on many forms, but given the under-constrained nature of the system, we assume one normally distributed pool to minimize the number of free parameters. We also adopt constraints similar to those used in Chapter 4 in order to the narrow the range of possible values for μ_{mill} and σ_{mill}. These include limiting the age offset of the millennial fraction to within 2σ of sediment age and assuming a constant millennial age distribution for all time horizons. The first condition effectively excludes a millennial fraction with a narrow age distribution about some very old age (as in Figure 2b in Chapter 4). This condition is reasonable given the low probability that a pool of waxes of uniform old age could be isolated in soil or other reservoirs without some mixing in of younger compounds. The one exception is in the case of a radiocarbon dead millennial fraction, which would appear of uniform age regardless of true age distribution due to the limits of radiocarbon dating. This case is calculated as an end member in addition to model results. The second condition of an unchanging millennial age distribution

through time is likely an oversimplification due to the many climatic and geomorphologic factors that could influence the age distribution of soil and other reservoir carbon pools. However, the very old age (>5000 yr) of the millennial pool necessary to produce some of the lowest observed $F^{14}R_{wax}$ values indicate this pool is generally stable over multiple millennia and thus not very sensitive to perturbations on shorter timescales.

We calculate the relative sizes of decadal and millennial fractions for *n*-C_{30}-C_{32} waxes as a function of μ_{mill} and σ_{mill} for four representative scenarios (Table 8, Figure 9). For all scenarios, μ_{dec} and σ_{dec} are set at 0 and 20 years, respectively. Varying the decadal offset and standard deviation has little effect on results for downcore samples since atmospheric ^{14}C content was relatively stable on decadal timescales in the pre-bomb atmosphere. However, for modern river samples, F_m of the decadal fraction can range from 1.05-1.16 by varying σ_{dec} from 0 to 40 yr (holding μ_{dec} constant at 0). While we consider an offset of 0 to be reasonable for a decadal pool mostly derived from standing vegetation/leaf litter, we show the possible range of f_{mill} for different σ_{dec} values in Figure 9.

As expected, the magnitude of f_{mill} varies inversely with $F^{14}R_{wax}$, although f_{mill} for modern river samples are larger than downcore samples with similar $F^{14}R_{wax}$ values due to the influence of post-bomb carbon with $F_m > 1$. In all scenarios, *n*-C_{30}-C_{32} wax mixtures from both modern river sediments and <8 ka horizons contain significant amounts of old waxes ($f_{mill} \geq \sim 0.2$). If we assume constant σ_{mill} and μ_{mill} values for all samples, the minimum average age of the millennial pool must be >8,000 years. The millennial pool would have to be even older in order to allow significant contribution from the decadal pool. Therefore, a substantial amount of the millennial pool must have been synthesized in the last glacial period (or earlier) and preserved until the Holocene in order to be of sufficient age by 7.5 ka.

5.4.4 Links between wax age structure and climate variability

The differences between *n*-C_{30}-C_{32} age structure before and after ~8 ka are likely related to drier conditions in the Titicaca catchment that resulted in a ~100 m lake level drop in the mid-Holocene (~8-4 ka) (Cross et al., 2000; D'Agostino et al., 2002). This lake level drop is reflected by a large increase in $CaCO_3$ content in LT01-2B sediments at a depth of ~167 cm (~8.4 ka) (Figure 10). A link between hydrologic variability and *n*-C_{30}-C_{32} age structure is further supported by the general correlation between higher $F^{14}R_{wax}$ values and wetter periods during the late glacial period and late Holocene as indicated by leaf wax δD records (Figure 10).

Based on all available evidence, we consider climate-driven changes in erosional patterns over the past 15 kyr to be the most plausible explanation for observed changes in the age distribution of *n*-C_{30}-C_{32} waxes. During the last glacial period, generally wet conditions as well as the presence of well developed glaciers within the catchment led to high erosion rates and sediment accumulation on river floodplains (Farabaugh, 2005; Rigsby et al., 2003). Colder glacial temperatures also reduced the density of vegetation cover in the catchment (Paduano et al., 2003). The high erosion rates facilitated by glaciers led to the delivery of highly recalcitrant organic carbon observed during PyrOx analysis of glacial sediments, along with mostly fresh biospheric carbon reflected in high $F^{14}R_{wax}$ values. Such a mixture between fresh vegetation-derived carbon and highly recalcitrant organic carbon has been observed in small mountainous river systems, where high rates of mass-wasting inject organic carbon derived from standing vegetation and highly processed soils directly into rivers (Rosenheim and Galy, 2012). Thus, it is likely that soil storage of waxes was reduced in the Titicaca basin under glacial conditions due to more intense microbial soil organic carbon processing in a wetter but sparsely vegetated landscape and/or higher erosion rates supported by regional glaciation. However, given the very

old age of millennial wax pool required to produce very depleted $F^{14}R_{wax}$ values during the Holocene, some vegetation-derived carbon had to be deposited and stored in soils or sediments that accumulated on river floodplains. Moreover, lower *n*-C_{26} $F^{14}R_{wax}$ values do point to some stock of aged biospheric carbon during the glacial period.

After the retreat of glaciers around ~15 ka, erosion rates dropped significantly, as evidenced by the dramatic drop in the lake sedimentation rate. The supply of recalcitrant carbon to the lake was also cut off, as indicated by the lack of any significant contribution of old carbon in PyrOx fractions from YD sediments. During the deglaciation and early Holocene, the level of Lake Titicaca remained relatively high despite evidence of significant variability in SASM precipitation linked to millennial-scale temperature variability at high northern latitudes (Baker et al., 2001; Blard et al., 2011; Fornace et al., 2014). Thus, river discharge likely remained high and continued to aggrade sediment, especially under wet conditions coincident with the YD. While vegetation-derived carbon likely started to accumulate at greater levels in soils due to decreased erosion rates and increased vegetation density that accompanied deglacial warming, generally high $F^{14}R_{wax}$ values in YD and early Holocene indicate that fresh waxes were the dominant component of material transported to the lake. Occasional episodes of deeper soil/river sediment erosion, however, could explain the lower $F^{14}R_{wax}$ value for *n*-C_{28} observed in the 250 cm horizon.

Following this glacial-interglacial transition period, lake level and river discharge dropped dramatically after 8 ka. Lower base level and reduced flow led to river sediment instability, leading to downcutting episodes and sustained erosion of floodplain sediment deposits during the mid-Holocene (Farabaugh, 2005; Rigsby et al., 2003). The low $F^{14}R_{wax}$ values in mid-Holocene horizons thus likely reflect contributions of very old waxes from glacial-age

river sediment deposits, exposed lacustrine sediments, and/or soil mobilized by erosion events. As precipitation increased into the late Holocene, our data suggest that the contribution of old waxes was diluted by increased delivery of fresh waxes. Since pollen records do not show evidence of dramatic changes in vegetation density through the Holocene (Paduano et al., 2003), precipitation increases likely acted to increase the efficiency of fresh wax transport to lake sediments rather than increasing the available wax supply from standing vegetation. Increased efficiency of fresh wax transport could have been a result of increases in overland flow and mobilization of waxes in extant vegetation and leaf litter/young soil carbon, as proposed in Chapter 4. There is also the possibility that the supply of old waxes decreased through the Holocene due to removal of fluvial deposits through previous erosion or lake level rise. However, the link between *n*-C_{30}-C_{32} relative concentration and $F^{14}R_{wax}$ (Figure 8) would tend to support the model of increasing dilution of an old end member by fresh material.

In the wetter conditions of the late Holocene (~4-2 ka to the present), lake level rose to modern levels and rivers returned to an aggradation phase (Farabaugh, 2005; Rigsby et al., 2003). Unlike earlier Holocene samples, all measured FAMEs homologs from modern river samples show some degree of ^{14}C depletion ($F^{14}R_{wax} \leq 0.90$) even with likely contributions of some waxes synthesized in the post-bomb era. Calculated f_{mill} values for *n*-C_{30}-C_{32} waxes in river samples are similar to values calculated for the 3.7 ka horizon (Figure 9) despite some indication of increasing precipitation over the last several millennia in some Andean climate records (e.g., Bird et al., 2011). Lower wax δD signatures in modern river samples compared to those at 3.7 ka also suggest increased precipitation in the present day. One factor that could account for low $F^{14}R_{wax}$ values in all chain lengths in river samples is the effects of extensive agriculture and other human activities in the Titicaca drainage basin over the last three millennia (Erickson,

2002). In the present day, land use patterns on the Altiplano have caused moderate to severe erosion in large areas throughout the Titicaca catchment (PNUMA, 2011). Such disturbances to the natural landscape have likely increased the mobilization of biospheric carbon stored in deep soil horizons (e.g., Torn et al., 2009), thus increasing the size and/or age of the millennial wax pool and drawing down $F^{14}R_{wax}$ values. Therefore, it is possible that in the absence of human activity, f_{mill} values would have continued to decrease throughout the Holocene.

Overall, the patterns observed in $F^{14}R_{wax}$ values show that *n*-C_{30}-C_{32} wax age structure in the Titicaca catchment was highly dynamic over the past 15 kyr, while shorter chain lengths were generally derived from extant vegetation/young soil material despite climate and landscape changes. Furthermore, our results provide strong evidence of a connection between hydrologic variability in the Titicaca catchment and *n*-C_{30}-C_{32} wax age structure. In contrast, the effect of temperature variability seems to be confined to its role in regulating glacier expansion and recession, as well as its impact on vegetation density. When considered in conjunction with existing records of geomorphologic changes in the lake catchment, our results further suggest this relationship between climate and wax age structure is largely driven by climate-mediated changes in erosion and sediment transport. Our findings from this study are thus consistent with those from the Cariaco Basin catchment (Chapter 4), where physical erosion processes linked to hydrologic variability also appear to be the dominant control of wax age structure.

5.4.5 Implications for stable isotope records

As discussed in Chapter 4, the relative contributions of millennial and decadal pools have important implications for the timing and magnitude of wax stable isotope signals used in paleoclimate reconstructions. As f_{mill} increases, the amplitude of stable isotope signals is distorted

due to a buffering effect by older waxes. Moreover, when $f_{mill} > \sim 0.5$, noticeable lags also begin to develop between the true timing of climate events and the expression of those events in stable isotope records. Titicaca wax δD records offer a further opportunity to explore the effects of wax age structure on stable isotope signals. While the uncertainties associated with sediment age assignment as well as wax δD signals (e.g., vegetation effects) preclude a rigorous analysis similar to that for Cariaco wax $\delta^{13}C$, comparison of *n*-C_{28} and *n*-C_{30} δD records reveals some patterns consistent with age-biasing in stable isotope records. As discussed in Fornace et al. (2014), *n*-C_{28} δD is highly correlated to precipitation δD recorded in a nearby ice core record, a result consistent with the relative freshness of *n*-C_{28} waxes over the past 15 kyr. While *n*-C_{30} δD generally tracks *n*-C_{28} δD, there are two periods of noticeable discrepancy between the two records. These periods occur during the mid-Holocene and end of the YD. During the Holocene, after a period of very high δD values from the onset of Holocene to ~7.5 ka, *n*-C_{30} δD drops sharply to lower values, which are sustained throughout the remainder of the record (Figure 10). This pattern is different from the steadier decreasing trend in *n*-C_{28} δD through the Holocene. This interval corresponds to the period of low lake level and considerably depleted *n*-C_{30}-C_{32} $F^{14}R_{wax}$ values. The drop in *n*-C_{30} δD could thus reflect the introduction of a significant amount of glacial waxes with lower δD signatures.

The second discrepancy between *n*-C_{28} and *n*-C_{30} δD records occurs at the end of the YD and transition into the Holocene. While *n*-C_{28} shows a period of low δD values of roughly the same duration of the YD stadial (~1.2 cal kyr), the onset of the Holocene in the *n*-C_{30} δD record occurs significantly later. While this lag could be caused by a range of factors, one possible explanation is a large shift in the proportions of millennial and decadal waxes during that time. While we do not have any data from that period to support this hypothesis, we note this interval

corresponds to a small peak in sediment $CaCO_3$ (Figure 10), suggesting that there could have been a period of drier conditions/lower lake level that would favor increases in deep soil/floodplain sediment erosion similar to those that occurred in the mid-Holocene.

5.5 Conclusions

This study builds on the results found for Cariaco Basin described in the previous chapter and bolsters the case for a link between climate variability and the age structure of terrestrial biomarkers primarily driven by changes in erosion and transport of waxes to sediments. As in Cariaco, we find evidence of storage of waxes in the Titicaca catchment for very long periods (>8000 yr). Contributions from this pool have the largest effect the age structures of the least concentrated fatty acid homologs (n-C_{30}-C_{32}), in contrast to much more concentrated shorter chain lengths that are generally dominated by fresh waxes. The transport of old waxes to lake sediments appears to have been limited until the dry conditions of the early-mid Holocene led to enhanced erosion of floodplain sediments, deep soil horizons and/or exposed lacustrine sediments. Increasing precipitation through the Holocene appears to have increased the transport of fresh waxes to lake sediments, diluting background levels of old waxes. As discussed in Chapter 4, increased transport of fresh biospheric carbon to relatively inactive sediment reservoirs under wetter conditions represents a potential negative climate feedback on geological timescales. On shorter timescales, the net flux of CO_2 to the atmosphere due to changing erosion patterns in the Titicaca catchment is difficult to assess without knowledge of relative rates of respiration of terrestrial biospheric carbon in soil versus in rivers and lakes. Furthermore, unlike in Cariaco, where contributions of old waxes were more consistent over the last 15 kyr, results from the Titicaca catchment suggest large-scale mobilization of old material due to a climate-

driven shift in erosion patterns during the Holocene. Thus, there is some climate feedback associated with variability in the mobilization of old carbon previously stabilized in terrestrial reservoirs in addition to variability in fresh carbon transport. In any case, it is clear that climate change does impact the mobilization of both fresh and aged terrestrial biospheric carbon and that deciphering the complex relationship between climate, erosion, and organic carbon transport represents an important direction for future research.

Comparison of wax radiocarbon and stable isotope records from this site reveals the potential for pre-aged waxes to distort stable isotope signals used for climate reconstruction. While the *n*-C_{28} δD record is largely unaffected by age-biasing due to the consistent freshness of *n*-C_{28} waxes, the *n*-C_{30} δD signal is likely significantly impacted by large contributions (>50%) of very old waxes during some intervals. The large difference in age structure between these two chain lengths also suggests that disparities in chain length distribution between fresh and old wax pools can disproportionately affect the least concentrated compounds. Analysis of multiple homologs and/or compound classes would thus help to improve the robustness of interpretations of leaf wax stable isotope records. Furthermore, the potential for distortion of stable isotope records due to pre-aging of biomarkers is yet another argument for the use of multiple proxies for climate reconstruction.

Acknowledgements

This chapter is co-authored by Valier Galy and Konrad Hughen. I thank the NOSAMS staff, especially Ann McNichol and Al Gagnon, for their help with radiocarbon sample preparation and analysis, LacCore staff for assistance with core sampling, and Nick Hawco for

his help with river sample collection. This work was supported by an EPA STAR fellowship and an Ocean Ventures Fund grant to K.L.F.

References

Baker, P., Seltzer, G., Fritz, S., Dunbar, R., Grove, M., Tapia, P., Cross, S., Rowe, H., Broda, J., 2001. The history of South American tropical precipitation for the past 25,000 years. Science 291, 640.

Bird, B.W., Abbott, M.B., Rodbell, D.T., Vuille, M., 2011. Holocene tropical South American hydroclimate revealed from a decadally resolved lake sediment $\delta^{18}O$ record. Earth Planet. Sci. Lett. 310, 192–202.

Blard, P.-H., Sylvestre, F., Tripati, A., Claude, C., Causse, C., Coudrain, A., Condom, T., Seidel, J.-L., Vimeux, F., Moreau, C., Dumoulin, J.-P., Lavé, J., 2011. Lake highstands on the Altiplano (Tropical Andes) contemporaneous with Heinrich 1 and the Younger Dryas: new insights from ^{14}C, U–Th dating and $\delta^{18}O$ of carbonates. Quat. Sci. Rev. 30, 3973–3989.

Blard, P.H., Lavé, J., Sylvestre, F., Placzek, C.J., Claude, C., Galy, V., Condom, T., Tibari, B., 2013. Cosmogenic ^{3}He production rate in the high tropical Andes (3800 m, 20°S): Implications for the local last glacial maximum. Earth Planet. Sci. Lett. 377-378, 260–275.

Blodgett, T., Isacks, B., Lenters, J., 1997. Constraints on the origin of paleolake expansions in the central Andes. Earth Interact. 1, 1.

Cranwell, P., 1985. Long-chain unsaturated ketones in recent lacustrine sediments. Geochim. Cosmochim. Acta 49, 1545–1551.

Cross, S., Baker, P., Seltzer, G., Fritz, S., Dunbar, R., 2000. A new estimate of the Holocene lowstand level of Lake Titicaca, central Andes, and implications for tropical palaeohydrology. The Holocene 10, 21–32.

D'Agostino, K., Seltzer, G., Baker, P., Fritz, S., Dunbar, R., 2002. Late-Quaternary lowstands of Lake Titicaca: evidence from high-resolution seismic data. Palaeogeogr. Palaeoclimatol. Palaeoecol. 179, 97–111.

Douglas, P.M.J., Pagani, M., Eglinton, T.I., Brenner, M., Hodell, D.A., Curtis, J.H., Ma, K.F., Breckenridge, A., 2014. Pre-aged plant waxes in tropical lake sediments and their influence on the chronology of molecular paleoclimate proxy records. Geochim. Cosmochim. Acta 141, 346–364.

Drenzek, N.J., 2007. The temporal dynamics of terrestrial organic matter transfer to the oceans: initial assessment and application. PhD Thesis. MIT/WHOI Joint Program in Oceanography/Applied Ocean Science & Engineering.

Eglinton, G., Hamilton, R., 1967. Leaf epicuticular waxes. Science 156, 1322.

Erickson, C. L., 2000. The Lake Titicaca Basin: A Pre-Columbian built landscape. In *Imperfect balance: Landscape transformations in the Precolumbian Americas*, D. Lentz, Ed., Columbia University Press, 311-356.

Farabaugh, R.L., 2005. Climatic Influence on Sedimentology and Geomorphology of the Rio Ramis Valley, Peru. J. Sediment. Res. 75, 12–28.

Fernandez, A., Santos, G.M., Williams, E.K., Pendergraft, M.A., Vetter, L, Rosenheim, B.E., 2014. Blank Corrections for Ramped Pyrolysis Radiocarbon Dating of Sedimentary and Soil Organic Carbon. Anal. Chem. 86, 12085-12092.

Fornace, K.L., Hughen, K.A., Shanahan, T.M., Fritz, S.C., Baker, P.A., Sylva, S.P., 2014. A 60,000-year record of hydrologic variability in the Central Andes from the hydrogen isotopic composition of leaf waxes in Lake Titicaca sediments. Earth Planet. Sci. Lett. 408, 263–271.
Fritz, S., Baker, P., Seltzer, G., Ballantyne, A., Tapia, P., Cheng, H., Edwards, R., 2007. Quaternary glaciation and hydrologic variation in the South American tropics as reconstructed from the Lake Titicaca drilling project. Quat. Res. 68, 410–420.
Galy, V., Eglinton, T., 2011. Protracted storage of biospheric carbon in the Ganges-Brahmaputra basin. Nature Geosci. 4, 843–847.
Galy, V., Eglinton, T., unpublished data.
Garreaud, R., Vuille, M., Clement, A., 2003. The climate of the Altiplano: observed current conditions and mechanisms of past changes. Palaeogeogr. Palaeoclimatol. Palaeoecol. 194, 5–22.
Gustafsson, O., van Dongen, B.E., Vonk, J.E., Dudarev, O.V., Semiletov, I.P., 2011. Widespread release of old carbon across the Siberian Arctic echoed by its large rivers. Biogeosciences 8, 1737–1743.
Hanselman, J., Bush, M., Gosling, W., Collins, A., Knox, C., Baker, P., Fritz, S., 2011. A 370,000-year record of vegetation and fire history around Lake Titicaca (Bolivia/Peru). Palaeogeogr. Palaeoclimatol. Palaeoecol. 305, 201-214.
Klein, A., Seltzer, G., Isacks, B., 1999. Modern and last local glacial maximum snowlines in the Central Andes of Peru, Bolivia, and Northern Chile. Quat. Sci. Rev. 18, 63–84.
Kusch, S., Rethemeyer, J., Schefuß, E., Mollenhauer, G., 2010. Controls on the age of vascular plant biomarkers in Black Sea sediments. Geochim. Cosmochim. Acta 74, 7031–7047.
Paduano, G., Bush, M., Baker, P., Fritz, S., Seltzer, G., 2003. A vegetation and fire history of Lake Titicaca since the Last Glacial Maximum. Palaeogeogr. Palaeoclimatol. Palaeoecol. 194, 259–279.
Plante, A.F., Fernández, J.M., Haddix, M.L., Steinweg, J.M., Conant, R.T., 2011. Biological, chemical and thermal indices of soil organic matter stability in four grassland soils. Soil Biol. Biochem. 43, 1051–1058.
Rasmussen, S.O., Andersen, K.K., Svensson, A.M., Steffensen, J.P., Vinther, B.M., Clausen, H.B., Siggaard-Andersen, M.-L., Johnsen, S.J., Larsen, L.B., Dahl-Jensen, D., Bigler, M., Röthlisberger, R., Fischer, H., Goto-Azuma, K., Hansson, M.E., Ruth, U., 2006. A new Greenland ice core chronology for the last glacial termination. J. Geophys. Res 111, D06102.
Rigsby, C., Baker, P., Aldenderfer, M., 2003. Fluvial history of the Rio Ilave valley, Peru, and its relationship to climate and human history. Palaeogeogr. Palaeoclimatol. Palaeoecol. 194, 165–185.
Roche, M. A., Bourges, J., Cortes, J. & Mattos, R., 1992. Climatology and hydrology of the Lake Titicaca basin. In *Lake Titicaca: A Synthesis of Limnological Knowledge*, C. Dejoux, A. Iltis, Eds., Kluwer Academic Publishing, 63-88.
Rosenheim, B.E., Day, M.B., Domack, E., Schrum, H., Benthien, A., Hayes, J.M., 2008. Antarctic sediment chronology by programmed-temperature pyrolysis: Methodology and data treatment. Geochem. Geophys. Geosyst. 9, Q04005.
Rosenheim, B.E., Galy, V., 2012. Direct measurement of riverine particulate organic carbon age structure. Geophys. Res. Lett 39, L19703.
Rowe, H.D., Guilderson, T.P., Dunbar, R.B., Southon, J.R., Seltzer, G.O., Mucciarone, D.A., Fritz, S.C., Baker, P.A., 2003. Late Quaternary lake-level changes constrained by radiocarbon and stable isotope studies on sediment cores from Lake Titicaca, South America.

Global Planet. Change 38, 273–290.
Smittenberg, R., Eglinton, T., Schouten, S., Damsté, J., 2006. Ongoing buildup of refractory organic carbon in boreal soils during the Holocene. Science 314, 1283–1286.
Soulet, G., Skinner, L.C., Beaupré, S.R., Galy, V., 2015. A note on reporting of reservoir ^{14}C disequilibria and age offsets. Radiocarbon, in press.
Tao, S., Eglinton, T.I., Montluçon, D.B., McIntyre, C., Zhao, M., 2015. Earth and Planetary Science Letters. Earth Planet. Sci. Lett. 414, 77–86.
Theissen, K., Zinniker, D., Moldowan, J., Dunbar, R., Rowe, H., 2005. Pronounced occurrence of long-chain alkenones and dinosterol in a 25,000-year lipid molecular fossil record from Lake Titicaca, South America. Geochim. Cosmochim. Acta 69, 623–636.
Torn, M.S., Swanston, C.W., Castanha, C., Trumbore, S.E., 2009. Storage and Turnover of Organic Matter in Soil. In *Biophysico-Chemical Processes Involving Natural Nonliving Organic Matter in Environmental Systems*, N. Senesi, B. Xing, P.M. Huang, Eds., John Wiley & Sons, Inc., 219–272.

Table 1. LT01 sediment horizon descriptions.

Hole	Section	Top depth (cm)	Bottom depth (cm)	Total depth[1] (midpoint, cm below lake floor)	Sediment extracted (g)
2B	2H1	2	4	26	5.3
2B	2H1	72	74	96	9.4
2B	2H1	120	124	145	6.1
2B	2H1	142	144	166	2.7
2B	2H1	146	148	170	2.3
2B	2H2	74	78	250	11.9
2B	2H2	78	82	254	5.2
2B	2H2	93	98	271.5	12.9
2B	2H2	98	102	274	3.6
2A	1H2	33	38	383.5	24.6
2A	1H2	43	48	393.5	26.7
2A	1H2	53	58	403.5	19.1
2A	1H2	103	108	453.5	19.4
2A	1H2	108	113	458.5	23.1

1. 2B equivalent depth for 2A samples.

Table 2. River site and sediment descriptions.

River	Collection date	Latitude	Longitude	Distance from lake[1] (km)	Sediment type	Volume filtered (L)	Sediment weight (g)
Ramis	3/23/2014	15.295°S	69.978°W	35	Suspended	106	22.7
					Bank	n/a	52.2
Ilave	3/25/2014	16.088°S	69.632°W	31	Suspended	113	0.2
					Bank	n/a	52.0

1. Approximate distance of collection site upstream of river outlet to lake.

Table 3. LT01 alkenone radiocarbon data. Gray italics indicate likely contaminated sample.

Sample	Depth (cm)	Mass C (μg)	Raw F_m	Raw F_m error	Corrected F_m	Corrected F_m error	^{14}C Age
2B 2H1-2	26	392.2	0.6484	0.0018	0.6498	0.0019	3463
2B 2H1-72	96	233.4	0.5044	0.0020	0.5060	0.0022	5472
2B 2H1-118	142	125.5	0.4443	0.0022	0.4468	0.0026	6472
2B 2H1-140	164	88.6	0.3965	0.0018	0.3995	0.0025	7371
2B 2H2-98	*274*	*212.4*	*0.2928*	*0.0015*	*0.2935*	*0.0016*	*9848*

Table 4. Ramped pyrolysis-oxidation radiocarbon and stable carbon isotope data.

Sample	Depth (cm)	Fraction	T_1 (°C)	T_2 (°C)	Mass C (μg)	F_m	F_m error	^{14}C Age (yr BP)	$\delta^{13}C$ (‰ VPDB)
2B 2H2-78	254	1	110	282	150.7	0.2730	0.0013	10450	-26.66
		2	282	329	180.0	0.2725	0.0013	10450	-25.86
		3	329	386	256.2	0.2757	0.0015	10350	-24.01
		4	386	476	145.4	0.2660	0.0014	10650	-23.99
		5	476	706	79.3	0.2562	0.0027	10950	-25.19
2A 1H2-53	403.5	1	125	297	145.4	0.1952	0.0012	13100	-29.43
		2	297	361	140.6	0.1899	0.0013	13350	-28.09
		3	361	429	144.8	0.1688	0.0013	14300	-28.41
		4	429	497	152.6	0.1084	0.0013	17850	-28.01
		5	497	627	178.0	0.0746	0.0012	20800	-28.09
2A 1H2-103	453.5	1	126	289	132.6	0.1965	0.0013	13050	-31.45
		2	289	359	177.2	0.1889	0.0015	13400	-29.02
		3	359	420	151.6	0.1703	0.0014	14200	-28.31
		4	420	551	338.1	0.0996	0.0012	18550	N/A
		5	551	700	80.4	0.0979	0.0020	18650	-27.48

Table 5. Revised chronology for LT01 sediment horizons.

Sample	Depth (cm)	Revised ^{14}C age (yr BP)	^{14}C age error (yr)	Original ^{14}C age (yr BP)	Revised calendar age range (yr BP)	Original calendar age (yr BP)
2B 2H1-2	26	3463	23	3438	3614-3703	3654
2B 2H1-72	96	5472	34	5910	6209-6284	6678
2B 2H1-120	145	6594	46	7640	7419-7561	8795
2B 2H1-142	166	7453	50	8381	8175-8328	9702
2B 2H1-146	170	7616	68	8523	8321-8448	9875
2B 2H2-74	250	10191	67	11347	11629-11962	13331
2B 2H2-78	254	10350	44	11489	11969-12368	13504
2B 2H2-93	271.5	N/A	N/A	12107	N/A	14260
2B 2H2-98	274	N/A	N/A	12195	N/A	14368
2A 1H2-33	383.5	12669	426	16061	14166-15534	19098
2A 1H2-43	393.5	12669	426	16414	14166-15534	19530
2A 1H2-53	403.5	12669	426	16768	14166-15535	19962
2A 1H2-103	453.5	12669	426	18533	14166-15536	22122
2A 1H2-108	458.5	12669	426	18710	14166-15537	22246

Table 6. Reported and calculated radiocarbon results for individual wax chain lengths. Gray italics indicate excluded measurements due to suspected contamination. All ages are in calendar or radiocarbon years before present.

Sample name	Sediment calendar age	Sediment ^{14}C age	Chain length	Mass (μg)	Raw F_m	Raw F_m error	Corrected F_m	Total F_m error	Wax ^{14}C age	Wax ^{14}C age error	$F^{14}R_{wax}$	$F^{14}R_{wax}$ error
Ramis filter (RRF)	-64	-373[1]	26	22.8	0.7831	0.0050	0.902	0.029	830	260	0.861	0.028
			28	20.9	0.8072	0.0070	0.939	0.034	510	290	0.896	0.033
			30-32	18.1	0.6846	0.0061	0.799	0.035	1810	350	0.762	0.033
Ramis bank (RRB)	-64	-373[1]	26	28.3	0.7803	0.0044	0.879	0.022	1040	200	0.839	0.021
			28	27.2	0.8361	0.0046	0.946	0.025	450	210	0.903	0.024
			30-32	19.0	0.7429	0.0055	0.867	0.035	1140	330	0.828	0.034
Ilave bank (RIB)	-64	-373[1]	26	88.2	0.8324	0.0031	0.887	0.007	967	66	0.846	0.007
			28	79.6	0.8869	0.0026	0.946	0.008	447	69	0.903	0.008
			30-32	30.7	0.8238	0.0047	0.918	0.021	680	190	0.877	0.020
2B 2H1-2	3669	3463	26	84.0	0.3983	0.0022	0.417	0.005	7020	100	0.642	0.008
			28	22.9	0.6092	0.0054	0.686	0.024	3030	280	1.056	0.036
			30-32	21.3	0.4606	0.0053	0.505	0.022	5480	350	0.778	0.034
2B 2H1-72	6238	5472	26	46.6	0.4334	0.0031	0.460	0.009	6240	160	0.909	0.018
			28	21.3	0.4323	0.0056	0.472	0.022	6040	370	0.932	0.043
			30-32	16.1	0.3118	0.0071	0.321	0.029	9120	720	0.635	0.057
2B 2H1-120	7463	6594	26	49.5	0.3927	0.0030	0.414	0.008	7080	160	0.940	0.020
			28-32	25.1	0.3356	0.0043	0.351	0.017	8420	390	0.796	0.038
2B 2H1-142	8243	7453	26	41.1	0.3467	0.0034	0.363	0.010	8140	220	0.918	0.026
			30-32	*15.9*	*0.2239*	*0.0068*	*0.205*	*0.030*	*12740*	*1180*	*0.518*	*0.076*
2B 2H1-146	8382	7616	28-32	36.9	0.3608	0.0046	0.379	0.012	7810	250	0.977	0.031
2B 2H2-74	11784	10191	28	47.2	0.2153	0.0027	0.215	0.009	12360	320	0.764	0.031
			30-32	*49.6*	*0.1083*	*0.0027*	*0.096*	*0.009*	*18850*	*740*	*0.340*	*0.031*
2B 2H2-78	12095	10350	26	254.4	0.2620	0.0013	0.271	0.002	10480	60	0.984	0.008
			28	84.3	0.2613	0.0020	0.268	0.005	10570	140	0.973	0.018
			30	42.9	0.2670	0.0060	0.262	0.030	10770	920	0.95	0.11

2B 2H2-93	*n/a*	*n/a*	*28*	*93.7*	*0.2791*	*0.0021*	*0.288*	*0.004*	*10010*	*120*	*n/a*	*n/a*
			30-32	*43.9*	*0.2708*	*0.0032*	*0.276*	*0.009*	*10350*	*270*	*n/a*	*n/a*
2B 2H2-98	*n/a*	*n/a*	*28*	*53.6*	*0.2805*	*0.0027*	*0.288*	*0.008*	*10000*	*210*	*n/a*	*n/a*
			30-32	*33.1*	*0.2184*	*0.0037*	*0.214*	*0.013*	*12390*	*480*	*n/a*	*n/a*
2A 1H2-33	14891	12243-13095	26	19.8	0.1781	0.0055	0.155	0.024	15000	1220	0.75	0.12
			28-32	*47.9*	*0.0960*	*0.0027*	*0.082*	*0.009*	*20140*	*910*	*0.394*	*0.047*
2A 1H2-43	14166-15534	12243-13095	28-32	35.0	0.1946	0.0034	0.188	0.012	13450	510	0.908	0.063
2A 1H2-53	14166-15534	12243-13095	28-32	18.7	0.2434	0.0049	0.235	0.024	11640	820	1.14	0.12
2A 1H2-103	14166-15534	12243-13095	28-32	21.0	0.2235	0.0045	0.212	0.021	12450	790	1.03	0.11
2A 1H2-108	14166-15534	12243-13095	26	16.4	0.2021	0.0059	0.178	0.029	13860	1310	0.86	0.14
			28-32	25.2	0.2114	0.0038	0.202	0.017	12870	680	0.976	0.086

1. Calculated with average of 2010-2011 atmospheric F_m measurements (1.0475, n = 10) from Hua et al. (2013).

Table 7. Hydrogen isotopic composition of FAMEs from river samples.

River	Sediment type	Compound	δD (‰ VSMOW)	Error (1σ, ‰)
Ramis	Suspended (filter)	*n*-C_{24}	-208	4.4
		n-C_{26}	-213	4.1
		n-C_{28}	-212	2.8
		n-C_{30}	-189	3.1
Ramis	Bank	*n*-C_{24}	-223	3.5
		n-C_{26}	-229	3.1
		n-C_{28}	-226	3.1
		n-C_{30}	-212	3.0
Ilave	Bank	*n*-C_{28}	-229	2.8
		n-C_{30}	-216	2.6
		n-C_{32}	-206	2.6

Table 8. Description of parameters for age structure simulation scenarios.

Scenario	σ_{dec} (yr)	μ_{dec} (yr)	σ_{mill} (yr)	μ_{mill} range (yr)	Millennial fraction average age range (yr)
1	20	0	5,000	0 - 10,000	3,986 - 10,276
2	20	0	10,000	0 - 20,000	7,976 - 20,552
3	20	0	20,000	0 - 40,000	15,954 - 40,821
4	20	0	---	>50,000	>50,000

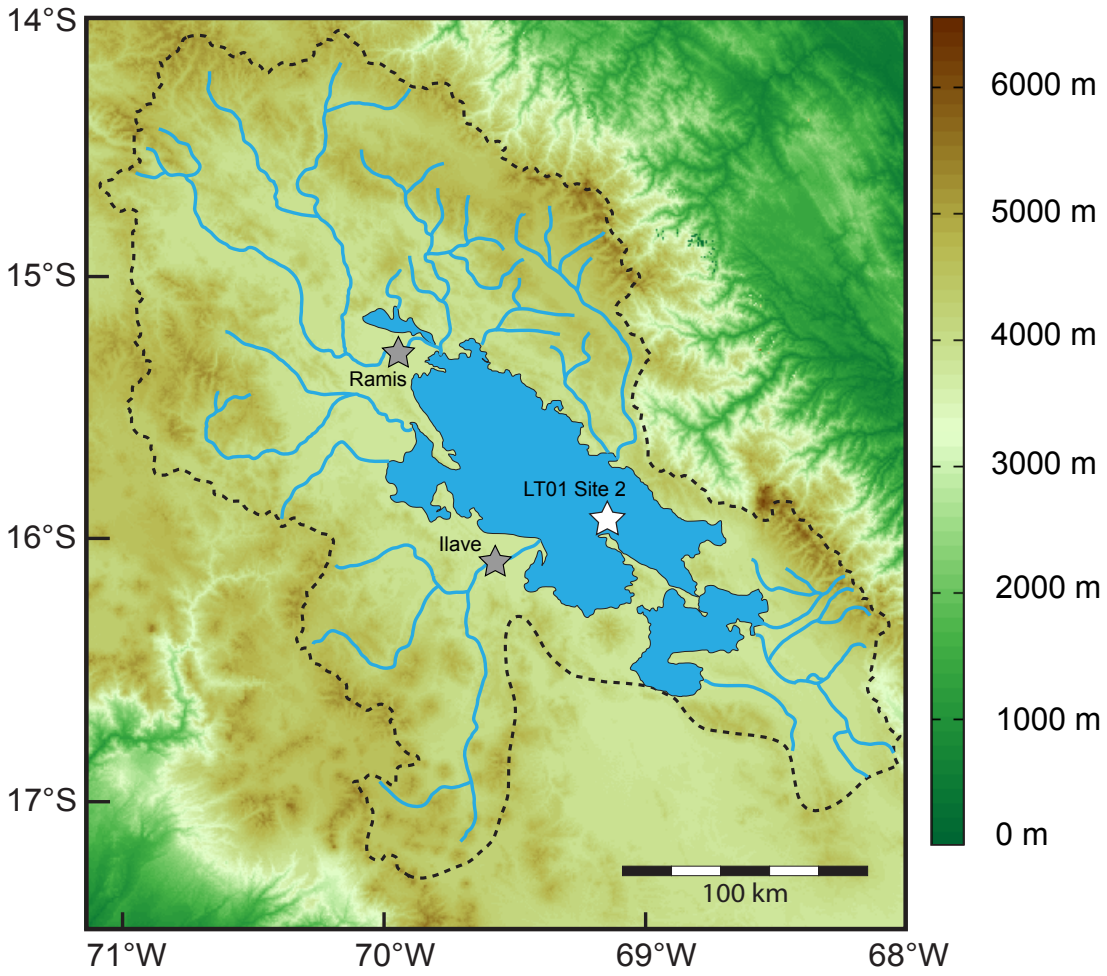

Figure 1. Map of Lake Titicaca watershed and river sampling and core sites. Gray stars indicate Ramis and Ilave river sampling locations and white star shows core site. Black dashed line shows approximate extent of lake drainage basin.

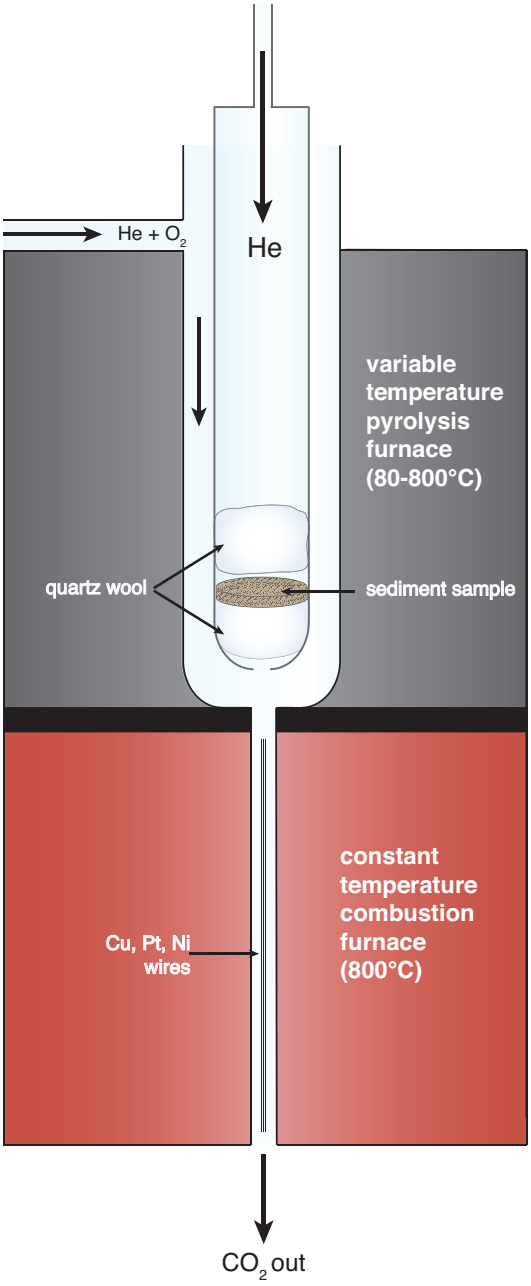

Figure 2. Schematic of ramped pyrolysis-oxidation (PyrOx) system. Sediment sample is heated at 5°C/min from 80°C to 800°C and volatile pyrolysis products are carried by constant He flow into oxygenated combustion furnace (800°C). Evolved CO_2 is then isolated and purified on vacuum line.

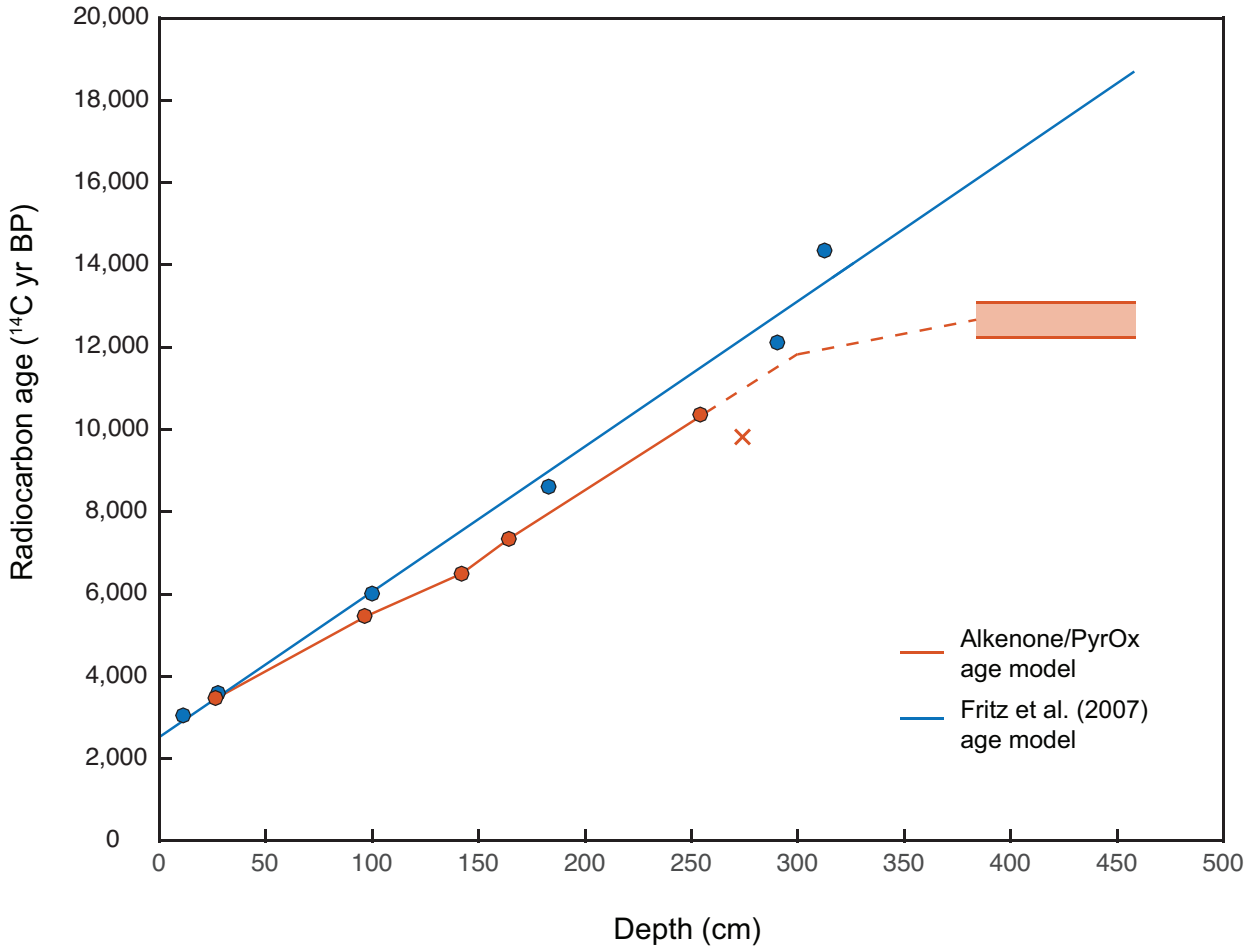

Figure 3. Comparison of age-depth models from Fritz et al. (2007) and this study. Bulk organic ^{14}C dates and linear regression from Fritz et al. (2007) are shown in blue. Alkenone and ramped pyrolysis-oxidation dates are shown by orange circles. The orange line shows the linearly interpolated age-depth model used to assign sediment age, while the dashed line shows a possible age-depth curve for the deglacial interval. The orange shaded box shows the age range for 383.5-458.5 cm horizons constrained by ramped pyrolysis-oxidation. The alkenone ^{14}C date excluded from the age model due to likely contamination is indicated by an x.

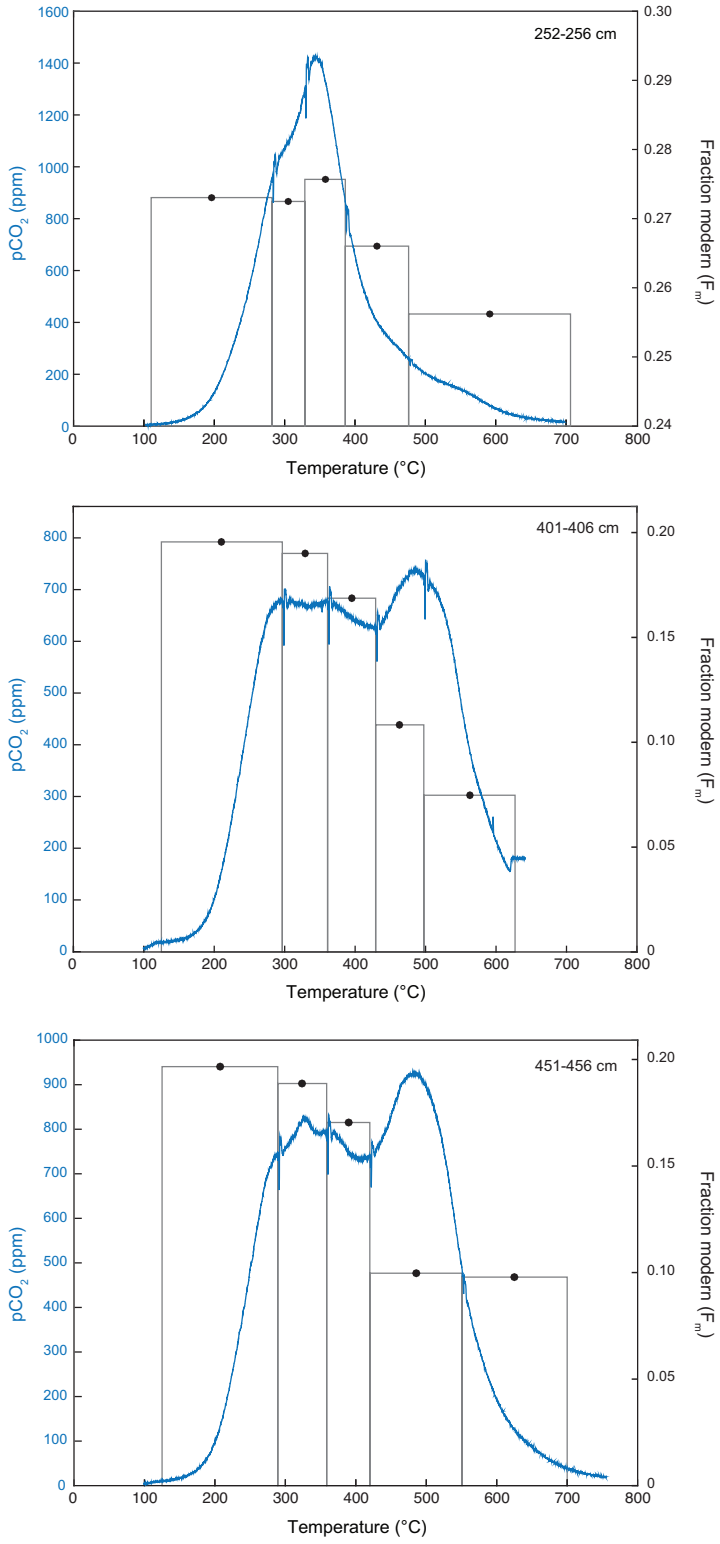

Figure 4. Thermograms from ramped pyrolysis-oxidation (PyrOx) analysis of LT01 sediments. From top: 252-256 cm, 401-406 cm, 451-456 cm sediment horizons.

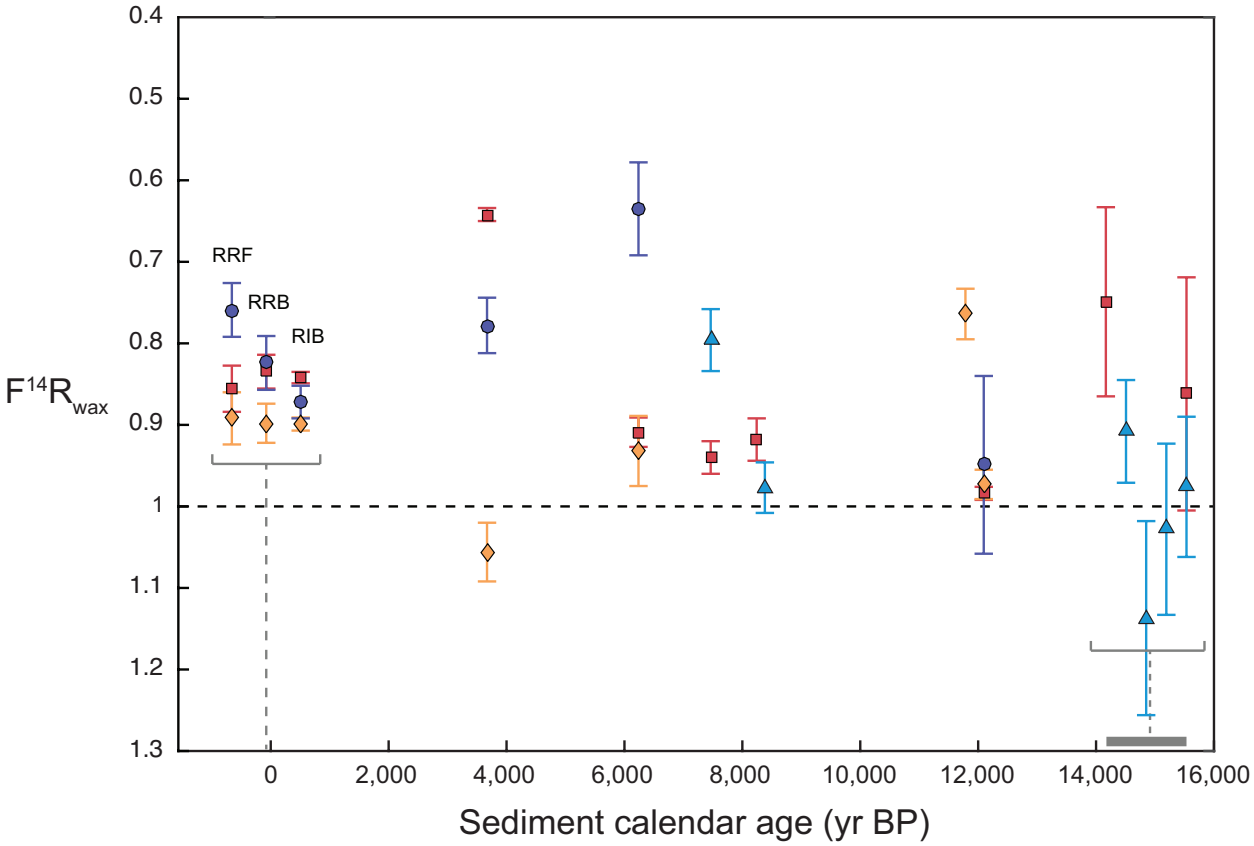

Figure 5. Time series of all measured Titicaca *n*-alkanoic acid $F^{14}R_{wax}$ values vs. sediment horizon age, including *n*-C_{26} (red squares), *n*-C_{28} (orange diamonds), *n*-C_{30}-C_{32} (purple circles), and *n*-C_{28}-C_{32} (blue triangles). Modern river samples include Ramis filter sediment (RRF), Ramis bank sediment (RRB), and Ilave bank sediment (RIB). Error bars represent 1σ analytical uncertainty. Uncertainty in glacial horizon age is shown with gray bar.

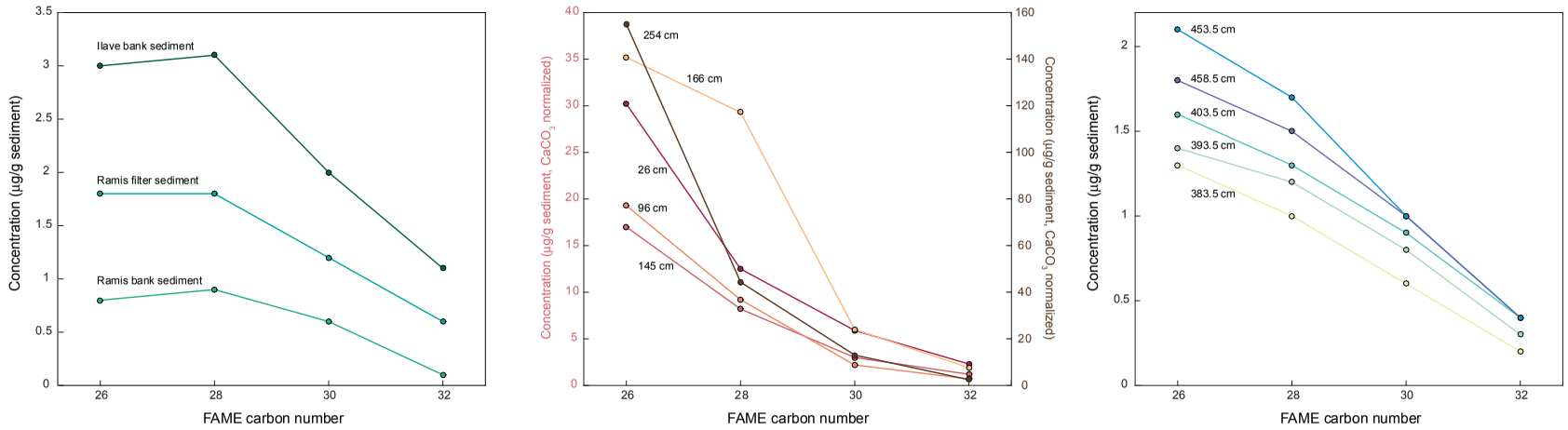

Figure 6. Concentrations of FAME homologs in river sediments (left), Holocene and deglaciation sediments (middle), and glacial sediments (right). Note that in middle plot, concentration data for the 254 cm horizon is plotted on secondary (right) y-axis.

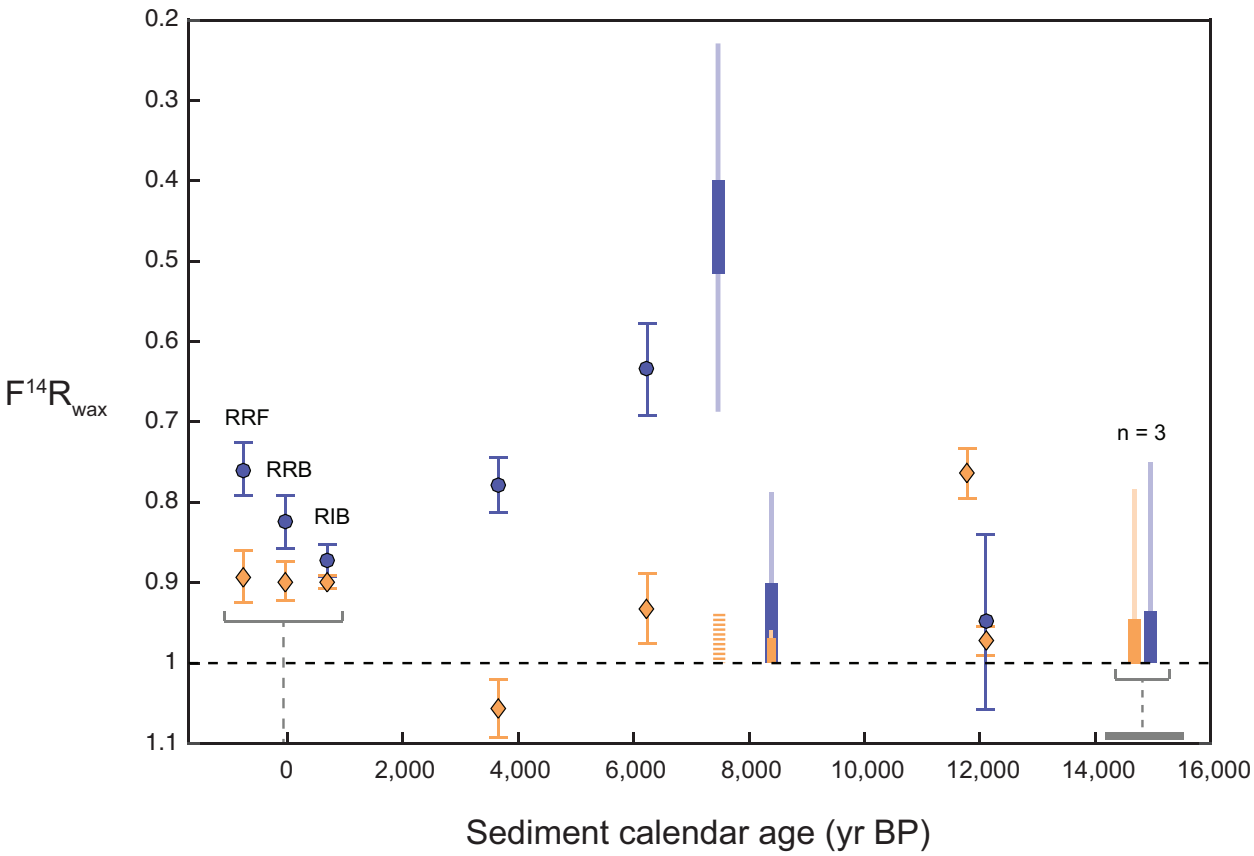

Figure 7. Time series of Titicaca measured and calculated *n*-C_{28} and *n*-C_{30}-C_{32} $F^{14}R_{wax}$ values vs. sediment horizon age. Measured values for *n*-C_{28} and *n*-C_{30}-C_{32} are shown in orange diamonds and purple circles, respectively. Calculated ranges for *n*-C_{28} and *n*-C_{30}-C_{32} are shown in orange and purple bars, respectively. The dashed orange bar at 7.5 ka represents estimated *n*-C_{28} $F^{14}R_{wax}$ as derived from *n*-C_{26} value. *n*-C_{28} and *n*-C_{30}-C_{32} values for glacial horizons (14.2-15.5 ka) represent the average of 3 samples. Error bars represent 1σ analytical uncertainty.

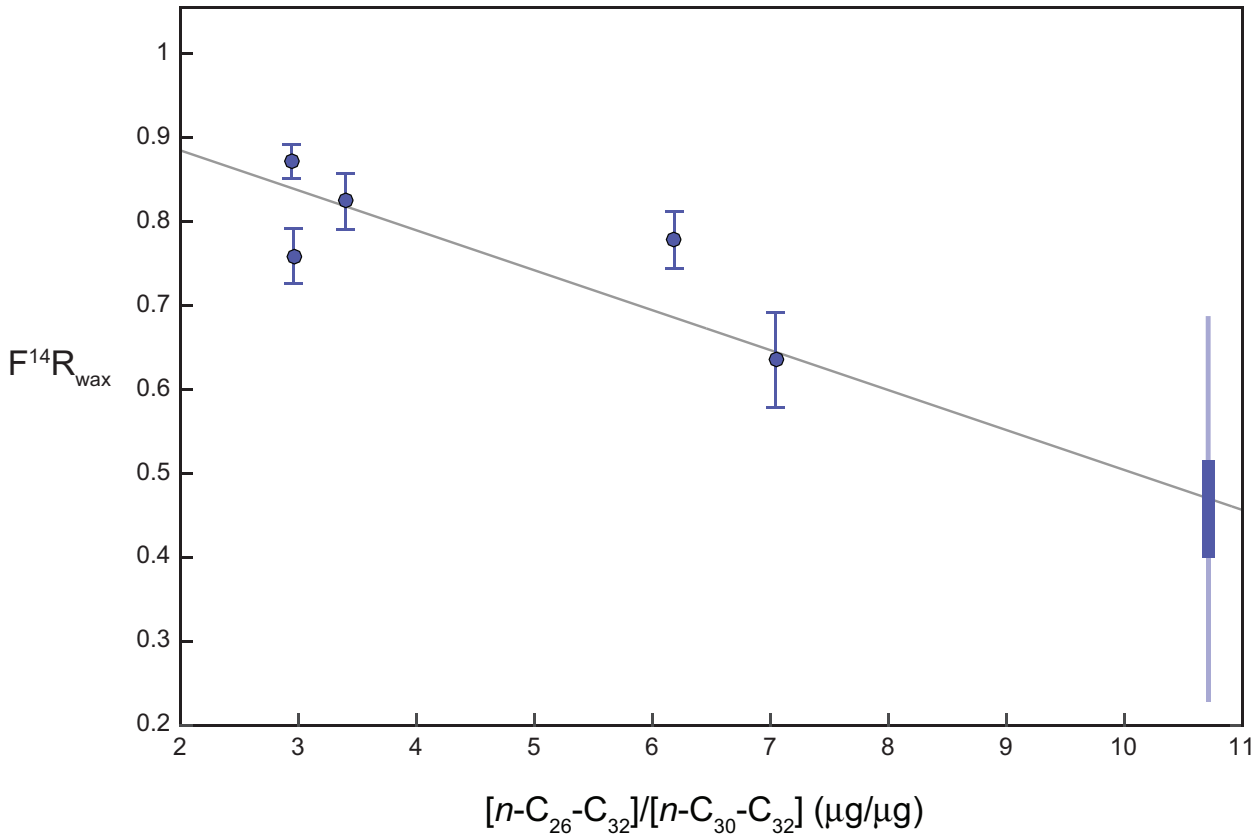

Figure 8. Plot of *n*-C_{30}-C_{32} $F^{14}R_{wax}$ values vs. inverse concentration of *n*-C_{30}-C_{32} in total (*n*-C_{26}-C_{30}) long-chain FAME pool for modern river samples and <8 ka Holocene sediment horizons.

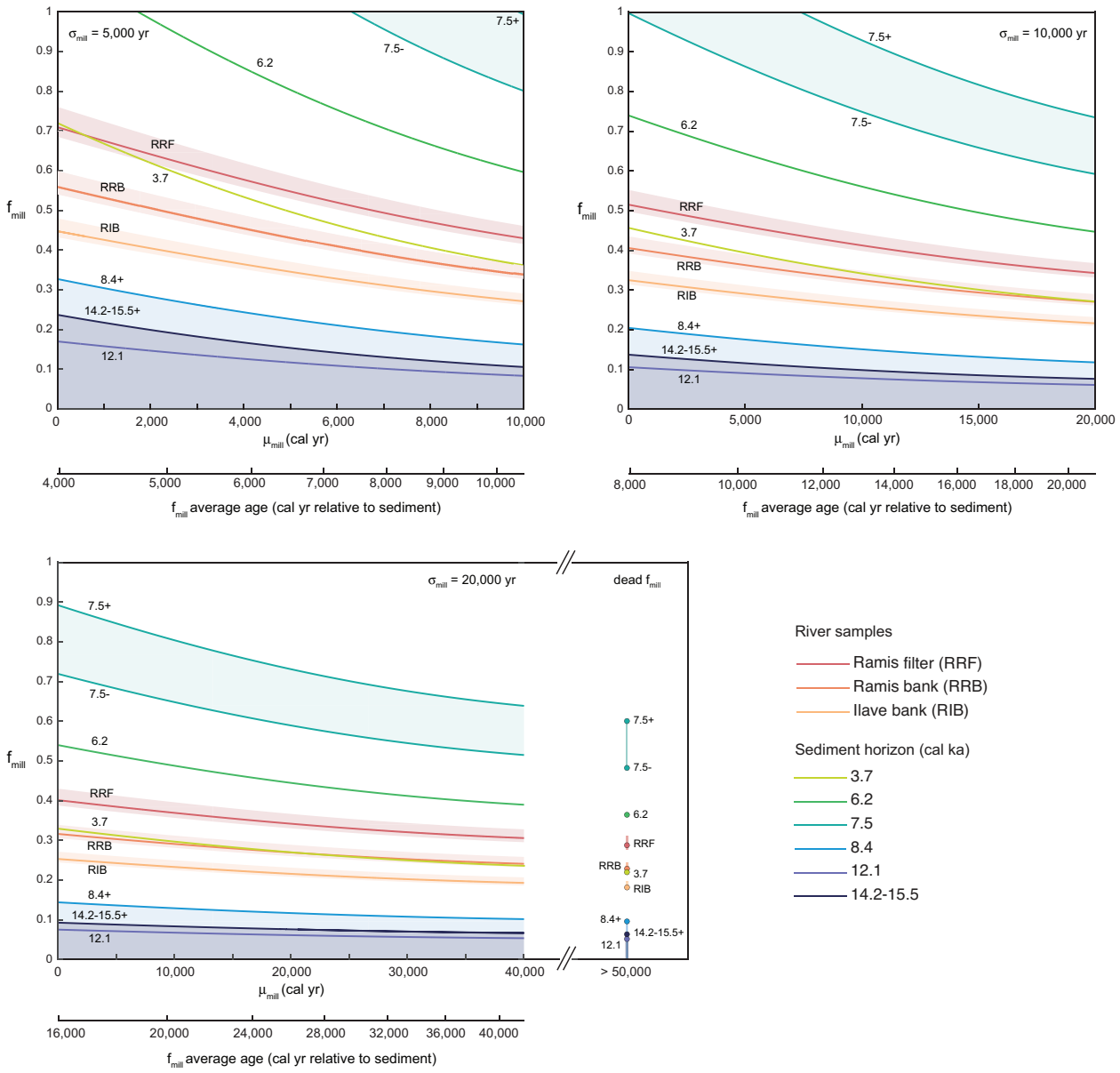

Figure 9. Calculated ranges of f_{mill} values for *n*-C_{30}-C_{32} as a function of millennial fraction age offset (μ_{mill}) for different standard deviation (σ_{mill}) values. Top left: σ_{mill} = 5,000 yr, top right: σ_{mill} = 10,000 yr, bottom left: σ_{mill} = 20,000 yr, bottom right: radiocarbon dead millennial fraction end member. Lines are labeled with sample sediment horizon age, and +/- signs represent maximum and minimum f_{mill} for samples with calculated $F^{14}R_{wax}$ ranges. Shading around lines corresponding to river samples represents range of f_{mill} for range of decadal fraction F_m of 1.05-1.16 (σ_{dec} = 0-40 yr).

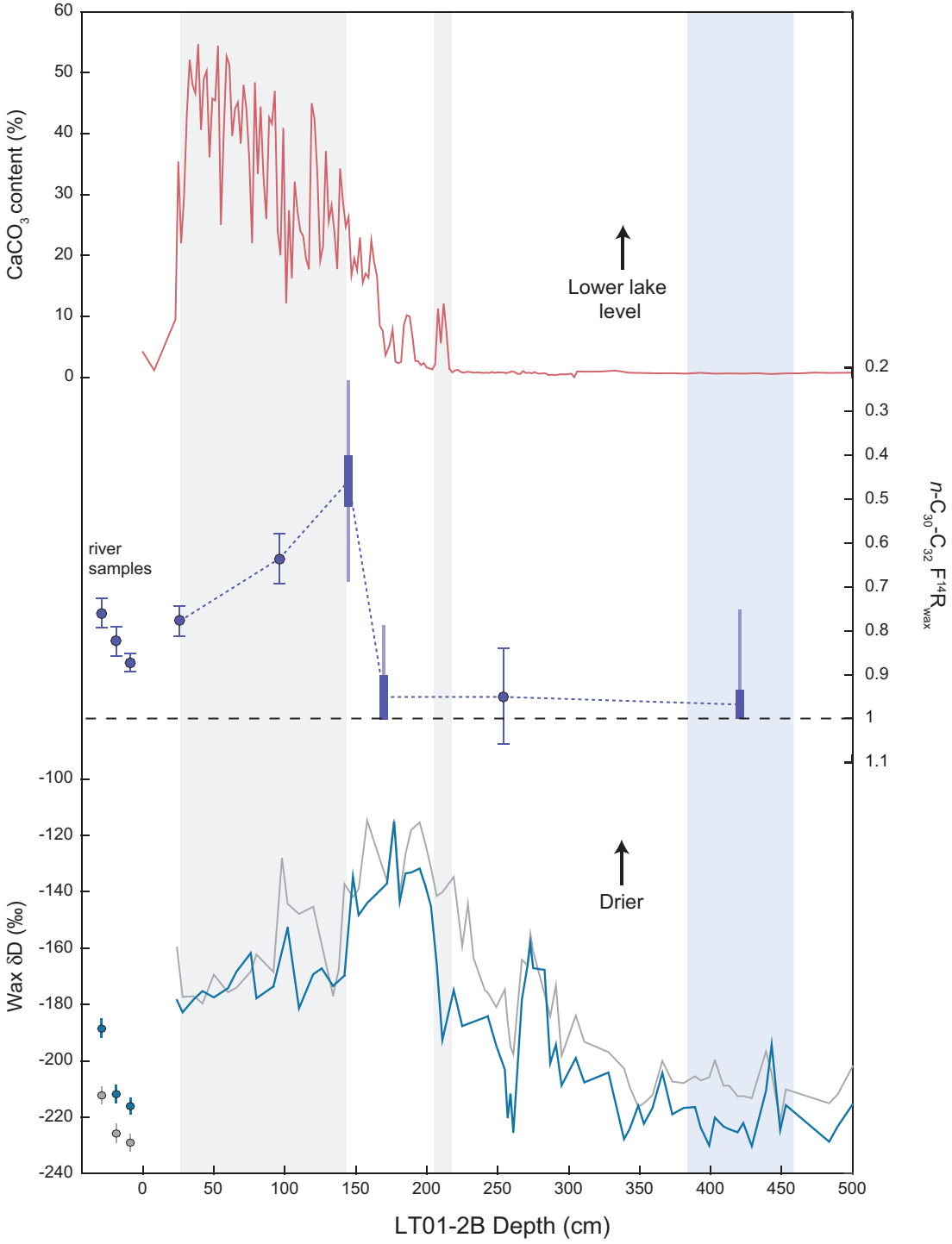

Figure 10. Comparison of *n*-C_{30}-C_{32} $F^{14}R_{wax}$ values and other LT01-2B sediment proxies. From top: $CaCO_3$ content (Fritz et al., 2007); *n*-C_{30}-C_{32} $F^{14}R_{wax}$; *n*-C_{30} (blue) and *n*-C_{28} (gray) δD (Fornace et al., 2014). $F^{14}R_{wax}$ and δD data for river samples are plotted to the left of the LT01-2B depth axis. Blue shading shows glacial horizon depths, and gray shading highlights periods of lower lake level discussed in text.

Chapter 6. Concluding remarks

The work presented in the preceding chapters has potential significance for both our understanding of connections between past and future climate and carbon cycle variability as well as the tools we use to study these questions. Climate reconstructions from the Altiplano and Pantanal presented in Chapters 2 and 3, respectively, provide new perspectives on long-term controls of South American Summer Monsoon dynamics since the last glacial period. Both records show that the transition from the last glacial period to the Holocene caused major changes in SASM precipitation patterns. However, differences in glacial-interglacial precipitation trends between the two sites offer clear evidence of heterogeneous regional expressions of SASM variability. The complex relationship between regional SASM precipitation and global temperature change is also reflected in conflicting results from different regional and global climate modeling simulations of future precipitation trends for both the Altiplano and Pantanal (e.g., Marengo et al., 2009; Minvielle and Garreaud, 2011; Thibeault et al., 2010). Future studies of past climate variability at different sites throughout the southern hemisphere South American tropics, particularly in underrepresented areas like the Amazon Basin, will thus help to elucidate the fundamental controls on SASM precipitation.

The results of radiocarbon analysis of leaf waxes in Cariaco Basin and Lake Titicaca sediments presented in Chapters 4 and 5 reveal a multicomponent age structure reflecting contributions from both fresh (age < ~100 years) and old (age > ~5000 years) terrestrial pools. These pools are likely derived from standing vegetation/leaf litter/young soil organic matter and aged soil organic matter, respectively. Comparison of wax age structures to the climate history of the Cariaco catchment clearly shows that hydrologic variability is a significant control on mobilization and transport of fresh terrestrial carbon to the ocean, a conclusion also supported by

data from Lake Titicaca. Results from Lake Titicaca also provide evidence of a link between hydrologic variability and the mobilization of very old terrestrial biospheric carbon. Together these two studies demonstrate that climate-driven erosion and transport of biospheric terrestrial carbon constitute a potentially significant climate feedback mechanism. Based on the positive relationship between global temperature and hydrologic cycle intensity (IPCC, 2013), a link between increased precipitation and increased export of fresh vegetation-derived carbon likely represents a negative climate feedback on geologic timescales (Figure 1).

Assessing the magnitude and direction of this feedback on shorter timescales (e.g., decades to centuries) will require further study in a range of locations, as well as a better understanding of the fate of terrestrial organic matter in the ocean. The main uncertainty is the relative rates of organic carbon respiration during transport of biospheric carbon through the rivers to the coastal ocean versus in terrestrial reservoirs. If, for instance, the vast majority of terrestrial organic carbon is quickly respired before it can be buried in marine sediments, then the "cost" (i.e., flux of CO_2 to the atmosphere) associated with mobilization would likely be greater than the cost of remaining in soils. Recent estimates of the average residence time of organic carbon in the terrestrial biosphere range from 14 to 65 years for different ecosystems with a global average of 22.5 years (Carvalhais et al., 2014). These estimates are comparable to soil carbon turnover times ranging from 10-520 years (global average: 32 years) derived from soil respiration rate measurements (Raich and Schlesinger, 1992), as well as an average of ~50 years for bulk soil organic matter turnover in temperate ecosystems from 20 long-term (multiyear) field experiments (Schmidt et al., 2011). Assuming steady state conditions and that the rate of organic carbon respiration scales linearly with concentration, and excluding losses from wildfires or transport processes, these rate estimates imply that ~1-10% of vegetation-derived organic

carbon transferred to soil will be respired within one year. In comparison, based on recent estimates of global remineralization rates in rivers (Aufdenkampe et al., 2011) and in the coastal ocean (Blair and Aller, 2012), the majority (~80-90%) of biospheric organic carbon that enters rivers is respired before it can be preserved in marine sediments. However, these estimates are not well constrained and may vary significantly in different coastal systems. Moreover, the average transit time of biospheric carbon between land and marine sediments is not known, preventing estimation of a true rate of respiration of mobilized biospheric carbon.

In recent years, many within the soil science community have been considering similar issues as they try to assess the net impact of agriculture-driven soil erosion and organic carbon mobilization. While some have argued that soil carbon mobilization results in a net positive flux of CO_2 to the atmosphere due to enhanced respiration during the transport process (e.g., Lal, 2003), others maintain that soil erosion represents a significant carbon sink (~1 Pg/year, enough to offset ~10% of annual fossil fuel emissions; Berhe et al., 2013) due to organic carbon burial and preservation in deposition centers. However, these arguments generally do not consider the complex processing of biospheric carbon in freshwater and coastal systems. Assessing the movement and transformations of biospheric carbon at each point along the path from vegetation/soil to marine sediments is thus a key direction for future research and important opportunity for collaboration between the soil science and oceanography communities.

Finally, the fact that each chapter of this thesis represents a different application of leaf wax isotopic signatures is a testament to the power of these proxies for investigating past climate and terrestrial carbon cycle variability. However, the results of the preceding chapters also offer important perspective on the nuances of leaf wax isotopic signatures that should be considered in future studies. In Chapter 3, I presented evidence that vegetation composition can be the

dominant influence on leaf wax δD, complicating the reconstruction of precipitation δD signals. Furthermore, as shown in Chapter 4 and 5, the mobilization of both fresh and very old leaf waxes from the terrestrial biosphere affects the amplitude and timing of leaf wax stable isotope signals. While leaf wax stable isotope records from Cariaco Basin and Lake Titicaca do not show significant distortion due to age-biasing, contributions of aged waxes may be more important at higher latitude sites with larger reservoirs of aged biospheric carbon (e.g., permafrost). Such complications reaffirm one of the fundamental principles of paleoclimatology that regardless of initial enthusiasm, no climate proxy is without its limitations. However, increased awareness of these limitations will allow for more robust results of future leaf wax-based climate reconstructions.

References

Aufdenkampe, A.K., Mayorga, E., Raymond, P.A., Melack, J.M., Doney, S.C., Alin, S.R., Aalto, R.E., Yoo, K., 2011. Riverine coupling of biogeochemical cycles between land, oceans, and atmosphere. Front. Ecol. Environ. 9, 53–60.

Berhe, A.A., Harte, J., Harden, J.W., Torn, M.S., 2013. The Significance of the Erosion-induced Terrestrial Carbon Sink. BioScience 57, 337–346.

Blair, N., Aller, R., 2012. The Fate of Terrestrial Organic Carbon in the Marine Environment. Annu. Rev. Marine Sci. 4, 401-423.

Carvalhais, N., Forkel, M., Khomik, M., Bellarby, J., Jung, M., Migliavacca, M., Mu, M., Saatchi, S., Santoro, M., Thurner, M., Weber, U., Ahrens, B., Beer, C., Cescatti, A., Randerson, J.T., Reichstein, M., 2014. Global covariation of carbon turnover times with climate in terrestrial ecosystems. Nature 514, 213–217.

IPCC, 2013. *Climate Change 2013: The Physical Science Basis. Contribution of Working Group I to the Fifth Assessment Report,* T.F. Stocker, et al., Eds., Cambridge University Press.

Lal, R., 2003. Soil erosion and the global carbon budget. Environ. Int. 29, 437–450.

Marengo, J.A., Ambrizzi, T., da Rocha, R.P., Alves, L.M., Cuadra, S.V., Valverde, M.C., Torres, R.R., Santos, D.C., Ferraz, S.E.T., 2009. Future change of climate in South America in the late twenty-first century: intercomparison of scenarios from three regional climate models. Clim. Dyn. 35, 1073–1097.

Minvielle, M., Garreaud, R.D., 2011. Projecting Rainfall Changes over the South American Altiplano. J. Clim. 24, 4577–4583.

Raich, J.W., Schlesinger, W.H., 1992. The global carbon dioxide flux in soil respiration and its relationship to vegetation and climate. Tellus 44, 81–99.

Schmidt, M.W.I., Torn, M.S., Abiven, S., Dittmar, T., Guggenberger, G., Janssens, I.A., Kleber,

M., Kögel-Knabner, I., Lehmann, J., Manning, D.A.C., Nannipieri, P., Rasse, D.P., Weiner, S., Trumbore, S.E., 2011. Persistence of soil organic matter as an ecosystem property. Nature 478, 49–56.

Thibeault, J.M., Seth, A., Garcia, M., 2010. Changing climate in the Bolivian Altiplano: CMIP3 projections for temperature and precipitation extremes. J. Geophys. Res. 115, D08103.

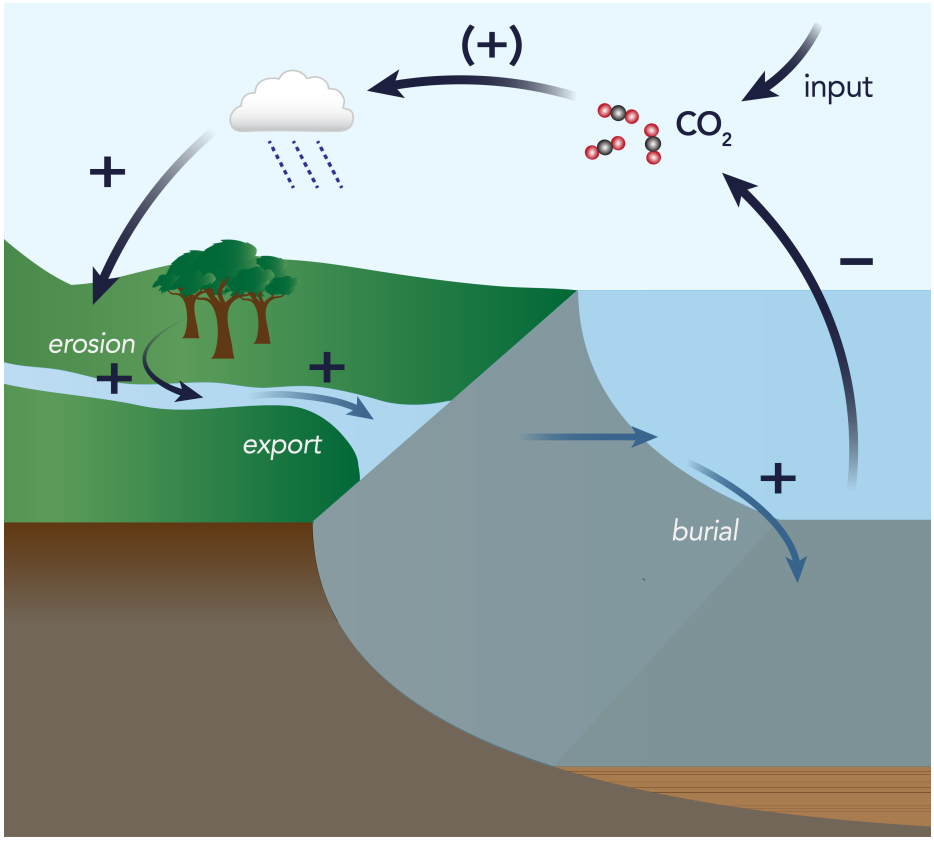

Figure 1. Schematic of climate-driven erosion feedback loop on geological timescales. Starting at top right, increased CO_2 leads to warmer global temperatures and increased precipitation globally (although precipitation trends vary regionally). Higher precipitation drives increased erosion, export, and burial of fresh terrestrial biospheric carbon in marine sediments. Increased sequestration of organic carbon in marine sediments then leads to lower atmospheric CO_2 concentrations.

Appendix 1: Blank characterization and correction for radiocarbon measurements

1. Assessment of combustion blanks

To assess the carbon added during the combustion process, a series of FAMEs ^{14}C standards of similar size to samples (~20-40 μg C) was transferred to quartz tubes and combusted using the same procedure as for samples (see Chapter 4). These CO_2 aliquots were submitted to NOSAMS for radiocarbon analysis. In total, three replicates of three standards with a range of F_m values were combusted (Table 1). However, one sample was lost during the combustion process due to a malfunctioning cracker.

Table 1. Combustion blank assessment sample description and results.

Compound	Predetermined F_m	Mass C combusted (μg)	F_m measured	F_m error (1σ)
n-C_{18}	1.1124	33.6	1.0617	0.0050
n-C_{18}	1.1124	25.5	1.0695	0.0081
n-C_{24}	0.5823	38.8	0.5785	0.0043
n-C_{24}	0.5823	24.8	0.5634	0.0062
n-C_{24}	0.5823	19.6	0.5627	0.0059
n-C_{30}	0	27.7	0.0102	0.0037
n-C_{30}	0	23.3	0.0052	0.0043
n-C_{30}	0	22.1	0.0061	0.0044

The blank contribution to the measured F_m value of an unknown sample can be represented as a mass balance equation:

$$m_m F_{m,m} = m_t F_{m,t} + m_{b,tot} F_{m,b} \quad (1)$$

where m_m is the measured mass of carbon, $F_{m,m}$ is the measured fraction modern, m_t is the true sample mass, $F_{m,t}$ is the true sample fraction modern, $m_{b,tot}$ is the total mass of blank carbon, and $F_{m,b}$ the fraction modern of the blank. The blank term can be split into modern ($F_m = 1$) and dead ($F_m = 0$) components for algebraic convenience:

$$m_m F_{m,m} = m_t F_{m,t} + m_{b,mod} F_{m,\,mod} + m_{b,dead} F_{m,dead} \quad (2)$$

which reduces to:

$$m_m F_{m,m} = m_t F_{m,t} + m_{b,mod} \quad (3)$$

In the case of the *n*-C_{30} ^{14}C dead standard ($F_{m,t} = 0$), equation (3) simplifies to:

$$m_m F_{m,m} = m_{b,mod} \quad (4)$$

and can be used to calculate the modern component of the blank (Table 2).

Table 2. Calculated values for modern blank mass from ^{14}C dead standards.

Measured mass (μg)	Modern blank mass (μg)	Error (1σ)
27.7	0.28	0.10
23.3	0.12	0.10
22.1	0.13	0.098
	Average: 0.18	0.10

Using this value of 0.18 μg for the modern blank mass, the remaining standards can be used to calculate the dead blank mass (Table 3). To solve for the dead blank mass, we can substitute $m_m - m_{b,mod} - m_{b,dead}$ (measured – blank mass) for the true mass (m_t) in equation 3.

$$m_m F_{m,m} = (m_m - m_{b,mod} - m_{b,dead}) F_{m,t} + m_{b,mod} \quad (5)$$

Rearranging this equation (5) to solve for $m_{b,dead}$:

$$m_{b,dead} = -\left(m_m F_{m,m} - m_{b,mod}\right) \Big/ F_{m,t} + m_m - m_{b,mod} \quad (6)$$

Table 3. Calculated values for dead blank mass.

Compound	Measured mass (μg)	Dead blank mass (μg)	Error (1σ)
n-C_{18}	33.6	1.52	0.17
n-C_{18}	25.5	0.97	0.19
n-C_{24}	38.8	0.38	0.29
n-C_{24}	24.8	0.94	0.27
n-C_{24}	19.6	0.79	0.20
		Average: 0.92	0.23

Thus, the total combustion blank mass ($m_{b,dead} + m_{b,mod}$) is 1.1 ± 0.3 μg with a F_m value ($m_{b,mod}/m_{b,tot}$) of 0.16 ± 0.09.

2. Assessment of PCGC process blanks

To assess the carbon added during fraction collection on the PCGC, a series of ^{14}C FAMEs standards was collected in 4 PCGC runs while varying concentration and number of injections

(Table 4). Trapped compounds were then collected and combusted using the same procedure as for samples, and the resulting aliquots of CO_2 were submitted to NOSAMS for radiocarbon analysis.

Table 4. PCGC blank assessment sample description and results.

Run	Injections	Compound	Predetermined F_m	Mass C recovered (μg)	F_m measured	F_m error (1σ)
1	40	*n*-C_{18}	1.1124	35.7	1.0075	0.0039
		n-C_{24}	0.5823	36.4	0.5447	0.0033
		n-C_{30}	0	15.6	0.0597	0.0060
2	20	*n*-C_{18}	1.1124	38.8	1.0398	0.0035
		n-C_{24}	0.5823	40.4	0.5503	0.0030
		n-C_{30}	0	41.5	0.0124	0.0027
3	40	*n*-C_{18}	1.1124	n/a	n/a	n/a
		n-C_{24}	0.5823	16.8	0.5254	0.0055
		n-C_{30}	0	25.0	0.0272	0.0039
4	20	*n*-C_{18}	1.1124	24.4	1.0258	0.0051
		n-C_{24}	0.5823	24.5	0.5250	0.0038
		n-C_{30}	0	27.3	0.0103	0.0037

Due to the larger range of concentrations in this series of tests, we opted to calculate modern and dead blank contributions graphically. We do not observe any significant difference between tests with 20 or 40 injections so all data from the 4 tests were combined to calculate a total PCGC + combustion process blank. To calculate the mass of modern blank, we use results from dead *n*-C_{30} replicates and rearrange equation 4 to:

$$F_{m.m} = {}^{m_{b,mod}}/_{m_m} \qquad (7)$$

Plotting $F_{m,m}$ vs. $1/m_m$ yields a line with slope $m_{b,mod}$ (Figure 1). A best-fit line for *n*-C_{30} data was calculated using an uncertainty-weighted Model II regression Matlab routine (lsqcubic.m, E.T. Peltzer, http://www.mbari.org/staff/etp3/regress.htm). This regression yields a value of 1.1 ± 0.4 μg for the modern component of the total blank. Other calculated parameters for the regression line are listed in Table 5.

To calculate the dead component of the blank, we elect to use data from *n*-C_{24} standards due to the missing *n*-C_{18} replicate from run 3. We rearrange equation 5 to solve for $F_{m,m}$ as a function of

$1/m_m$:

$$F_{m,m} = \frac{m_{b,mod} - F_{m,t}(m_{b,mod} + m_{b,dead})}{m_m} + F_{m,t} \quad (8)$$

Applying the same uncertainty-weighted Model II regression routine, we find a slope of -0.90 (Figure 2, Table 5). Using the modern blank mass calculated from dead standard data, we find that $m_{b,dead} = 2.4 \pm 0.6$ μg. Thus the total process blank mass is 3.5 ± 0.7 μg with a F_m of 0.32 ± 0.08. We check our calculated values by applying blank corrections to *n*-C_{18} data. As shown in Table 6, corrected F_m values for *n*-C_{18} average to 1.1125, which is very close to the known value of 1.1124.

Table 5. Calculated regression parameters for *n*-C_{24} and *n*-C_{30} data. Linear regression was calculated with form y = mx + b.

Parameter	*n*-C_{24}	*n*-C_{30}
m	-0.90	1.12
b	0.570	-0.019
m error (1σ)	0.33	0.43
b error (1σ)	0.011	0.015
r	-0.88	0.94

Table 6. Measured and blank-corrected F_m values for *n*-C_{18} replicates.

Run	Measured mass C (μg)	Measured F_m	Corrected F_m
1	35.7	1.0075	1.0823
2	38.8	1.0398	1.1112
4	24.4	1.0258	1.1441
		Average:	1.1125

Combining our estimates of the combustion only and PCGC + combustion blanks, we estimate that 2.4 μg C with $F_m = 0.4$ is added during the PCGC process before combustion.

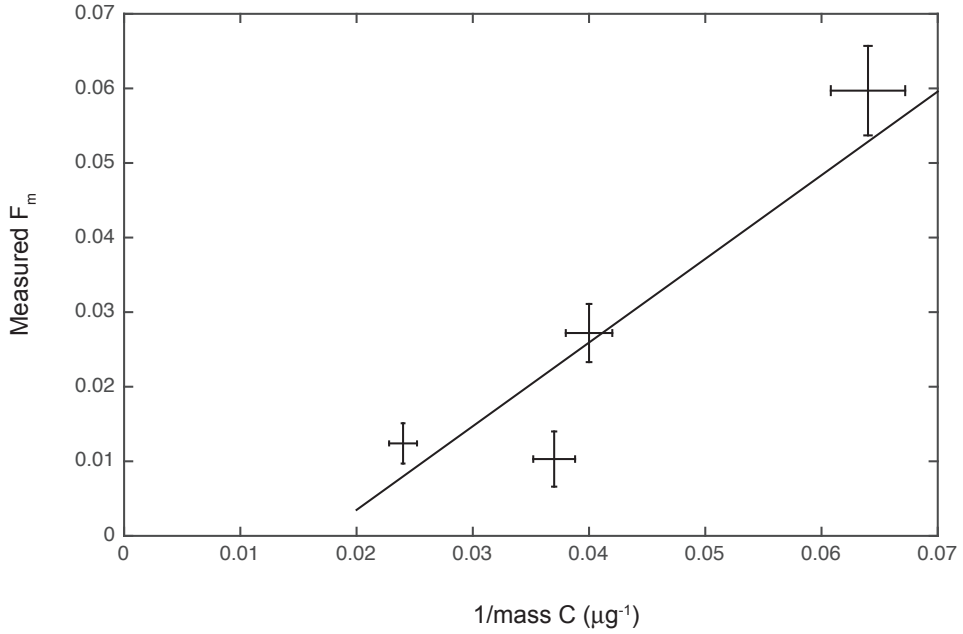

Figure 1. Measured F_m values vs. 1/mass C for *n*-C_{30} standards and uncertainty-weighted Model II regression line.

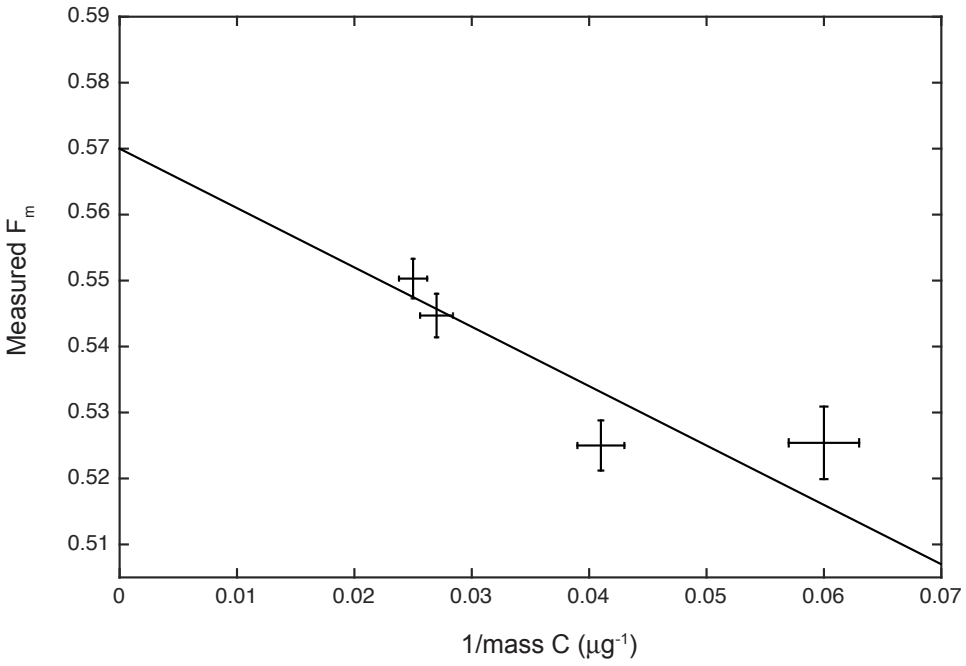

Figure 2. Measured F_m values vs. 1/mass C for *n*-C_{24} standards and uncertainty-weighted Model II regression line.

Appendix 2: Matlab scripts for calculating f_{mill} and f_{dec} for pre- or post-bomb spike samples

1. GaussFxnCalc for pre-bomb samples

```
function [fmill,millOffset,millAvgAge] =
GaussFxnCalc(sedCal,F14R,decOffset,calAge,Atm14C,sigmaDec,sigmaMill,maxOffset
,dead)
%Calculates millennial and decadal fractions using wax F14R value, sediment
calendar
%age, age of decadal pool, and 50kyr atmospheric 14C curve (calendar age, atm
%delta14C). Decadal and millennial pools are normally distributed around
%offset ages with input standard deviations.

%Important: all ages in calendar years!

%Inputs:
%sedCal = sediment age
%F14R = wax F14R value = Fm,wax/Fm,sed
%decOffset = decadal pool offset from sediment (center of normal
distribution)
%calAge = vector of time domain of atmospheric 14C curve from Intcal
%Atm14C = vector of atmospheric delta 14C values
%sigmaDec = standard deviation of decadal pool age distribution
%sigmaMill = standard deviation of millennial pool age distribution
%maxOffset = maximum millennial offset (e.g. within 2 sigma of t0)
%dead = include dead endmember (1) or do not include dead endmember (0)

%Outputs:
%millOffset = millennial age offset (center of normal distribution)
%fmill = fraction millennial with age distribution centered on millOffset
%millAvgAge = average age of millennial pool (can differ from MillOffset
since distribution is
%truncated at t0)

%Other notes:
%This program uses a time step of 10y to minimize run time.

%Create yearly atm 14C curve
x=(0:1:50000);
y=interp1(calAge, Atm14C, x);

%Define time domain for fractions
t1=sedCal;
t2=sedCal+maxOffset;
t=(t1:10:100000); %extend potential age range to 100000 yr BP to account for
very wide distributions
trange=(t1:10:t2); %range of millennial age offset

%Calculate Fm at t0 (sediment calendar age) for all t
z=size(t,2);
Fm=zeros(1,z);
for i=t1:10:100000
    index=(i-t1)/10+1;
if i<50001
    Fm(index)=(1+y(i+1)/1000).*exp(-(i-sedCal)/8267);
else
```

```
    Fm(index)=0; %set Fm=0 for any time before 50000 yr BP
end
end

Fmsed=Fm(1);

%Calculate Fm of decadal fraction
dec = normpdf(t,sedCal+decOffset,sigmaDec);
Fmdec=sum(dec.*Fm)/sum(dec);

%Create empty vectors for fmill and millAvgAge
a=size(trange,2);
fmill=zeros(a,1);
millAvgAge=zeros(a,1);

%Calculate fmill and millAvgAge for all t
for i=t1:10:t2
    norm = normpdf(t,i,sigmaMill);
    Fm1=sum(norm.*Fm)/sum(norm);
    f=(F14R-Fmdec/Fmsed)/(Fm1/Fmsed-Fmdec/Fmsed);
    avg=sum(norm.*t)/sum(norm);
    index=(i-t1)/10+1;
    fmill(index)=f;
    millAvgAge(index)=avg-sedCal;
end

%Set dead endmember
if dead==1
fmill(a+1)=1-F14R/(Fmdec/Fmsed);
millAvgAge(a+1)=50000;

millOffset(1:a,1)=trange-sedCal;
millOffset(a+1)=50000;

else
    millOffset(1:a,1)=trange-sedCal;
end
```

2. GaussFxnCalcBomb for post-bomb samples

```
function [ fmill,millOffset,millAvgAge,Fmdec ] =
GaussFxnCalcBomb( sedCal,F14R,decOffset,calAge,Atm14C,sigmaDec,sigmaMill,maxO
ffset,dead )
%Same as GaussFxnCalc but for post-bomb samples. Atm14C curve must now
%include post-bomb years (1950-2014). This program is slower than
%GaussFxnCalc since it uses a time step of 1 year instead of 10 years.

%Important: all ages in calendar years!

%Inputs:
%sedCal = sediment age
%F14R = wax F14R value = Fm,wax/Fm,sed
%decOffset = decadal pool offset from sediment (center of normal
distribution)
%calAge = vector of time domain of atmospheric 14C curve from Intcal
%Atm14C = vector of atmospheric delta 14C values
%sigmaDec = standard deviation of decadal pool age distribution
%sigmaMill = standard deviation of millennial pool age distribution
%maxOffset = maximum millennial offset (e.g. within 2 sigma of t0)
%dead = include radiocarbon dead endmember (1) or do not include dead
endmember (0)

%Outputs:
%millOffset = millennial age offset (center of normal distribution)
%fmill = fraction millennial with age distribution centered on millOffset
%millAvgAge = average age of millennial pool (can differ from MillOffset
since distribution is
%truncated at t0)

%Create yearly atm 14C curve
x=(-64:1:50000);
y=interp1(calAge, Atm14C, x);

%Define time domain for fractions
t1=sedCal;
t2=sedCal+maxOffset;
t=(t1:1:100000); %extend to 100000 yr BP to account for very wide
distributions
trange=(t1:1:t2); %potential range of millennial age offset

%Calculate Fm at t0 (sediment calendar age) for all t
z=size(t,2);
Fm=zeros(1,z);
for i=t1:1:100000
    index=i-t1+1;
if i<50001
    Fm(index)=(1+y(i+65)/1000).*exp(-(i-sedCal)/8267);
else
    Fm(index)=0; %set Fm=0 for any time before 50000 yr BP
end
end

Fmsed=Fm(1);
```

```
%Calculate Fm of decadal fraction
dec = normpdf(t,sedCal+decOffset,sigmaDec);
Fmdec=sum(dec.*Fm)/sum(dec);

%Create empty vector for fmill and millAvgAge
a=size(trange,2);
fmill=zeros(a+1,1);
millAvgAge=zeros(a+1,1);

%Calculate fmill and millAvgAge for all t
for i=t1:1:t2
    norm = normpdf(t,i,sigmaMill);
    Fm1=sum(norm.*Fm)/sum(norm);
    f1=(F14R-Fmdec/Fmsed)/(Fm1/Fmsed-Fmdec/Fmsed);
    avg=sum(norm.*t)/sum(norm);
    index=i-t1+1;
    fmill(index)=f1;
    millAvgAge(index)=avg-sedCal;
end

%Set dead endmember
if dead==1
fmill(a+1)=1-F14R/(Fmdec/Fmsed);
millAvgAge(a+1)=50000;

millOffset(1:a,1)=trange-sedCal;
millOffset(a+1)=50000;

else
    millOffset(1:a,1)=trange-sedCal;
end
```